Understanding the Current and Forecasting the Future Behaviour of DEF and ASR-Affected Concrete Beams

RENNAN MEDEIROS

Thesis submitted to the University of Ottawa
In partial fulfillment of the requirements for the degree of
DOCTOR OF PHILOSOPHY IN CIVIL ENGINEERING



Department of Civil Engineering
Faculty of Engineering
University of Ottawa

© Rennan Medeiros, Ottawa, Canada, 2026

To my family, for their unwavering encouragement and for the values that sustained me throughout this journey.

To my wife, Monica, for her patience, continuous support, and steadfast presence through every demanding stage of this work. This doctoral journey would not have been possible without you.

Abstract

Delayed ettringite formation (DEF) and alkali–silica reaction (ASR) are amongst the most harmful damage mechanisms affecting critical concrete infrastructure worldwide. Very often, these mechanisms are seen combined in the field due to physicochemical synergy. Among the factors influencing the induced development of DEF and ASR, moisture gradients and reinforcement-induced restraint are the most significant, since they modify the magnitude and distribution of induced expansion and damage. The impact of moisture gradients and reinforcement-induced restraint has been investigated individually in recent research. Yet the combined influence of these factors on the reaction kinetics and amplitude of damage over time remains insufficiently quantified at the material scale.

This PhD thesis focuses on a detailed multi-level investigation aiming to better understand how moisture gradients and reinforcement configurations modify the development of microscopic deterioration, the associated mechanical response, and the potential for further expansion in DEF- and DEF+ASR-affected concrete members. An experimental program was conducted on concrete beams affected by DEF of various damage potential (i.e., moderate and high), and by DEF+ASR, subjected to controlled moisture gradients representative of partial wetting and late water supply (rewetting). Beams included non-reinforced members and members with distinct reinforcement-induced restraint levels (i.e., moderately, and heavily). Cores were extracted along selected heights and orientations (i.e., transverse, longitudinal, and vertical) to enable direction- and depth-dependent assessment. Current condition was comprehensively assessed through a multi-level protocol integrating microscopic analysis using the Damage Rating Index (DRI) and mechanical testing using the Stiffness Damage Test (SDT). The potential for further expansion was appraised through residual expansion testing under favourable moisture and temperature conditions. A semi-empirical moisture-transfer model was further developed to support exposure-history interpretation, and a Bayesian formulation of residual expansion was implemented to produce probabilistic projection intervals, adding uncertainty to the analysis.

Results demonstrate that moisture history plays a major role in height-dependent deterioration and that reinforcement-induced restraint redistributes induced damage through direction-dependent constraints. Microscopy confirmed that, in combined mechanisms, DEF-induced damage features

are predominant in high water availability locations, whereas ASR-induced damage features are highly present in location under less favourable moisture. A DRI-based partitioning approach enabled interpretation of mechanism contributions to the “overall damage” under moisture gradients. The diagnosis-to-prognosis framework revealed that residual expansion potential depends on both exposure history and the current damage extent, while the Bayesian formulation provided bounded uncertainty envelopes suitable for conservative screening.

Finally, the findings provided a better understand of the impact of the moisture gradients and reinforcement-induced restraint on the reaction kinetics and damage development over time, which in turn can improve protocols for conditions assessment of affected concrete.

Keywords: Delayed ettringite formation (DEF); alkali–silica reaction (ASR); moisture gradients; reinforcement-induced restraint; Damage Rating Index (DRI); Stiffness Damage Test (SDT); residual expansion.

Acknowledgments

I first express my deepest gratitude to my wife, Monica, for your patience, unwavering support, and steady presence throughout every demanding stage of this doctoral journey. Your encouragement sustained my focus during periods of uncertainty and fatigue, and your confidence in me remained constant when mine wavered. This work, and the growth that accompanied it, would not have been possible without you. You inspire me, and you are the love of my life.

I thank my mother, Elita de Medeiros, for her unconditional love, sacrifices, and lifelong commitment to my education and aspirations. I also thank my sisters, Rayani Medeiros and Rayssa Medeiros, for their affection, encouragement, and pride in my path, even across distance and time. Their support provided a foundation of belonging and motivation that I carried through the most challenging parts of the PhD.

I express my sincere gratitude to Professor Dr. Leandro Sanchez, my supervisor and a trusted mentor, for accepting me as his PhD student and for opening the opportunity that initiated a new chapter of my life. I arrived with a clear aspiration to build a scientific career and with the long-standing goal of pursuing doctoral training in an international institution beyond my home country, Brazil. Professor Sanchez transformed that goal into a concrete and achievable path. He provided rigorous guidance, direct advice, and exceptional opportunities, and he consistently held my work to high standards while ensuring the support needed to meet them. His mentorship extended beyond supervision. He offered a professional reference point that combined scientific discipline with genuine care, and he became a friend whose judgment and counsel I will continue to value throughout my career. I am deeply grateful for his trust in me and for enabling me to contribute to a unique research programme developed in collaboration with leading international partners.

I thank Dr. Renaud-Pierre Martin, my co-supervisor, for trusting me with the responsibility of working on his unique and valuable experimental beams. His confidence in my work and his openness in sharing experimental history, practical insights, and analytical perspectives provided essential learning that influenced both the technical depth and the coherence of this thesis. I am also grateful to the personnel of the *Laboratoire* EMGCU for welcoming me and supporting the execution of the experimental programme, including the planning and completion of tests that were central to this research. I additionally thank Dr. François Toutlemonde for his thoughtful revisions

and constructive feedback, which strengthened the clarity, structure, and scientific positioning of this work.

I thank my friends, who consistently encouraged me in my endeavours and provided companionship that made this period of intense work more balanced and meaningful. Their friendship, conversations, and shared moments offered relief during difficult stretches and reminded me of the importance of community beyond the laboratory and the office.

I also acknowledge my colleagues from the μStructure Research Group and the broader μStructure family at the University of Ottawa. I am especially grateful to Dr. Diego de Souza, Dr. Mayra de Grazia, Dr. Olusola Olajide, and Dr. Cassandra Trottier, who welcomed me when I arrived in Canada and helped me navigate the research environment with generosity and collegiality. I also thank Dr. Yane Coutinho, Yuri Mello, Chengkai Wang, Zichun Xia, and Kiarash Kianpour for the collaboration, discussions, and shared work over the last years. I am also grateful to Maria Eduarda Coutinho for her friendship, which this PhD journey brought into my life. Working alongside all of you was an invaluable professional experience and a genuine privilege.

Finally, I acknowledge everyone who, directly or indirectly, contributed to the completion of this thesis. This journey demanded sustained effort, and it was made possible through the support, trust, and presence of many people who accompanied me along the way.

List of Contents

Abstract iii
Acknowledgments v
List of Contents vii
List of Tables xiv
List of Figures xvi
List of abbreviations xxiii
Foreword xxiv
Chapter 1 : Introduction 1
1.1 Context and motivation of the study 1
1.2 Research scope and overall organization of the PhD thesis 2
1.3 References 4
Chapter 2 : Literature Review 8
2.1 Delayed ettringite formation 8
2.1.1 Microscopic deterioration of DEF-affected concrete 12
2.1.2 Effect on mechanical properties of DEF-affected concrete under free expansion 13
2.1.3 Effect of restraint condition on DEF-induced development 16
2.2 Alkali–silica reaction (ASR) 18
2.2.1 Microscopic deterioration of ASR-affected concrete 19
2.2.2 Effect on mechanical properties of ASR-affected concrete under free expansion 20
2.2.3 Effect of restraint conditions on ASR-induced development 22
2.3 DEF+ASR-induced deterioration 25
2.4 Management protocols and advanced tools for assessing concrete affected by DEF, ASR, and DEF+ASR 26
2.4.1 Management protocol of ISR 26
2.4.2 Management protocol of ASR-affected concrete infrastructure 28
2.4.3 Advanced tools to assess the cause and extent of damage 30
2.4.3.1 Damage rating index (DRI) 31

2.4.3.2 Stiffness damage test (SDT) 32
2.4.4 Potential for further expansion 33
2.4.4.1 Residual expansion test (RE) 33
2.4.4.2 Predicting DEF and ASR expansion at the material's scale through analytical modelling 34
2.5 References 36
Chapter 3 : Problem Statement 47
Chapter 4 : Research program 49
4.1 Characteristics of the structural members investigated 49
4.1.1 Member geometry and identification 50
4.1.2 Concrete mixtures and constituent materials 50
4.1.3 Thermal treatment 52
4.1.4 Reinforcement configurations 53
4.1.5 Moisture exposure histories 53
4.1.6 Post-programme storage and transfer history 54
4.2 Sampling 55
4.2.1 Sampling from the non-reinforced beam affected by moderate DEF (P1) 55
4.2.2 Sampling from the non-reinforced beam affected by severe DEF (P2) 56
4.2.3 Sampling from the moderately reinforced beam affected by severe DEF (P3) 57
4.2.4 Sampling from the heavily reinforced beam affected by severe DEF (P4) 58
4.2.5 Sampling from the non-reinforced beam affected by severe DEF+ASR (P5) 59
4.2.6 Sampling from the heavily reinforced beam affected by severe DEF+ASR (P6) 60
4.3 Experimental procedures 60
4.3.1 Damage Rating Index and crack measurements 60
4.3.2 Stiffness Damage Test 61
4.3.3 Residual expansion 62
4.4 References 62
Chapter 5 : Core of the thesis – Scientific Papers 64
5.1 General Overview 64
5.2 Scope and objectives of the scientific papers 65

5.2.1 Paper I (Chapter 6): Microscopic assessment of DEF- and DEF+ASR-affected concrete under severe moisture gradients 65
5.2.2 Paper II (Chapter 7): Influence of moisture gradients on diagnosis and prognosis of non-reinforced DEF-affected members 66
5.2.3 Paper III (Chapter 8): Reinforcement-induced restraint effects on diagnosis and prognosis under moisture gradients in DEF-affected members 66
5.2.4 Paper IV (Chapter 9): Combined influence of moisture gradients and reinforcement-induced restraint in DEF and DEF+ASR members 67
Chapter 6 : Paper I - Microscopic assessment of DEF- and DEF+ASR-affected concrete under severe moisture gradients 68
6.1 Introduction 68
6.2 Background 69
6.2.1 DEF and DEF+ASR mechanisms 69
6.2.2 Effect of moisture gradients on DEF and DEF+ASR-induced development 71
6.2.3 DEF and DEF+ASR induced deterioration 72
6.2.4 Damage rating index (DRI) 74
6.3 Scope of the work 76
6.4 Materials and methods 76
6.4.1 Description of the specimens 76
6.4.2 Experimental procedures 79
6.5 Results 80
6.5.1 Quantitative assessment of “overall damage” through DRI 80
6.5.2 Crack density and microscopic distress features 81
6.5.3 Crack widths/lengths versus full height, upper height, and lower height 84
6.6 Discussion 86
6.6.1 Understanding the water-transfer behavior in moderate DEF, severe DEF, and DEF+ASR-affected concrete 86
6.6.2 Effect of water imbibition on the “stratified” DEF- and DEF+ASR-induced damage 95
6.6.3 Understanding DEF- and DEF+ASR-induced deterioration 99

6.6.4 Evaluating DEF- and DEF+ASR-induced distressing features as a function of the depth 102
6.6.5 Estimating the contribution of DEF and ASR to the overall deterioration 106
6.6.6 Qualitative descriptive models to describe ASR, DEF, and DEF+ASR-induced damage initiation and propagation 108
6.7 Conclusion 114
6.8 References 115
Chapter 7 : Paper II - Impact of moisture gradients on the current condition and future deterioration potential of non-reinforced beams affected by DEF 122
7.1 Introduction 122
7.2 DEF-induced damage in concrete 123
7.2.1 DEF mechanism 123
7.2.2 Advanced Appraisal of DEF-Induced Current Deterioration (Diagnosis) 125
7.2.2.1 Damage Rating Index (DRI) 125
7.2.2.2 Stiffness Damage test (SDT) 127
7.2.2.3 Multi-level assessment 128
7.2.3 Assessing the potential for future DEF-induced expansion (Prognosis) 129
7.2.3.1 Laboratory testing – Residual expansion (RE) 129
7.2.3.2 Analyzing residual expansion outcomes 130
7.3 Scope of the work 131
7.4 Materials and Methods 132
7.4.1 Description of the specimens 132
7.4.2 Experimental procedures 136
7.4.2.1 Damage rating index (DRI) 136
7.4.2.2 Stiffness damage test (SDT) 136
7.4.2.3 Residual expansion (RE) 136
7.5 Results 137
7.5.1 Damage rating index (DRI) 137
7.5.2 Stiffness damage test 138
7.5.3 Residual expansion (RE) 139

7.6 Discussion 141
7.6.1 Understanding the impact of water saturation gradients on DEF-induced deterioration 141
7.6.2 Current damage extent – multi-level assessment 153
7.6.3 DEF-induced residual expansion potential and Bayesian inference 156
7.6.4 Reconstruction of DEF-induced development 161
7.6.5 Integrated diagnosis-to-prognosis approach 166
7.7 Conclusion 168
7.8 References 169
Chapter 8 : Paper III - Evaluation of the influence of reinforcement configurations on the diagnosis and prognosis of DEF-affected concrete under moisture gradients 175
8.1 Introduction 175
8.2 Background 176
8.2.1 DEF-induced deterioration under unrestrained conditions 176
8.2.2 DEF-induced deterioration under restrained conditions: implications for current and future performance 177
8.2.3 Advanced Appraisal of DEF-Induced Current Deterioration and potential for future development 179
8.2.3.1 Multi-level assessment protocol – diagnosis 179
8.2.3.2 Potential for future deterioration – prognosis 182
8.3 Scope of the work 184
8.4 Materials and methods 185
8.4.1 Description of the specimens 185
8.4.2 Experimental procedures 188
8.4.2.1 Damage rating index (DRI) 188
8.4.2.2 Stiffness damage test (SDT) 189
8.4.2.3 Residual expansion (RE) 190
8.4.3 Interpretation framework for multi-level assessment and RE tests 190
8.5 Results 191
8.5.1 Damage rating index (DRI) 191

8.5.2 Stiffness damage test (SDT) 192
8.5.3 Residual expansion (RE) 194
8.6 Discussion 197
8.6.1 Evaluating the impact of reinforcement on the moisture gradients 197
8.6.2 Understanding the role of the reinforcement on DEF-induced development 203
8.6.3 Current damage condition 208
8.6.4 Integrated diagnostic-to-prognostic approach 211
8.7 Conclusions 214
8.8 References 215
Chapter 9 : Paper IV - Understand the impact of distinct reinforcement configurations (i.e., none and heavily reinforced) and different moisture gradients on the current and future deterioration of DEF+ASR-affected concrete 221
9.1 Introduction 222
9.2 Background 223
9.2.1 DEF- and DEF+ASR-induced damage development under unrestrained conditions 223
9.2.2 Influence of restraint and moisture gradients on DEF- and DEF+ASR-induced development 224
9.2.3 Diagnostic and prognostic tools 225
9.2.3.1 Diagnosis: microscopic and mechanical tools 225
9.2.3.2 Prognosis: Residual expansion testing and modeling 229
9.3 Research significance 230
9.4 Materials and methods 230
9.4.1 Description of the specimens 230
9.4.2 Experimental procedures 235
9.4.2.1 Damage rating index (DRI) 235
9.4.2.2 Stiffness damage test (SDT) 236
9.4.2.3 Residual expansion 236
9.4.3 Interpretation of the multi-level assessment and residual expansion 237
9.5 Results 237
9.5.1 Damage rating index (DRI) 237

9.5.2 Stiffness damage test (SDT) 238
9.5.3 Residual expansion 240
9.6 Discussion 245
9.6.1 Water-transfer boundary conditions during aging exposure 245
9.6.1.1 Semi-empirical moisture-transfer modelling and moisture-front interpretation.. 245
9.6.1.2 Microscopic assessment 251
9.6.1.3 Mechanical assessment 254
9.6.1.4 Potential for further expansion 257
9.6.2 Current damage extent condition 259
9.6.2.1 Deterioration-based estimations of induced expansion 259
9.6.2.2 “Potential chemical advancement”-based estimations of current expansion 260
9.6.2.3 Comparison of estimating induced expansion approaches: Multi-level assessment protocol (deterioration-based) and reconstruction of residual expansion (“potential chemical advancement”). 262
9.6.3 Projection of future expansion potential from the current condition 265
9.7 Conclusions 269
9.8 References 270
Chapter 10 : Scientific and Engineering contributions of the PhD thesis 279
Chapter 11 : Conclusion and recommendations 281
11.1 Conclusions 281
11.2 Recommendations for future works 283

List of Tables

Table 4.1 - Identification and boundary-condition summary for beams P1–P6. 50
Table 4.2 - Concrete mixtures, cements, and material properties for beams P1–P6 51
Table 4.3 – Identification and location of cores and slices extracted from the non-reinforced beam affected by moderate DEF (P1) 56
Table 4.4 – Identification and location of cores and slices extracted from the non-reinforced beam affected by severe DEF (P2) 57
Table 4.5 – Identification and location of cores and slices extracted from the moderately reinforced beam affected by severe DEF (P3) 58
Table 4.6 – Identification and location of cores and slices extracted from the heavily reinforced beam affected by severe DEF (P4) 59
Table 4.7 – Identification and location of cores and slices extracted from the non-reinforced beam affected by severe DEF+ASR (P5) 59
Table 4.8 – Identification and location of cores and slices extracted from the heavily reinforced beam affected by severe DEF+ASR (P6) 60
Table 6.1 – Parameter calibration for modeling the drying profiles [7] 88
Table 6.2 – Parameters used to estimate the water-transfer behavior of moderate DEF, severe DEF, and DEF+ASR-affected concrete beams. 92
Table 7.1 – Benchmark table of ISR-induced development on affected concrete [27] 129
Table 7.2 – Location and identification of cores and slices extracted from beams affected by moderate and severe DEF, including nominal coring depth, spatial coordinates, and associated testing program (DRI, SDT, and RE) 135
Table 7.3 – Parameters used to estimate the water-transfer behaviour of moderate DEF and severe DEF-affected concrete beams. 144
Table 8.1 – Benchmark table of ISR-induced development on affected concrete [7]. 182
Table 8.2 – Location and identification of cores and slices extracted from non-, moderately, and heavily reinforced beams affected by severe DEF, including nominal coring depth, spatial coordinates, and associated testing program (DRI, SDT, and RE). 187

Table 8.3 – Parameters used to estimate the water-transfer behavior of non-, moderately, and heavily reinforced DEF-affected concrete beams. 200
Table 9.1 – Benchmark table of ISR-induced development on affected concrete [18]. 228
Table 9.2 – Location and identification of cores and slices extracted from non- and heavily reinforced beams affected by DEF and DEF+ASR, including nominal coring depth, spatial coordinates, and associated testing program (DRI, SDT, and RE). 234
Table 9.3 – Parameters used to estimate the water-transfer behavior of non-reinforced (NR) and heavily reinforced (HR) beams affected by delayed ettringite formation (DEF) and combined delayed ettringite formation and alkali–silica reaction (DEF+ASR). 248

List of Figures

Figure 2.1 - Backscattered electron (BSE) images of concrete affected by delayed ettringite formation (DEF). a) 200 μm and b) 60 μm, highlighting ettringite-rich rims and cracks along the ITZ [16]..... 9
Figure 2.2 – Calibrated parameters of Larive's law. a) Ultimate expansion - ε∞; b) characteristic time - τc; c) latency time - τl [32]..... 10
Figure 2.3 - Progressive development of DEF-induced cracking in polished sections of concrete at different expansion levels: a) 0.12%, b) 0.39%, c) 0.50%, and d) 0.80%, illustrating crack initiation in the interfacial transition zone, propagation into paste and aggregates, and aggregate debonding at advanced damage stages [42]..... 13
Figure 2.4 - μCT images and binarized crack maps of DEF-affected concrete with free expansion ≈ 2%, showing closure of gaps around aggregates in the loading direction, radial opening, and progressive linking of cracks into a connected network under step loading until failure [35]..... 15
Figure 2.5 - Profiles of volumetric expansion. The red dashed lines indicate the volumetric expansion of the stress-free cylindrical specimen at each duration [50]. 16
Figure 2.6 - a) Orientation of cracks and density b) of plain stress-free, c) of reinforced specimens, c) of specimens reinforced and with stirrups, d) and prestressed specimens, e) after 336 days of immersion [34]..... 17
Figure 2.7 - Amorphous and crystalline ASR products in a cracked aggregate in concrete C1–60. Dotted line indicates boundary between amorphous and crystalline products. Interface to the cement paste at a distance of ~30 μm from upper left corner of image. HFW = 186 μm [55]..... 19
Figure 2.8 - Qualitative AAR damage model vs. levels of expansion between 0.05 and 0.30% [50]. 20
Figure 2.9 - Reductions in a) compressive strength and b) modulus of elasticity, relative to companion sound concrete of equivalent maturity, as a function of concrete expansion [73]..... 21
Figure 2.10 - Effect of relative humidity on ASR-induced mechanical deterioration a) stiffness damage index (SDI), b) plastic deformation index (PDI), c) direct shear strength reduction, and d) compressive strength reduction for ASR-affected concrete cylinders conditioned at 62%, 75%, 82%, 90%, and 100% RH at 38 °C [62]. 22

Figure 2.11 - Typical ASR-induced crack orientation obtained through image analysis on cores extracted from: a) Unrestrained block (Top view), b) 2D Confined block (Top view), b) 2D Confined block (Side/Longitudinal view) [94]. 23
Figure 2.12 - DRI number as a function of coring depth for specified coring direction and expansion level in concrete blocks. a) Unrestrained block, b) 1D Confined block, and c) 2D Confined block [94]. 24
Figure 2.13 - Reduction of mechanical properties considering various coring orientations and restraint conditions. a) SDI. b) Modulus of elasticity. c) Compressive strength [94]. 24
Figure 2.14 – LCPC flowchart for managing ISR-affected structures [2]. 27
Figure 2.15 - Global flowchart for the evaluation and management of concrete structures for ASR [103]. 29
Figure 2.16 – Damage rating index (DR). a) Damage features [110], and b) Micrograph section displaying most of the damage features [111]. 32
Figure 2.17 – Stiffness damage test. a) Test setup, and b) Definition of Stiffness damage index (SDI) and Plastic deformation index (PDI) [120]. 33
Figure 2.18 – Graphical representation of Larive's analytical model [128]. 35
Figure 4.1 – Overall structure of the PhD project. 49
Figure 4.2 – Thermal treatment applied to all the beams. a) Temperature evolution during the heat treatment compared to the results of an adiabatic test. b) Experimental temperature profile in the tank during a heat treatment. c) Heat treatment device 52
Figure 4.3 - Reinforcement configurations. a) Moderately reinforced. b) Heavily reinforced 53
Figure 4.4 – Moisture exposure. a) Phase (a). b) Phase (b) 54
Figure 5.1 – Core of the PhD Thesis – links between the scientific papers. 65
Figure 6.1 – Qualitative AAR damage model vs. levels of expansion between 0.05 and 0.30% [12]. 74
Figure 6.2 – Damage Rating Index, conventional method. a) Damage features classified in DRI analysis [57]. b) Micrograph section (1x1 cm) illustrates most of the damage features [59]..... 75
Figure 6.3 – Schematic illustration of a) the dimensions of the beams, and the locations where the slices were extracted for DRI analyses. b) the water exposure setup. Slices of c) moderate DEF, d) severe DEF, and e) severe DEF+ASR. 78

Figure 6.4 – Calculated mass of hydrates in a) moderate DEF Cement and b) severe DEF Cement as a function of time. 79
Figure 6.5 – DRI number of the full height, upper height, and lower height. 81
Figure 6.6 – Crack density of the full height, upper height, and lower height. 82
Figure 6.7 – Microscopic features of deterioration: a) Counts normalized to 100 cm². b) Percentage without applying the weighting factors. 84
Figure 6.8 – Maximum a) width and b) length of the full height, upper height, and lower height. 86
Figure 6.9 – Global mass variation (Δm/m). a) Moderate DEF, b) Severe DEF. c) DEF+ASR. 91
Figure 6.10 – Water transfer behavior. a) Moderate DEF, b) Severe DEF. c) DEF+ASR. 92
Figure 6.11 – DRI chart of all beams. a) Moderate DEF, b) Severe DEF. c) DEF+ASR. 97
Figure 6.12 – Heatmap of damage distribution over the cross-section. a) Moderate DEF, b) Severe DEF. c) DEF+ASR. 99
Figure 6.13 – Crack density as a function of depth of Moderate DEF, Severe DEF, and DEF+ASR-affected concrete. 101
Figure 6.14 – Maximum a) width and b) length as a function of depth of Moderate DEF, Severe DEF, and DEF+ASR-affected concrete. 101
Figure 6.15 – Microscopic features of deterioration as counts normalized for 100 cm^2 as a function of depth of a) Moderate DEF, b) Severe DEF, and c) DEF+ASR-affected concrete. 104
Figure 6.16 – Microscopic features of deterioration as percentage as a function of depth of a) Moderate DEF, b) Severe DEF, and c) DEF+ASR-affected concrete. 106
Figure 6.17 – Estimation of the contribution of DEF and ASR to the overall deterioration (a) counts (b) percentage as a function of depth of Moderate DEF, Severe DEF, and DEF+ASR-affected concrete. 108
Figure 6.18 – Micrographics highlighting features of deterioration across the depths of Moderate DEF, Severe DEF. DEF+ASR affected concrete. 110
Figure 6.19 – Qualitative descriptive model of a) ASR low damage potential, b) ASR high damage potential, c) DEF, and d) DEF+ASR-induced damage. 113
Figure 7.1 – Damage Rating Index method. a) Damage features classified in DRI analysis [34]. b) Micrograph section (1x1 cm) illustrating most of the damage features [38]. 126

Figure 7.2 – SDT outcomes definition. Stiffness damage index (SDI). Plastic deformation index (PDI). Non-linear index (NLI). Modulus of elasticity (ESDT). 128
Figure 7.3 – Schematic illustration of a) the dimensions of the beams (cm), and the locations where the slices and cylindrical cores were extracted. b) the water exposure setup. c) Coring process. 133
Figure 7.4 – Calculated mass of hydrates in moderate DEF Cement and severe DEF Cement as a function of time. 134
Figure 7.5 – DRI number as a function of the depths. a) Moderate DEF- and b) Severe DEF-affected beam. 137
Figure 7.6 – SDT outcomes as a function of the depths. a) Moderate DEF- and b) Severe DEF-affected beam. 139
Figure 7.7 – Residual expansion results. a) Moderate DEF- and b) Severe DEF-affected beam. 140
Figure 7.8 – Mass variation during residual expansion testing. a) Moderate DEF- and b) Severe DEF-affected beam. 141
Figure 7.9 – Estimating moisture-transfer behaviour. a) Phase a, b) Phase b. 143
Figure 7.10 – Moisture-transfer estimated behaviour. a) Moderate DEF- and b) Severe DEF-affected beam. 145
Figure 7.11 – Heatmap of damage distribution over the cross-section. a) Moderate DEF, b) Severe DEF. 149
Figure 7.12 – Residual modulus of elasticity (E/ E_0). a) Moderate DEF, b) Severe DEF. 151
Figure 7.13 – Ultimate expansion measured after 406 days of RE testing (moderate: Phases (a)+(b) - 854 days; severe: Phase (a) until 330 days only due to premature failure). a) Moderate DEF and b) Severe DEF. 152
Figure 7.14 – Global analysis of damage degree. a) Moderate DEF and b) Severe DEF. 156
Figure 7.15 – Estimated current damage extent through the multi-level protocol. a) Moderate DEF and b) Severe DEF. 156
Figure 7.16 – Probabilistic confidence interval of residual expansion via Bayesian modeling. a) Moderate DEF and b) Severe DEF. 159

Figure 7.17 – Probabilistic ranges of the apparent parameters of the residual expansion obtained via Bayesian modeling. a) Moderate DEF and b) Severe DEF. 160
Figure 7.18 – DEF-induced expansion over time for each height in beams affected by a) moderate and b) severe DEF, obtained through the reconstruction approach combined with the Bayesian modeling. 163
Figure 7.19 – Probabilistic ranges of the parameters of the sigmoidal expansion law for each height in beams affected by a) moderate and b) severe DEF, obtained from the reconstruction approach combined with Bayesian modelling. 164
Figure 7.20 – Diagnosis-to-prognosis representation of a) moderate and b) severe DEF, obtained by combining the current induced-expansion estimated through the multi-level assessment protocol with the Bayesian modeling of residual expansion. 168
Figure 8.1 – Damage Rating Index, conventional method. a) Damage features classified in DRI analysis [30]. b) Micrograph section (1x1 cm) illustrates most of the damage features [33]..... 180
Figure 8.2 – SDT outcomes definition. Stiffness damage index (SDI). Plastic deformation index (PDI). Non-linear index (NLI). Modulus of elasticity (E_{SDT}). 181
Figure 8.3 – Schematic illustration of a) the dimensions of the beams, the reinforcement configuration, and the locations where the slices and cylindrical cores were extracted. b) the water exposure setup. c) coring process. 186
Figure 8.4 – DRI number of the non-, moderately, and heavily reinforced beams. 192
Figure 8.5 – SDT outcomes a) SDI, b) PDI, c) modulus of elasticity of non-, moderately, and heavily reinforced beams as a function of coring direction (transverse, longitudinal, vertical). 194
Figure 8.6 – Residual expansion: a) non-, b) moderately, and c) heavily reinforced beams..... 196
Figure 8.7 – Residual expansion: a) non-, b) moderately, and c) heavily reinforced beams..... 197
Figure 8.8 – Estimating moisture-transfer behavior. a) Phase a, b) Phase b. 199
Figure 8.9 – Global mass variation of non- (NR), moderately (MR), and heavily (HR) reinforced beams 200
Figure 8.10 – Water transfer behavior as a function of time of a) non-, b) moderately, and c) heavily reinforced beams affected by DEF. 202
Figure 8.11 – Microscopic features of deterioration: a) Counts normalized to 100 cm^2. b) Percentage without applying the weighting factors. 203

Figure 8.12 – Crack characteristics of DEF-affected beams with distinct reinforcement configurations: a) crack density; b) maximum crack width; and c) maximum crack length for the upper and lower halves of the non-, moderately, and heavily reinforced beams..... 204
Figure 8.13 – Mechanical response from SDT for DEF-affected beams with distinct reinforcement configurations: a) residual modulus of elasticity and b) non-linear index (NLI) for the upper and lower parts of the non-, moderately, and heavily reinforced beams. 206
Figure 8.14 – Maximum residual expansion measured of non-, moderately, and heavily reinforced beams. 208
Figure 8.15 – Estimated current condition through a) multi-level induced expansion estimates (ε_{ML}) and b) reconstruction-based equivalent free-expansion offsets (ε_{rec}) 210
Figure 8.16 – Diagnostic-to-prognostic representation of a) non-, b) moderately, and c) heavily reinforced beams, obtained by combining the current induced-expansion estimated through the multi-level assessment protocol with the Bayesian modeling of residual expansion. 213
Figure 9.1 – Damage Rating Index, conventional method. a) Damage features classified in DRI analysis [67]. b) Micrograph section (1x1 cm) illustrates most of the damage features [72]..... 226
Figure 9.2 – SDT outcomes definition. Stiffness damage index (SDI). Plastic deformation index (PDI). Non-linear index (NLI). Modulus of elasticity (E_{SDT}). 227
Figure 9.3 – Schematic illustration of a) the dimensions of the beams (cm), and the locations where the slices and cylindrical cores were extracted. b) the water exposure setup. c) coring process.233
Figure 9.4 – DRI numbers of non-reinforced (NR) and heavily reinforced (HR) beams affected by delayed ettringite formation (DEF) and combined delayed ettringite formation and alkali–silica reaction (DEF+ASR). 238
Figure 9.5 – SDT outcomes a) SDI, b) PDI, c) modulus of elasticity of non-reinforced (NR) and heavily reinforced (HR) beams affected by delayed ettringite formation (DEF) and combined delayed ettringite formation and alkali–silica reaction (DEF+ASR). 239
Figure 9.6 – Residual expansion: a) non-reinforced (DEF), b) non-reinforced (DEF+ASR), and c) heavily reinforced (DEF), and d) heavily reinforced (DEF+ASR) beams. 243
Figure 9.7 – Mass gain during residual expansion testing: a) non-reinforced (DEF), b) non-reinforced (DEF+ASR), and c) heavily reinforced (DEF), and d) heavily reinforced (DEF+ASR) beams. 244

Figure 9.8 – Global mass variation: a) non-reinforced (DEF), b) non-reinforced (DEF+ASR), c) heavily reinforced (DEF), and d) heavily reinforced (DEF+ASR)..... 248
Figure 9.9 – Water transfer behavior as a function of time of a) non-reinforced (DEF), b) non-reinforced (DEF+ASR), c) heavily reinforced (DEF), and d) heavily reinforced (DEF+ASR). 250
Figure 9.10 – Microscopic features of deterioration: a) Counts normalized to 100 cm². b) Percentage without applying the weighting factors. 252
Figure 9.11 – Crack characteristics: a) crack density; b) maximum crack width; and c) maximum crack length. 253
Figure 9.12 – Mechanical response from SDT for of non-reinforced (NR) and heavily reinforced (HR) beams affected by delayed ettringite formation (DEF) and combined delayed ettringite formation and alkali–silica reaction (DEF+ASR): a) residual modulus of elasticity and b) non-linear index (NLI). 255
Figure 9.13 – Maximum residual expansion measured of non-reinforced (NR) and heavily reinforced (HR) beams affected by DEF and DEF+ASR. 258
Figure 9.14 – Current damage extent condition estimated through the multi-level assessment protocol. 260
Figure 9.15 – Current expansion estimated through the reconstruction approach. 262
Figure 9.16 – Comparison between deterioration-based induced expansion and “potential chemical advancement”-based expansion estimates. 265
Figure 9.17 – Diagnostic-to-prognostic representation of a) non-reinforced (DEF), b) non-reinforced (DEF+ASR), c) heavily reinforced (DEF), and d) heavily reinforced (DEF+ASR) obtained by combining the current induced-expansion estimated through the multi-level assessment protocol with the Bayesian modeling of residual expansion. 267

List of abbreviations

Acronym	Definition
AAR	Alkali-aggregate reaction
ACI	American Concrete Institute
ACR	Alkali-Carbonate Reaction
ASR	Alkali-Silica Reaction
CAD	Coarse aggregate de-bonded
CCA	Closed Crack in the Aggregate
CCP	Crack in the Cement Paste
CCP-RP or CCP-G	Crack in the cement paste with reaction products
DAP	Disaggregate/corroded aggregate particle
DEF	Delayed ettringite formation
DRI	Damage Rating Index
EMGCU	Laboratoire Expérimentation et Modélisation pour le Génie Civil et Urbain
GU	General Use Portland Cement
HDI	Highest Density Interval
HR	Heavily reinforced
ICAAR	International Conference on Alkali-Aggregate Reaction in Concrete
ISA	Internal sulfate attack
ISR	Internal swelling reaction
ITZ	Interfacial Transition Zone
L	Longitudinal cores
LCPC	Laboratoire Central des Ponts et Chaussées
L_{max}	Maximum length of the cracks
MCMC	Markov chain Monte Carlo
E	Modulus of elasticity
NLI	Non-Linearity Index
NR	Non-reinforced
OCA	Open Crack in the Aggregate
OCA-RP or OCA-G	Open crack in the aggregate with reaction products
PDI	Plastic Deformation Index
RE	Residual expansion
RH	Relative humidity
RMSE	Root mean square error
SDI	Stiffness Deformation Index
SDT	Stiffness Damage Test
T	Transverse cores
V	Vertical cores
W_{max}	Maximum width of the cracks

Foreword

This PhD thesis evaluates the impact of moisture gradients and reinforcement-induced restraint on concrete beams affected by delayed ettringite formation (DEF) and combined DEF and alkali–silica reaction (DEF+ASR). The objective of the work is to better understand the impact of the abovementioned factors on the reaction kinetics and damage development over time, which in turn will improve protocols for conditions assessment (i.e., characterizing current and potential for future damage) of affected concrete.

This document follows a paper-based format. The core of the thesis consists of four scientific papers that address complementary aspects of the research objectives. The introductory chapters provide the general context, a focused literature review, the problem statement and objectives, and a summary of the experimental programme and analysis procedures adopted to support the four studies.

The experimental testing was carried out at Université Gustave Eiffel with the assistance of the technical staff of the *Laboratoire* EMGCU (*Expérimentation et Modélisation pour le Génie Civil et Urbain*). The author performed the full treatment and analysis of the datasets used in the thesis and prepared the initial manuscript versions of the papers included in this document. The manuscripts were reviewed by the supervisors and co-authors, who provided comments and recommendations for revision.

Finally, the last chapters of this document present the conclusions and recommendations derived from the results obtained in this study.

Chapter 1: Introduction

1.1 Context and motivation of the study

Internal swelling reactions (ISR) are among the most harmful processes that compromise the durability and serviceability of critical concrete infrastructure worldwide [1–4]. The most prevalent ISR mechanisms are alkali-silica reaction (ASR) [5] and delayed ettringite formation (DEF) [6], which can occur independently and in combination. Their mutual occurrence leads to physicochemical synergy, which enhances their manifestation in practice [7–9]. Among the factors influencing the induced development of DEF and ASR, moisture gradients and reinforcement-induced restraint are the most significant, since they modify the magnitude and distribution of induced expansion and damage [1-9].

In recent years, numerous recommendations and testing protocols have been introduced to evaluate the reactivity potential, preventive measures, diagnosis, and prognosis of these harmful mechanisms. Before the concrete is placed, the potential reactivity of aggregates to ASR (e.g., accelerated mortar bar test - AMBT [10–12] and concrete prism test – CPT [13–15]), concrete mixes to DEF (e.g., DEF-performance testing [16]), and the effectiveness of preventive measures (i.e., controlling concrete alkali and sulfate content, using supplementary cementing materials (SCM), and managing temperature development during early stages) are assessed. While there is consensus that constructing concrete infrastructure with a low risk of ASR and DEF is nowadays achievable, there is no general agreement on implementing effective methods to mitigate ASR and DEF once they occur in the field [2,17–22].

In this scenario, several optimized test protocols have been developed to assess condition (i.e., diagnose the cause and extent of damage) and appraise the potential for further deterioration in ASR- and DEF-affected concrete at the material[1] scale. These steps are essential for informing structural modeling, selecting appropriate rehabilitation strategies, and determining reassessment periods [2,20,22–25]. Among the proposed protocols, the multi-level assessment, which combines

[1] The materials scale in this work refers to laboratory-made specimens and cores extracted from structural members, usually with approximate dimensions of 100mm x 200mm (North America) or 110mm x 220mm (France), diameter x length, respectively.

microscopic (Damage Rating Index - DRI) and mechanical (Stiffness Damage Test - SDT) evaluations, has proven suitable for appraising ASR, DEF, and DEF+ASR-induced deterioration under unrestraint (i.e., free expansion) [26–29] and under restraint configurations associated with ASR-induced deterioration (i.e., 1D, 2D) [30–34]. This protocol was developed using a database obtained from concrete mixtures produced and exposed under constant, controlled conditions selected to accelerate reaction development (i.e., 38°C and >95% relative humidity). A few recent studies have highlighted the efficiency of the multi-level assessment approach in evaluating aging infrastructure affected by ISR [35–38]. Additionally, residual expansion testing has been widely used to appraise the potential for further deterioration of ASR and DEF-affected structures, with varying degrees of efficiency depending on the structure's type and condition [21,22,39–41].

Although DEF and ASR induced development and associated deterioration have been better understood through the advancement of diagnostic and prognostic tools [2,21,22,35], the combined influence of moisture gradients and reinforcement-induced restraint on the reaction kinetics and amplitude of damage over time remains insufficiently quantified at the material scale. This gap includes crack patterns and their orientation and distribution, the resulting impact on mechanical properties, the interplay between both mechanisms, and the residual expansion potential used to forecast further swelling and damage development.

1.2 Research scope and overall organization of the PhD thesis

This PhD thesis is centred on the evaluation of the current damage and the potential of future deterioration of concrete beams affected by delayed ettringite formation (DEF) and combined DEF and alkali–silica reaction (DEF+ASR) under distinct moisture gradients and reinforcement-induced restraint. The work builds on a unique and comprehensive experimental program initiated at *Université Gustave Eiffel* [9], in which beams were cast with controlled mixture designs and thermal histories, conditioned to trigger DEF or DEF+ASR, and subsequently exposed to long-term moisture gradients. The thesis focuses on a set of non-reinforced and reinforced beams that exhibit different deterioration potentials, reinforcement configurations, and moisture exposure histories, and applies a consistent set of diagnostic and prognostic tools to assess their current condition and residual expansion potential at the material scale.

Three main elements define the scope of the work. First, the thesis adopts a multi-level assessment strategy that combines microscopic observations (Damage Rating Index - DRI), mechanical indices derived from the Stiffness Damage Test (SDT), and residual expansion measurements on cores extracted along the height and length of the beams in different directions. These techniques are applied systematically to characterise DEF- and DEF+ASR-induced damage evolution under moisture gradients, to investigate the influence of reinforcement on the anisotropy of deterioration and stiffness loss, and to explore the consistency between microscopic, mechanical, and residual expansion indicators throughout the members. Second, the study addresses the role of moisture gradients and reinforcement configurations, contrasting non-reinforced DEF-affected beams with beams incorporating different reinforcement layouts and with beams in which DEF+ASR develops under similar exposure conditions. Third, the thesis is restricted to the condition assessment aspects (i.e., diagnosis and prognosis) of internal swelling reactions (i.e., DEF and DEF+ASR); it does not develop mitigation or repair strategies, nor does it include full structural modelling of the beams.

The thesis follows a paper-based format. After the present introduction, Chapter 2 provides a brief literature review, where a discussion on the current understanding of the physicochemical mechanisms of DEF, ASR, and combined DEF+ASR takes place. Chapter 2 also examines the induced expansion and deterioration associated with DEF and ASR, and their impact on mechanical properties under free and restrained conditions The chapter further synthesises the influence of moisture gradients and reinforcement-induced restraint on the development of deterioration. Finally, it summarises current management protocols applied to ASR- and DEF-affected structures and reviews advanced diagnostic and prognostic tools used to assess current condition and forecast further deterioration.

Chapter 3 presents the problem statement and the thesis objective, while Chapter 4 describes the beam series, including concrete compositions and initial mechanical properties, thermal treatments, deterioration potential, and reinforcement configurations. It then details the exposure conditions and moisture histories, distinguishing the phases of water supplied, and explains the coring strategy adopted to capture variations of damage. The chapter also summarises the testing protocols for DRI, SDT, and residual expansion, together with the data analysis procedures used to construct damage and expansion estimation profiles and to interpret the results in light of semi-empirical modelling of moisture transfer.

Chapter 5 introduces the core of the PhD thesis through scientific papers. It outlines how the four papers collectively achieve the research objectives, explains the rationale for their sequencing, and delineates the specific contribution of each paper.

Chapters 6 to 9 reproduce, with minor adaptations for consistency of notation and cross-referencing, the four scientific papers that constitute the core of the thesis. Each chapter follows the conventional structure of a journal article, including its own introduction, background, experimental framework, results, discussion, and conclusions. Where appropriate, cross-references to Chapters 2, 3, and 4 are included to situate each study within the broader context and research programme, while preserving the integrity of the individual papers as standalone contributions.

Finally, the conclusions and recommendations for future research are presented in Chapters 10 and 11.

1.3 References

[1] B. Fournier, M.-A. Bérubé, Alkali-aggregate reaction in concrete: a review of basic concepts and engineering implications, Canadian Journal of Civil Engineering 27 (2000) 167–191. https://doi.org/10.1139/l99-072.

[2] P. Fasseu, B. Mahut, Aide à la gestion des ouvrages atteints de réactions de gonflement interne : Guide méthodologique, GUIDES TECHNIQUES, Laboratoire Central des Ponts et Chaussées (LCPC), Paris, 2003.

[3] L.F.M. Sanchez, Internal Swelling Reactions in Concrete: Mechanisms and Condition Assessment, 1st ed., CRC Press, Boca Raton, 2024. https://doi.org/10.1201/9781003188155.

[4] F. Toutlemonde, Structural implications and management of infrastructure assets affected by ISR: example of French experience on road bridges, Canadian Journal of Civil Engineering 52 (2025) 1843–1851. https://doi.org/10.1139/cjce-2025-0120.

[5] A. Poole, I. Sims, eds., Alkali-Aggregate Reaction in Concrete A World Review, 1st ed., CRC Press, Boca Raton, 2020.

[6] B. Godart, L. Divet, Lessons learned from structures damaged by delayed ettringite formation and the French prevention strategy, in: Fifth International Conference on Forensic Engineering, Institution of Civil Engineers, London (UK), 2013: pp. 389–400.

[7] B. Godart, J. Wood, Interaction of DEF and AAR, a review, Revista Portuguesa de Engenharia de Estruturas. Ed. LNEC. 3 (2021) 25–34.

[8] K.L. Scrivener, J.P. Skalny, Conclusions of the International RILEM TC 186-ISA workshop on Internal Sulfate Attack and Delayed Ettringite Formation (4–6 September 2002, Villars, Switzerland), Materials and Structures/Materiaux et Constructions 38 (2005) 659–663. https://doi.org/10.1617/14111.

[9] R.P. Martin, Analyse sur structures modèles des effets mécaniques de la réaction sulfatique interne du béton, PhD thesis, Université Paris Est., 2010. https://theses.hal.science/tel-00558200.

[10] Canadian Standards Association (CSA Group), CSA A23.2-25A:24 Test Method for detection of alkali-silica reactive aggregate by accelerated expansion of mortar bars, in: CSA A23.1:24/CSA A23.2:24 Concrete Materials and Methods of Concrete Construction/Test Methods and Standard Practices for Concrete, 14th ed., CSA Group, Toronto, Ontario, Canada, 2024: pp. 599–607.

[11] ASTM, C1260-23: Test Method for Potential Alkali Reactivity of Aggregates (Mortar-Bar Method), West Conshohocken, PA, USA, 2023. https://doi.org/10.1520/C1260-23.

[12] P.J. Nixon, I. Sims, RILEM Recommended Test Method: AAR-2—Detection of Potential Alkali-Reactivity—Accelerated Mortar-Bar Test Method for Aggregates, in: P.J. Nixon, I. Sims (Eds.), RILEM Recommendations for the Prevention of Damage by Alkali-Aggregate Reactions in New Concrete Structures: State-of-the-Art Report of the RILEM Technical Committee 219-ACS, Springer Netherlands, Dordrecht, 2016: pp. 61–77. https://doi.org/10.1007/978-94-017-7252-5_4.

[13] Canadian Standards Association (CSA Group), CSA A23.2-14A:24 Test Method for potential expansivity of aggregates due to alkali-aggregate reaction in concrete prisms, in: CSA A23.1:24/CSA A23.2:24 Concrete Materials and Methods of Concrete Construction/Test Methods and Standard Practices for Concrete, 14th ed., CSA Group, Toronto, Ontario, Canada, 2024: pp. 514–527.

[14] ASTM, C1293/C1293M: Test Method for Determination of Length Change of Concrete Due to Alkali-Silica Reaction, West Conshohocken, PA, USA, 2024. https://doi.org/10.1520/C1293_C1293M-23AE01.

[15] P.J. Nixon, I. Sims, RILEM Recommended Test Method: AAR-3—Detection of Potential Alkali-Reactivity—38 °C Test Method for Aggregate Combinations Using Concrete Prisms, in: P.J. Nixon, I. Sims (Eds.), RILEM Recommendations for the Prevention of Damage by Alkali-Aggregate Reactions in New Concrete Structures: State-of-the-Art Report of the RILEM Technical Committee 219-ACS, Springer Netherlands, Dordrecht, 2016: pp. 79–97. https://doi.org/10.1007/978-94-017-7252-5_5.

[16] A. Pavoine, L. Divet, Réactivité d'un béton vis-à-vis d'une réaction sulfatique interne: Essai de performance. Méthode d'essai no 66, Techniques et méthodes des laboratoires des ponts et chaussées, Laboratoire Central des Ponts et Chaussées (LCPC), Paris, France, 2007. https://www.ifsttar.fr/fileadmin/user_upload/editions/lcpc/MethodeDEssai/MethodeDEssai-LCPC-ME66.pdf.

[17] B. Fournier, M.A. Bérubé, K. Folliard, M. Thomas, Report on the Diagnosis, Prognosis, and Mitigation of Alkali-Silica Reaction (ASR) in Transportation Structures, FHWA-HIF-09-004, Federal Highway Administration (FHWA), U.S. Department of Transportation, Washington, D.C., USA, 2010. https://www.fhwa.dot.gov/pavement/concrete/pubs/hif09004/hif09004.pdf.

[18] B. Godart, B. Mahut, P. Fasseu, M. Michel, The guide for aiding to the management of structures damaged by concrete expansion in France, in: 12th International Conference on AAR in concrete ICAAR, Beijing, China, 2004: pp. 1219–1228.

[19] B. Godart, M. Rooij, J.G.M. Wood, Guide to Diagnosis and Appraisal of AAR Damage to Concrete in Structures: Part 1 Diagnosis (AAR 6.1), RILEM, Springer, 2013.

[20] M.-A. Bérubé, N. Smaoui, B. Bissonnette, B. Fournier, Outil d'évaluation et de gestion des ouvrages d'art affectés de réactions alcalis-silice (RAS), Ministère des Transports du Québec, Québec, QC, Canada, 2005. https://numerique.banq.qc.ca/patrimoine/details/52327/51188.

[21] K.J. Folliard, M.D.A. Thomas, B. Fournier, Protocol for the Diagnosis and Prognosis of Concrete Structures Affected by Alkali-Silica Reaction and/or Delayed Ettringite Formation, Concrete Durability Center, The University of Texas at Austin, Austin, Texas, USA, 2007.

[22] B. Fournier, M.-A. Bérubé, K.J. Folliard, M. Thomas, ASR Testing and Evaluation Protocols Protocol B: Diagnosis Prognosis and Mitigation of Alkali-Silica Reaction (ASR) in Transportation Structures, The Transtec Group, prepared for the Federal Highway Administration, Final Version, 2008.

[23] R.V. Gorga, L.F.M. Sanchez, B. Martín-Pérez, FE approach to perform the condition assessment of a concrete overpass damaged by ASR after 50 years in service, Eng Struct 177 (2018) 133–146. https://doi.org/10.1016/j.engstruct.2018.09.043.

[24] R.V. Gorga, L.F.M. Sanchez, B. Martín-Pérez, M. Noël, Engineering-based finite element approach to appraise reinforced concrete structures affected by alkali-aggregate reaction, Magazine of Concrete Research 74 (2022) 379–391. https://doi.org/10.1680/jmacr.20.00235.

[25] R.V. Gorga, L.F.M. Sanchez, B. Martín-Pérez, P.L. Fecteau, A.J.C.T. Cavalcanti, P.N. Silva, Finite Element Assessment of the ASR-Affected Paulo Afonso IV Dam, Journal of Performance of Constructed Facilities 34 (2020) 04020065. https://doi.org/10.1061/(asce)cf.1943-5509.0001456.

[26] L.F.M. Sanchez, T. Drimalas, B. Fournier, D. Mitchell, J. Bastien, Comprehensive damage assessment in concrete affected by different internal swelling reaction (ISR) mechanisms, Cem Concr Res 107 (2018) 284–303. https://doi.org/10.1016/j.cemconres.2018.02.017.

[27] L.F.M. Sanchez, B. Fournier, M. Jolin, D. Mitchell, J. Bastien, Overall assessment of Alkali-Aggregate Reaction (AAR) in concretes presenting different strengths and incorporating a wide range of reactive aggregate types and natures, Cem Concr Res 93 (2017) 17–31. https://doi.org/10.1016/j.cemconres.2016.12.001.

[28] L.F.M. Sanchez, Contribution to the assessment of damage in aging concrete infrastructures affected by alkali-aggregate reaction, PhD thesis, Université Laval, 2014. https://www.collectionscanada.ca/obj/thesescanada/vol2/QQLA/TC-QQLA-30764.pdf.

[29] E.R. Giannini, L.F.M. Sanchez, A. Tuinukuafe, K.J. Folliard, Characterization of concrete affected by delayed ettringite formation using the stiffness damage test, Constr Build Mater 162 (2018) 253–264. https://doi.org/10.1016/j.conbuildmat.2017.12.012.

[30] A. Zahedi, C. Trottier, L.F.M. Sanchez, M. Noël, Microscopic assessment of ASR-affected concrete under confinement conditions, Cem Concr Res 145 (2021) 106456. https://doi.org/10.1016/j.cemconres.2021.106456.

[31] A. Zahedi, C. Trottier, L. Sanchez, M. Noël, Evaluation of the induced mechanical deterioration of alkali-silica reaction affected concrete under distinct confinement conditions through the Stiffness Damage Test, Cem Concr Compos 126 (2022) 104343. https://doi.org/10.1016/j.cemconcomp.2021.104343.

[32] A. Zahedi, L. F M Sanchez, M. Noël, Appraisal of visual inspection techniques to understand and describe ASR-induced development under distinct confinement conditions, Constr Build Mater 323 (2022) 126549. https://doi.org/10.1016/j.conbuildmat.2022.126549.

[33] A. Zahedi, C. Trottier, L.F. M. Sanchez, M. Noël, Condition assessment of alkali-silica reaction affected concrete under various confinement conditions incorporating fine and coarse reactive aggregates, Cem Concr Res 153 (2022) 106694. https://doi.org/10.1016/j.cemconres.2021.106694.

[34] A. Zahedi, Evaluating ASR Physicochemical Process Under Distinct Restraint Conditions for a Better Assessment of Affected Concrete Infrastructure, PhD thesis, University of Ottawa, 2022.

[35] L.F.M. Sanchez, B. Fournier, D. Mitchell, J. Bastien, Condition assessment of an ASR-affected overpass after nearly 50 years in service, Constr Build Mater 236 (2020) 117554. https://doi.org/10.1016/j.conbuildmat.2019.117554.

[36] H. Ahmed, A. Zahedi, L.F.M. Sanchez, P.-L. Fecteau, Condition assessment of ASR-affected reinforced concrete columns after nearly 20 years in service, Constr Build Mater 347 (2022) 128570. https://doi.org/10.1016/j.conbuildmat.2022.128570.

[37] R. Medeiros, L. Sanchez, A.C. dos Santos, Exploring microscopic and mechanical tools to uncover the anisotropic damage evolution of prestressed concrete sleepers affected by internal swelling reactions, Magazine of Concrete Research 77 (2025) 891–902. https://doi.org/10.1680/jmacr.25.00060.

[38] R. Medeiros, D.J. De Souza, L.F.M. Sanchez, A.C. Santos, Condition assessment of pre-tensioning prestressed concrete sleepers distressed by internal swelling reactions (ISR), CEMENT 21 (2025) 100154. https://doi.org/10.1016/j.cement.2025.100154.

[39] N. Zubaida, Evaluation of the potential of residual expansion of concrete affected by alkali aggregate reaction, Master, University of Ottawa, 2020.

[40] R.-P. Martin, L. Sanchez, B. Fournier, F. Toutlemonde, Evaluation of different techniques for the diagnosis & prognosis of Internal Swelling Reaction (ISR) mechanisms in concrete, Constr Build Mater 156 (2017) 956–964. https://doi.org/10.1016/j.conbuildmat.2017.09.047.

[41] M.-A. Bérubé, D. Chouinard, M. Pigeon, J. Frenette, M. Rivest, D. Vézina, Effectiveness of sealers in counteracting alkali-silica reaction in highway median barriers exposed to wetting and drying, freezing and thawing, and deicing salt, Canadian Journal of Civil Engineering 29 (2002) 329–337. https://doi.org/10.1139/l02-010.

Chapter 2: Literature Review

Internal swelling reaction (ISR) mechanisms are deterioration processes that generate internal pressure within the concrete microstructure, usually in the presence of moisture. This pressure induces expansion and progressive damage in the affected concrete, which manifests as cracking, stiffness reduction, and strength loss and, in turn, impairs the mechanical response of the material and the structural performance and serviceability of critical concrete infrastructure. These mechanisms are among the main deterioration processes affecting the durability of concrete structures worldwide [1–4].

One of the major challenges in managing aging, deteriorating concrete structures is converting valuable data gathered from petrographic and microscopic analyses, along with mechanical testing at the material scale, into insights on how structural performance changes at both serviceability and ultimate limit states. Consequently, information on the nature of the deterioration mechanisms affecting the structures, their current condition, and the potential for future damage is crucial for engineers selecting suitable rehabilitation strategies. Within this context, delayed ettringite formation (DEF) and alkali–silica reaction (ASR) have been identified as key ISR mechanisms affecting concrete infrastructure in many countries, acting either individually [5–9] or simultaneously in combined DEF+ASR deterioration [7,10,11].

2.1 Delayed ettringite formation

Ettringite ($Ca_6Al_2(SO_4)_3(OH)_{12}\cdot 26H_2O$) is a critical hydration product in Portland cement, existing primarily in three forms, namely primary ettringite, secondary ettringite, and heat-induced late ettringite [12–14]. Understanding these forms and their implications is essential to comprehend the deterioration phenomena associated with harmful ettringite formation. Primary ettringite forms during initial cement hydration when tricalcium aluminate (C_3A) reacts with gypsum ($CaSO_4\cdot 2H_2O$) and water. These needle-like crystals typically occupy space in the bulk cement paste and interfacial transition zone (ITZ), filling the pores within the cement paste. Scanning Electron Microscopy (SEM) images reveal that primary ettringite crystals range from 1 to 10 micrometers in length and 0.1 to 0.5 micrometers in width [14].

Secondary ettringite otherwise forms in hardened concrete due to both external and internal sources of sulfate. External sources involve sulfates from the environment penetrating concrete and reacting with calcium aluminate monosulfate within its porous structure, leading to expansion and potential damage. Internally, secondary ettringite may arise from sources such as sulfate-contaminated aggregates or over-sulfated cement, where the SO_3 content typically exceeds 3% [14,15]. This internal sulfate can react with available calcium aluminates, forming ettringite and causing expansion and cracking [16,17] (Figure 2.1).

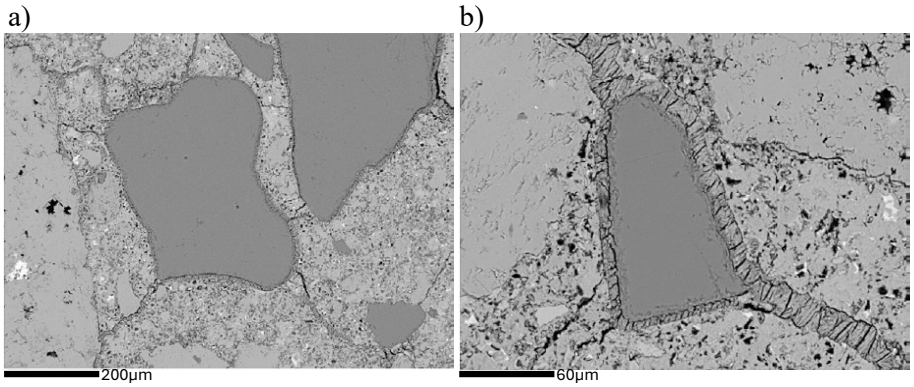
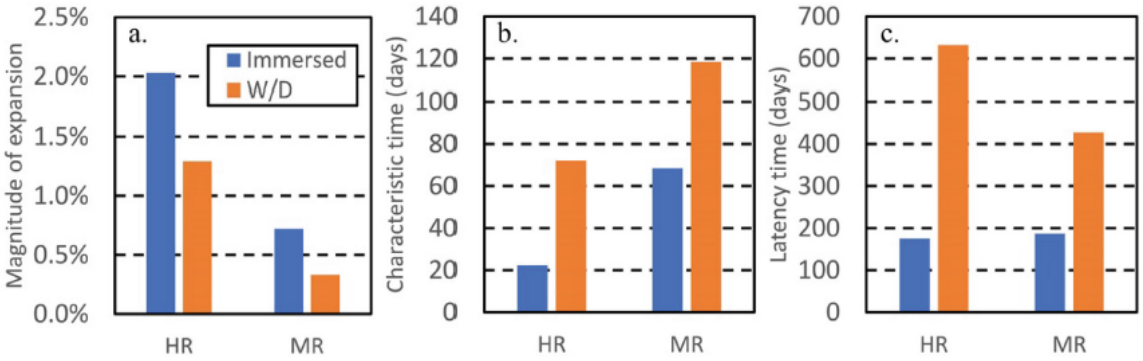


Figure 2.1 - Backscattered electron (BSE) images of concrete affected by delayed ettringite formation (DEF). a) 200 µm and b) 60 µm, highlighting ettringite-rich rims and cracks along the ITZ [16].

DEF is a particular type of secondary ettringite that requires two conditions to occur: temperature exceeding approximately 65°C after an important portion undergoes setting and sustained periods of high relative humidity [19]. Additionally, it does not involve penetration/diffusion of supplementary sulfate external sources. Such a temperature condition is commonly seen in concrete elements that are steam-cured or large structures where significant heat is generated during cement hydration [19–22]. The combined influence of maximum temperature, duration of heating, and possible thermal cycles can be represented by an effective thermal energy, defined as the time–temperature integral above a critical threshold [23,24]; for a given concrete mixture, DEF-induced expansion becomes significant once this effective thermal energy exceeds a triggering value and often shows a pessimum response, with intermediate values producing the largest ultimate expansions [25]. These high temperatures can dissolve primary ettringite or transform it into a less stable phase, such as monosulfate and other sulfate forms, also known as 'ettringite precursors'. After a dormant period, ranging from days to months, the 'ettringite precursors'

recrystallize when sufficient moisture is available. Such a dissolution or transformation of primary ettringite under high temperature characterizes DEF [14,15,20].

Moisture plays a crucial role in initiating and controlling the rate and magnitude of DEF-induced expansion and deterioration, since water acts as a reactant, medium for chemical reactions, facilitator of alkali leaching, and transport medium for 'ettringite precursors' [20,22,26–28]. Graf [29] further investigated this dependence, finding negligible DEF-induced expansion below 92% relative humidity. Furthermore, experimental investigations demonstrated that both constant and variable moisture conditions, such as wetting-drying cycles, influence the mechanism of DEF expansion differently. Under long wetting–drying cycles, concretes affected by moderate and severe DEF reached ultimate expansions similar to those under continuous immersion, although with slower kinetics [30,31]. Under short wetting–drying cycles (W/D), designed with relatively brief immersion and long drying phases, the maximum expansions were reduced by approximately 54% and 36% for the moderate and severe DEF mixtures, respectively, when compared with continuously immersed specimens [32] (Figure 2.2).



Legend: ε_∞ denotes the ultimate expansion (asymptotic plateau); τ_c denotes the characteristic time governing the expansion rate around the main growth phase (controls curve steepness); τ_l denotes the latency time, equal to the time at the inflection point (onset of rapid expansion).

Figure 2.2 – Calibrated parameters of Larive's law. a) Ultimate expansion - ε_∞; b) characteristic time - τ_c; c) latency time - τ_l [32].

These findings underscore the critical role of moisture in DEF progress, affecting both the rate and the extent of DEF-induced expansion. The study highlights that understanding the precise impact of different moisture conditions on the mechanism is essential for predicting the behavior of DEF-affected concrete [30,32].

Although DEF-induced expansion and deterioration have been described through different approaches, two mechanisms of DEF deterioration are most widely accepted in the literature: (a) localized crystallization in the ITZ, where ettringite growth induces stress concentration and cracking at the aggregate–paste interface [33,34]; and (b) homogeneous expansion of the cement paste, driven by ettringite formation in confined micropores within the outer calcium silicate hydrate (C–S–H), particularly near the boundary with inner C–S–H [35,36].

Scrivener and Skalny [14] discussed DEF as damage mechanisms that can develop through homogeneous expansion of the cement paste at the micro-scale; however, this hypothesis has not been systematically supported by microscopic observations [37]. Moreover, a purely homogeneous cement paste expansion does not fully explain the experimentally reported influence of ITZ characteristics and aggregate nature, because an invariant expansion would be expected if the cement paste response alone governed the deterioration pattern, which is not observed experimentally.

Taylor et al. [19], described homogeneous cement paste expansion in DEF-affected concrete, supported by microscopic evidence of monosulfate dispersed within C–S–H. The proposed interpretation distinguishes "outer C–S–H," located between unhydrated cement grains, from "inner C–S–H," in direct contact with unhydrated cement grains, and attributes the damage-driving pressure to ettringite formation in fine porosity within densified outer C–S–H zones near the outer-to-inner C–S–H boundary. When sulfates are released, monosulfate conversion to ettringite within confined pore volumes generates crystallization pressure, and a broadly uniform monosulfate distribution supports a homogeneous swelling response that contributes to ITZ cracking. Scrivener and Skalny [14] further associated DEF-related expansion with growth pressure of submicroscopic ettringite crystals throughout the paste, leading to generalized paste expansion and the formation of gaps around aggregate particles. Thomas et al. [18] reported that damaging DEF is associated with aggregate particles surrounded by ettringite-filled gaps and that aggregate particles can detach, leaving sockets, with abundant ettringite at the cement–aggregate interface. Additionally, Goltermann [38] explains that swelling generates hydrostatic tension within aggregate particles, radial tension within the cement paste, and tangential stresses in compression, with crack locations governed by the relative tensile strengths of the aggregate particles and the surrounding zone.

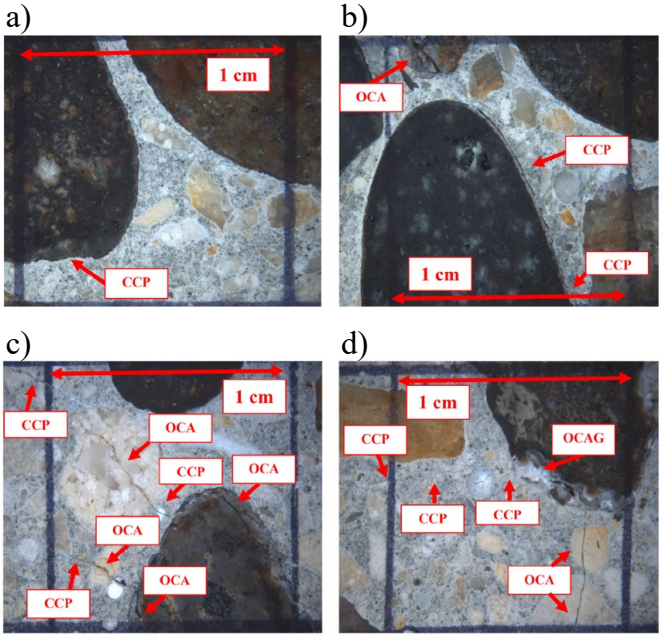
These mechanistic interpretations provide the conceptual basis for the microscopic deterioration induced by DEF discussed in the next section.

2.1.1 Microscopic deterioration of DEF-affected concrete

The microscopic deterioration of concrete due to DEF has been studied, focusing on diagnosing its contribution to overall deterioration using SEM-EDS analyses [18,39]. High-magnification microscopy enables the identification of reaction products at specific locations and supports the interpretation of local cracking processes; however, this approach remains limited for quantifying the extent of induced deterioration and for correlating it with induced expansion because increasing magnification restricts the analysed area to a scale that is not representative of the heterogeneous crack network, making outcomes sensitive to field selection and sampling density [40,41]. In contrast, the deterioration progression of DEF-affected concrete at the mesoscale has been investigated using Damage Rating Index (DRI) analyses, which provide a quantitative description of cracking development and damage accumulation as expansion increases [42,43]. In the DEF program reported by Sanchez et al. [30], laboratory-made concrete specimens were produced using a concrete prism test (CPT) mixture and subjected to a heat-curing regime to trigger DEF: 4 hours after mixing, specimens were placed in an oven, heated up to 95 °C over a 4 hour period, held at 95 °C for 12 hours, and then cooled down to 23 °C over 12 hours before subsequent immersion in water at 23 °C and monitoring of expansion levels.

Experimental observations indicate that DEF-induced deterioration initiates at relatively low expansion levels (0.10–0.12%), with open cracks forming in the interfacial transition zone (ITZ) [42]. As expansion increases, these cracks widen and extend along the paste–aggregate interface, propagate into the bulk paste, and additional cracks may develop, occasionally within aggregate particles [42]. At higher expansion levels (>0.30–0.50%), cracking becomes more widespread, crack density increases, and ITZ damage intensifies, while coarse aggregate debonding is mainly observed at advanced stages of damage rather than at early stages of DEF development [42], in contrast with classical deterioration schemes that suggest earlier debonding [38,44,45]. The resulting crack networks markedly reduce the stiffness and mechanical properties of the concrete [42,43] (Figure 2.3). Additionally, DEF can develop more rapidly and appear more severe in concrete that already contains microcracking (e.g., induced by freezing–thawing, alkali–silica

reaction, shrinkage, loading, etc.) [16,46]. On the one hand, the pre-formed cracks facilitate the transport of moisture and ions, thereby accelerating DEF precipitation. On the other hand, this pre-existing cracking provides additional space for ettringite crystallization, influencing the resulting induced expansion.



Legend: Crack in the cement paste (CCP); Open crack in the aggregate (OCA); Open crack in the aggregate with gel (OCAG).

Figure 2.3 - Progressive development of DEF-induced cracking in polished sections of concrete at different expansion levels: a) 0.12%, b) 0.39%, c) 0.50%, and d) 0.80%, illustrating crack initiation in the interfacial transition zone, propagation into paste and aggregates, and aggregate debonding at advanced damage stages [42].

2.1.2 Effect on mechanical properties of DEF-affected concrete under free expansion

Conventional undamaged concrete is characterized by relatively high compressive strength and modulus of elasticity, while its tensile strength remains comparatively low. However, these mechanical properties may undergo significant changes over time when concrete is affected by deterioration mechanisms, such as DEF [43,47]. The microscopic processes described previously for DEF, namely the progressive formation and connection of cracks in the cement paste and in the interfacial transition zone, translate directly into changes in the mechanical response of the affected material. DEF-induced expansion progressively alters the strength, stiffness, and fracture behaviour of concrete under free expansion and restrained conditions.

The reductions in mechanical properties of DEF-affected concrete under free expansion have been studied on laboratory-made specimens. The mechanism of such reductions in mechanical properties has been evaluated at the microscopic level.

The compressive strength of concrete affected by DEF is usually significantly impacted, particularly at moderate to high expansion levels (e.g., > 0.12%). Sanchez et al. [43] studied laboratory-made samples produced with a CPT concrete mixture design and subjected to a heating cycle to trigger DEF (i.e., a) 4 h after mixing, specimens were placed in an oven; b) temperature raised to 95 °C over a 4 h period; c) 12 h at 95 °C; d) temperature lowered to 23 °C throughout 12 h), after which specimens were immersed in water and monitored until reaching predefined expansion levels used to relate cracking development (Section 2.1.1) to mechanical-property losses. The compressive strength reductions were demonstrated to range from 9-34% at moderate expansion level (0.12%), 29-43% at very high expansion level (≥ 0.30%), to 40-47% and 40-50% at ultra high expansion levels (0.50 and ≥ 1.00%, respectively). Such progressive reduction is explained based on the failure mechanism of concrete under compression, which involves the initial formation of cracks in the ITZ and localized bulk cement paste, where DEF-induced cracks initiate. At very high expansions (> 0.50%), cracks propagate and interconnect, forming extensive cracking networks outlining the aggregate particles, leading to aggregate debonding and a level-off in compressive strength reduction. Complementary, Joshi et al. [48] investigated the reduction of the mechanical properties of DEF-affected laboratory-made concrete with expansions greater than 2%. Such concrete was produced with a specific concrete mixture (i.e., cement: 337kg, sand: 798kg, coarse aggregate: 965kg, and a 0.5 water-to-cement ratio). The cement used had an SO3 content of 8.65%. DEF was triggered under a) 4.5 hours at 20 °C [upon casting], a) heating ramp – 8.75 °C every 30 min until 90 °C, c) 11 hours at 90 °C, and d) cooling ramp 4.67 °C every 1 hour until 20 °C. Reductions in compressive strength of 85% were observed, and computational tomography (μCT scan) imaging was used to quantify the crack propagation under different loading patterns (Figure 2.4).

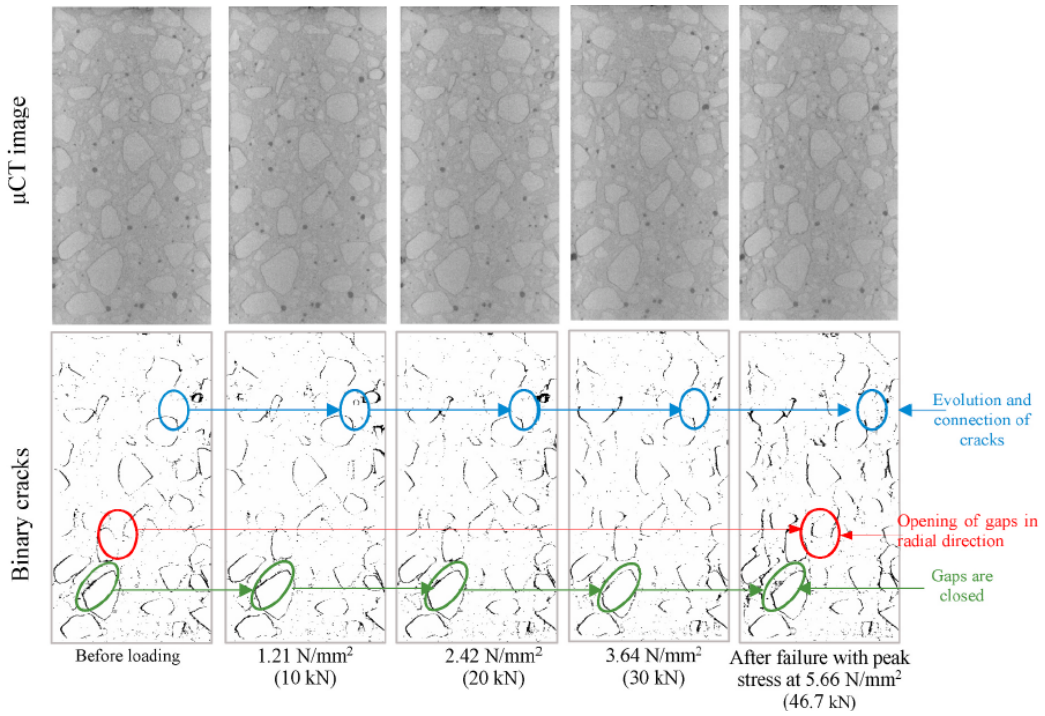


Figure 2.4 - µCT images and binarized crack maps of DEF-affected concrete with free expansion ≈ 2%, showing closure of gaps around aggregates in the loading direction, radial opening, and progressive linking of cracks into a connected network under step loading until failure [35].

Before loading, gaps around the coarse aggregates were observed, typical of DEF deterioration. These gaps closed axially and opened perpendicularly under loading. At stress levels exceeding 60% of the strength, large cracks formed around the aggregates and propagated to connect with neighboring aggregates, creating a network of cracks leading to failure. The volume of cracks, particularly those greater than 326 µm, increased significantly under high-stress levels, demonstrating the progressive nature of DEF-induced damage.

The modulus of elasticity in DEF-distressed concrete is substantially affected, with reductions ranging from 35-56% at moderate expansion levels (0.12%), 55-62% at very high expansion levels (≥ 0.30%), and 56-77% and 60-86% at ultra high expansion levels (0.50% and ≥ 1.00%, respectively). The formation of cracks in the ITZ due to DEF leads to the debonding of aggregate particles from the cement paste, thereby limiting their contribution to the system's stiffness. As these cracks continuously grow and reach significant lengths while outlining the aggregate particles, the modulus of elasticity is drastically reduced [43].

2.1.3 Effect of restraint condition on DEF-induced development

Restraint conditions significantly influence the expansion behaviour and the subsequent evolution of the mechanical properties of concrete affected by DEF. Bouzabata et al. [49] reported, in externally restrained mortar prisms, that longitudinal DEF expansion decreased by about 75–90% relative to stress-free specimens, while transverse strains remained similar or slightly larger, and volumetric expansion decreased by approximately 20%. Thiebaut et al. [47] showed, in concrete prisms subjected to uniaxial restraint, triaxial restraint, and prestress, that the final volumetric expansion relative to stress-free decreased by 27%, 56%, and 34%, respectively. Kawabata et al. [50] found, in reinforced concrete prisms, that reinforcement and stirrup confinement reduce measured DEF expansion, with lower longitudinal and transverse expansions when stirrups are present (Figure 2.5). Across mortar and concrete systems, reported reductions in measurable expansion range from approximately 27% to 87%, depending on the restraint configuration and degree of confinement [47,49,50].

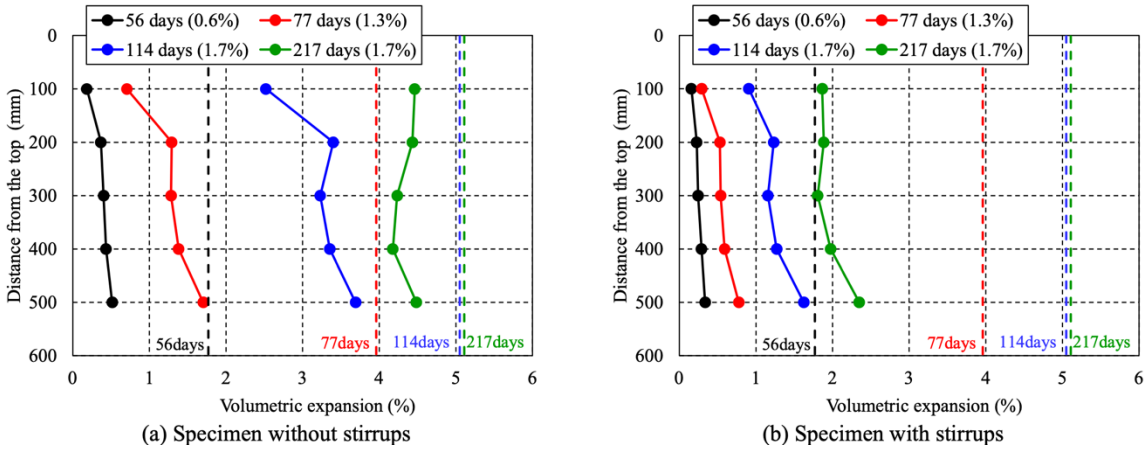


Figure 2.5 - Profiles of volumetric expansion. The red dashed lines indicate the volumetric expansion of the stress-free cylindrical specimen at each duration [50].

Microstructural observations indicate that DEF-induced cracking persists under restraint and that crack width, length, orientation, and spatial distribution differ from those in stress-free specimens due to the imposed stress state [47–50]. Bouzabata et al. [49] found that, in restrained mortars, cracks remain narrower than in stress-free specimens and are predominantly oriented parallel to the imposed compressive restraint. Thiebaut et al. [47] showed that restrained and prestressed concrete presents directional cracking aligned with the direction of restraint (Figure 2.6), with

cracking concentrated at the ITT and in the cement paste. Kawabata et al. [50] reported cracking and local damage along the rebar–concrete interface, including radial cracks and gaps that reduce the effective restraint capacity along the bonding length.

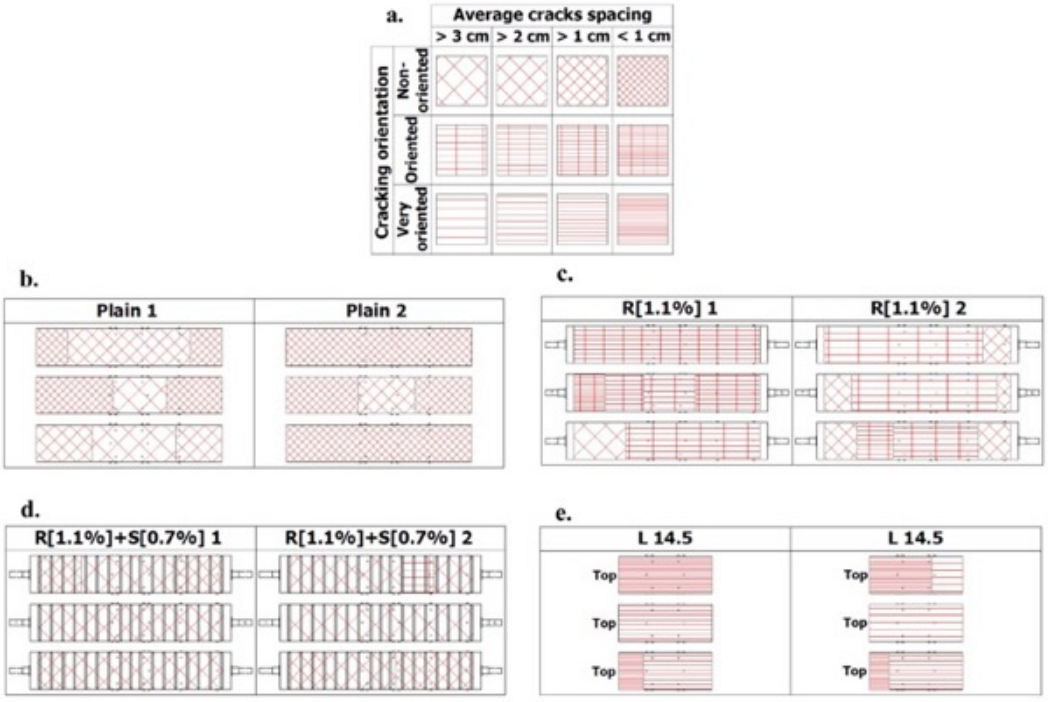


Figure 2.6 - a) Orientation of cracks and density b) of plain stress-free, c) of reinforced specimens, c) of specimens reinforced and with stirrups, d) and prestressed specimens, e) after 336 days of immersion [34].

The mechanical properties of DEF-affected concrete are impacted by restraint conditions. Restrained material can retain higher compressive strength and modulus of elasticity than stress-free material at a given exposure duration because induced strains are reduced and crack opening is limited along restrained axes [48,49]. Microstructural evidence across restrained configurations shows that internal damage continues to develop even when apparent expansion is partly suppressed, with anisotropic cracking in the paste and ITZ and cracks and gaps frequently outlining aggregate particles [47–50]. Apparent induced strain measured along a restrained axis can therefore underestimate the current internal condition when expansion records are interpreted without complementary damage indicators [47–51].

Restraint also influences the bond at the steel–concrete interface in DEF-affected members. Kawabata et al. [50] demonstrated that, in reinforced prisms without stirrups, tensile strains in

longitudinal rebars can decrease once transverse expansion reaches approximately 0.4–0.6%, indicating debonding and progressive loss of effective restraint along the bonded length; fluorescent-epoxy observations show radial cracking and local interface detachment with non-uniform stress transfer [50]. Pull-out test programs reported that average bond strength can decrease to less than half of the initial value at advanced expansion levels in specimens without confinement, accompanied by increased slip and localisation of bond stress, while stirrup confinement stabilises the bond–slip response and prevents pull-out failure within the investigated expansion range [51].

Reinforcement and restraint modify the magnitude and distribution of DEF-induced expansion and influence the development of anisotropic cracking, interfacial transition zone (ITZ) damage, and bond deterioration. Restraint should therefore be considered when interpreting measured expansion, internal damage, and residual mechanical performance in DEF-affected concrete structures.

2.2 Alkali–silica reaction (ASR)

ASR, in contrast to DEF, is a chemically distinct reaction that can produce comparable macroscopic deterioration. It involves alkali hydroxides (Na^+, K^+, OH^-) from the pore solution and metastable silica in certain aggregates (coarse and/or fine), leading to the formation of secondary products commonly referred to as ASR gel, reported as amorphous or crystalline phases (Figure 2.7) [1,52–55]. These products induce internal stresses within the reactive aggregate particles through swelling associated with water uptake and through solidification pressures developed during precipitation in confined spaces [52–54]. Moisture availability controls ASR development because water is required for ionic transport and for the expression of swelling-related stresses. Reviews and experimental evidence have commonly associated ASR expansion with external relative humidity (RH) typically above the order of 70–85% [56–59], while temperature modifies this range and can lead to measurable expansion at lower RH under elevated-temperature exposure [60].

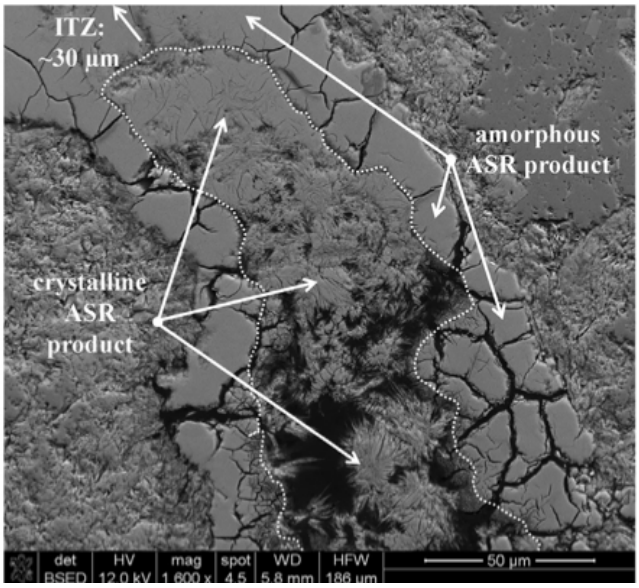


Figure 2.7 - Amorphous and crystalline ASR products in a cracked aggregate in concrete C1–60. Dotted line indicates boundary between amorphous and crystalline products. Interface to the cement paste at a distance of ~30 µm from upper left corner of image. HFW = 186 µm [55].

Moisture effects in ASR should be treated through both "level" (magnitude of expansion) and "history" (kinetics). In addition to RH thresholds, the hydric history influences the apparent expansion potential because drying, rewetting, and mass exchange modify transport and the amount of water available at reaction sites. Poyet et al. [59] explicitly treat ASR swelling as linked to mass variations and emphasise the importance of water intake history for interpreting expansion development. At the structural-member scale, Multon and Toutlemonde [61] investigated beams subjected to a unidirectional moisture gradient and used continuous measurements to relate water transfer and internal moisture distribution to swelling development. Multon and Toutlemonde [62] further examined changes in moisture conditions applied after an initial gradient exposure and documented that a late water supply can rapidly increase expansions and lead to significant cracking, illustrating the sensitivity of ASR response to boundary-condition changes and rewetting exposure.

2.2.1 Microscopic deterioration of ASR-affected concrete

The understanding of the deterioration of concrete due to ASR has evolved significantly over the years. Sanchez et al. [63] investigated concretes affected by ASR incorporating distinct aggregate

types and sources and proposed a qualitative descriptive model in which ASR-induced cracking initiates within reactive aggregate particles and, at moderate to high expansion levels, extends into the adjacent cement paste, progressively increasing crack connectivity and the extent of damage (Figure 2.8).

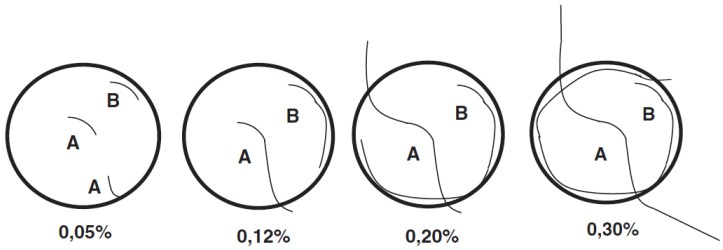


Figure 2.8 - Qualitative AAR damage model vs. levels of expansion between 0.05 and 0.30% [50].

Leemann et al. [54] provided microstructural evidence of precipitation in confined features within aggregates and near the aggregate–paste interface, identifying pressure development and crack propagation sequences that later translate into mesoscale cracking described by Sanchez et al. [63]. Olajide [60] further reported that the progression of ASR-induced deterioration, observed under different relative humidity conditions, indicated that changes in moisture availability modify the rate and magnitude of damage while preserving the aggregate-initiated nature of the cracking process.

2.2.2 Effect on mechanical properties of ASR-affected concrete under free expansion

The deterioration of ASR-affected concrete has been investigated in free expansion conditions and considered as benchmark studies to validate the effectiveness of tools in understanding the progress of deterioration and its impact on a range of mechanical properties essential for structural stability. The impact of ASR-induced expansion and deterioration on stiffness, compressive, tensile, and shear strength was comprehensively investigated in the last decade [64,65]. Despite some variability related to the material's characteristics (concrete strengths, aggregate types, and natures [fine and coarse aggregates], etc.), interesting envelopes of those mechanical properties reduction versus expansion attained depicted insights into understanding the deterioration of ASR-affected concrete. Figure 2.9a demonstrates that negligible reductions in compressive strength are observed in low and moderate deterioration levels, while important reductions are obtained at 0.20% of expansion and onwards. Similar results corroborate with those findings; concrete produced with

low to moderate reactive aggregates presented no significant impact on compressive strength [66–69], whereas important reductions in compressive strength of ASR-affected concrete may range from 40 to 60% at expansion levels higher than 0.30% [70,71]. Such behavior is explained by the combination of the ASR cracking propagation revealed by [54,63] and the mechanism of failure of concrete under compression. Such a mechanism of failure is characterized by the formation of cracks initially in the ITZ at distinct locations, propagating to the bulk cement paste and connecting to one another at later stages, causing instability and, ultimately, failure of the system under compression [72]. Thus, since cracks due to ASR start reaching the cement paste only at a moderate level of expansion and onward, no reduction in compressive strength may be expected at deterioration levels below 0.20% of the expansion.

The modulus of elasticity of concrete affected by ASR has been observed to reduce significantly at low expansion levels (i.e., 0.05%) in progressive evolution, reducing the slope of the envelope at 0.12% (Figure2.9b) [73]. Such behavior is explained based on the dependence of the modulus of elasticity of concrete on the stiffness of the aggregate, which is importantly diminished from early stages of ASR-induced deterioration levels until around 0.12% when the cracking propagation reaches the cement paste. The reduction in the modulus of elasticity impacts the stiffness of the structural members affected by ASR, making reliable assessments of such a property essential for structural appraisal.

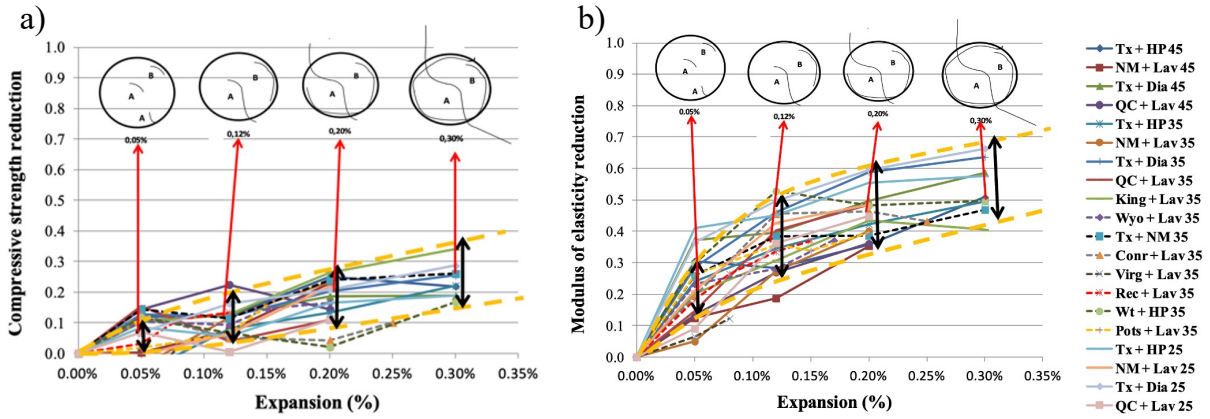


Figure 2.9 - Reductions in a) compressive strength and b) modulus of elasticity, relative to companion sound concrete of equivalent maturity, as a function of concrete expansion [73].

The ASR effect on mechanical properties under various relative humidity has been investigated in a few studies [74–76]. Olajide et al. [77] conditioned ASR-affected concrete cylinders at relative

humidities of 62%, 75%, 82%, 90%, and 100% and quantified deterioration using stiffness-damage indices (SDI, PDI), direct shear, and conventional strength metrics. They indicated that the initial SDI values measured at 38 °C (six months) at 62–82% relative humidity remained comparable to those measured at 90–100% relative humidity. They also quantified the direct shear strength loss at 38 °C as 11–25% after six months and 17–34% after 12 months, with larger losses generally associated with higher relative humidity (Figure 2.10).

Overall, ASR-induced reductions in mechanical properties as a function of RH have been observed to change, with comparable responses at 62–75% RH and increased reductions at ≥82% RH.

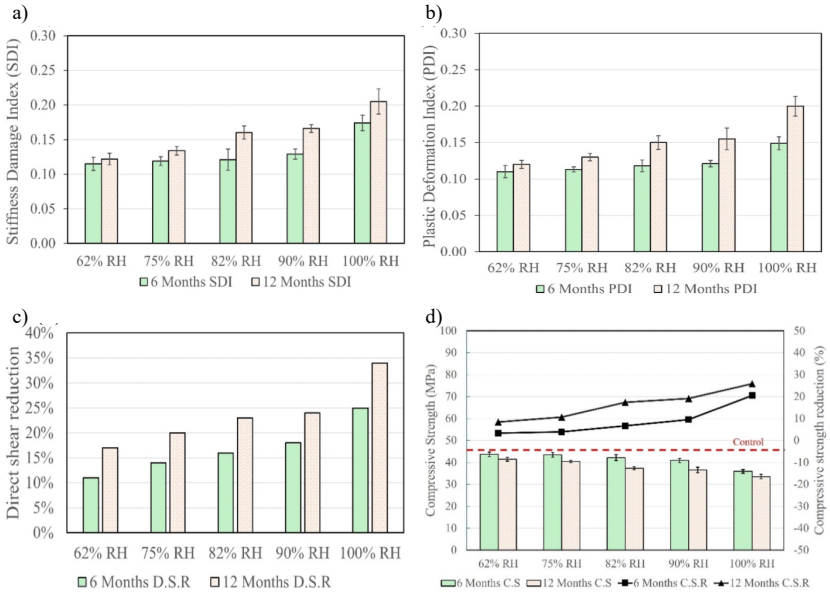


Figure 2.10 - Effect of relative humidity on ASR-induced mechanical deterioration a) stiffness damage index (SDI), b) plastic deformation index (PDI), c) direct shear strength reduction, and d) compressive strength reduction for ASR-affected concrete cylinders conditioned at 62%, 75%, 82%, 90%, and 100% RH at 38 °C [62].

2.2.3 Effect of restraint conditions on ASR-induced development

ASR-induced expansion and deterioration have often been reported as fairly isotropic under free-expansion conditions. Restraint, however, has been found to reduce expansion in the restrained direction, with reported reductions ranging from 15 to 70% [78–83] The suppressed expansion is transferred to the less restrained or unrestrained directions [78–81,84–88]. This redistribution leads to an anisotropic development of ASR-induced damage, with the degree of anisotropy increasing with the level of deterioration [89]. Boundary conditions and the configuration of reinforcement

within concrete structures heavily influence the progression and orientation of cracks induced by ASR. When concrete is confined and elastically restrained in the direction of the reinforcement, tensile stresses are developed in the reinforcing bars, leading to the suppression of ASR-induced expansion in the primary reinforcement direction. Consequently, the majority of ASR-induced cracks in such reinforced concrete members typically align parallel to the main reinforcement bars, as observed in both laboratory and field studies [89–93] (Figure 2.11).

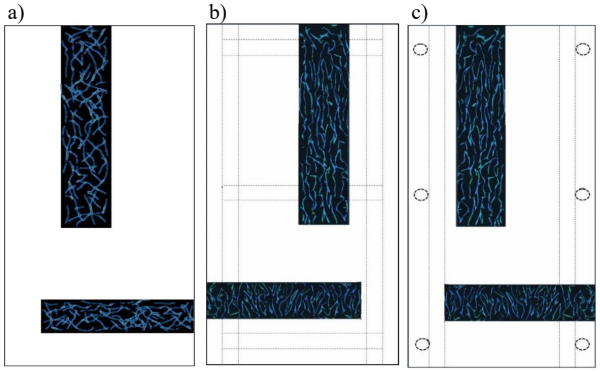


Figure 2.11 - Typical ASR-induced crack orientation obtained through image analysis on cores extracted from: a) Unrestrained block (Top view), b) 2D Confined block (Top view), b) 2D Confined block (Side/Longitudinal view) [94].

This behavior was thoroughly investigated in laboratory-made blocks under different restraint conditions (1D, 2D, and 3D) to better understand the impact on ASR-induced deterioration [25]. The investigation combined microscopic (DRI) and mechanical (SDT) testing protocols [19]. Microscopic analyses at the mesoscale using DRI revealed that unrestrained concrete blocks generally exhibit higher DRI numbers, indicating more extensive microcracking compared to restrained blocks. Specifically, at 0.15% expansion, unrestrained concrete blocks displayed DRI values around 565-580, whereas 1D and 2D restrained blocks showed lower DRI values in the range of 540-580 (Figure 2.12). Additionally, the type of reactive aggregates further influences the microscopic damage. Concrete with reactive coarse aggregates tends to develop sharper and more localized cracks, while those with reactive fine aggregates display a more diffuse cracking pattern [21].

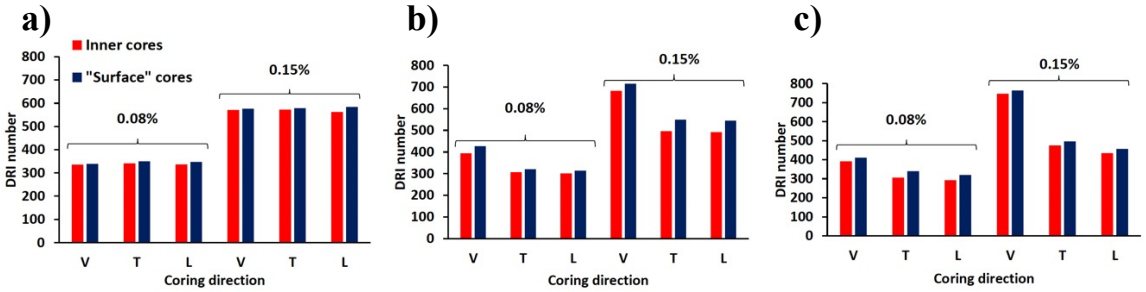


Figure 2.12 - DRI number as a function of coring depth for specified coring direction and expansion level in concrete blocks. a) Unrestrained block, b) 1D Confined block, and c) 2D Confined block [94].

Mechanically, ASR-induced expansion and deterioration vary with the direction of restraint. The modulus of elasticity and compressive strength of ASR-affected concrete are significantly impacted, with anisotropic damage observed in specimens from restrained blocks. For example, at 0.15% expansion, confined concrete blocks show a modulus of elasticity loss ranging from 35% to 44%, while compressive strength reduction varies from 17% to 24%. In contrast, unconfined blocks exhibit a slightly higher modulus of elasticity loss, indicating that confinement mitigates some of the ASR-induced mechanical degradation. The Stiffness Damage Test (SDT) results further illustrate these differences, with confined specimens showing lower SDI values (0.25-0.27) compared to unconfined ones (0.26-0.31) (Figure 2.13).

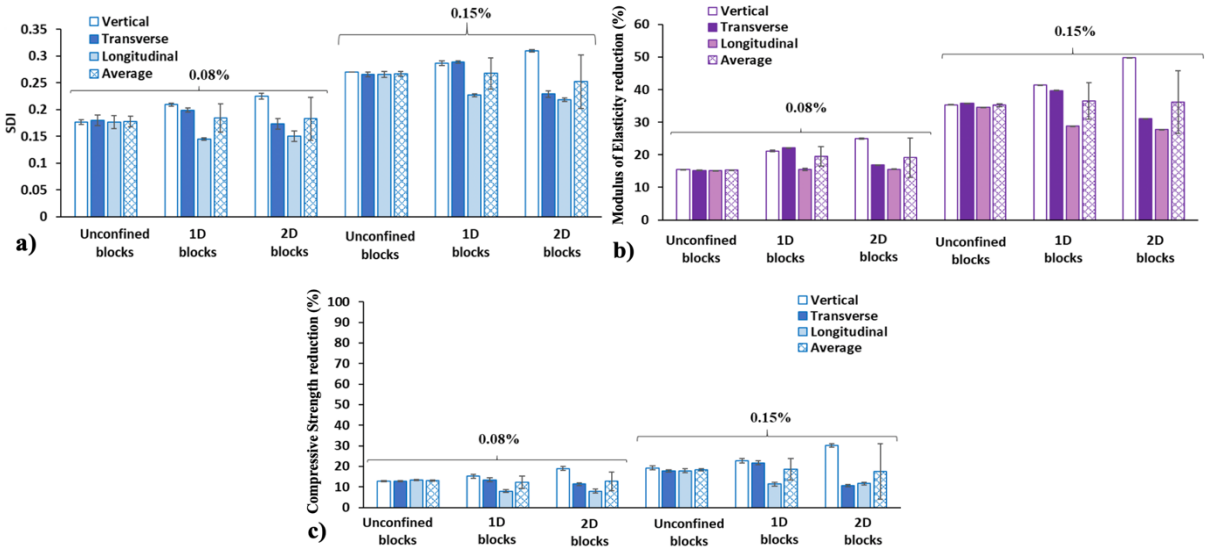


Figure 2.13 - Reduction of mechanical properties considering various coring orientations and restraint conditions. a) SDI. b) Modulus of elasticity. c) Compressive strength [94].

The orientation of microcracks also plays a critical role in the mechanical performance of ASR-affected concrete. Cores extracted parallel to the main reinforcement direction generally have fewer cracks and show less reduction in mechanical properties compared to those extracted perpendicular to the reinforcement. For instance, vertical cores from 2D confined blocks exhibited a 25-26% increase in SDI and a 10-13% decrease in ME compared to longitudinal and transverse cores. The type of reactive aggregate influences the degree of mechanical degradation, with specimens incorporating reactive fine aggregates (TX) demonstrating higher modulus of elasticity losses compared to those with reactive coarse aggregates (SP), potentially due to the different cracking mechanisms [94].

2.3 DEF+ASR-induced deterioration

Critical concrete infrastructures have been damaged by combined-induced deterioration due to delayed ettringite formation (DEF) and alkali–silica reaction (ASR) [20,95,96]. The development of DEF+ASR is facilitated by physicochemical synergies that couple local chemistry, cracking, and transport. Chemically, the formation of ASR secondary products reduces the concentration of free alkalis in the pore solution and can modify the sulfate balance and the stability conditions of sulfate-bearing phases, which supports ettringite recrystallization under favourable conditions [19,27]. Physically, cracking induced by DEF or ASR, and by other mechanisms (e.g., shrinkage, freeze–thaw, dynamic loading), increases pore-network connectivity and permeability, thereby enhancing moisture and ion transport and promoting coupled deterioration [16,46]. Cracking generated by ASR itself can further increase crack-network connectivity and facilitate moisture ingress and ionic transfer, which can support sulfate redistribution and renewed ettringite precipitation within paste-connected cracks and voids, particularly under rewetting or changing boundary conditions [97,98]. Bouzabata et al. [97] showed that boundary conditions associated with storage, leaching, and water supply can lead to markedly different expansion developments for ASR and DEF, including situations where measurable ASR-induced expansion develops under sealed conditions while DEF-induced expansion is only expressed when external water becomes available.

2.4 Management protocols and advanced tools for assessing concrete affected by DEF, ASR, and DEF+ASR

The assessment and management of concrete affected by alkali–silica reaction and delayed ettringite formation require an approach that addresses both the current condition and the future implications of the induced deterioration. Diagnosis must employ techniques capable of identifying the reaction mechanism(s) responsible for the observed damage (i.e., cause) and of quantifying the extent of induced deterioration (i.e., extent), whereas prognosis must estimate the potential for further deterioration and its structural implications [3,65].

This section discusses two protocols developed in Canada and France for managing concrete structures affected by DEF, ASR, and DEF+ASR, as well as the advanced tools developed over the last few decades.

2.4.1 Management protocol of ISR

The *Laboratoire Central des Ponts et Chaussées* (LCPC) formalised a staged protocol for managing concrete structures affected by internal swelling reactions (ISR), with emphasis on alkali–aggregate reaction (AAR) and delayed ettringite formation (DEF) [2]. The protocol begins with prioritisation based on the affected structural zone and the severity of damage, with immediate measures when user safety or structural integrity may be compromised. The initial evaluation establishes a baseline through compilation of construction and exposure information, quantified cracking assessment using a stablished cracking index [99], and installation of monitoring bases for dimensional change (Dm), complemented by internal temperature sensing and, when prognosis is required, humidity sensing; monitoring periodicity is then defined from the initial crack indexing and from the presence of isolated cracks exceeding specified openings (Figure 2.14) [2].

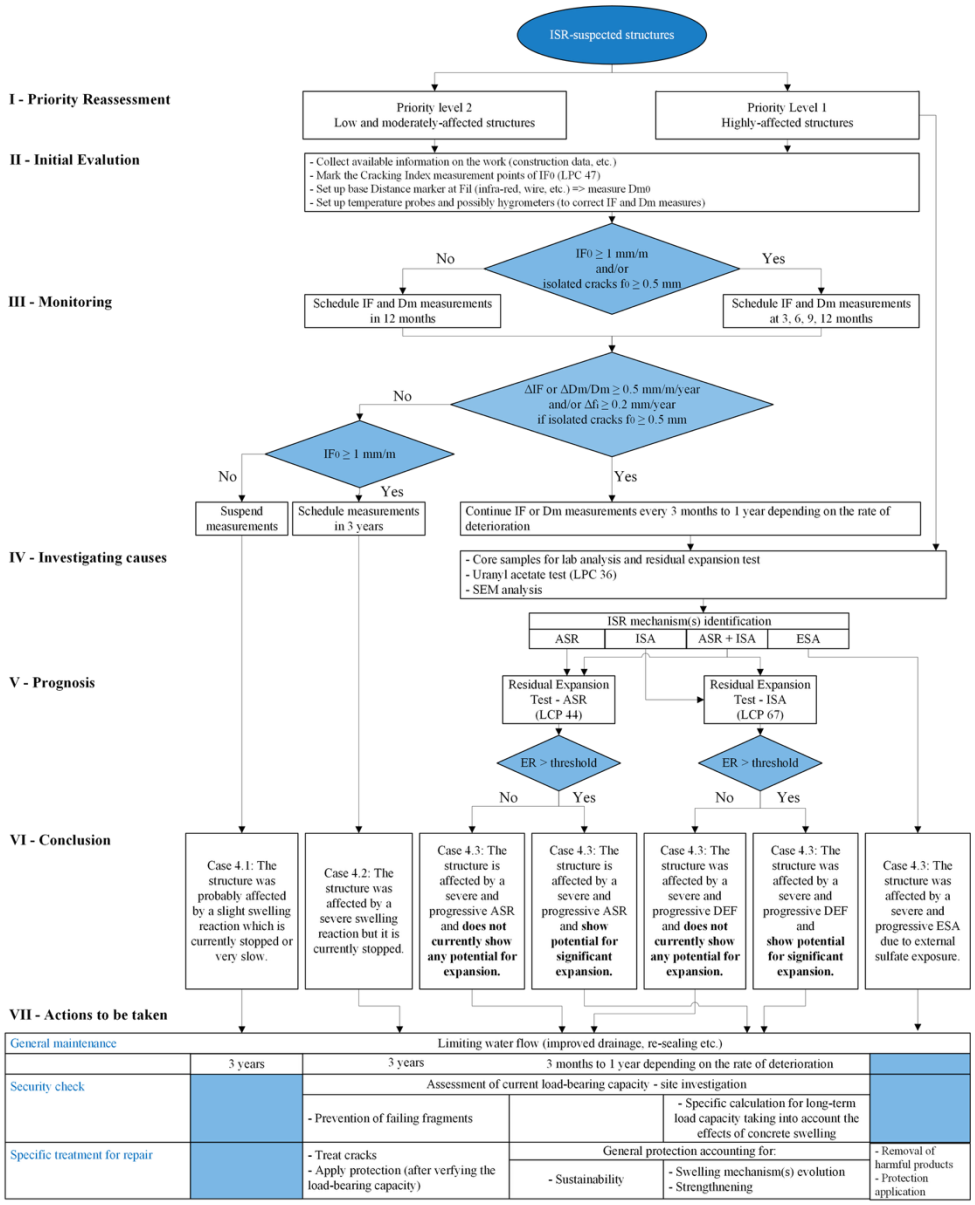


Figure 2.14 – LCPC flowchart for managing ISR-affected structures [2].

When monitoring confirms significant evolution, the protocol escalates to an in-depth study based on coring in damaged zones and in apparently sound reference zones, followed by laboratory diagnosis. Rapid screening may include uranyl acetate fluorescence for AAR products, whereas confirmation relies on microstructural identification by scanning electron microscopy (SEM) coupled with microanalysis to distinguish reaction products associated with AAR and DEF and to avoid over-interpretation of non-deleterious ettringite occurrences [2]. Prognosis relies on the

potential for further swelling, evaluated through accelerated residual expansion testing on cores, with the procedure selected according to the identified reaction mechanism (LPC 44 [100] for AAR; LPC 67 [101] for DEF) and interpreted jointly with field kinetics [2]. Recommended actions then scale with the initial damage state and the measured evolution rate, ranging from standard surveillance for lightly affected and slowly evolving structures, to crack sealing and protective systems compatible with continued movement for damaged but slowly evolving structures, and to load testing, structural recalculation, confinement/strengthening, partial replacement, or demolition in rare cases where rapid evolution and capacity concerns converge; moisture ingress reduction remains a central preventive measure across all cases [2].

Toutlemonde [4] reaffirmed that the LCPC approach remains the backbone of French practice for ISR-affected bridge management and highlighted the benefit of implementing global deformation monitoring as early as possible to reduce uncertainty in condition appraisal. The author also noted that the cracking index provides an efficient first-stage screening tool, but its interpretation is affected by reinforcement, moisture gradients, stresses, seasonal variability, and operator sensitivity, which justifies repeated measurements and complementary indicators within the decision framework.

2.4.2 Management protocol of ASR-affected concrete infrastructure

A protocol for the evaluation and management of critical concrete infrastructure affected by alkali–silica reaction (ASR) was proposed by Bérubé et al. [102], while Fournier et al. [103] presented a complementary, tiered investigation framework that organises escalation from screening to detailed diagnosis and prognosis. The protocol uses concrete expansion as the primary variable for prioritisation and follow-up intensity, since the expansion attained and expansion rate allow estimation of the remaining time before reinforcement yielding is expected. A critical expansion threshold of 0.20% is adopted as an intervention-oriented criterion, under the assumption of effective strain transfer between concrete and reinforcement. Decisions therefore rely on the expansion attained, the expansion rate, and the projected time to the 0.20% threshold.

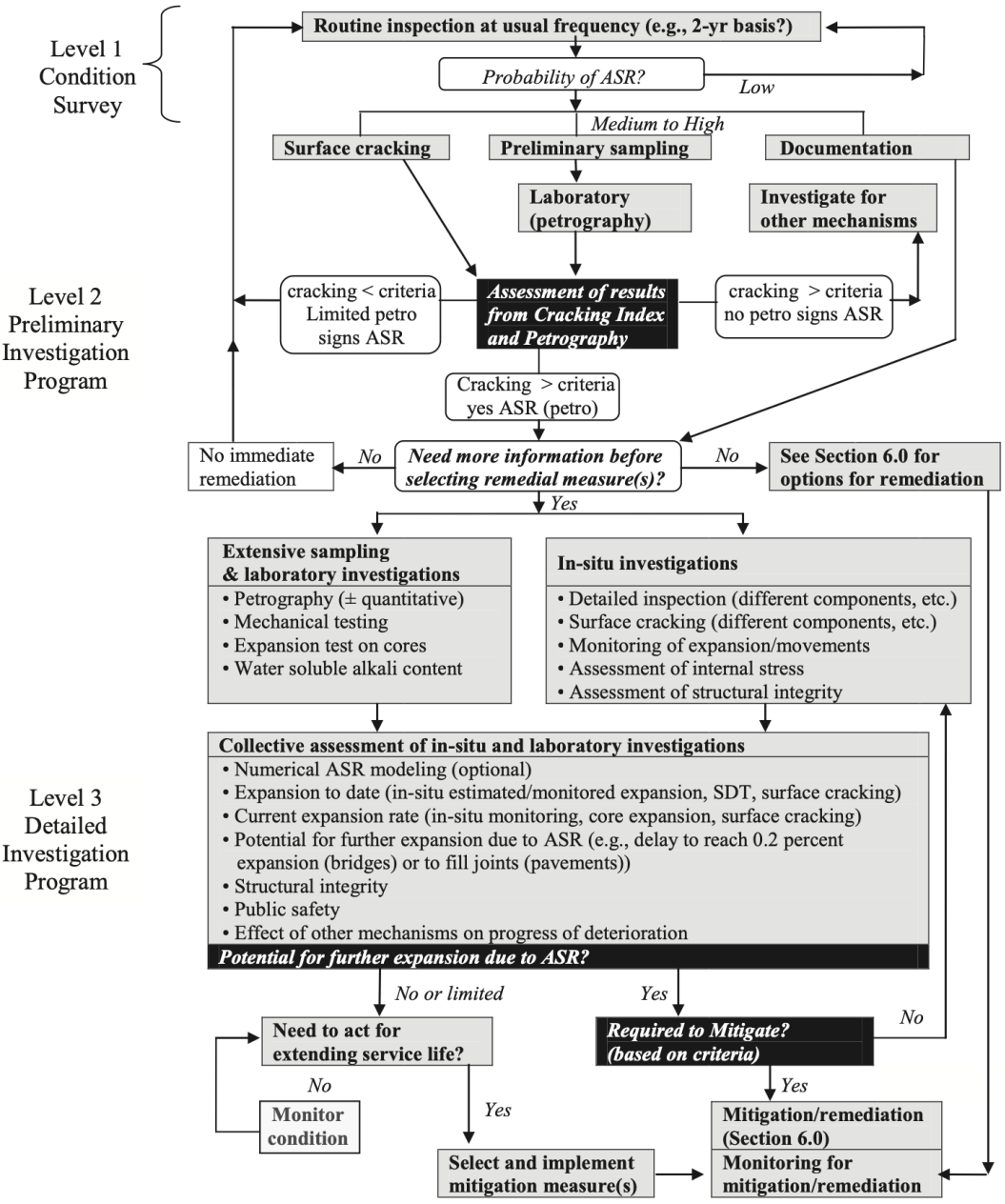


Figure 2.15 - Global flowchart for the evaluation and management of concrete structures for ASR [103].

The condition assessment begins with a visual inspection to identify damage features commonly associated with ASR and to document their extent and distribution. A classification system structures the observations using indicators such as deformation and displacement, cracking, surface discoloration, and exudations, while recognising that field observations alone cannot

confirm ASR when other deterioration processes may coexist. The protocol then applies quantified crack readings in the most exposed areas and, when needed, targeted coring for laboratory confirmation, consistent with the investigation framework proposed by Fournier et al. [103]. Mechanical testing on cores, including the stiffness damage test (SDT), is used to refine the estimate of expansion attained in critical and highly exposed members, strengthening the subsequent prognosis.

When an expansion of 0.20% is expected within five years, coring is recommended to support an intensified evaluation that includes SDT, direct tensile strength testing, and assessment of the potential for further expansion (PFE). The PFE classification integrates contributing factors associated with the residual expansion capacity of the concrete (coefficient RCE), the residual expansion capacity of the aggregate (coefficient RAR), the availability of water-soluble alkalis (coefficient ALK), and the effect of reinforcement and other restraints (coefficient STR), together with the humidity effect (HUM) and temperature effect (TEM). The resulting PFE level is classified as negligible, very low, low, medium, high, or very high [104,105], and it is used to guide intervention planning and the intensity of subsequent monitoring within the flowchart presented in Figure 2.15 [103].

2.4.3 Advanced tools to assess the cause and extent of damage

Management protocols for ISR-affected infrastructure rely on external cracking and displacement monitoring to estimate current damage and inform decision-making on mitigation and rehabilitation strategies. A central limitation remains the difficulty in establishing robust correlations between the field-observed ISR-induced damage features and the associated reductions in mechanical properties and durability of the affected concrete members. This limitation has motivated the development of diagnostic test protocols developed to quantify the expansion attained and the degree of damage at specific locations of an affected structure. Among these approaches, the multi-level protocol that combines microscopic and mechanical tests, particularly the Damage Rating Index (DRI) and the Stiffness Damage Test (SDT), is the most common and is considered reliable.

2.4.3.1 Damage rating index (DRI)

The DRI is a semi-quantitative microscopic method initially proposed by Grattan-Bellew and Danay for assessing ASR-affected concrete [106,107]. The test is conducted on polished concrete sections divided into 1 × 1 cm grid, where microscopic damage features are counted using a stereomicroscope under 15–16× magnification using white light illumination. Ideally, at least 200 cm^2 of concrete polished section should be analyzed [106,107].

In the conventional DRI protocol, each microscopic damage feature is counted and then multiplied by a weighting factor that reflects its relative contribution to the induced deterioration. Closed cracks in aggregates (CCA) are typically interpreted as caused by natural flaws or pre-existing conditions within aggregates and receive the lowest weight (0.25). Open cracks in aggregates without (OCA) and with reaction products (OCA-RP) are associated with ASR-induced cracking and are weighted at 2. Cracks in the cement paste, whether observed without reaction products (CCP) or with reaction products (CCP-RP), are commonly associated with DEF-related paste cracking and with advanced stages of ASR-related deterioration once cracking has propagated beyond the aggregate. They receive a weighting factor of 3 since these cracks reflect more severe deterioration in concrete. Disaggregated aggregate particles (DAP) are weighted at 2, while coarse aggregate debonding (Debon), which indicates advanced loss of aggregate–paste continuity, is weighted at 3 (Figure 2.16).

Sanchez et al. [108,109] developed an extended version of the DRI to better understand deterioration processes. They applied this method to evaluate concrete affected by various ISR mechanisms, including DEF. Additionally, the technique was used to connect microscopic deterioration with changes in mechanical responses. The DRI measures the distribution and severity of deterioration features in aggregate particles, cement paste, and the interfacial transition zone.

a)

Features of deterioration		Weighing factor
Aggregate	Closed crack (CCA)	0.25
	Opened crack (OCA)	2
	Opened crack with reaction product (OCA_RP)	2
Cement paste	Crack in the cement paste (CCP)	3
	Crack in the cement with reaction product (CCP_RP)	3
Disaggregate/corroded aggregate particle (DAP)		2
Coarse aggregate debonded (Debon)		3
$DRI_{number} = \left[\frac{\sum_{i=1}^{i=n} 0.25(CCA)+2(OCA+OCA_{RP}+DAP)+3(CCP+CCP_{RP}+Debon)}{n\ of\ analyzed\ \ 1\ cm\ by\ 1\ cm\ squares}\right] \times 100\ cm^2$		

b)

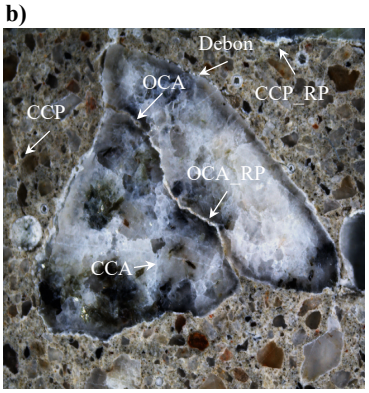


Figure 2.16 – Damage rating index (DR). a) Damage features [110], and b) Micrograph section displaying most of the damage features [111].

2.4.3.2 Stiffness damage test (SDT)

The Stiffness Damage Test (SDT) is a cyclic mechanical procedure used to quantify internal damage in concrete affected by internal swelling reactions (ISR), including alkali–silica reaction (ASR) and delayed ettringite formation (DEF), through the analysis of the stress–strain response under repeated uniaxial loading [43,112]. The method originally proposed by Walsh [113] for characterizing microcrack development in rocks, and it was subsequently adapted for concrete and later applied to ASR-affected materials by Crouch [114] and Crisp et al. [115,116]. The SDT procedure was initially performed using fixed maximum loads of 5.5 MPa (Crisp et al. [115,116]) or 10 MPa (Smaoui et al. [117]) at a loading rate of 0.10 MPa/s. The test outcomes typically include the modulus of elasticity, the dissipated energy quantified by the hysteresis area, the accumulated plastic strain, and the non-linearity index (NLI), defined as the ratio between Sec 1 and Sec 2 (Figure 2.17). It was found that the NLI provided information on crack orientation (i.e., NLI >1 denotes cracks perpendicular to the load axis, and NLI <1 denotes parallel cracks) [43,112].

Sanchez et al. [112,118,119] further developed the SDT protocol through a comprehensive research program, using concrete mixtures of multiple strengths and incorporating diverse reactive aggregate types. It was observed that a maximum load relative to the compressive strength of the sound concrete mixture (i.e., 40%) increased the repeatability and diagnostic aspect of the tool. The Stiffness Damage Index (SDI) and Plastic Deformation Index (PDI) were introduced as indices for describing internal damage, defined as the ratios of dissipated energy and accumulated plastic

deformation, respectively, to the corresponding total energy and total deformation over the five loading–unloading cycles.

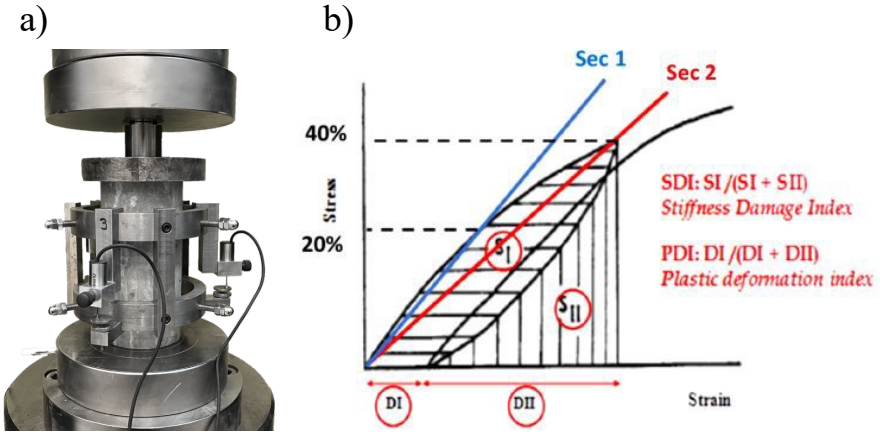


Figure 2.17 – Stiffness damage test. a) Test setup, and b) Definition of Stiffness damage index (SDI) and Plastic deformation index (PDI) [120].

2.4.4 Potential for further expansion

As previously discussed, monitoring the current condition and extent of damage, as well as the potential for further expansion, is required to optimise rehabilitation strategies for concrete infrastructure affected by DEF, ASR, and DEF+ASR. Estimating future induced expansion and associated damage development generally relies on a combination of field and laboratory investigations. In situ expansion monitoring provides direct evidence of structural response under restraint but typically requires multi-year records to separate seasonal and thermal effects from reaction-driven trends. One complementary part of prognosis approaches [2,103] is residual expansion tests conducted on cores extracted from the affected members under evaluation. It provides a complementary quantification of the remaining swelling capacity of the material, typically within 6 to 12 months, while requiring explicit consideration of stress release at coring, moisture re-equilibration, and ionic leaching during conditioning [2,103].

2.4.4.1 Residual expansion test (RE)

Several residual expansion protocols have been proposed to assess future induced expansion of DEF, ASR, and DEF+ASR affected concrete [18,121–126]. These tests are performed on cores extracted from the affected structure and aim to quantify the remaining swelling reserve by

exposing specimens to boundary conditions that promote continued reaction, while monitoring length change as a function of time. For DEF and DEF+ASR appraisal, well-disseminated procedures rely on sustained water immersion of instrumented cores at controlled temperature, with measurements initiated after a short conditioning period to homogenize moisture and temperature and continued until expansion stabilizes; these outcomes are then used as inputs for condition management and time-dependent forecasting [2,123]. Other protocols involve immersion in lime-saturated water at near-room temperature (i.e., 23 °C), which maintains calcium-rich conditions while allowing ionic exchange with the surrounding solution; this setup has been used to evaluate residual swelling potential in concretes where DEF and ASR may coexist [39,124,127].

2.4.4.2 Predicting DEF and ASR expansion at the material's scale through analytical modelling

The kinetics of DEF-, ASR-, and combined DEF+ASR-induced expansion have been investigated using analytical, numerical, and empirical approaches, with the objective of representing time-dependent swelling under defined exposure and restraint conditions. Larive's analytical formulation is frequently adopted as a basis for describing ISR expansion histories and for supporting prognosis interpretations that couple laboratory measurements with time-dependent reconstruction [2,20,122,128]. Larive [128] proposed a three-parameter sigmoidal law (Equation 2.1) to represent the initiation, acceleration, and subsequent stabilisation of ASR-induced expansion, and the same functional form was later applied to DEF in subsequent studies [20,129,130]. In this analytical model, the expansion at time $\varepsilon(t)$ evolves toward an ultimate value ε_∞, which represents the maximum swelling potential attainable under the imposed conditions. The transition from the initial low-rate stage to the rapid-expansion stage is governed by the latency time τ_L, which corresponds to the inflection point of the curve (Figure 2.15). The kinetics of the main expansion stage are controlled by the characteristic time τ_C, which scales the reaction rate and determines the slope in the vicinity of the inflection point (Figure 2.15) [128].

Brunetaud [129] proposed a modified form of the Larive law for DEF by retaining the sigmoidal core and introducing an additional corrective term intended to reproduce the late-stage behaviour frequently observed for DEF-induced expansion, in which expansion can continue to increase after the main acceleration phase rather than approaching a strict plateau. This formulation introduces

two parameters, ϕ and δ, and applies a multiplicative factor $\left(1-\frac{\phi}{\delta+t}\right)$ that progressively tends toward unity as time increases, thereby adjusting the end-of-reaction curvature while preserving the early-stage structure governed by τ_C and τ_L (Equation 2.2) [20,129].

$$\varepsilon(t) = \varepsilon_\infty \cdot \frac{1-e^{\frac{t}{\tau_C}}}{1+e^{-\frac{t-\tau_L}{\tau_C}}} \tag{2.1}$$

$$\varepsilon(t) = \varepsilon_\infty \cdot \frac{1-e^{\frac{t}{\tau_C}}}{1+e^{-\frac{t-\tau_L}{\tau_C}}} \cdot \left(1-\frac{\phi}{\delta+t}\right), 0 < \phi < \delta \tag{2.2}$$

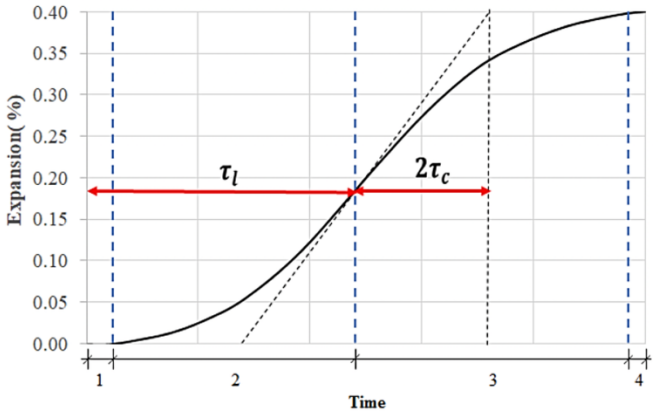


Figure 2.18 – Graphical representation of Larive's analytical model [128].

Multon et al. [122] introduced, in the ASR context, a reconstruction approach in which the residual expansion of drilled cores is interpreted with respect to a pre-calibrated free-expansion law of Larive (Equation 2.1) that describes the full ASR-induced expansion of the concrete under 100% relative humidity [128]. In this experimental programme, expansion was monitored on cylinders (160 x 320 mm) and prisms (140 x 140 x 280 mm) before coring (denoted as "pre-coring expansion"), and on cores thereafter; residual expansion tests on cores (110 x 220 mm) were therefore interpreted as the continuation of the same free-expansion curve from an advanced reaction age, with a non-zero expansion at the time of coring. Under these controlled conditions, the "pre-coring + residual" expansion history can be directly reconstructed by summing the measured expansion before and after coring and comparing the result with the reference 100% relative humidity curve [122]. Martin [20] adopted this conceptual framework for DEF and combined DEF+ASR, and proposed introducing explicit time and expansion offsets, fitted together

with the free-expansion parameters to align residual expansion curves from cores with the laboratory free-swelling reference. This extension to DEF preserves the same key assumptions (i) the approach assumes that the affected material follows a parametric free-expansion law (Equation 2.1) calibrated on laboratory free-swelling specimens under well-defined high-humidity conditions; (ii) residual expansion tests represent the continuation of that law from an advanced reaction state; and (iii) the sum of pre-coring and residual expansion converges toward a common ultimate swelling under favourable moisture.

2.5 References

[1] B. Fournier, M.-A. Bérubé, Alkali-aggregate reaction in concrete: a review of basic concepts and engineering implications, Canadian Journal of Civil Engineering 27 (2000) 167–191. https://doi.org/10.1139/l99-072.

[2] P. Fasseu, B. Mahut, Aide à la gestion des ouvrages atteints de réactions de gonflement interne : Guide méthodologique, GUIDES TECHNIQUES, Laboratoire Central des Ponts et Chaussées (LCPC), Paris, 2003.

[3] L.F.M. Sanchez, Internal Swelling Reactions in Concrete: Mechanisms and Condition Assessment, 1st ed., CRC Press, Boca Raton, 2024. https://doi.org/10.1201/9781003188155.

[4] F. Toutlemonde, Structural implications and management of infrastructure assets affected by ISR: example of French experience on road bridges, Canadian Journal of Civil Engineering 52 (2025) 1843–1851. https://doi.org/10.1139/cjce-2025-0120.

[5] L.F.M. Sanchez, B. Fournier, D. Mitchell, J. Bastien, Condition assessment of an ASR-affected overpass after nearly 50 years in service, Constr Build Mater 236 (2020) 117554. https://doi.org/10.1016/j.conbuildmat.2019.117554.

[6] B. Godart, D. Loič, Lessons Learned from Structures Damaged by Delayed Ettringite Formation and the French Prevention Strategy, in: Forensic Engineering: Informing the Future with Lessons from the Past - Proceedings of the 5th International Conference on Forensic Engineering, 2013: pp. 389–400.

[7] R.C. Mielenz, S.L. Marusin, W.G. Hime, Z.T. Jugovic, Investigation of prestressed concrete railway tie distress, Concrete International 17 (1995) 62–68.

[8] C.A. Rogers; T., Tharmabala, Presstressed concrete members affected by alkali-silica reaction, ACI Mater J (1990) 35–39.

[9] P. Tepponen, B.E. Eriksson, Damages in Concrete Railway Sleepers in Finland., Nordic Concrete Research (1987) 199–209.

[10] N.P. Hasparyk, S.C. Kuperman, Revisiting Concrete Structures from a Hydroelectric Power Plant Affected by ASR in Brazil, with a New Diagnose of Coupled Attack (ASR + DEF), in: L.F.M. Sanchez, C. Trottier (Eds.), Proceedings of the 17th International Conference on Alkali-

Aggregate Reaction in Concrete ICAAR 2024, Springer, Ottawa, 2024: pp. 400–410. https://doi.org/10.1007/978-3-031-59349-9_46.

[11] A.S. Silva, A.F. Gonçalves, M. Pipa, Diagnosis and prognosis of Portuguese concrete railway sleepers degradation – A combination of ASR and DEF, in: M.A.T.M. Broekmans, B.J. Wigum (Eds.), 13th International Conference on Alkali-Aggregate Reaction in Concrete (13th ICAAR), NGU/ICAAR, Trondheim, Norway, 2008.

[12] K.L. Scrivener, D. Damidot, C. Famy, Possible Mechanisms of Expansion of Concrete Exposed to Elevated Temperatures During Curing (Also Known as DEF) and Implications for Avoidance of Field Problems, Cement, Concrete, and Aggregates 21 (1999) 93–101. https://doi.org/10.1520/CCA10513J.

[13] C. Famy, H.F.W. Taylor, Ettringite in Hydration of Portland Cement Concrete and its Occurrence in Mature Concretes, ACI Mater J 98 (2001). https://doi.org/10.14359/10404.

[14] K.L. Scrivener, J.P. Skalny, Conclusions of the International RILEM TC 186-ISA workshop on Internal Sulfate Attack and Delayed Ettringite Formation (4–6 September 2002, Villars, Switzerland), Materials and Structures/Materiaux et Constructions 38 (2005) 659–663. https://doi.org/10.1617/14111.

[15] B. Godart, L. Divet, Recommendations for preventing disorders due to delayed ettringite formation: technical guide, Ifsttar, Techniques et Méthodes - Guide Technique - GTI5 (2018).

[16] M. Collepardi, A state-of-the-art review on delayed ettringite attack on concrete, Cem Concr Compos 25 (2003) 401–407. https://doi.org/10.1016/S0958-9465(02)00080-X.

[17] M. Collepardi, Damage by Delayed Ettringite Formation, Concrete International 21 (1999) 69–74.

[18] M. Thomas, K. Folliard, T. Drimalas, T. Ramlochan, Diagnosing delayed ettringite formation in concrete structures, Cem Concr Res 38 (2008) 841–847. https://doi.org/10.1016/j.cemconres.2008.01.003.

[19] H.F.W. Taylor, C. Famy, K.L. Scrivener, Delayed ettringite formation, Cem Concr Res 31 (2001) 683–693. https://doi.org/10.1016/S0008-8846(01)00466-5.

[20] R.P. Martin, Analyse sur structures modèles des effets mécaniques de la réaction sulfatique interne du béton, PhD thesis, Université Paris Est., 2010. https://theses.hal.science/tel-00558200.

[21] B. Godart, O. Omikrine-Metalssi, B. Kchakech, S. Lavaud, The effects of delayed ettringite formation on the expansion of a massive bridge pier and a precast prestressed concrete beam of a bridge, in: International Conference on Alkali Aggregate Reaction (ICAAR), São Paulo (Brazil), 2016.

[22] G. Escadeillas, J.-E. Aubert, M. Segerer, W. Prince, Some factors affecting delayed ettringite formation in heat-cured mortars, Cem Concr Res 37 (2007) 1445–1452. https://doi.org/10.1016/j.cemconres.2007.07.004.

[23] B. Kchakech, Etude de l'influence de l'échauffement subi par un béton sur le risque d'expansions associées à la réaction sulfatique interne., PhD, Université Paris-Est, 2015.

[24] B. Kchakech, R.-P. Martin, O. Omikrine Metalssi, J.-C. Renaud, L. Baron, Effect of temperature and curing duration of early heat treatments on the risk of expansion associated with delayed ettringite formation, in: 15th International Conference on Alkali Aggregate Reaction (ICAAR), São Paulo (Brazil), 2016.

[25] F. Toutlemonde, B. Kchakech, O. Omikrine Metalssi, R.-P. Martin, DEF coupled to thermal history: Recent Advances, in: Concrack 5, JCI-Rilem International Workshop, Tokyo, Japan, 2017: pp. 175–188.

[26] R.-P. Martin, L. Sanchez, B. Fournier, F. Toutlemonde, Evaluation of different techniques for the diagnosis & prognosis of Internal Swelling Reaction (ISR) mechanisms in concrete, Constr Build Mater 156 (2017) 956–964. https://doi.org/10.1016/j.conbuildmat.2017.09.047.

[27] R.P. Martin, J.C. Renaud, F. Toutlemonde, Experimental investigations concerning combined delayed ettringite formation and alkali aggregate reaction, in: P. Castro-Borges, E.I. Moreno, K. Sakai, O.E. Gjørv, N. Banthia (Eds.), 6th International Conference on Concrete under Severe Conditions (CONSEC10), CRC Press, Mérida, Yucatán, Mexico, 2010: pp. 287–295. https://hal.science/hal-00904253.

[28] M. Al Shamaa, S. Lavaud, L. Divet, G. Nahas, J.M. Torrenti, Influence of relative humidity on delayed ettringite formation, Cem Concr Compos 58 (2015) 14–22. https://doi.org/10.1016/j.cemconcomp.2014.12.013.

[29] L. Graf, Effect of relative humidity on expansion and microstructure of heat- cured mortars, Skokie, Illinois, USA: RD139, 2007.

[30] R.-P. Martin, A. Bonnet, J.-C. Renaud, R. Chlela, F. Toutlemonde, C. Sauvaget, Influence of moisture on the development of delayed ettringite formation, Magazine of Concrete Research 75 (2023) 747–754. https://doi.org/10.1680/jmacr.22.00282.

[31] M. Malbois, B. Nedjar, S. Lavaud, C. Rospars, L. Divet, J.-M. Torrenti, On DEF expansion modelling in concrete structures under variable hydric conditions, Constr Build Mater 207 (2019) 396–402. https://doi.org/10.1016/j.conbuildmat.2019.02.142.

[32] R.-P. Martin, F. Toutlemonde, C. Sauvaget, Effects of Alternative Wetting and Drying on the Development of Delayed Ettringite Formation, in: L.F.M. Sanchez, C. Trottier (Eds.), 17th International Conference on Alkali-Aggregate Reaction in Concrete (ICAAR), RILEM Bookseries, Volume 49, Springer, Ottawa, 2024: pp. 176–183. https://doi.org/10.1007/978-3-031-59419-9_21.

[33] D. Heinz, U. Ludwig, Mechanism of Secondary Ettringite Formation in Mortars and Concretes Subjected to Heat Treatment, in: SP-100: Concrete Durability: Proceedings of Katharine and Bryant Mather International Symposium, American Concrete Institute, 1987. https://doi.org/10.14359/3827.

[34] Y. Fu, J.J. Beaudoin, Mechanisms of Delayed Ettringite Formation in Portland Cement Systems, ACI Mater J 93 (1996). https://doi.org/10.14359/9818.

[35] C. Famy, Expansion of Heat-Cured Mortars, PhD, University of London, 1999.

[36] G.W. Scherer, Crystallization in pores, Cem Concr Res 29 (1999) 1347–1358. https://doi.org/10.1016/S0008-8846(99)00002-2.

[37] S. Diamond, Delayed Ettringite Formation-Processes and Problems, Cem Concr Compos 18 (1996) 205–215. https://doi.org/https://doi.org/10.1016/0958-9465(96)00017-0.

[38] P. Goltermann, Mechanical Predictions of Concrete Deterioration; Part 2: Classification of Crack Patterns, ACI Mater J 92 (1995) 58–63. https://doi.org/10.14359/1177.

[39] E. Giannini, K. Folliard, J. Zhu, O. Bayrak, K. Kreitman, B. Hanson, Non-Destructive Evaluation of In-Service Concrete Structures Affected by Alkali-Silica Reaction (ASR) or Delayed Ettringite Formation (DEF)—Final Report, Part I, 2013.

[40] M. Ben Haha, E. Gallucci, A. Guidoum, K.L. Scrivener, Relation of expansion due to alkali silica reaction to the degree of reaction measured by SEM image analysis, Cem Concr Res 37 (2007) 1206–1214. https://doi.org/10.1016/j.cemconres.2007.04.016.

[41] K.L. Scrivener, Backscattered electron imaging of cementitious microstructures: understanding and quantification, Cem Concr Compos 26 (2004) 935–945. https://doi.org/10.1016/j.cemconcomp.2004.02.029.

[42] L.F.M. Sanchez, T. Drimalas, B. Fournier, Assessing condition of concrete affected by internal swelling reactions (ISR) through the Damage Rating Index (DRI), Cement 1–2 (2020) 100001. https://doi.org/10.1016/j.cement.2020.100001.

[43] L.F.M. Sanchez, T. Drimalas, B. Fournier, D. Mitchell, J. Bastien, Comprehensive damage assessment in concrete affected by different internal swelling reaction (ISR) mechanisms, Cem Concr Res 107 (2018) 284–303. https://doi.org/10.1016/j.cemconres.2018.02.017.

[44] British Cement Association (BCA), The Diagnosis of Alkali Silica Reaction – Report of a Working Party, England, 1992.

[45] A.B. Poole, I. Sim, Concrete Petrography: A handbook of investigative techniques, 2nd ed., CRC Press, Boca Raton, FL, 2016. https://doi.org/10.1201/b18688.

[46] S.O. Ekolu, M.D.A. Thomas, R.D. Hooton, Implications of pre-formed microcracking in relation to the theories of DEF mechanism, Cem Concr Res 37 (2007) 161–165. https://doi.org/10.1016/j.cemconres.2006.10.014.

[47] Y. Thiebaut, S. Multon, A. Sellier, L. Lacarrière, L. Boutillon, D. Belili, L. Linger, F. Cussigh, S. Hadji, Effects of stress on concrete expansion due to delayed ettringite formation, Constr Build Mater 183 (2018) 626–641. https://doi.org/10.1016/j.conbuildmat.2018.06.172.

[48] N.R. Joshi, A. Matsumoto, S. Asamoto, T. Miura, Y. Kawabata, Investigation of the mechanical behaviour of concrete with severe delayed ettringite formation expansion focusing on internal damage propagation under various compressive loading patterns, Cem Concr Compos 128 (2022) 104433. https://doi.org/10.1016/j.cemconcomp.2022.104433.

[49] H. Bouzabata, S. Multon, A. Sellier, H. Houari, Effects of restraint on expansion due to delayed ettringite formation, Cem Concr Res 42 (2012) 1024–1031. https://doi.org/10.1016/j.cemconres.2012.04.001.

[50] Y. Kawabata, T. Miura, M. Fujishima, N. Ueda, Y. Takahashi, S. Asamoto, S. Multon, R.-P. Martin, J.-F. Seignol, Influence of Reinforcing Rebar on Expansion due to Delayed Ettringite Formation along the Bonding Length – Part I: The Role of Bond on Expansive Behavior of Concrete, Journal of Advanced Concrete Technology 21 (2023) 851–868. https://doi.org/10.3151/jact.21.851.

[51] T. Miura, M. Fujishima, Y. Kawabata, S. Multon, R.-P. Martin, N. Ueda, Y. Takahashi, S. Asamoto, J.-F. Seignol, Influence of Reinforcing Rebar on Expansion due to Delayed Ettringite Formation along the Bonding Length – Part II: Bond Performance of Reinforced Concrete Affected by DEF Expansion, Journal of Advanced Concrete Technology 21 (2023) 869–888. https://doi.org/10.3151/jact.21.869.

[52] S. Chatterji, A.D. Jensen, N. Thaulow, P. Christensen, Studies of alkali-silica reaction. Part 3. Mechanisms by which NaCl and Ca(OH)2 affect the reaction, Cem. Concr. Res. 16 (1986) 246–254. https://doi.org/https://doi.org/10.1016/0008-8846(86)90141-9.

[53] L.J. Struble, S. Diamond, Swelling properties of synthetic alkali silica gels, Am. Ceram. Soc. 64 (1981) 652–655. https://doi.org/https://doi.org/10.1111/j.1151-2916.1981.tb15864.x.

[54] A. Leemann, M. Góra, B. Lothenbach, M. Heuberger, Alkali silica reaction in concrete - Revealing the expansion mechanism by surface force measurements, Cem Concr Res 176 (2024) 107392. https://doi.org/10.1016/j.cemconres.2023.107392.

[55] A. Leemann, Z. Shi, J. Lindgård, Characterization of amorphous and crystalline ASR products formed in concrete aggregates, Cem Concr Res 137 (2020) 106190. https://doi.org/10.1016/j.cemconres.2020.106190.

[56] O.D. Olajide, M.R. Nokken, L.F.M. Sanchez, Alkali–Silica Reactions: Literature Review on the Influence of Moisture and Temperature and the Knowledge Gap, Materials 17 (2023) 10. https://doi.org/10.3390/ma17010010.

[57] L.-O. Nilsson, O. Peterson, Alkali-silica reactions in Scania, Sweden: a moisture problem causing pop-outs in concrete floors, Lund, Sweden, 1983. https://portal.research.lu.se/files/4604450/1594285.pdf.

[58] H. Ólafsson, The Effect of Relative Humidity and Temperature on Alkali Expansion of Mortar Bars, in: P.E. Grattan-Bellew (Ed.), Concrete Alkali-Aggregate Reactions: Proceedings of the 7th International Conference, 1986, Ottawa, Canada, Noyes Publications, Ottawa, ON, Canada, 1987: pp. 461–465. https://icaarconcrete.org/wp-content/uploads/2024/04/7ICAAR-OlafssonH-1.pdf.

[59] S. Poyet, A. Sellier, B. Capra, G. Thèvenin-Foray, J.-M. Torrenti, H. Tournier-Cognon, E. Bourdarot, Influence of Water on Alkali-Silica Reaction: Experimental Study and Numerical Simulations, Journal of Materials in Civil Engineering 18 (2006) 588–596. https://doi.org/10.1061/(ASCE)0899-1561(2006)18:4(588).

[60] O.D. Olajide, Multilevel Assessment of The Role of Moisture and Temperature in ASR-Induced Expansion and Deterioration, PhD, Concordia University, 2025.

[61] S. Multon, F. Toutlemonde, Water distribution in concrete beams, Mater Struct 37 (2004) 378–386. https://doi.org/10.1007/BF02479634.

[62] S. Multon, F. Toutlemonde, Effect of moisture conditions and transfers on alkali silica reaction damaged structures, Cem Concr Res 40 (2010) 924–934. https://doi.org/10.1016/j.cemconres.2010.01.011.

[63] L.F.M. Sanchez, B. Fournier, M. Jolin, J. Duchesne, Reliable quantification of AAR damage through assessment of the Damage Rating Index (DRI), Cem Concr Res 67 (2015) 74–92. https://doi.org/10.1016/j.cemconres.2014.08.002.

[64] D.J. De Souza, L.F.M. Sanchez, M.T. De Grazia, Evaluation of a direct shear test setup to quantify AAR-induced expansion and damage in concrete, Constr Build Mater 229 (2019) 116806. https://doi.org/10.1016/j.conbuildmat.2019.116806.

[65] L.F.M. Sanchez, Contribution to the assessment of damage in aging concrete infrastructures affected by alkali-aggregate reaction, PhD thesis, Université Laval, 2014. https://www.collectionscanada.ca/obj/thesescanada/vol2/QQLA/TC-QQLA-30764.pdf.

[66] E. Boehm-Courjault, S. Barbotin, A. Leemann, K. Scrivener, Microstructure, crystallinity and composition of alkali-silica reaction products in concrete determined by transmission electron microscopy, Cem Concr Res 130 (2020) 105988. https://doi.org/10.1016/j.cemconres.2020.105988.

[67] F. Rajabipour, E. Giannini, C. Dunant, J.H. Ideker, M.D.A. Thomas, Alkali–silica reaction: Current understanding of the reaction mechanisms and the knowledge gaps, Cem Concr Res 76 (2015) 130–146. https://doi.org/10.1016/j.cemconres.2015.05.024.

[68] S. Chatterji, Chemistry of alkali–silica reaction and testing of aggregates, Cem Concr Compos 27 (2005) 788–795. https://doi.org/10.1016/j.cemconcomp.2005.03.005.

[69] L.S.D. Glasser, N. Kataoka, The chemistry of "alkali-aggregate" reaction, Cem. Concr. Res. (1981) 1–9. https://doi.org/https://doi.org/10.1016/0008-8846(81)90003-X.

[70] R. Esposito, C. Anaç, M.A.N. Hendriks, O. Çopuroğlu, Influence of the Alkali-Silica Reaction on the Mechanical Degradation of Concrete, Journal of Materials in Civil Engineering 28 (2016). https://doi.org/10.1061/(ASCE)MT.1943-5533.0001486.

[71] Y. Kubo, M. Nakata, Effect of reactive aggregate on mechanical properties of concrete affected by alkali-silica reaction., in: 14th ICAAR - Int. Conf. Alkali-Aggregate React. Concr., Ausin (Texas), 2012.

[72] S. Mindess, J.F. Young, D. Darwin, Concrete, Pearson Education Ltd, 2003.

[73] L.F.M. Sanchez, B. Fournier, M. Jolin, D. Mitchell, J. Bastien, Overall assessment of Alkali-Aggregate Reaction (AAR) in concretes presenting different strengths and incorporating a wide range of reactive aggregate types and natures, Cem Concr Res 93 (2017) 17–31. https://doi.org/10.1016/j.cemconres.2016.12.001.

[74] A. Saccani, V. Bonora, P. Monari, Laboratory short-term evaluation of ASR, Cem Concr Res 31 (2001) 739–742. https://doi.org/10.1016/S0008-8846(01)00477-X.

[75] L. Yang, M. Pathirage, H. Su, M. Alnaggar, G. Di Luzio, G. Cusatis, Computational modeling of temperature and relative humidity effects on concrete expansion due to alkali–silica reaction, Cem Concr Compos 124 (2021) 104237. https://doi.org/10.1016/j.cemconcomp.2021.104237.

[76] D. Lenzner, Influence of the Amount of Mixing Water on the Alkali-Silica Reaction, in: Proceedings of the 5th International Conference on Alkali-Aggregate Reaction, Cape Town, South Africa, 1981: pp. 1–6.

[77] O.D. Olajide, M.R. Nokken, L.F.M. Sanchez, Evaluation of the induced mechanical deterioration of ASR-affected concrete under varied moisture and temperature conditions, Cem Concr Compos 157 (2025) 105942. https://doi.org/10.1016/j.cemconcomp.2025.105942.

[78] P. Morenon, S. Multon, A. Sellier, E. Grimal, F. Hamon, E. Bourdarot, Impact of stresses and restraints on ASR expansion, Constr Build Mater 140 (2017) 58–74. https://doi.org/10.1016/j.conbuildmat.2017.02.067.

[79] D. Wald, G.A. Martinez, O. Bayrak, Expansion behavior of a biaxially reinforced concrete member affected by alkali-silica reaction, Structural Concrete 18 (2017) 550–560. https://doi.org/10.1002/suco.201600143.

[80] D.M. Wald, M.T. Allford, O. Bayrak, T.D. Hrynyk, Development and multiaxial distribution of expansions in reinforced concrete elements affected by alkali–silica reaction, Structural Concrete 18 (2017) 914–928. https://doi.org/10.1002/suco.201600220.

[81] S. Multon, F. Toutlemonde, Effect of applied stresses on alkali–silica reaction-induced expansions, Cem Concr Res 36 (2006) 912–920. https://doi.org/10.1016/j.cemconres.2005.11.012.

[82] W. Koyangi, K. Rokugo, Y. Uchida, Properties of Concrete Deteriorated by Alkali Aggregate Reaction under Various Reinforcement Ratios, in: Proc. 9th Int. Conf. Alkali-Aggregate React. Concr., London (UK), 1992: pp. 556–563.

[83] S. Farooq, G. Aoki, T. Miura, Y. Kawabata, H. Nakamura, Anisotropic expansion behavior and crack orientation of reinforced concrete due to the alkali–silica reaction, Cem Concr Compos 151 (2024) 105568. https://doi.org/10.1016/j.cemconcomp.2024.105568.

[84] M. Noël, L.F.M. Sanchez, R.-P. Martin, B. Fournier, J. Bastien, Structural Implications of Internal Swelling Reactions in Concrete : a Review, in: 15th Int. Conf. Alkali-Aggregate React., Sao Paulo (Brazil), 2016.

[85] H. Kagimoto, Y. Yasuda, M. Kawamura, ASR expansion, expansive pressure and cracking in concrete prisms under various degrees of restraint, Cem Concr Res 59 (2014) 1–15. https://doi.org/10.1016/j.cemconres.2014.01.018.

[86] M. Berra, G. Faggiani, T. Mangialardi, A.E. Paolini, Influence of stress restraint on the expansive behaviour of concrete affected by alkali-silica reaction, Cem Concr Res 40 (2010) 1403–1409. https://doi.org/10.1016/j.cemconres.2010.05.002.

[87] S. Multon, J.F. Seignol, F. Toutlemonde, Structural Behavior of Concrete Beams Affected by Alkali-Silica Reaction, ACI Mater J 102 (2005) 67–76. https://doi.org/10.14359/14299.

[88] C. Gravel, G. Ballivy, Expansion of AAR Concrete under Triaxial Stresses: Simulation with Instrumented Concrete Block, in: Proc. 11th Int. Conf. Alkali Aggreg. React., Quebec (Canada), 2000.

[89] A. Allard, S. Bilodeau, F. Pissot, B. Fournier, J. Bastien, B. Bissonnette, Expansive behavior of thick concrete slabs affected by alkali-silica reaction (ASR), Constr Build Mater 171 (2018) 421–436. https://doi.org/10.1016/j.conbuildmat.2018.03.159.

[90] R.A. Barbosa, S.G. Hansen, K.K. Hansen, L.C. Hoang, B. Grelk, Influence of alkali-silica reaction and crack orientation on the uniaxial compressive strength of concrete cores from slab bridges, Constr Build Mater 176 (2018) 440–451. https://doi.org/10.1016/j.conbuildmat.2018.03.096.

[91] S.G. Hansen, R.A. Barbosa, Prestressing of reinforcing bars in concrete slabs due to concrete expansion induced by Alkali-Silica Reaction, in: Fib Symp., 2016.

[92] R.A. Barbosa, K.K. Hansen, Alkali-Silica Reaction in Reinforced Concrete Structures Part II : Shear Strength of Severe ASR Damaged Concrete Beams, in: XXII Nord. Concr. Res. Symp., Iceland, 2014: pp. 69–72.

[93] A. McLeish, Structural implications of the alkali silica reaction in concrete, Wokingham, Berkshire United Kingdom, 1990.

[94] A. Zahedi, Evaluating ASR Physicochemical Process Under Distinct Restraint Conditions for a Better Assessment of Affected Concrete Infrastructure, PhD thesis, University of Ottawa, 2022.

[95] B. Godart, J. Wood, Interaction of DEF and AAR, a review, Revista Portuguesa de Engenharia de Estruturas. Ed. LNEC. 3 (2021) 25–34.

[96] K. Scrivener, J.P. Skalny, eds., Internal sulfate attack and delayed ettringite formation: Proceedings of the International RILEM TC 186-ISA Workshop, Villars, Switzerland, 4–6 September 2002, RILEM Proceedings PRO 35, RILEM publications, in: 2004.

[97] H. Bouzabata, S. Multon, A. Sellier, H. Houari, Swellings due to alkali-silica reaction and delayed ettringite formation: Characterisation of expansion isotropy and effect of moisture conditions, Cem Concr Compos 34 (2012) 349–356. https://doi.org/10.1016/j.cemconcomp.2011.10.006.

[98] V. Johansen, N. Thaulow, J. Skalny, Simultaneous presence of alkali — silica gel and ettringite in concrete, Advances in Cement Research 5 (1993) 23–29. https://doi.org/10.1680/adcr.1993.5.17.23.

[99] P. Fasseu, M. Michel, Détermination de l'indice de fissuration d'un parement de béton; Méthode d'essai LCPC N0. 47, Paris, 1997.

[100] A. Pavoine, Alcali-réaction du béton: Essai d'expansion résiduelle sur béton durci: Méthode d'essai n°44, Techniques et méthodes des laboratoires des ponts et chaussées., Paris, 1997.

[101] A. Pavoine, L. Divet, Réactivité d'un béton vis-à-vis d'une réaction sulfatique interne: Essai de performance. Méthode d'essai no 66, Techniques et méthodes des laboratoires des ponts

et chaussées, Laboratoire Central des Ponts et Chaussées (LCPC), Paris, France, 2007. https://www.ifsttar.fr/fileadmin/user_upload/editions/lcpc/MethodeDEssai/MethodeDEssai-LCPC-ME66.pdf.

[102] M.A. Berube, B. Fournier, Outil d'évaluation et de gestion des ouvrages d'art affectés de réactions alcalis-silice (RAS), 2005.

[103] B. Fournier, M.A. Bérubé, K. Folliard, M. Thomas, Report on the Diagnosis, Prognosis, and Mitigation of Alkali-Silica Reaction (ASR) in Transportation Structures, FHWA-HIF-09-004, Federal Highway Administration (FHWA), U.S. Department of Transportation, Washington, D.C., USA, 2010. https://www.fhwa.dot.gov/pavement/concrete/pubs/hif09004/hif09004.pdf.

[104] A. Bérubé; A. Peneault; J. Frenette; M. Rivest, Laboratory assessment of potential for future expasion and deterioration of concrete affected by ASR, in: CANMET/ACI International Workshop on Alkali-Aggregate Reactions in Concrete, Dartmouth, Nova Scotia, 1995: pp. 267–292.

[105] M.A. Bérubé, J. Frenette, A. Pedneault, M. Rivest, Laboratory Assessment of the Potential Rate of ASR Expansion of Field Concrete, Cement, Concrete, and Aggregates 24 (2002) 13–19.

[106] P.A. Dunbar, P.E. Grattan-Bellew, Results of damage rating evaluation of condition of concrete from a number of structures affected by AAR, in: B. Fournier (Ed.), Proceedings of the CANMET/ACI International Workshop on Alkali-Aggregate Reactions in Concrete, CANMET/ACI, Dartmouth (Nova Scotia), 1995: pp. 257–265.

[107] P.E. Grattan-Bellew, A. Danay, Comparison of laboratory and field evaluation of alkali-silica reaction in large dams, in: Proceedings of the International Conference on Concrete Alkali–Aggregate Reactions in Hydroelectric Plants and Dams, Canadian Electrical Association; Canadian National Committee of the International Commission on Large Dams, Fredericton, New Brunswick, Canada , 1992: p. 23.

[108] L.F.M. Sanchez, B. Fournier, M. Jolin, J. Duchesne, Reliable quantification of AAR damage through assessment of the Damage Rating Index (DRI), Cem Concr Res 67 (2015) 74–92. https://doi.org/10.1016/j.cemconres.2014.08.002.

[109] L. Sanchez, B. Fournier, M. Jolin, M.A.B. Bedoya, J. Bastien, J. Duchesne, Use of Damage Rating Index to Quantify Alkali-Silica Reaction Damage in Concrete: Fine versus Coarse Aggregate, ACI Mater J 113 (2016) 395–407. https://doi.org/10.14359/51688983.

[110] V. Villeneuve, B. Fournier, J. Duchesne, Determination of the Damage in Concrete Affected by ASR—The Damage Rating Index (DRI), in: T. Drimalas, J. H. Ideker, B. Fournier (Eds.), 14th International Conference on Alkali-Aggregate Reaction (ICAAR), University of Texas at Austin, Austin, Texas, USA, 2012: p. 10. https://icaarconcrete.org/wp-content/uploads/2022/10/14ICAAR-VilleneuveV-1.pdf.

[111] R. Medeiros, L. Sanchez, A.C. dos Santos, Assessing Alkali-Carbonate Reaction-Induced Damage in Critical Concrete Infrastructure: The First ACR-Affected Field Structure Reported in Brazil, in: L.F. Sanchez, C. Trottier (Eds.), Proceedings of the 17th International Conference on Alkali-Aggregate Reaction in Concrete. ICAAR 2024.RILEM Bookseries, Springer, 2024: pp. 445–452. https://doi.org/10.1007/978-3-031-59349-9_51.

[112] L.F.M. Sanchez, B. Fournier, M. Jolin, J. Bastien, Evaluation of the Stiffness Damage Test (SDT) as a tool for assessing damage in concrete due to alkali-silica reaction (ASR): Input parameters and variability of the test responses, Constr Build Mater 77 (2015) 20–32. https://doi.org/10.1016/j.conbuildmat.2014.11.071.

[113] J.B. Walsh, The effect of cracks on the compressibility of rock, J Geophys Res 70 (1965) 381–389.

[114] R.S. Crouch, Specification for the Determination of Stiffness Damage Parameters from the Low Cyclic Uniaxial Compression of Plain Concrete Cores, Revision A, Mott, Hay & Anderson, Special Services Division, Internal Technical Note. (1987).

[115] T.M. Crisp, J.G.M. Wood, P. Norris, Towards Quantification of Microstructural Damage in AAR Deteriorated Concrete, in: International Conference on Recent Developments on the Fracture of Concrete and Rock, 1993.

[116] T.M. Crisp, P. Waldron, J.G.M. Wood, Development of a non destructive test to quantity damage in deteriorated concrete, Magazine of Concrete Research 45 (1989).

[117] N. Smaoui, M.-A. Bérubé, B. Fournier, B. Bissonnette, B. Durand, Evaluation of the expansion attained to date by concrete affected by alkali–silica reaction. Part I: Experimental study, Canadian Journal of Civil Engineering 31 (2004) 826–845. https://doi.org/10.1139/l04-051.

[118] L.F.M. Sanchez, B. Fournier, M. Jolin, J. Bastien, Evaluation of the stiffness damage test (SDT) as a tool for assessing damage in concrete due to ASR: Test loading and output responses for concretes incorporating fine or coarse reactive aggregates, Cem Concr Res 56 (2014) 213–229. https://doi.org/10.1016/j.cemconres.2013.11.003.

[119] L.F.M. Sanchez, B. Fournier, M. Jolin, J. Bastien, D. Mitchell, Practical use of the Stiffness Damage Test (SDT) for assessing damage in concrete infrastructure affected by alkali-silica reaction, Constr Build Mater 125 (2016) 1178–1188. https://doi.org/10.1016/j.conbuildmat.2016.08.101.

[120] Y. Zhu, A. Zahedi, L.F.M. Sanchez, B. Fournier, S. Beauchemin, Overall assessment of alkali-silica reaction affected recycled concrete aggregate mixtures derived from construction and demolition waste, Cem Concr Res 142 (2021) 106350. https://doi.org/10.1016/j.cemconres.2020.106350.

[121] C. Merz, A. Leemann, Assessment of the residual expansion potential of concrete from structures damaged by AAR, Cem Concr Res 52 (2013) 182–189. https://doi.org/10.1016/j.cemconres.2013.07.001.

[122] S. Multon, F.-X. Barin, B. Godart, F. Toutlemonde, Estimation of the Residual Expansion of Concrete Affected by Alkali Silica Reaction, Journal of Materials in Civil Engineering 20 (2008) 54–62. https://doi.org/10.1061/(asce)0899-1561(2008)20:1(54).

[123] A. Pavoine, L. Divet, Réaction sulfatique interne au béton : Essai d'expansion résiduelle sur carotte de béton extraite de l'ouvrage : Méthode d'essai n° 67, Techniques et méthodes des laboratoires des ponts et chaussées., Paris, 2009. https://doi.org/https://doi.org/10.3829/me67-fr.

[124] K.J. Folliard, M.D.A. Thomas, B. Fournier, Protocol for the Diagnosis and Prognosis of Concrete Structures Affected by Alkali-Silica Reaction and/or Delayed Ettringite Formation, Concrete Durability Center, The University of Texas at Austin, Austin, Texas, USA, 2007.

[125] R.-P. Martin, B. Godart, F. Toutlemonde, Accelerated Expansion Test: France, IFSTTAR, in: 2021: pp. 183–199. https://doi.org/10.1007/978-3-030-44014-5_8.

[126] V.E. Saouma, ed., Diagnosis & Prognosis of AAR Affected Structures: State-of-the-Art Report of the RILEM Technical Committee 259-ISR, 1st ed., Springer Cham, 2021. https://doi.org/10.1007/978-3-030-44014-5.

[127] T. Ramlochan, P. Zacarias, M.D.A. Thomas, R.D. Hooton, The effect of pozzolans and slag on the expansion of mortars cured at elevated temperature, Cem Concr Res 33 (2003) 807–814. https://doi.org/10.1016/S0008-8846(02)01066-9.

[128] C. Larive, Apports combinés de l'expérimentation et de la modélisation à la compréhension de l'alcali-réaction et de ses effets mécaniques, PhD, Ecole Nationale des Ponts et Chaussées, 1997. https://theses.hal.science/tel-00520676.

[129] X. Brunetaud, Étude de l'influence de différents paramètres et de leurs interactions sur la cinétique de l'amplitude de la réaction sulfatique interne au béton, Ph.D. thesis, Châtenay-Malabry, Ecole centrale de Paris, 2005. https://theses.fr/2005ECAP1025.

[130] A. Pavoine, X. Brunetaud, Développement et validation d'une méthode d'essai vis-à-vis de la formation différée de l'ettringite Application à l'étude d'impact de différents paramètres sur la cinétique et l'amplitude de gonflement, (2010). https://doi.org/10.3829/erlpc.oa65-fr.

Chapter 3: Problem Statement

As discussed in the literature review, the influence of moisture gradients and reinforcement configurations on the development of delayed ettringite formation (DEF) and combined delayed ettringite formation and alkali–silica reaction (DEF+ASR) remains insufficiently quantified and interpreted at the material scale. Previous studies have reported the effects of these mechanisms on expansion, cracking, and mechanical properties in laboratory specimens and selected structural components. Information remains limited, however, on how moisture gradients and reinforcement-induced restraint shape the current damage condition and the remaining potential for deterioration of affected members when assessed at the material scale. Progress in deterioration-oriented condition assessment at this scale is required to better support management protocols and rehabilitation decisions for DEF- and DEF+ASR-affected beams under service and ultimate limit states.

A multi-level assessment protocol has recently been developed that combines microscopic observations using the Damage Rating Index (DRI) with mechanical testing using the Stiffness Damage Test (SDT). This protocol provides a coherent basis to characterise internal cracking and the associated reduction in mechanical response in concrete affected by internal swelling reactions, and it is well suited to investigate how moisture gradients and reinforcement configurations influence the current damage condition in DEF- and DEF+ASR-affected members. In parallel, residual expansion testing is widely used to estimate the remaining swelling potential and to support prognosis interpretations. Uncertainty nevertheless persists regarding how prior exposure history influences the initial deterioration state at the onset of residual expansion testing, and regarding how residual expansion curves should be interpreted for concretes that have already experienced pronounced swelling under non-uniform moisture conditions and reinforcement-induced restraint.

In light of the gaps identified in the current literature and the considerations outlined above, this PhD thesis has been structured to address the following objectives:

- Advance the understanding of DEF (i.e., moderate and high) and DEF+ASR-induced microscopic deterioration under different moisture gradients through the damage rating index (DRI);

- Investigate the impact of distinct moisture gradients on the current damage condition and residual expansion potential of DEF-affected concrete with distinct deterioration potentials (i.e., moderate and severe DEF);
- Improve the understanding of the influence of distinct reinforcement-induced restraint on the diagnosis and prognosis of DEF-affected concrete under different moisture gradients;
- Evaluate the current condition and potential for further expansion of the concrete affected by DEF and DEF+ASR under reinforced-induced restraint and moisture gradient.

Chapter 4: Research program

As mentioned before, the objective of this study is to improve the current understanding of how moisture gradients and reinforcement-induced restraint influence the induced damage and residual expansion potential of concrete affected by DEF and DEF+ASR. Upon completion, this work should enhance optimization of management protocols to better inform rehabilitation strategies of DEF- and DEF+ASR-deteriorated concrete infrastructure. To achieve the proposed objective, a series of studies was conducted on cores and slices extracted from non- and reinforced structural elements that underwent different moisture gradients. The characteristics of the investigated structural member and the experimental program proposed for this research are described in the following sections, as illustrated in Figure 4.1.

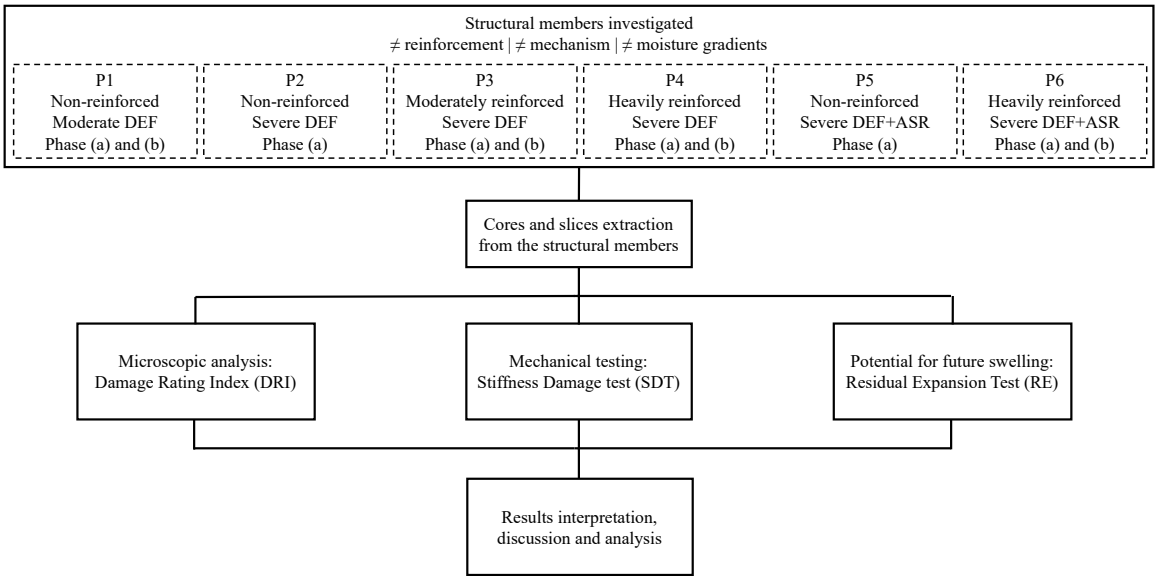


Figure 4.1 – Overall structure of the PhD project.

4.1 Characteristics of the structural members investigated

The structural members investigated in this research program were originally designed and manufactured during Martin's research program [1] at the former *Laboratoire Central des Ponts et Chaussées* (LCPC), now integrated within the *Laboratoire Expérimentation et Modélisation pour le Génie Civil et Urbain* (EMGCU) of *Université Gustave Eiffel* (Paris). This section summarizes the member geometry, concrete mixtures, heat treatment, reinforcement layouts, and

moisture exposure histories that define the boundary conditions governing deterioration development in beams P1 to P6.

4.1.1 Member geometry and identification

The member series comprises six prismatic beams, originally identified as P1-P6 [1]. Each beam measured 0.25 m × 0.50 m × 3.00 m and was tested on a supported span of 2.80 m in the original program [1]. The six members were cast to represent three concrete mixtures targeting distinct deterioration potentials (moderate DEF, severe DEF, and severe DEF+ASR) and distinct restraint configurations (non-reinforced and reinforced members with various reinforcement ratios). The association between beam identification and these characteristics is summarized in Table 4.1 and detailed in the following sections.

Table 4.1 - Identification and boundary-condition summary for beams P1–P6.

Beam ID	Mix ID	Mechanisms	Reinforcement	Moisture exposure	Manufacturing Year
P1	NR	Moderate DEF	Non-reinforced	Phase (a) + Phase (b)	2008
P2	R1	Severe DEF	Non-reinforced	Phase (a)	2008
P3	R1	Severe DEF	Moderately reinforced	Phase (a) + Phase (b)	2008
P4	R1	Severe DEF	Heavily reinforced	Phase (a) + Phase (b)	2008
P5	R2	Severe DEF+ASR	Non-reinforced	Phase (a)	2009
P6	R2	Severe DEF+ASR	Heavily reinforced	Phase (a) + Phase (b)	2009

4.1.2 Concrete mixtures and constituent materials

Three concrete mixtures were proportioned to promote moderate DEF, severe DEF, and severe DEF+ASR while targeting an average compressive strength of about 40 MPa, using a water-to-cement ratio of 0.46 [1]. The moderate DEF mixture used a Portland cement with low tricalcium aluminate content, whereas the severe DEF and DEF+ASR mixtures used a Portland cement with higher tricalcium aluminate and sulfate contents and higher alkali availability. The severe DEF+ASR mixture incorporated an ASR-reactive coarse aggregate, whereas moderate and severe DEF mixtures contained a non-ASR-reactive siliceous coarse aggregate [1]. All mixes contained a non-ASR-reactive siliceous sand. The cement characteristics, aggregate types, mixture proportions, measured mechanical properties, and maximum free-expansion potentials reported in the original program are compiled in Table 4.2.

Table 4.2 - Concrete mixtures, cements, and material properties for beams P1–P6

Mix ID	Associated beams	Targeted deterioration mechanism / potential	Cement designation	Key cement characteristics (wt %)	Aggregates	Mix design (kg per m³)	28-day mechanical and physical properties[1]	Maximum induced expansion potential[2]
NR	P1	Moderate DEF potential (reference DEF mix)	Ciment_NR (CEM I type)	C_3S: 43.22 C_2S: 32.16 C_3A: 2.35 C_4AF: 11.63 CSH_2: 5.61 CC: 3.80 Al_2O_3: 3.33 SO_3: 2.61 Na_2Oeq: 0.44	Coarse agg: Gravillon_NR (siliceous, non-reactive to ASR, fractions 4/8 and 8/12 mm). Fine_agg: Sable_NR (siliceous, non-reactive to ASR, 0/2 mm).	Cement: 410 Water: 199.1 Fine_agg: 856.0 Coarse_agg 4/8: 100.3 Coarse _agg 8/12: 831.0 KOH (added): 0 w/c: 0.46 C/F: 1.09	Compressive strength (MPa): 39.3 [±1.5] Tensile strength (MPa): 4.5 [±0.4] Modulus of elasticity (GPa) 32.8 [± 1.2] Poisson's ratio (ν): 0.176 [±0.022] Bulk density (kg/m³): 2328 [±22] (cure under hydric sealing, 28 days).	0.35%
R1	P2, P3, P4	Severe DEF potential (high-sulfate cement, higher alkali)	Ciment_R (CEM I type, higher C_3A and SO_3)	C_3S: 41.45 C_2S: 27.15 C_3A: 4.97 C_4AF: 11.54 CSH_2: 7.44 CC: 4.18 Al_2O_3: 4.30 SO_3: 3.46 Na_2Oeq: 0.83	Coarse_agg: Gravillon_NR (siliceous, non-reactive to ASR, 4/8 and 8/12 mm). Fine_agg: Sable_NR (siliceous, non-reactive to ASR, 0/2 mm).	Cement: 410 Water: 199.0 Fine_agg: 854.0 Coarse_agg 4/8: 100.0 Coarse _agg 8/12: 829.0 KOH (added): 1.745 w/c: 0.46 C/F:1.09	Compressive strength (MPa): 38.7 [±5.5] Tensile strength MPa): 5.0 [±0.0] Modulus of elasticity (GPa): 30.8 [±3.2] Poisson's ratio (ν): 0.181[±0.014] Bulk density (kg/m³): 2320 [±11] (cure under hydric sealing, 28 days).	1.79%
R2	P5, P6	Combined DEF + ASR potential (high-sulfate, higher alkali, reactive coarse aggregate)			Coarse_agg: Gravillon_PR (primary-era limestone, potentially reactive to ASR, fractions 4/7.1, 7.1/10, 10/14 mm). Fine_agg: Sable_NR (siliceous, non-reactive to ASR, 0/2 mm).	Cement: 410 Water: 199.2 Fine_agg: 797.0 Coarse_agg 4/7.1: 114.3 Coarse_agg 7.1/10: 29.0 Coarse_agg 10/14: 843.0 KOH (added): 1.745 w/c: 0.46 C/F:1.24	Compressive strength (MPa): 41.4 [±2.5] Tensile strength (MPa): 4.6 [±0.6] Modulus of elasticity (GPa): 31.5 [±0.8] Poisson's ratio (ν): 0.247 [±0.003] Bulk density (kg/m³): 2363 [±33] (cure under hydric sealing, 28 days).	1.77%

[1]28-day mechanical and physical properties (after thermal treatment + specimens were cured under sealed, moisture-tight conditions); numbers in square brackets correspond to standard deviation.

[2]Free expansion under initially immersed in water and then transferred to drying at 30 % relative humidity

4.1.3 Thermal treatment

All beams were subjected to a controlled heat treatment designed to activate DEF through a temperature history representative of mass concrete elements [1]. The heat treatment was designed to generate a homogeneous. DEF potential throughout the specimens, and thus avoid expansion potential gradients The beams were transferred approximately 2 h after casting to a temperature-controlled water bath and subjected to a programmed thermal cycle comprising a heating stage aligned with the adiabatic temperature rise of the mixture, a constant plateau at 81 °C for 72 h, and controlled cooling at approximately 1 °C h^{-1}, for a total duration of about 6 d [1,2]. The heat treatment applied to beams P1 to P6 is summarized in Figure 4.2.

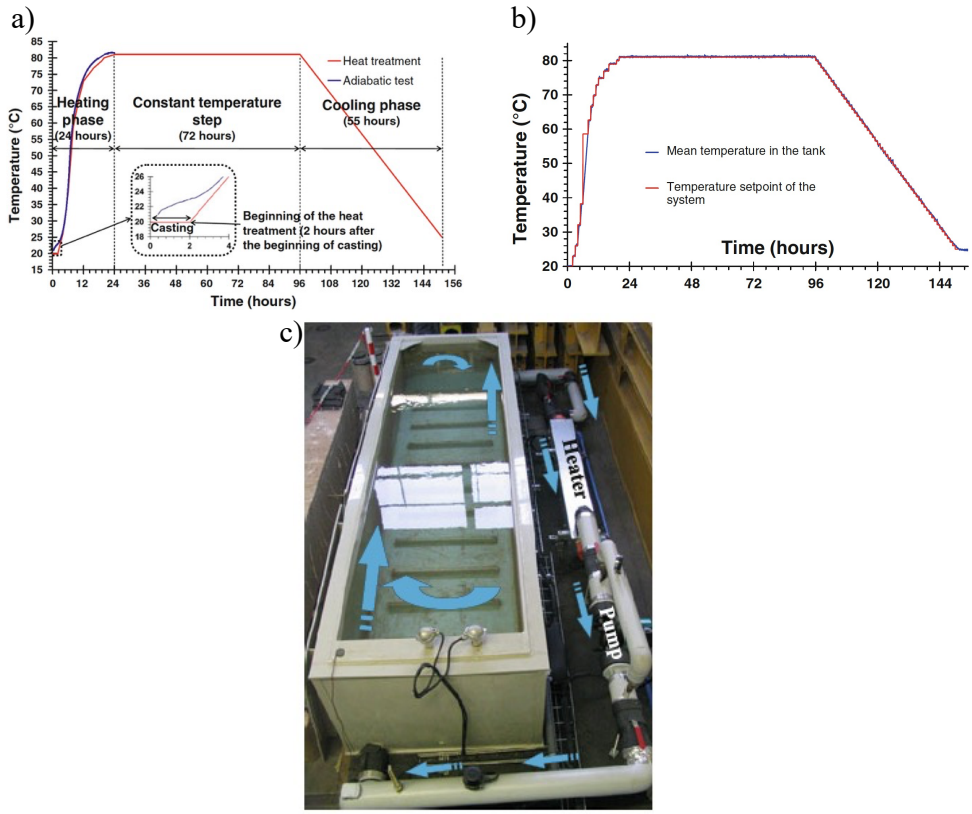


Figure 4.2 – Thermal treatment applied to all the beams. a) Temperature evolution during the heat treatment compared to the results of an adiabatic test. b) Experimental temperature profile in the tank during a heat treatment. c) Heat treatment device

4.1.4 Reinforcement configurations

The member series includes non-reinforced and reinforced configurations to generate distinct levels of restraint to swelling-induced deformation at the member scale. The non-reinforced configuration contains no structural reinforcement. The moderately reinforced configuration comprises two 16 mm longitudinal bars in the tensile (bottom) zone and two 10 mm longitudinal bars in the compression (top) zone, with 8 mm stirrups at 0.35 m spacing. The heavily reinforced configuration comprises two 32 mm longitudinal bars in the tensile zone and two 20 mm longitudinal bars in the compression zone, with 12 mm stirrups at 0.20 m spacing. These layouts correspond to longitudinal reinforcement ratios of approximately 0.45% and 1.8% and transverse reinforcement ratios of approximately 0.12% and 0.45% for the moderately and heavily reinforced configurations, respectively. The reinforcement layouts are illustrated in Figure 4.3.

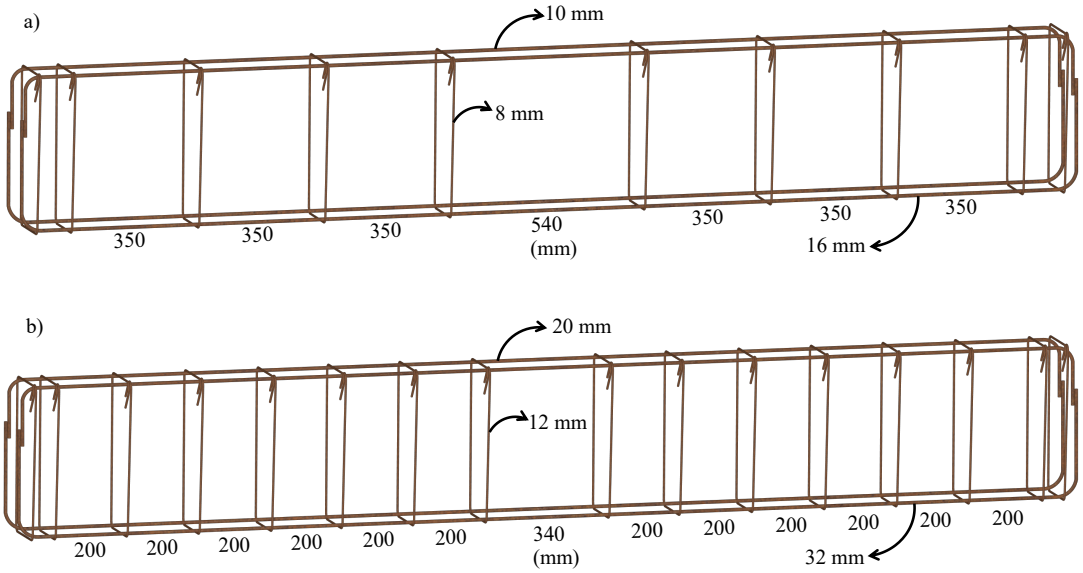


Figure 4.3 - Reinforcement configurations. a) Moderately reinforced. b) Heavily reinforced

4.1.5 Moisture exposure histories

After heat treatment, the beams were subjected to imposed moisture boundary conditions designed to generate vertical moisture gradients while limiting lateral moisture exchange [1]. The aging program was implemented in two phases. Phase (a) consisted of partial immersion of the bottom 7 cm for 14 months, while the top surface was exposed to drying conditions at approximately 30% relative humidity. Phase (b) consisted of a continued bottom water supply combined with

additional water supply at the top surface for a further 14 months to evaluate the effect of late wetting. During these exposures, the members were stored at 38 ± 1 °C with the lateral faces sealed to limit transverse moisture exchange [1]. Because deterioration progression differed across members, the exposure sequence effectively reached differed between beams; the moisture exposure boundary conditions are shown in Figure 4.4, and the resulting exposure histories are reported in Table 4.1. Two non-reinforced members experienced premature structural failure during Phase (a), with beam P2 (severe DEF) failing after approximately 330 days of exposure and beam P5 (Severe DEF+ASR) failing after 180 days of monitoring [1].

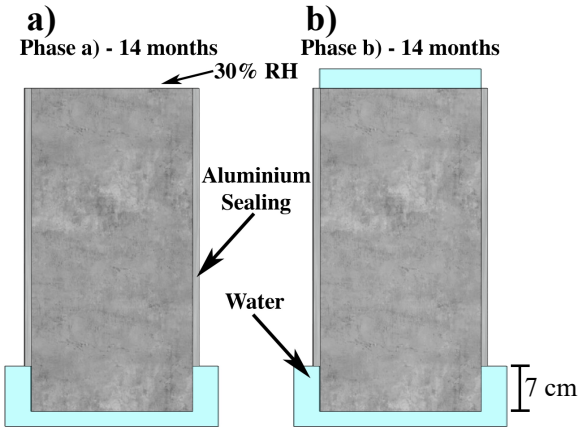


Figure 4.4 – Moisture exposure. a) Phase (a). b) Phase (b)

4.1.6 Post-programme storage and transfer history

Beams P1 to P6 were manufactured between May 2008 and March 2009 as part of Martin's experimental program and were subjected to the heat-treatment and moisture-exposure histories described in Sections 4.1.3 and 4.1.5 [1]. During the aging stage, deterioration progressed at different rates across members. Post-failure coring was then carried out on beams P2 and P5 to support residual-expansion testing and complementary observations during Martin's program [1]. The beams P1, P3, P4, and P6 were tested to determine the residual bearing capacity (i.e., four-point bending tests). Following completion of Martin's research program [1], the remaining portions of the beams were conserved as segments under laboratory storage conditions, experiencing the administrative modification of LCPC, IFFSTAR, and Université Gustave Eiffel, being transferred from the facilities where they were manufactured and tested during Martin's program, to the current facilities of EMGCU. In 2012, P2 and P5 experienced another coring

campaign. P5 results are discussed in Martin et al. [3]. Only the remaining segments were then available for investigation in the present research program. The segments were maintained under laboratory storage until the start of the present program in 2023, after which the sampling and experimental procedures described in Section 4.2 were implemented.

4.2 Sampling

Sampling was conducted on the beam segments available from Martin's program. Cores and slices were extracted from locations selected to represent the imposed moisture gradients while preserving specimen integrity. Sampling locations were therefore defined to avoid major visible cracks and, where applicable, to limit direct intersection with reinforcement and embedded sensors. Despite this selection strategy, the severely damaged condition of several members constrained the number of intact cores that could be recovered, which limited the level of replication achievable for some test series.

The sampling plan was designed to (i) characterize deterioration development along the beam height in non-reinforced members exposed to vertical moisture gradients and (ii) examine direction-dependent response in reinforced members to assess reinforcement-induced restraint effects under the same exposure history. In reinforced members, cores were extracted in multiple orientations (transverse, longitudinal, and vertical) to support the interpretation of damage anisotropy. Microscopic assessment was restricted to the transverse direction, and dedicated transverse slices were prepared for Damage Rating Index (DRI) measurements. Stiffness Damage Test (SDT) and residual expansion (RE) testing were performed on selected cores depending on recovery quality and test prioritization, as summarized in Tables 4.4 to 4.8.

4.2.1 Sampling from the non-reinforced beam affected by moderate DEF (P1)

Beam P1 was sampled along the height to capture the vertical deterioration profile induced by the imposed moisture gradient. Cores were extracted from nominal height intervals spanning 0–10 cm to 40–50 cm. The extracted specimens were allocated to SDT and RE testing, with additional transverse slices prepared for DRI measurements. Table 4.3 summarizes the identification, coordinates, and test assignment of the P1 cores and slices.

Table 4.3 – Identification and location of cores and slices extracted from the non-reinforced beam affected by moderate DEF (P1)

Sample_ID	Location of coring			Testing 1			Testing 2
	Nominal location	Length [cm]	Height [cm]	DRI	SDT	RE	RE
P1_0,08 (2)	0-10cm	60.7	10.2		✓		✓
P1_0,17 (2)	10-20cm	74.2	18.6		✓		✓
P1_0,27 (2)	20-30cm	60.7	27.1		✓		✓
P1_0,37 (2)	30-40cm	70.8	34.7		✓		✓
P1_0,44 (2)	40-50cm	60.7	43.2		✓		✓
P1_0,08 (3)	0-10cm	89.5	7.6			✓	
P1_0,08 (4)	0-10cm	115.8	6.8			✓	
P1_0,17 (3)	10-20cm	104.7	17.8			✓	
P1_0,23 (2)	20-30cm	17.0	27.5			✓	
P1_0,27 (3)	20-30cm	88.6	28.8			✓	
P1_0,34 (1)	30-40cm	103.7	36.8			✓	
P1_0,44 (3)	40-50cm	88.7	42.4			✓	
P1_S1	Cross-section	137.6	-	✓			

4.2.2 Sampling from the non-reinforced beam affected by severe DEF (P2)

Beam P2 was sampled to characterize severe DEF-induced deterioration under the moisture exposure history reached in Phase (a). Coring locations were selected along the height while avoiding major damage zones to the extent possible. Due to the impaired integrity of the member, specimen recovery constrained replication for some test series. Transverse slices were prepared for DRI, and retrieved cores were assigned to SDT and RE depending on suitability. The SDT specimens were extracted in 2015 as part of a previous coring campaign; the corresponding SDT data were processed and interpreted within the present research program. Table 4.4 summarizes the identification, coordinates, and test assignment of the P2 cores and slices.

Table 4.4 – Identification and location of cores and slices extracted from the non-reinforced beam affected by severe DEF (P2)

Sample_ID	Location of coring			Testing 1		
	Nominal location	Length [cm]	Height [cm]	DRI	SDT	RE
P2_0,08 (2)	0-10cm	32.8	7.1			✓
P2_0,17 (2)	10-20cm	22.0	18.0			✓
P2_0,27 (2)	20-30cm	29.0	29.0			✓
P2_0,37 (2)	30-40cm	39.0	38.0			✓
P2_0.08_1	0-10cm	116.1	8.0		✓	
P2_0.08_2	0-10cm	135.0	7.9		✓	
P2_0.17_1	10-20cm	121.0	17.8		✓	
P2_0.17_2	10-20cm	148.0	18.0		✓	
P2_0.27_1	20-30cm	116.2	27.2		✓	
P2_0.27_2	20-30cm	139.0	27.1		✓	
P2_0.37_1	30-40cm	128.0	37.3		✓	
P2_0.37_2	30-40cm	157.0	37.4		✓	
P2_0.44_1	40-50cm	117.1	44.3		✓	
P2_0.44_2	40-50cm	141.0	44.1		✓	
P2_S1	Cross-section	59.7	-	✓		

4.2.3 Sampling from the moderately reinforced beam affected by severe DEF (P3)

For beam P3, the sampling strategy was configured to capture both the deterioration profile along the height of the member and the direction-dependent response imposed by reinforcement restraint. Two nominal elevations were used to represent the upper and lower parts of the member, located at 0.17 m and 0.37 m from the top surface, respectively. Transverse cylindrical cores were allocated to DRI assessment, and additional cores were retrieved in transverse, longitudinal, and vertical orientations to support SDT and residual expansion testing. Coring locations were selected to minimize direct reinforcement interception and to maximize the likelihood of retrieving intact specimens suitable for each test. Specimen identification, coordinates, and test allocation are reported in Table 4.5.

Table 4.5 – Identification and location of cores and slices extracted from the moderately reinforced beam affected by severe DEF (P3)

Sample_ID	Direction T – transverse L – longitudinal V - vertical	Location of coring			Testing 1			Testing 2
		Nominal location	Length [cm]	Height [cm]	DRI	SDT	RE	RE
P3a_0,17 (1)	T	Upper	27.8	16.7	✓			
P3a_0,34 (1)	T	Lower	28.9	35.2	✓			
P3b_0,17 (1)	T	Upper	162.7	14.3	✓			
P3b_0,34 (1)	T	Lower	166.9	36.9	✓			
P3a_0,17 (2)	T	Upper	133.3	16.7		✓		✓
P3a_0,17 (4)	T	Upper	41.7	16.7		✓		✓
P3a_0,34 (2)	T	Lower	130.6	33.3		✓		✓
P3a_0,34 (4)	T	Lower	41.2	35.2		✓		✓
P3b_0,17 (2)	T	Upper	269.9	19.1		✓		✓
P3b_0,24	T	Upper	193.1	22.8		✓		✓
P3b_0,32	T	Lower	218.3	33.3		✓		✓
P3a_0,17 (3a)	L	Upper	114.2	16.7		✓		✓
P3a_0,34 (3a)	L	Lower	114.2	36.1		✓		✓
P3a_H (1)	V	Upper	65.5	12.5		✓		✓
P3a_H (3)	V	Lower	65.5	37.5		✓		✓
P3a_0,17 (3b)	T	Upper	94.4	16.7			✓	
P3a_0,34 (3b)	T	Lower	94.4	36.1			✓	
P3a_H (2)	V	Upper	78.5	12.5			✓	
P3a_H (4)	V	Lower	78.5	37.5			✓	

4.2.4 Sampling from the heavily reinforced beam affected by severe DEF (P4)

Beam P4 represents the highest reinforcement restraint level within the severe DEF series, and sampling was organized to investigate the associated anisotropic damage response under the imposed moisture history. Two nominal elevations were used to represent the upper and lower parts of the member, located at 0.17 m and 0.37 m from the top surface, respectively. Transverse cylindrical cores were used to support DRI measurements, and complementary cores were retrieved in transverse, longitudinal, and vertical orientations to enable SDT and residual expansion testing when specimen integrity permitted. Coring locations were distributed between these elevations and selected to minimize reinforcement interception while maintaining representative coverage of the member height. Specimen identification, coordinates, and test allocation are reported in Table 4.6.

Table 4.6 – Identification and location of cores and slices extracted from the heavily reinforced beam affected by severe DEF (P4)

Sample_ID	Direction T – transverse L – longitudinal V - vertical	Location of coring			Testing 1			Testing 2
		Nominal location	Length [cm]	Height [cm]	DRI	SDT	RE	RE
P4a_0,17 (1)	T	Lower	27.7	33.3	✓			
P4a_0,34 (1)	T	Upper	27.7	16.7	✓			
P4a_0,17 (2)	T	Lower	67.9	32.2		✓		✓
P4a_0,34 (2)	T	Upper	67.9	17.7		✓		✓
P4b_0,34 (2)	T	Upper	233.4	15.8		✓		✓
P4a_0,17 (3)	L	Upper	137.5	15.4		✓		✓
P4a_0,34 (3)	L	Lower	137.5	30.1		✓		✓
P4a_H (1)	V	Lower	47.6	37.5		✓		✓
P4a_H (2)	V	Upper	47.6	12.5		✓		✓
P4b_0,17 (1)	L	Upper	198.9	18.4			✓	
P4b_0,34 (1)	L	Lower	198.9	34.2			✓	
P4a_H (3)	V	Lower	87.1	37.5			✓	
P4a_H (4)	V	Upper	87.1	12.5			✓	

4.2.5 Sampling from the non-reinforced beam affected by severe DEF+ASR (P5)

Beam P5 was sampled to characterize combined DEF+ASR deterioration under the available exposure history. Sampling in the present program was constrained both by the advanced damage state of the member and by the limited remaining intact volume resulting from previous coring campaigns. Coring locations were therefore restricted to zones providing sufficient integrity for the planned testing. Transverse slices were prepared for DRI, and retrieved cores were allocated to SDT and/or residual expansion testing depending on suitability. Table 4.7 summarizes specimen identification, coring coordinates, and test assignment.

Table 4.7 – Identification and location of cores and slices extracted from the non-reinforced beam affected by severe DEF+ASR (P5)

Sample_ID	Location of coring			Testing 1		
	Nominal location	Length [cm]	Height [cm]	DRI	SDT	RE
P5_0,17 (2)	Upper	33.3	20.4			✓
P5_0,17 (3)	Upper	66.8	16.2		✓	
P5_S1	Cross-section	98.0	-	✓		

4.2.6 Sampling from the heavily reinforced beam affected by severe DEF+ASR (P6)

Beam P6 was sampled to characterize combined DEF+ASR deterioration under reinforcement-induced restraint and moisture gradients. Two nominal elevations were used to represent the upper and lower parts of the member, located at 0.17 m and 0.37 m from the top surface, respectively. Transverse cylindrical cores were allocated to DRI assessment, and additional cores were retrieved in transverse and vertical orientations to support SDT and residual expansion testing, depending on specimen integrity. Coring locations were selected to preserve specimen integrity and to limit direct reinforcement interception to the extent possible. Specimen identification, coordinates, and test assignment are summarized in Table 4.8.

Table 4.8 – Identification and location of cores and slices extracted from the heavily reinforced beam affected by severe DEF+ASR (P6)

Sample_ID	Direction T – transverse L – longitudinal V - vertical	Location of coring			Testing 1			Testing 2
		Nominal location	Length [cm]	Height [cm]	DRI	SDT	RE	RE
P6a_0,17 (1)	T	Upper	21.4	18.0	✓			
P6b_0,17 (1)	T	Upper	177.7	17.0	✓			
P6a_0,34 (1)	T	Lower	21.4	33.3	✓			
P6a_0,17 (3b)	T	Upper	100.0	18.0		✓		✓
P6a_0,34 (3b)	T	Lower	100.0	33.3		✓		✓
P6a_0,17 (2)	T	Upper	65.5	180		✓		✓
P6_ 0,34 (2)	T	Lower	65.5	33.3		✓		✓
P6a_H (1)	V	Lower	43.4	37.5		✓		✓
P6a_H (2)	V	Upper	43.4	12.5		✓		✓
P6a_H (3)	V	Lower	82.7	37.5			✓	
P6a_H (4)	V	Upper	82.7	12.5			✓	
P6b_0,16	T	Upper	260.6	16.2			✓	
P6b_0,18	T	Upper	233.2	19.3			✓	

4.3 Experimental procedures

4.3.1 Damage Rating Index and crack measurements

The conventional and extended versions of the Damage Rating Index (DRI) were conducted on the specimens defined in Section 4.2, using transverse slices for the non-reinforced beams and

transverse cylindrical core faces for the reinforced beams. The samples were polished using a handheld device and diamond-impregnated pads in the following grit order: no. 50, 120, 200, 400, 800, 1500, and 3000 [4]. After polishing, DRI analysis was performed on each specimen over a minimum investigated surface area of 200 cm^2, in accordance with the DRI procedure [5,6]. The features of deterioration were

counted and classified following the revised protocol of Villeneuve and Fournier [5,6], and the corresponding weighting factors were applied, resulting in a summation that was normalized to a reference area of 100 cm^2 [5,6].

The extended DRI version was conducted in parallel to analyze the crack density (CD), defined as the total number of open cracks per unit area, and to determine the maximum crack width and maximum crack length on the investigated surface, following Sanchez et al. [4,7].

Crack widths were initially screened using a transparent comparator card under a 15× magnification loupe. Final crack width and crack length values were obtained from calibrated digital images processed in ImageJ (National Institutes of Health, NIH). Comparator-card measurements were not retained because many crack apertures were below its practical reading limit (0.05 mm). For each image, a steel rule was positioned within the field of view and aligned with the specimen surface to maintain a common focal plane. The reference length of the rule was verified using a digital caliper with 0.01 mm resolution. Image calibration was performed by matching a known rule distance, typically 1 mm, to its pixel count, yielding a representative scale of 100 pixels per mm, corresponding to 0.01 mm per pixel. Crack width was taken as the maximum visible opening, and crack length was obtained by tracing the crack trajectory along the surface. Each measurement was performed twice, and the average value was retained. Under the assumption of one-pixel accuracy in manual point placement, the effective measurement resolution was 0.01 mm, and crack widths and lengths are reported in mm to two decimal places.

4.3.2 Stiffness Damage Test

The SDT was conducted on cylindrical cores of 110 mm in diameter and 220 mm in height, as detailed in section 4.2. An automatic grinding machine was used to finish the cross-section of specimens. The specimens were then stored at 100% relative humidity and 20 ± 2°C for 48 hours to re-establish moisture equilibrium and reduce variability in the mechanical response [8]. The

Stiffness Damage Test (SDT) was conducted using five successive loading–unloading cycles under uniaxial compression. Given the advanced deterioration of the concrete, the peak stress was limited to 30% of the reference compressive strength (40 megapascal) and was applied at a loading rate of 0.10 megapascal per second. Test outputs were interpreted through the stiffness damage index (SDI), the plastic deformation index (PDI), and the modulus of elasticity (E).

4.3.3 Residual expansion

Residual expansion (RE) testing was conducted on cylindrical concrete cores, as detailed in Section 4.2, using specimens with nominal dimensions of 110 mm in diameter and 250 mm in height. The procedure followed the protocol described by Martin et al. [3]. Stainless-steel measurement pins were installed along the specimen axis at 120-degree intervals, enabling longitudinal deformation to be monitored using a digital extensometer with a 100 mm gauge length. After drilling and pin installation, the specimens were immersed in water at 38 degrees Celsius for 24 hours to restore moisture conditions and to reach thermal equilibrium prior to establishing the reference reading. Length measurements were then taken to define the zero reference. This preconditioning step reduced the contribution of early hygric swelling to the recorded deformation response, improving the interpretation of expansion associated with internal swelling reactions during the test period. Following the reference reading, specimens were stored in water at 38 °C for the monitoring period, which extended to approximately 406 days. Axial expansion and mass gain were measured at regular intervals throughout the test. The storage conditions were selected to reproduce the temperature and moisture conditions governing the beam aging phases, so that the measured residual expansion could be interpreted as the remaining swelling potential of the extracted concrete under favourable exposure conditions [3].

4.4 References

[1] R.P. Martin, Analyse sur structures modèles des effets mécaniques de la réaction sulfatique interne du béton, PhD thesis, Université Paris Est., 2010. https://theses.hal.science/tel-00558200.

[2] R.-P. Martin, F. Toutlemonde, Theoretical and experimental validation of a simple method to reproduce representative DEF-prone conditions in laboratory, Mater Struct 46 (2013) 1245–1255. https://doi.org/10.1617/s11527-012-9967-2.

[3] R.-P. Martin, L. Sanchez, B. Fournier, F. Toutlemonde, Evaluation of different techniques for the diagnosis & prognosis of Internal Swelling Reaction (ISR) mechanisms in concrete, Constr Build Mater 156 (2017) 956–964. https://doi.org/10.1016/j.conbuildmat.2017.09.047.

[4] L.F.M. Sanchez, B. Fournier, M. Jolin, J. Duchesne, Reliable quantification of AAR damage through assessment of the Damage Rating Index (DRI), Cem Concr Res 67 (2015) 74–92. https://doi.org/10.1016/j.cemconres.2014.08.002.

[5] V. Villeneuve, B. Fournier, J. Duchesne, Determination of the Damage in Concrete Affected by ASR—The Damage Rating Index (DRI), in: T. Drimalas, J. H. Ideker, B. Fournier (Eds.), 14th International Conference on Alkali-Aggregate Reaction (ICAAR), University of Texas at Austin, Austin, Texas, USA, 2012: p. 10. https://icaarconcrete.org/wp-content/uploads/2022/10/14ICAAR-VilleneuveV-1.pdf.

[6] V. Villeneuve, Détermination de l'endommagement du béton par méthode pétrographique quantitative, Master's thesis (Mémoire de maîtrise), Université Laval, 2011. https://www.collectionscanada.gc.ca/obj/thesescanada/vol2/QQLA/TC-QQLA-27962.pdf

[7] L. Sanchez, B. Fournier, M. Jolin, M.A.B. Bedoya, J. Bastien, J. Duchesne, Use of Damage Rating Index to Quantify Alkali-Silica Reaction Damage in Concrete: Fine versus Coarse Aggregate, ACI Mater J 113 (2016) 395–407. https://doi.org/10.14359/51688983.

[8] L.F.M. Sanchez, B. Fournier, M. Jolin, J. Bastien, D. Mitchell, Practical use of the Stiffness Damage Test (SDT) for assessing damage in concrete infrastructure affected by alkali-silica reaction, Constr Build Mater 125 (2016) 1178–1188. https://doi.org/10.1016/j.conbuildmat.2016.08.101.

Chapter 5: Core of the thesis – Scientific Papers

5.1 General Overview

To analyze the results obtained through the experimental program described in Chapter 4, four scientific papers were prepared as the core of this thesis. Each paper addresses a defined component of the research objective while maintaining methodological continuity through the multi-level assessment protocol applied to the beam series. The papers progress from detailed microscopic characterization of DEF- and DEF+ASR-affected concretes under severe moisture gradients to multi-level interpretations that integrate microscopic analysis, mechanical responses, and residual expansion testing to appraise the current condition and future potential for further expansion.

Paper I establishes the microscopic basis for interpreting deterioration under moisture gradients by applying the conventional and extended Damage Rating Index (DRI) to DEF and DEF+ASR members. Paper II then investigates how distinct moisture gradients influence the current damage condition and residual expansion potential in non-reinforced members affected by distinct DEF-induced deterioration potentials (i.e., moderate and severe). Paper III evaluates how reinforcement-induced restraint modifies the development of induced deterioration in DEF across moisture gradients by comparing non-, moderately, and heavily reinforced concrete members affected by DEF. Paper IV extends the scope to the combined role of moisture gradients and reinforcement-induced restraint in both DEF and DEF+ASR-affected members, with emphasis on linking current condition to the potential for further expansion under field-representative exposure histories. Figure 5.1 summarizes the conceptual and methodological links between Papers I - IV.

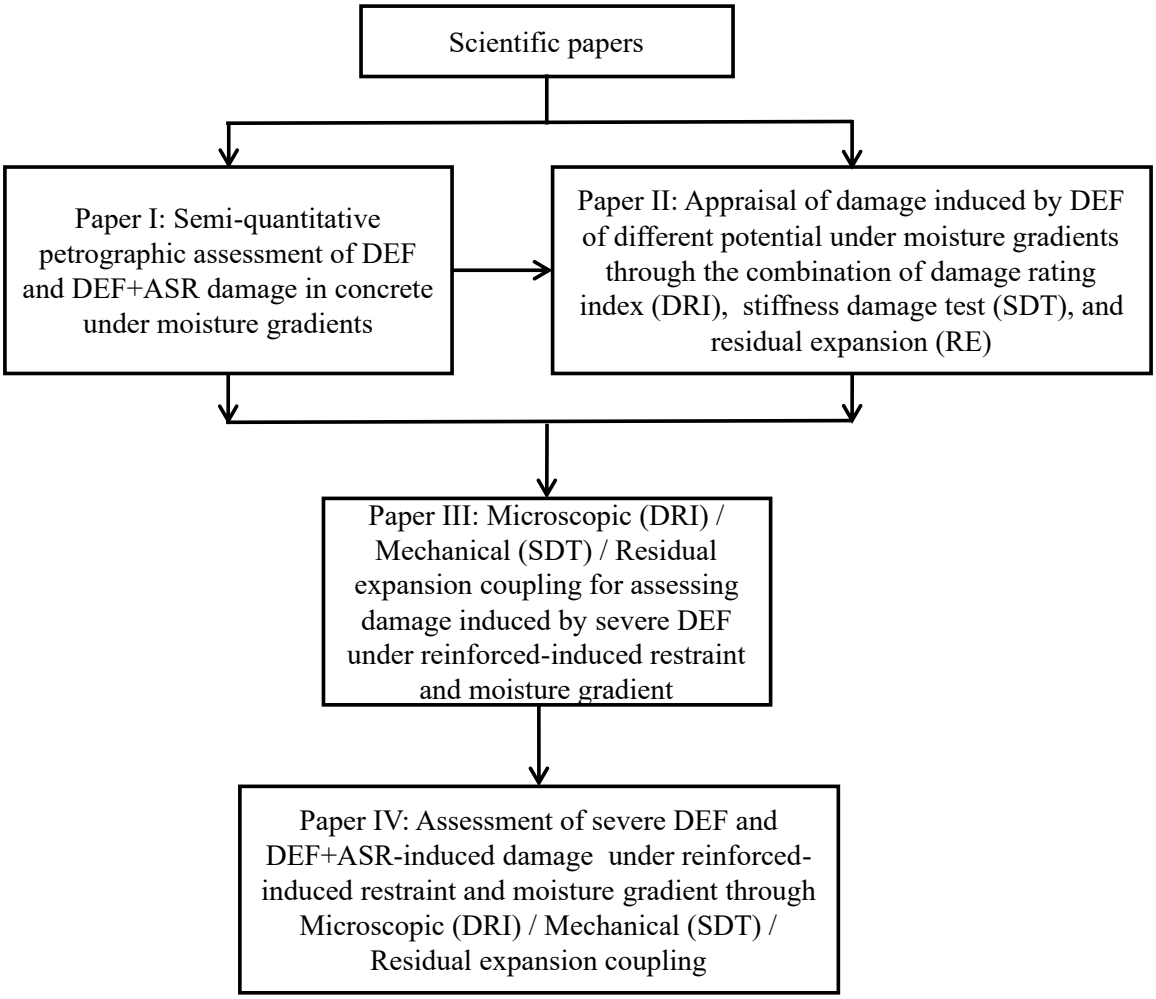


Figure 5.1 – Core of the PhD Thesis – links between the scientific papers.

5.2 Scope and objectives of the scientific papers

A concise description of the scope and primary objective of each paper is provided hereafter.

5.2.1 Paper I (Chapter 6): Microscopic assessment of DEF- and DEF+ASR-affected concrete under severe moisture gradients

Paper I investigates the distribution of microscopic deterioration in non-reinforced beam members affected by DEF (i.e., ≠ magnitudes) and DEF+ASR under distinct moisture gradients. The study applies the conventional and extended versions of the DRI to polished cross-sections extracted at selected locations, enabling interpretation of mechanism-specific microscopic features and cracking attributes as a function of moisture exposure for different DEF damage potentials and

DEF+ASR combined deterioration. The objective of this paper is to establish a microscopy-driven basis for describing how moisture gradients influence the location and intensity of deterioration in DEF and DEF+ASR, and to define the microstructural damage indicators needed to support subsequent coupling with mechanical response and residual expansion results.

5.2.2 Paper II (Chapter 7): Influence of moisture gradients on diagnosis and prognosis of non-reinforced DEF-affected members

Paper II evaluates how distinct vertical moisture gradients influence the current damage condition and the residual expansion potential of non-reinforced members manufactured with moderate and severe DEF deterioration potentials. The paper integrates DRI analysis with mechanical responses (SDT) and residual expansion testing on cores extracted along the member height. The objective is to interpret how moisture-driven heterogeneity affects (i) the present state of deterioration and (ii) the remaining swelling potential, with explicit consideration of deterioration potential differences between the investigated DEF mixtures.

5.2.3 Paper III (Chapter 8): Reinforcement-induced restraint effects on diagnosis and prognosis under moisture gradients in DEF-affected members

Paper III investigates how reinforcement configuration influences diagnosis and prognosis outputs for DEF-affected concrete members exposed to moisture gradients. The work evaluates members cast with the same DEF-prone mixture (i.e., severe DEF) and subjected to moisture gradients and varying restraint levels through non-, moderate-, and heavy-reinforcement layouts. The multi-level protocol combines DRI on transverse cylindrical cores, SDT testing on selected orientations (i.e., transverse, longitudinal, and vertical), and residual expansion measurements to interpret restraint-driven damage anisotropy and its implications for residual swelling potential. The objective is to understand how reinforcement-induced restraint and moisture gradients alter the current DEF-induced damage and the potential for future deterioration.

5.2.4 Paper IV (Chapter 9): Combined influence of moisture gradients and reinforcement-induced restraint in DEF and DEF+ASR members

Paper IV examines deterioration development when moisture gradients and reinforcement-induced restraint coexist in both DEF and DEF+ASR-affected members. The study evaluates non-reinforced and heavily reinforced members with distinct mechanisms exposed to moisture gradients and interprets current damage using a multi-level protocol that combines microscopic (i.e., DRI), mechanical (i.e., SDT), and residual expansion. The objective is to interpret how the interaction between moisture gradients, restraint level, and deterioration mechanism influences the present condition and the potential for further expansion.

Chapter 6: Paper I - Microscopic assessment of DEF- and DEF+ASR-affected concrete under severe moisture gradients

Rennan Medeiros [1]; Leandro Sanchez [2]; Renaud-Pierre Martin[3]; François Toutlemonde [4]

[1]PhD Candidate – University of Ottawa, Department of Civil Engineering
[2]Full Professor – University of Ottawa, Department of Civil Engineering
[3]Univ Gustave Eiffel, MAST-EMGCU, F-77454 Marne - la- Vallée, France
[4] Univ Gustave Eiffel, MAST-EMGCU, F-77454 Marne - la- Vallée, France

ABSTRACT

This study investigates microscopic deterioration in concrete beams affected by delayed ettringite formation (DEF) and combined DEF and alkali–silica reaction (DEF+ASR) under distinct vertical moisture gradients. Cross-sectional slices from laboratory-made non-reinforced beams, exposed to distinct moisture profiles, were analyzed using both the conventional and extended versions of the Damage Rating Index (DRI). Results confirmed that moisture uptake influences the distribution and extent of damage. In DEF-affected concrete, distress concentrated in zones with greater water ingress. In DEF+ASR-affected concrete, the overall severity was greater, and the contrast between wet and dry regions was less marked, reflecting the lower moisture dependence of ASR. A DRI-based approach was developed to separate DEF- and ASR-related contributions, demonstrating that ASR prevailed in drier regions, while DEF dominated in wetter regions. Qualitative models of crack initiation and propagation were proposed, providing a refined description of deterioration under non-uniform exposure and extending an established ASR model.

Keywords: Microscopic deterioration, Damage Rating Index (DRI), Delayed ettringite formation (DEF), Alkali–silica reaction (ASR), DEF+ASR, Moisture gradient. Non-uniform exposure. Concrete durability.

6.1 Introduction

Delayed ettringite formation (DEF) and alkali–silica reaction (ASR) are the most damaging internal swelling reaction (ISR) mechanisms affecting the durability and serviceability of concrete infrastructure [1–4]. These mechanisms may act independently or in combination, with their concurrent occurrence not rarely reported in field structures [5–7]. The development of combined

DEF and ASR is facilitated by physicochemical synergies. Chemically, the formation of ASR secondary products reduces the concentration of free alkalis in the pore solution, thereby increasing the availability of sulfate ions and fostering favorable thermodynamic conditions for ettringite recrystallization [8,9]. Physically, cracking produced by other mechanisms (i.e., shrinkage, freeze-thaw, dynamic loading) increases pore-network connectivity and permeability, thereby enhancing moisture and ion transport and promoting the coupled deterioration process [10,11].

Over the past decades, several test methods have been developed to assess both the current condition (i.e., diagnosis) and the potential for further deterioration (i.e., prognosis) of ISR-affected concrete. These tools are essential for optimizing maintenance protocols and guiding rehabilitation strategies for critical infrastructure. Among them, the damage rating index (DRI) has emerged as a reliable microscopic technique for detecting and characterizing distress features associated with distinct ISR mechanisms. It has been successfully applied to ASR-affected concrete under unrestrained (e.g., free-expansion specimens) [12] and restrained conditions (e.g., 1D and 2D) [13], along with evaluating affected structures in the field [14].

Despite its proven suitability in assessing ASR-induced deterioration, the application of the DRI to DEF and DEF coupled with ASR remains limited [15,16]. Furthermore, there is currently a lack of systematic quantification of how distinct moisture gradients, such as those resulting from partial immersion, wetting–drying cycles, or microclimatic exposure, affect the microscopic deterioration of DEF and DEF+ASR-induced damage, including damage generation and propagation, crack pattern, and orientation. This work aims to use the DRI to assess the condition of non-reinforced concrete beams affected by DEF and DEF+ASR, which have experienced varying moisture gradients.

6.2 Background

6.2.1 DEF and DEF+ASR mechanisms

Delayed ettringite formation (DEF) is a specific internal sulfate attack mechanism that occurs when concrete is subjected to elevated temperatures during the early stages of hydration. Exposure to temperatures above approximately 65 °C, for a sufficiently long duration [17], leads to the

decomposition of primary ettringite. Upon cooling, ettringite reprecipitates in a delayed manner, inducing expansive pressures and progressive deterioration throughout the hardened cement paste [8,18]. The initiation and severity of DEF-induced damage are influenced by several interrelated factors, including peak temperature and duration of early-age heating, sulfate availability, alkali content, the presence of early-age microcracking, moisture ingress, wetting–drying cycles, restraint conditions, and the presence of other distressing mechanisms (e.g., ASR) [7,11,17,19–22].

Alkali–silica reaction (ASR), by contrast, is a chemically distinct but similarly damaging reaction, at the macroscopic scale, involving alkali hydroxides (Na^+, K^+, OH^-) from the pore solution and metastable silica present in certain aggregates (i.e., coarse and/or fine). This reaction produces secondary products (i.e., ASR gel), which can manifest in either amorphous phases or crystalline structures. These products induce internal stresses through swelling caused by water uptake and solidification pressures [1,23–25]. The cumulative effect of this process results in the formation of cracks within the aggregates, which eventually extend into the adjacent cement paste at moderate to high expansion levels [12,25].

These two deterioration mechanisms may act concomitantly in concrete, especially in field structures where environmental and material conditions favor their coexistence, while both physical and chemical synergies support their coupled development. The formation of ASR gel reduces the concentration of free alkalis in the pore solution, thereby enhancing sulfate ion availability and promoting the thermodynamic conditions for the reformation of ettringite. Additional contributions may arise from early-age temperature rise, which can accelerate early-stage ASR kinetics [26], and from alkali partitioning between the pore solution and cement hydrates, which depends on hydrate chemistry (including Al-bearing C–S–H) and therefore affects pore-solution alkalinity [27]. Pre-existing cracking induced by other mechanisms, such as shrinkage, freeze-thaw cycling, or dynamic loading, increases pore-network connectivity and permeability, facilitating moisture and ion transport and accelerating the coupled deterioration process. These chemical and physical interactions facilitate ettringite recrystallization, accelerating crack initiation and propagation throughout the bulk cement paste and interfacial transition zone (ITZ), thus compromising the mechanical integrity of the concrete. The coupling between DEF and ASR is further intensified when thermal curing exceeds 65-70 °C, a condition

potentially encountered in precast elements subjected to steam curing or in massive cast-in-place members with limited heat dissipation [7,8,22,28].

6.2.2 Effect of moisture gradients on DEF and DEF+ASR-induced development

The presence and movement of moisture are critical factors influencing the initiation and progression of both DEF and ASR in concrete. Moisture plays multiple roles in the evolution of DEF and ASR. It serves as a direct reactant, facilitates ion transport, and promotes chemical changes in the pore solution that support the development of these deterioration mechanisms [29–32].

In DEF-affected concrete, water is essential for the reformation of ettringite. The precipitation of ettringite requires up to 32 H_2O molecules per ettringite molecule, making moisture availability a prerequisite for expansion and crack development [21]. In addition to this direct role, moisture movement may promote alkali leaching (Na^+, K^+), lowering the pH of the pore solution, and modify sulfate availability by dissolving and redistributing sulfates and by favoring sulfate release/exchange from the C–S–H phase, leading to thermodynamic conditions that favor ettringite crystallization [20,33]. Water also enables the movement of critical ions, such as SO_4^{2-}, Ca^{2+}, and Al^{3+}, all of which are necessary for DEF development, particularly under saturated or re-immersed conditions [20,21].

Experimental studies have shown that both constant and variable moisture conditions, such as wetting-drying cycles, influence the extent of DEF-induced expansion [19,29,34–36]. In particular, the mass variation monitoring and water transport modeling conducted on partially immersed beams demonstrated that moisture gradients across the element height led to distinct DEF distressing effects. Swelling localized in the highly saturated zones, indicating a direct relationship between local moisture content and DEF distress intensity [7]. Although the identification of a precise moisture threshold for DEF-induced development remains a challenge, continuous and alternate saturation clearly play a decisive role in driving the deterioration process [31,32].

Compared to DEF, ASR generally requires lower moisture availability, with damage development commonly occurring within a relative humidity (RH) range of 70-85% [37–39]. However, pronounced expansion and deterioration have also been well documented at lower RH values when

elevated temperatures are present [40]. The presence of water enables the transport of alkali and hydroxyl ions, enhancing the dissolution of metastable silica within aggregate particles [41,42]. These processes initiate the formation and growth of ASR secondary products. Under unsaturated conditions, ASR can proceed at a reduced rate with limited swelling pressure, but re-exposure to moisture often results in a sharp increase in both reaction kinetics and expansion magnitude [30,38,43]. Several studies have demonstrated a correlation between ASR-induced expansion and RH [30,43,44], while others suggest that the degree of capillary saturation (DCS) may provide a more accurate threshold [45,46].

Under combined DEF–ASR conditions, ASR may initiate earlier than macroscopic DEF expansion when reactive aggregates and early-age thermal exposure promote ASR-related microcracking, which can subsequently provide sites for delayed ettringite deposition; however, ASR represents only one of several possible sources of the microcracking that favours DEF [11]. ASR-induced microcracking facilitates water ingress and promotes sulfate-ion transport, thereby accelerating ion diffusion and DEF kinetics. Concurrently, the alkali uptake associated with ASR-gel formation lowers their concentration in the pore solution, thereby enhancing sulfate ion mobility and fostering favorable conditions for delayed ettringite recrystallization. While ASR can evolve under moderately humid environments, DEF remains highly moisture-dependent, with its onset strongly influenced by post-cracking saturation [11]. This interaction highlights the critical role of water in supporting individual ISR mechanisms and in intensifying their combined deterioration effects [7].

6.2.3 DEF and DEF+ASR induced deterioration

Microscopic deterioration induced by DEF typically originates within the bulk cement paste and along the interfacial transition zone (ITZ) surrounding aggregate particles. It results from internal stresses generated by the crystallization of secondary ettringite in hardened cement paste under sufficient moisture. These stresses induce radial tensile forces in the cement paste and tangential compressive forces near the ITZ, leading to crack initiation both within the cement paste and along the ITZ [47]. Initial cracking often follows the ITZ contour, outlining aggregate particles, and gradually extends into the bulk cement paste as DEF-induced expansion progresses. Although uncommon, open cracks may occasionally appear within aggregate particles when the tensile strength of the particles is exceeded by the stresses generated near the ITZ. These cracks are not a

direct consequence of DEF progression but rather a secondary effect of localized stress concentrations and constraints acting on weaker aggregate particles. These mechanisms weaken the interface bond and promote the debonding of aggregate particles. The gaps formed at the ITZ are frequently observed to be filled with secondary ettringite [7,8,48].

Experimental investigations indicate that DEF-related deterioration typically begins with open cracks in the ITZ, at relatively early expansion levels (e.g., ≤ 0.12%) [15]. As expansion increases, these cracks widen and lengthen around the ITZ, and propagate into the bulk cement paste, and new cracks may develop, occasionally within aggregate particles. At higher expansion levels (e.g., > 0.30%), cracking becomes more widespread, increasing crack density and progressively weakening the continuity between paste and aggregate, thereby intensifying ITZ degradation. For expansions greater than 0.50%, coarse aggregate debonding and disaggregation may occur. While classical deterioration schemes [47] suggest that debonding can begin early in DEF development, more recent observations indicate that significant debonding tends to occur only at advanced stages of damage [15]. This behavior supports a more gradual deterioration process, consistent with the interpretations of the British Cement Association and Poole and Sims [49,50]. The formation of extensive crack networks significantly compromises the mechanical properties and stiffness of the concrete [15].

Although DEF-induced deterioration at the microscopic level still requires further investigation, a descriptive model (Figure 6.1) for ASR-induced damage has been proposed by Sanchez et al. [12]. This model unveils the development of ASR-induced cracking under unrestrained conditions. At early expansion levels (e.g., 0.05%), cracks initiate within aggregate particles, often as sharp (type A) or onion-skin (type B) cracks. As expansion progresses to moderate levels (e.g., 0.12%), these cracks increase in length and width and may begin to extend into the surrounding cement paste. At expansion levels around 0.20%, cracks importantly propagate into the paste, affecting mechanical properties and compromising material durability [51,52]. At higher expansion levels (e.g., 0.30%), cracks originating from different aggregates may connect, forming a continuous network throughout the cement paste and aggregate particles. This stage is associated with significant reductions in mechanical properties and long-term durability of the affected concrete [53,54]. The proposed ASR model has been observed to align with recent microstructural

investigations under both high magnification (e.g., 10,000×) [25] and under restrained conditions (e.g., 1D and 2D) [13].

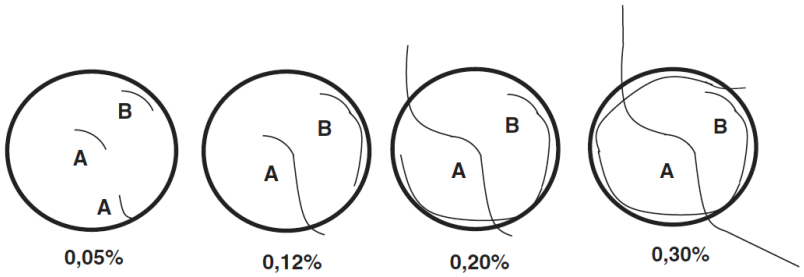


Figure 6.1 – Qualitative AAR damage model vs. levels of expansion between 0.05 and 0.30% [12].

Although significant progress has been made in describing ASR-induced deterioration, an experimentally grounded model that explains damage mechanisms and crack development for DEF and coupled DEF–ASR is still lacking. Moreover, the role of moisture gradients in DEF and in the combined evolution of DEF and ASR-induced cracking has yet to be systematically investigated.

6.2.4 Damage rating index (DRI)

The DRI is a semi-quantitative microscopic method widely used to assess microscopic deterioration in concrete affected by internal swelling reactions (ISR) [12,13,16,53]. Originally introduced by Grattan-Bellew and Danay [55,56] for evaluating damage caused by alkali–silica reaction (ASR), the method involves identifying and counting specific distress features within a 1 × 1 cm grid marked on polished concrete sections. Each observed feature is assigned a weighting factor that reflects its relative contribution to deterioration, as per the revised protocol established by Villeneuve and Fournier [57,58]. The weighted counts are then summed and normalized to a reference area of 100 cm^2 to enable comparison across samples with different analyzed surfaces (Figure 2) [12,55,56].

The main features identified in the DRI include closed cracks in aggregates (CCA), open cracks in aggregates with or without reaction products (OCA and OCA-RP, respectively), cracks in the cement paste with or without reaction products (CCP and CCP-RP, respectively), disaggregated aggregate particles (DAP), and coarse aggregate debonding (Debon). Among these, CCA is typically attributed to manufacturing flaws or natural weathering and receives the lowest weighting

factor (0.25). OCA and OCA-RP, commonly linked to ASR, are assigned a weighting factor of 2. Cracks in the cement paste (CCP and CCP-RP), often associated with DEF-related deterioration and advanced ASR damage, receive the highest weighting factor (3). DAP and Debon are weighted at 2 and 3, respectively (Figure 6.2).

a)

Features of deterioration		Weighing factor
Aggregate	Closed crack (CCA)	0.25
	Opened crack (OCA)	2
	Opened crack with reaction product (OCA_RP)	2
Cement paste	Crack in the cement paste (CCP)	3
	Crack in the cement with reaction product (CCP_RP)	3
Disaggregate/corroded aggregate particle (DAP)		2
Coarse aggregate debonded (Debon)		3

$$\boldsymbol{DRI_{number}} = \left[\frac{\sum_{i=1}^{i=n} 0.25(CCA)+2(OCA+OCA_{RP}+DAP)+3(CCP+CCP_{RP}+CAD)}{n_{\ num\ ber\ of\ analyzed\ \ 1\ cm\ by\ cm\ squares}}\right] \times 100\ cm^2$$

b)

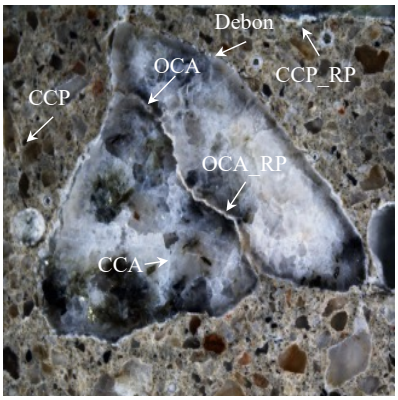


Figure 6.2 – Damage Rating Index, conventional method. a) Damage features classified in DRI analysis [57]. b) Micrograph section (1x1 cm) illustrates most of the damage features [59].

Sanchez et al. [12,60] later adopted the DRI conventional method to broaden its application to other ISR mechanisms, including DEF. The authors also proposed an extended version of the DRI, analyzing the unweighted absolute counts and relative percentages of each feature type. This version incorporates the calculation of crack density (CD), defined as the total number of open cracks per unit area, providing additional advanced analysis of the extent of microcracking. The extended DRI enables more detailed comparisons between samples and has been successfully used to explain reductions in mechanical performance through microstructural damage.

The DRI provides valuable information about the type, severity, and distribution of deterioration features across the aggregate particles, cement paste, and interfacial transition zones, supporting comprehensive assessments of ISR-affected concrete. Despite the growing understanding of individual ISR mechanisms, a clear knowledge gap remains in quantifying how moisture gradients influence the development of DEF- and DEF+ASR-induced damage.

6.3 Scope of the work

A detailed, systematic evaluation remains needed to quantify how moisture gradients influence the development of DEF- and DEF+ASR-induced deterioration, particularly with respect to damage initiation, propagation, and spatial distribution. To address this gap, three non-reinforced concrete beams exhibiting different deterioration mechanisms and damage severities were fabricated: moderate DEF, severe DEF, and severe DEF+ASR. All beams were subjected to a thermal curing regime representative of massive cast-in-place structures, followed by exposure to vertical moisture gradients. These gradients were generated by keeping the lower faces of the beams in contact with water (partial immersion) while the upper faces were exposed to drying conditions, creating a progressive variation in moisture content from bottom to top. The lateral faces were sealed to restrict water movement to the horizontal direction [7].

The damage rating index (DRI), in both conventional and extended versions, was applied to large polished cross-sections to quantify and characterize microstructural distress features. This program also provides an opportunity to benchmark the DRI methodology under non-uniform exposure and combined internal swelling reactions. Initially, the microscopic results were averaged across the upper and lower heights of each beam to compare the extent of deterioration among different mechanisms and exposure conditions. In a second step, the beams were stratified into five depths (i.e., 10 cm each) to evaluate deterioration development as a function of depth. This analysis was interpreted in conjunction with the moisture distribution data and the semi-empirical modeling framework proposed by Martin [7], enabling a detailed assessment of the relationship between water ingress and the spatial evolution of damage due to DEF- and DEF+ASR. Finally, a DRI-based approach was proposed to estimate the relative contribution of each deterioration mechanism to the overall damage observed in DEF+ASR-affected concrete.

6.4 Materials and methods

6.4.1 Description of the specimens

Three non-reinforced beams have been manufactured at the former *Laboratoire central des ponts et chaussées* (LCPC), currently the *Laboratoire Expérimentation et Modélisation pour le Génie Civil et Urbain* (EMGCU) from the *Département Matériaux et Structures* at *Université Gustave*

Eiffel in Paris, France, during the research program developed by Martin [7]. The beams, with dimensions of 0.25 x 0.50 x 3.00 m³ and simply supported at mid-height with a span of 2.8 m (Figure 6.3a), were cast with concretes designed to develop moderate DEF, severe DEF, and combined DEF+ASR. These beams were produced with a water-to-cement ratio of 0.46 and the following 28-day properties (compressive strength, modulus of elasticity): moderate DEF beam, 39.3 MPa and 32.8 GPa; severe DEF beam, 38.7 MPa and 30.8 GPa; severe DEF+ASR beam, 41.4 MPa and 31.5 GPa.

To replicate massive-element curing and activate DEF, the beams were transferred 2 hours after casting to a temperature-controlled water bath with a programmed thermal cycle comprising an initial heating stage aligned with the adiabatic temperature rise of the mix, a constant plateau at 81 °C for 72 hours, and a controlled cooling at about 1 °C h^{-1}, for a total duration of approximately 6 days [7,61]. Afterwards, the beams were subjected to vertical moisture gradients under two phases: (a) partial immersion of the bottom 7 cm for 14 months, with the top surface exposed to drying (≈30% RH), and (b) additional water supply at the top surface for another 14 months to homogenize vertical moisture distribution. During this period, the beams were stored at 38 ± 1 °C and 30% RH, with lateral faces sealed to prevent transverse water exchange (Figure 6.3b). The moderate DEF beam experienced both phases, followed by a 4-point bending test to evaluate its residual load-bearing capacity, whereas the severe DEF and DEF+ASR beams failed prematurely during phase (a) due to self-weight and advanced deterioration (i.e., 330 and 160 days, respectively) [7]. The premature failure is further discussed in Section 6. After the program developed by Martin [7], the members were stored under laboratory conditions (22 ± 4 °C; 50–70% RH) until coring and specimen preparation for the present microscopic program, without imposed wetting, thereby limiting further evolution compared with the prior temperature conditions and water-supplied exposure.

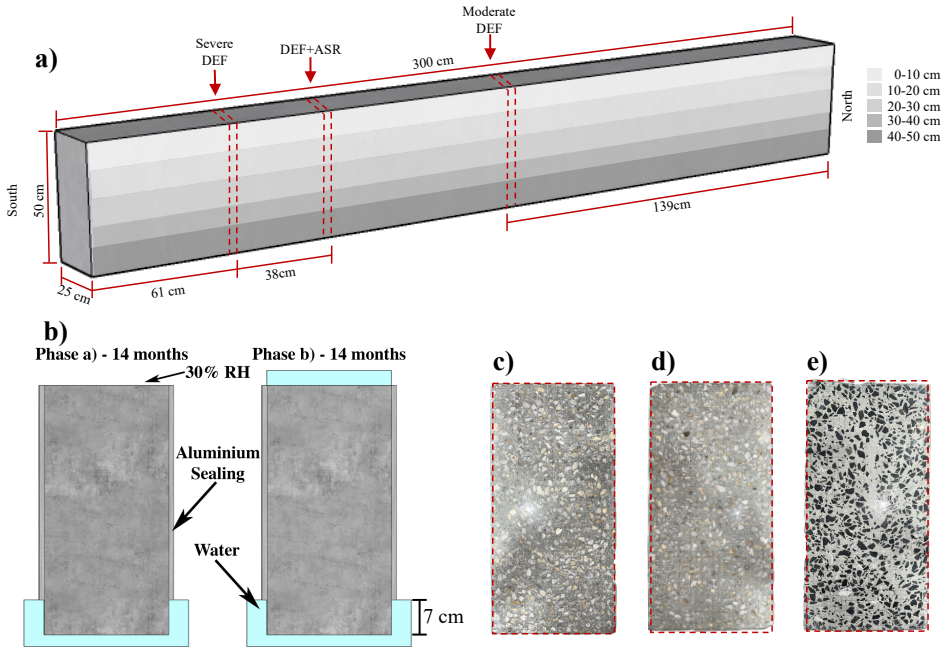


Figure 6.3 – Schematic illustration of a) the dimensions of the beams, and the locations where the slices were extracted for DRI analyses. b) the water exposure setup. Slices of c) moderate DEF, d) severe DEF, and e) severe DEF+ASR.

The distinct DEF severities were obtained using Portland cements with different chemical compositions and extra alkali content added to the concrete system. The cement for moderate DEF contained 2.35% C_3A, 2.61% SO_3, and 0.44% Na_2O_{eq}, while the cement for severe DEF contained 4.97% C_3A, 3.46% SO_3, and 0.83% Na_2O_{eq}. Alkali content of severe DEF and severe DEF+ASR beams was raised to 1.1% Na_2O_{eq} by adding 1.745 kg KOH per m^3 for two main reasons: (i) to enhance primary ettringite decomposition, and (ii) to enhance ASR development. The DEF beams (moderate and severe DEF) were produced with a non-reactive siliceous limestone aggregate, while the DEF+ASR beam used a highly reactive siliceous limestone aggregate with an expansion potential of 0.16% (i.e., soaked in water), classified according to ASTM C1778 – Table 1 [62].

To further investigate and quantitatively distinguish the differences in DEF-induced swelling potential, a thermodynamic simulation was performed using the Gibbs Energy Minimization Software (GEMS). This model computes stable hydrate phase assemblages based on the system's temperature, pressure, and bulk composition. The input data, including oxide composition and clinker phases of both cements, were obtained from Martin [7]. Figure 6.4 presents the evolution of hydrate masses in a closed system over 1000 days at 38°C (i.e., storage temperature of the

beams), assuming 100g of cement and a water-to-cement ratio of 0.46. The simulation indicated that most clinker phases were consumed within the first day of hydration. The severe DEF cement produced 18.43 g of ettringite, compared with 14.06 g for the moderate DEF cement, consistent with its higher SO_3 content. The elevated exposure temperature and the low C_3A content in both cements further destabilized the monosulfate and monocarbonate phases, promoting siliceous hydrogarnet formation [63,64]. The simulation demonstrates that sulfate availability was the main factor controlling the higher swelling potential of the severe DEF beams.

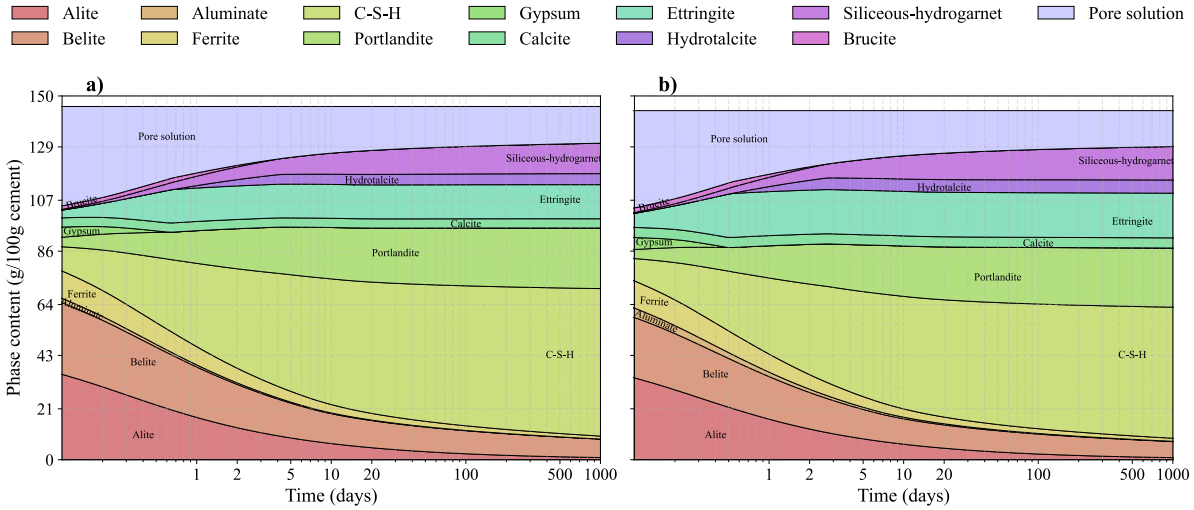


Figure 6.4 – Calculated mass of hydrates in a) moderate DEF Cement and b) severe DEF Cement as a function of time.

The beams were saw-cut perpendicular to their longitudinal axis, and one slice (50 × 25 × 5 cm) from each was extracted for microscopic analysis (Figure 6.3c-e). Locations with major cracks were avoided during the sampling process. Figure 6.3a demonstrates the locations of saw-cutting in all three beams (i.e., moderate DEF, severe DEF, and severe DEF+ASR).

6.4.2 Experimental procedures

The conventional and extended DRI versions were conducted on slices of the cross-section of DEF (i.e., moderate and severe) and DEF+ASR-affected beams that underwent different moisture gradients. After cutting (Figure 6.3), the slices were polished using a handheld polishing device with diamond-impregnated pads applied in a sequential grit order: no. 50 (coarse), 120, 200, 400, 800, 1500, and 3000 (very fine) [12]. DRI analysis was performed on polished specimens with a

surface area of 1,250 cm². The distress features were then appraised as per Villeneuve and Fournier (i.e., conventional method – Figure 6.2) [57,58] and Sanchez et al. (i.e., extended version) [12,60]. The DRI has been analyzed in two different yet complementary ways. First, the microscopic results were averaged for each beam (i.e., moderate DEF, severe DEF, and severe DEF+ASR), and separated into two halves of the beams' height (i.e., upper and lower height), to understand the impact of the mechanisms and the two moisture conditions (i.e., "phase a", and "phase b") of the beams on the "overall deterioration" of distressed concrete, considering that moderate DEF-affected beam experienced both water exposure phases while the beams affected by severe DEF and DEF+ASR experienced only "phase a". Second, the DRI was evaluated dividing the beams into five heights (i.e., 0-10, 10-20, 20-30, 30-40, 40-50 cm), to appraise and quantify the impact of water imbibition rate and magnitude on the distress features distribution, crack width and length, and damage degree (see discussion in section 6). Finally, the contributions of DEF and ASR to the deterioration are assessed based on the types of distress features generated by each mechanism and their interplay.

6.5 Results

6.5.1 Quantitative assessment of "overall damage" through DRI

The overall DRI numbers obtained for the full cross-section (1250 cm²) highlight clear differences in deterioration severity among the beams affected by moderate DEF, severe DEF, and DEF+ASR (Figure 6.5). The moderate DEF beam presented the lowest value, with an overall DRI of 517. The severe DEF beam exhibited a markedly higher value of 1209, while the DEF+ASR beam reached the highest overall DRI, at 1643.

The damage was also assessed separately for the upper and lower sections (625 cm² each), as shown in Figure 6.5. It is worth noting that 200 cm² is recommended as a representative area for DRI analysis [12,56,65]. For the beam affected by moderate DEF, the upper section presented a higher value of 625, while the lower section yielded a slightly lower value of 473. For the beam affected by severe DEF, the upper and lower sections presented DRI numbers of 733 and 1761, respectively. For the beam affected by DEF+ASR, the upper and lower sections yielded 1381 and 2050, respectively.

These results demonstrate that both the deterioration mechanisms and the moisture exposure conditions strongly influence the total overall damage (i.e., DRI number, which accounts for both the number and importance of the crack types). The beams subjected to more severe mechanisms (i.e., severe DEF and DEF+ASR) exhibited consistently higher DRI values throughout all sections analyzed, with totals approximately two to three times greater than those of the moderate DEF beam. Furthermore, a clear vertical gradient was also identified. For beams exposed to water from the bottom face only (i.e., severe DEF and DEF+ASR), the lower sections yielded substantially higher values than the corresponding upper sections, more than twice in the severe DEF (1761 vs. 733) and about 50% higher in the DEF+ASR (2050 vs. 1381). This distribution directly reflects the influence of moisture on the severity of damage. Conversely, the moderate DEF beam, which experienced both bottom and top water exposure cycles, presented a reversed distribution, with the upper section exceeding the lower DRI number (625 vs. 473). This inversion highlights the impact of the late water supply at the top surface, which increased deterioration in the upper half of the beam and reduced the contrast between sections.

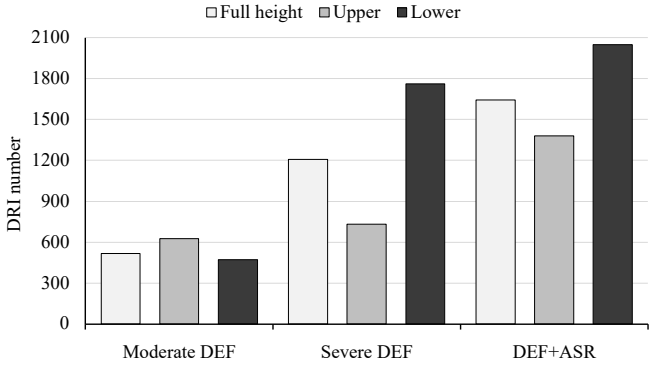


Figure 6.5 – DRI number of the full height, upper height, and lower height.

6.5.2 Crack density and microscopic distress features

The microscopic distress features and crack density (CD) of the DEF- and DEF+ASR-affected beams were assessed using the extended version of the DRI proposed by Sanchez et al. [12,60]. While the original classification was developed for ASR-affected concrete, an additional group was introduced in this study to better capture the deterioration patterns observed in DEF-affected concrete. This group, referred to as Group IV (Debon), accounts for the frequent presence of aggregate particles debonding in concrete damaged by DEF. The results presented in this section

refer to the overall microscopic features and CD values calculated over the full cross-section (1,250 cm²) and the layered upper and lower halves of each beam (625 cm² each).

Figure 6.6 presents the crack density (CD – crack counts/cm²) obtained for the full height and the layered upper and lower sections of the DEF- and DEF+ASR-affected beams. Similarly to the unweighted feature counts, higher CD values represent more advanced deterioration.

For the full cross-section, the moderate DEF beam exhibited a CD of 1.83 counts/cm². The severe DEF beam showed a higher value of 4.07 counts/cm², while the DEF+ASR beam reached the highest overall CD, at 6.02 counts/cm².

When separated into upper and lower sections, the moderate DEF beam yielded values of 2.05 and 1.61 counts/cm², respectively. For the severe DEF beam, the upper section exhibited 2.21 counts/cm², while the lower section presented a much higher value of 5.93 counts/cm². The DEF+ASR beam presented 4.67 counts/cm² in the upper section and 7.36 counts/cm² in the lower section.

These results reveal a clear pattern of deterioration, particularly in the highly deteriorated beams, with consistently higher crack densities observed in the lower sections of both severe DEF- and DEF-ASR-affected beams. Similarly to the overall damage assessment, the achieved crack density is driven by the severity of the distressing mechanisms (i.e., DEF+ASR > severe DEF > moderate DEF) when analyzing the full height, while shaped by water exposure when analyzed in two layers (i.e., $DEF+ASR_{lower}$ > severe DEF_{lower} > $DEF+ASR_{upper}$ > severe DEF_{upper} > moderate DEF_{upper} > moderate DEF_{lower})

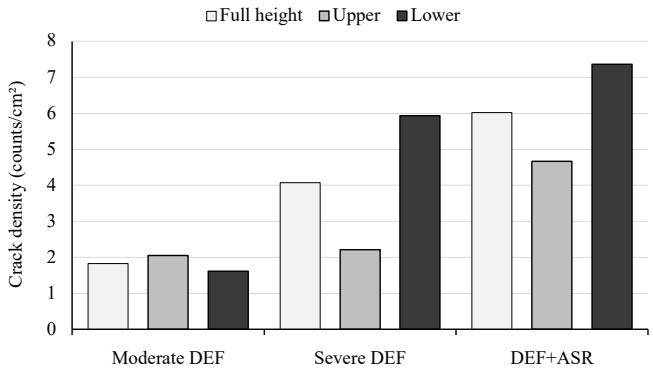


Figure 6.6 – Crack density of the full height, upper height, and lower height.

Figure 6.7a presents the unweighted feature counts, normalized to 100 cm². This representation facilitates direct comparison of different deterioration mechanisms and water-exposure conditions. In all assessed beams, the most frequently observed features corresponded to Group III, which includes cracks in the cement paste without reaction products (CCP) and with reaction products (CCP_RP), and to Group IV (Debon). In addition, the beam affected by DEF combined with ASR exhibited a notable number of Group II features, specifically open cracks in aggregate particles without (OCA) and with reaction products (OCA_RP), as typically observed in concrete affected by ASR [12]. The total number of features observed across the full cross-section was 183 for the beam affected by moderate DEF, 407 for the beam with severe DEF, and 602 for the beam with DEF+ASR. When separated into sections, the beam affected by moderate DEF showed 205 features at the upper height and 161 at the lower height. The beam distressed by severe DEF showed 221 features in the upper section and 593 in the lower section. The DEF+ASR-affected beam presented 467 counts in the upper part and 736 counts in the lower part. When appraising the full height of each cross-section, these values indicate that the development of microscopic distress is driven by the mechanism severity (i.e., DEF+ASR > severe DEF > moderate DEF), whereas influenced by the specific moisture exposure experienced by each beam when analyzed in a layered fashion (i.e., DEF+ASR_{lower} > severe DEF_{lower} > severe DEF+ASR_{upper} > DEF_{upper} > moderate DEF_{upper} > moderate DEF_{lower}).

Figure 6.7-b shows the relative proportions of distress features in each section (i.e., full height, upper section, lower section). For beams affected by DEF, the distribution of damage features was relatively similar between the upper and lower sections. On the other hand, the beam affected by DEF+ASR displayed a higher proportion of Group II features, highlighting the additional contribution of ASR to the overall deterioration. In terms of distribution throughout the entire cross-section, the proportion of Group III features (cracks in the cement paste) was 70%, while Group II features (open cracks in aggregates) attained 25%, and Group IV (Debon) accounted for 4% of the observed damage. In the lower sections, the proportion of Group III was 76%, Group II was 19%, and Group IV was 4%. In the upper sections, Group III features accounted for 61%, Group II accounted for 34%, and Group IV reached 4%.

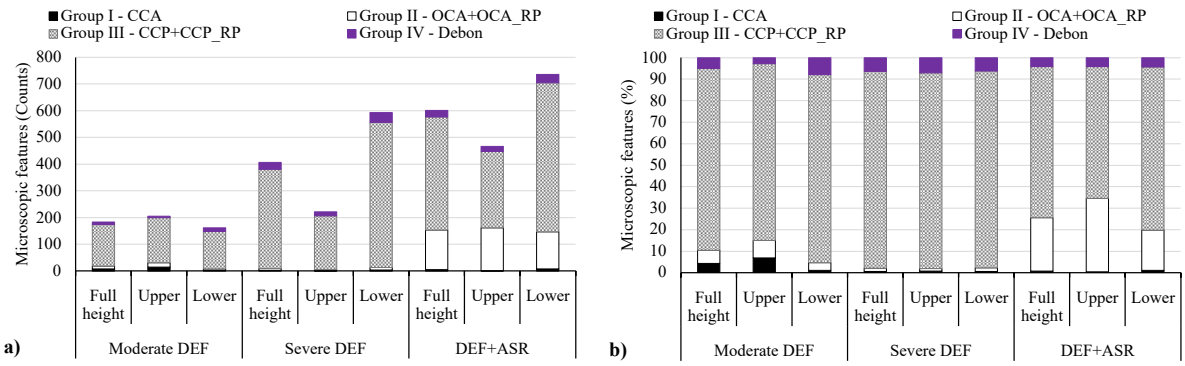


Figure 6.7 – Microscopic features of deterioration: a) Counts normalized to 100 cm². b) Percentage without applying the weighting factors.

6.5.3 Crack widths/lengths versus full height, upper height, and lower height

The maximum crack width (W_{max}) and length (L_{max}) may serve as indicators to assess the progression of DEF- and DEF+ASR-induced deterioration in concrete (Figure 6.8). While the original procedure proposed by Sanchez et al. [12,60] suggests focusing on the maximum crack width in aggregate particles when assessing concrete affected by ASR, both parameters were measured in this study, considering cracks occurring in both the cement paste and in the aggregate particles, thereby providing a more comprehensive assessment of damage progression due to both DEF and DEF+ASR. Crack widths were initially screened using a transparent comparator card under a 15× magnification loupe. However, all crack widths and lengths were quantified from calibrated digital images processed in ImageJ (National Institutes of Health - NIH) for the three beams. The measurements with the comparator card were not retained because many apertures were smaller than its practical reading limit (0.05 mm). Each image included a steel rule within the field of view, aligned with the specimen surface to maintain a common focal plane. The rule's reference dimension was verified using a digital caliper (0.01 mm resolution). Image calibration was then performed by matching a known distance on the rule (typically 1 mm) to its pixel count, yielding a scale of 100 pixels per millimetre, corresponding to 0.01 mm per pixel. Crack width was taken as the maximum visible opening, and crack length was obtained by tracing the crack trajectory along the surface. Measurements were performed twice and averaged. With manual point placement assumed accurate to one pixel, the effective resolution was 0.01 mm, and values are reported in millimetres to two decimal places. In this section, the overall crack length and width

results presented refer to the full cross-section (1,250 cm²) and to the upper and lower halves of each beam (625 cm² each).

For the full cross-section, the moderate DEF beam exhibited the smallest crack dimensions, with W_{max} of 0.02 mm and L_{max} of 5.90 mm. The severe DEF beam presented larger values, with W_{max} of 0.31 mm and L_{max} of 31.40 mm. The DEF+ASR beam reached the highest values overall, with W_{max} of 0.35 mm and L_{max} of 31.10 mm. When separated into layers, the moderate DEF beam presented W_{max} of 0.015 mm and L_{max} of 5.90 mm in the upper section, and W_{max} of 0.012 mm and L_{max} of 6.70 mm in the lower section. For the severe DEF beam, the upper section exhibited W_{max} of 0.31 mm and L_{max} of 18.90 mm, while the lower section showed W_{max} of 0.23 mm and L_{max} of 31.40 mm. The DEF+ASR beam presented W_{max} of 0.29 mm and L_{max} of 17.64 mm in the upper section, and W_{max} of 0.35 mm and L_{max} of 31.10 mm in the lower section.

The results demonstrate that larger crack widths and lengths are associated with more aggressive deterioration mechanisms and moisture exposure conditions. Notably, both the severe DEF and DEF+ASR beams exhibited relatively longer and wider cracks, particularly in the lower sections. As observed for the DRI number, distress features and crack density, the attained maximum crack width and length are driven by the severity of the distressing mechanisms (i.e., DEF+ASR > severe DEF > moderate DEF) when analyzing the full height, while shaped by water exposure when analyzed in layered fashion: (i) W_{max} (i.e., DEF+ASR_{lower} > severe DEF_{upper} > severe DEF+ASR_{upper} > DEF_{lower} > moderate DEF_{upper} > moderate DEF_{lower}) and (ii) L_{max} (i.e., DEF_{lower} > severe DEF+ASR_{lower} > severe DEF_{upper} > DEF+ASR_{lower} > moderate DEF_{lower} > moderate DEF_{upper}).

This trend further emphasizes the role of water exposure in driving the development and propagation of microscopic deterioration. The vertical distribution of crack dimensions between the lower and upper sections aligns with the deterioration profiles previously observed through the DRI number, distress feature counts, and crack density.

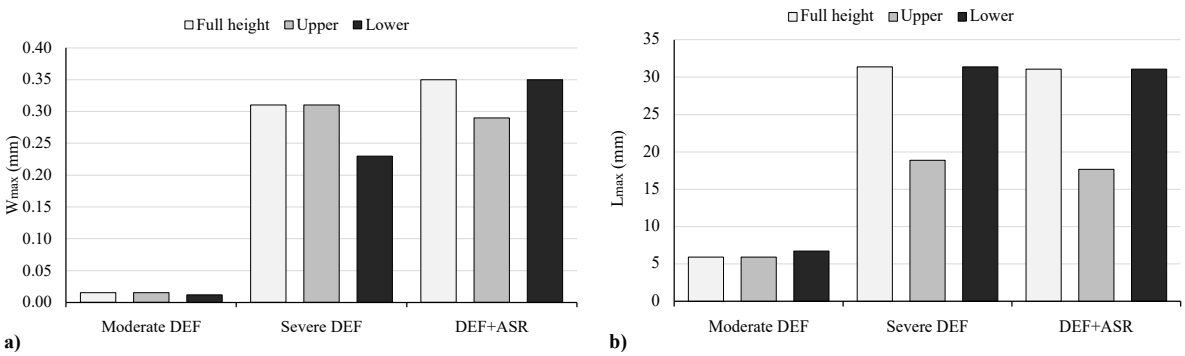


Figure 6.8 – Maximum a) width and b) length of the full height, upper height, and lower height.

6.6 Discussion

6.6.1 Understanding the water-transfer behavior in moderate DEF, severe DEF, and DEF+ASR-affected concrete

The microscopic assessment conducted in this study yielded key observations that contribute to a better understanding of DEF- and DEF+ASR-induced deterioration in concrete under distinct moisture gradients. The microscopic features of deterioration (Figure 6.5), cracking density (Figure 6.6), and maximum crack width and length (Figure 6.7) clearly demonstrated the combined effect of water gradients and swelling potential of the distressing mechanisms on the attained extent and distribution of DEF- and DEF+ASR-induced distress in concrete.

To further investigate the role of moisture in these deterioration patterns, the evolution of water transfer in beams affected by moderate and severe DEF- and DEF+ASR was analyzed within a vertical one-dimensional domain of total height $H = 0.50m$, with depth $z \in [0, H]$ measured from the top surface downward (Figure 6.3b). The global mass of the beams was monitored by Martin [7] using a setup that combined beam-scale weighing and automated γ-densimetry for local mass variation measurements. This technique was developed by Multon and Toutlemonde [30,68,69] for AAR-affected beams and was later extended by Martin [7] to DEF and DEF+ASR. In parallel, companion cylinders sampled from blocks were characterized to determine material-specific parameters such as moisture-saturation thresholds and free-expansion kinetics, which were required to interpret the beam-scale behavior.

Direct moisture measurements could not be performed in this study. Moisture transfer in partially immersed concrete members has been described using simplified front-based interpretations and diffusion-based formulations for drying and capillary rise, with more recent extensions in which transport parameters evolve with the local water state and damage development [44,68,70]. In contrast to a fully predictive moisture-transport simulation requiring dedicated parameter identification, the present work reconstructs the internal moisture state from Martin's datasets [7] and uses the resulting moisture fronts as semi-quantitative descriptors of water availability. This choice supports the objective of relating vertical moisture gradients to DRI-based microscopic indicators at beam scale, rather than predicting absolute moisture fields through coupled hygro-mechanical analysis. Accordingly, the moisture reconstruction is interpreted through three transfer fronts that govern water availability and swelling kinetics in the beams: during "phase a" (i) top-drying front, (ii) bottom imbibition front; during "phase b" (iii) top-rewetting front instead of (i). During "phase a", drying from the top occurred simultaneously with water uptake from the bottom (Equation 6.1). After a time t_b denoted as "phase b", bottom imbibition continued while the previously established top-drying front was overtaken by a top-rewetting front once water was supplied to the upper surface (Equation 6.2).

The global mass evolution of the beams, $\Delta M_{Global}(t)$, was expressed as the sum of contributions from the fronts active in each exposure phase, where t_b denotes the initiation of "phase b". Mass gains were considered positive, and drying was considered negative. Imbibition from the bottom face was treated as cumulative from $t = 0$, and evolved continuously through both "phase a" and "phase b".

$$\Delta M_{Global}(t) = \Delta M_{imbibition}(t) + \Delta M_{dry}(t), 0 \leq t \leq t_b \tag{6.1}$$

$$\Delta M_{Global}(t) = \Delta M_{imbibition}(t) + \Delta M_{drying}(t_b) + \Delta M_{rewetting}(t), t > t_b \tag{6.2}$$

These expressions provide a consistent global mass-balance framework aligned with Martin's observations and measurements. The following subsections detail the assumptions and formulations used for each transfer front.

(i) Drying front

The drying front $h_{dry}(t)$ is the depth at which drying reduces the local saturation to the expansion-onset threshold (Equation 6.3). The local relative mass-loss profile over time during "phase a" was

reconstructed from Martin's γ-densimetry modelling (Equation 6.4 [7]), which calibrates the asymptotic mass-loss magnitude $A(z)$ and the characteristic time determined experimentally at 10, 50, 70, and 90 mm below the top surface (Table 6.1).

$$h_{dry}(t) = z_0 \; where \; \delta m/m_{\gamma}\,(z_0, t) = \delta m/m_{iso} \tag{6.3}$$

$$\left(\frac{\delta\,\mathrm{m}}{\mathrm{m}}\right)_{\gamma}(\mathrm{z},\mathrm{t}) = A(z)\cdot\left(1 - e^{-\frac{t}{\tau(z)}}\right) \tag{6.4}$$

The parameters of the drying profile determined for the moderate DEF-affected beam (Table 6.1) were used for all beams evaluated in this work, considering the absence of measurements from severe DEF and severe DEF+ASR due to the technical issues. The comparable mix designs and transport-related properties among the three beams justify the use of a common drying profile.

Table 6.1 – Parameter calibration for modeling the drying profiles [7]

Depth (mm)	**10**	**50**	**70**	**90**
A (%)	2.60	1.60	1.84	1.06
τ (days)	10	80	1000	1000

The reference state corresponds to the initial degree of saturation S_0 measured at the end of the thermal treatment. The relation between relative mass loss and change in the local saturation ΔS follows the material balance in Equation 6.5, where p is the open porosity, V is the volume of concrete investigated, $S(t)$ is the degree of saturation at time t, $\rho_{concrete}$ is the concrete bulk density at the beginning of the test (i.e., with a degree of saturation S_0), and $\beta = \frac{\rho_{\mathrm{water}\,\cdot\,p}}{\rho_{\mathrm{concrete}}}$ (Table 6.2).

$$\frac{\delta m}{m_0} = \frac{\rho_{\mathrm{water}}\, V\cdot p\cdot(\mathrm{S(t)} - S_0)}{\rho_{\mathrm{concrete}}\cdot V} = \underbrace{\frac{\rho_{\mathrm{water}}\cdot p}{\rho_{\mathrm{concrete}}}}_{\beta}\cdot \Delta\mathrm{S} \tag{6.5}$$

Drying reaches the saturation threshold condition when the local saturation decreases from S_0 to S_{onset}. The corresponding iso-loss magnitude of relative mass loss is given by Equation (6).

$$\left(\frac{\delta m}{m_0}\right)_{iso} = \beta\cdot(S_{onset} - S_0) \tag{6.6}$$

The expansion-onset saturation threshold $S_{onset} = 0.90$ was adopted from recent EMGCU projects [19,71], while S_0 the material-specific maximum degree of saturation (Table 6.2) was

determined by Martin [7]. To respect the γ-densimetry repeatability (±0.18 %) investigated in [7], an instrument floor of 0.20 % was applied when $\delta m/m_{iso}\,(z,t) < -0.20\%$.

At each time t, the front depth $h_{dry}(t)$ was located as the first depth where $\delta m/m_{\gamma}\,(z,t) = \delta m/m_{iso}$. Linear interpolation between measurement depths provides a continuous front evolution. This procedure is consistent with Martin's γ-densimetry framework and gives a physically grounded representation of the advancing dry cap that governs moisture availability during "phase a". Table 6.2 presents a summary of the parameters used to determine the drying front.

(ii) Imbibition front

Martin [7] formulated the advance of the imbibition front in concrete beams subjected to partial immersion by combining experimental weighing with local γ-densimetry measurements. The approach begins with a square-root-in-time description of the front rise above the immersed base (equation 6.7).

$$\zeta = D_{imb}\sqrt{t} \tag{6.7}$$

Where D_{imb} is an absorption coefficient [m/$\sqrt{day}$]. Considering that the bottom-7cm immersed in water are immediately saturated at the beginning of "phase a", the absolute position of the imbibition front from the bottom surface is then expressed as $h_{imb}(t) = 0.07 + \zeta(\mathrm{t})$, with 0.07 m representing the immersed zone.

To transfer the material-scale kinetics of mass uptake (i.e., cylinders study from [7]) to the structural scale, Martin introduced a modified relative mass variation of the constitutive concrete of the beams (Equation 6.8).

$$\left(\frac{\delta m}{m}\right)_{modified\_imb}(t) = \left(\frac{\delta m}{m}\right)_{cylinders}(\infty) \cdot \frac{1 - exp\left(-\frac{t}{\tau_{c_m}}\right)}{1 + \exp\left(-\frac{t-\tau_{l_m}}{\tau_{c_m}}\right)} \tag{6.8}$$

Where τ_{c_m} is a characteristic time, τ_{l_m} is a latency time, $\left(\frac{\delta m}{m}\right)_{cylinders}(\infty)$ is the asymptotic mass variation (i.e., obtained in the material characterization in [7]) and adopted as the representative ultimate mass uptake of the beam concrete. The parameters τ_{c_m} and τ_{l_m} were calibrated in [7] by

fitting the model to the measured beam-scale mass-change histories, which reflect water exchange with the environment. Thus, this sigmoidal function reproduces the delayed and progressive nature of capillary water uptake observed experimentally. The global mass variation of the beam is then written as the sum of the imbibition and drying contributions (equation 6.9) derived from equation (6.1).

$$\Delta M_{global}(t) = \left(0.07 + D_{imb}\sqrt{t}\right) A_{imm} \cdot \rho_{\text{concrete}} \cdot \left(\frac{\delta m}{m}\right)_{modified\_imb}(t) + A_{imm} \cdot \rho_{\text{concrete}} \cdot \int_{\text{drying zone}} \left(\frac{\delta \text{m}}{\text{m}}\right)_{\gamma}(\text{z},\text{t}) \cdot dz \qquad (6.9)$$

Where A_{imm} is the longitudinal horizontal section of the beam, ρ_{concrete} is the concrete bulk density, and $\left(\frac{\delta m}{m}\right)_{\gamma}(z,t)$ is the local relative mass variation obtained by the γ-densimetry in the drying zone of the beams represented by equation (6.4).

This modeling approach (Equation 6.8 [7]) integrates mass variation measurements with a time-dependent framework that accounts for both drying (i.e., RH 30% in the upper part), capillary imbibition from partial immersion (i.e., 7 cm in the bottom), and swelling potential of the distressing mechanism (i.e., moderate and severe DEF, and severe DEF+ASR). The absorption coefficient D_{imb} was identified by minimizing the difference between the modeled global mass variation and the measured global weighing data. This procedure provides a consistent description of how the capillary front progresses and how the corresponding mass gain contributes to the overall moisture balance of the structure.

(iii) Rewetting front

In the present work, to complement the calculation from [7], the estimation of the rewetting front was formulated to account for the rapid mass gain observed on the first day of "phase b", associated with moisture uptake of the dried zone, followed by diffusion-controlled propagation toward the interior, while the imbibition front from the bottom water source continues progressively, which requires the $\left(\frac{\delta m}{m}\right)_{modified\_top}$ (Equation 6.10), where the kinetics term was simplified compared to $\left(\frac{\delta m}{m}\right)_{modified\_imb}$, considering the shape "phase b" mass variation. The continuous imbibition term (Equation 6.11) considered the contribution of the drying front at the initiation of "phase b" (t_b). The overall mass variation is then represented by equation 6.11.

$$\left(\frac{\delta m}{m}\right)_{modified\_top}(t_{>t_b}) = \left(\frac{\delta m}{m}\right)_{cylinders}(\infty)\cdot\left[1 - e^{-\frac{\langle t_{>t_b} - t_b\rangle}{\tau_{top}}}\right] \tag{6.10}$$

$$\Delta M(t) = \underbrace{\left(0.07 + D_{imb}\cdot\sqrt{t}\right)\cdot A_{imm}\cdot\rho_{\text{concrete}}\cdot\left(\frac{\delta m}{m}\right)_{modified\_imb}(t)}_{Continuous\ imbibition} + \underbrace{A_{imm}\cdot\rho_{\text{concrete}}\cdot\int_{drying\ zone}\left(\frac{\delta\,\text{m}}{\text{m}}\right)_{\gamma}(z,t_b).dz}_{Drying\ contribution\ (constant)\ from\ "phase\ a"}$$
$$+\underbrace{H_{inst} * A_{imm}\cdot\rho_{\text{concrete}}}_{Instantaneous\ rewetting} + \underbrace{\left(H_{inst} + D_{rwt}\cdot\sqrt{t_{>t_b} - t_b}\right)\cdot A_{imm}\cdot\rho_{\text{concrete}}\cdot\left(\frac{\delta m}{m}\right)_{modified\_top}(t)}_{diffusion-controlled\ rewetting} \tag{6.11}$$

Where t_b is the start of "phase b" (427 days), H_{inst} represents the thickness that gets back to initial saturation

S_0 when water is added to the top, D_{imb} is the diffusion imbibition coefficient determined in "phase a", $\left(\frac{\delta m}{m}\right)_{modified\_top}$ is the asymptotic mass variation obtained in the material characterization in [7], and τ_{top} top time constant. The H_{inst}, D_{rwt}, and τ_{top} were determined by minimizing the difference between the modeled global mass variation and the measured weighing data. This formulation provides a consistent description of how the capillary front progresses and how the corresponding mass gain contributes to the overall moisture balance of the structure. The absolute position of the rewetting front from the top surface is then expressed as $h_{rwt} = H_{inst} + D_{rwt}\cdot\sqrt{t_{>t_b} - t_b}$. Figure 6.11 illustrates the global mass variation, and Table 6.2 presents the parameters used to estimate the water-transfer of moderate DEF, severe DEF, and DEF+ASR-affected concrete beams.

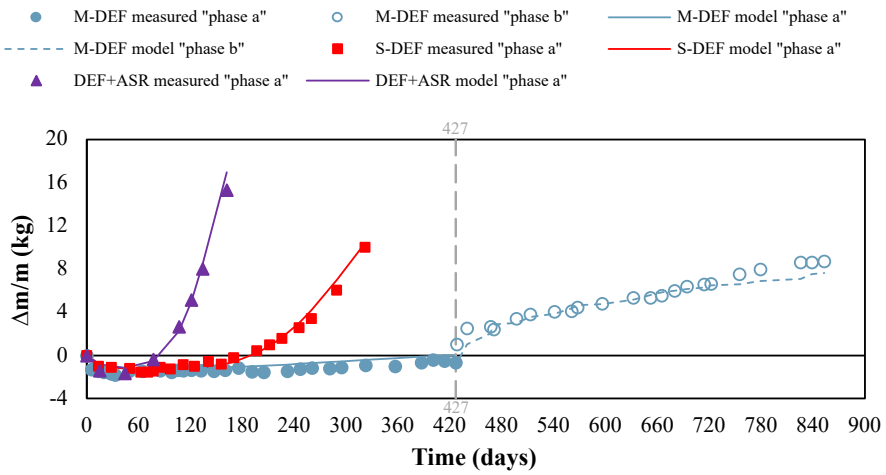


Figure 6.9 – Global mass variation (Δm/m). a) Moderate DEF, b) Severe DEF. c) DEF+ASR.

Table 6.2 – Parameters used to estimate the water-transfer behavior of moderate DEF, severe DEF, and DEF+ASR-affected concrete beams.

		Moderate DEF	Severe DEF	Severe DEF+ASR
Drying	$\rho_{concrete}$(kg/m³) [7]	2328	2320	2363
	p (%)[7]	14.6	14.6	14.6
	S_0 [7]	0.92	0.93	0.95
	β	0.06271	0.06293	0.06179
	ΔS	0.020	0.030	0.050
	Iso-loss (raw) %	0.125	0.189	0.309
	Iso-loss used %	0.200	0.200	0.309
Imbibition	$(\delta m/m)\ \infty$	0.0085	0.0241	0.0218
	$\tau_{c\,m}\ (t)$ [7]	150	50	22
	$\tau_{l\,m}\ (t)$ [7]	170	290	140
	$D_{imb}\ (m \cdot \sqrt{t})$ [7]	4.95×10^{-3}	2.12×10^{-2}	4.66×10^{-2}
	RMSE (kg)	0.6322	0.1588	0.6778
Rewetting	H_{inst} (m)	9.65×10^{-4}	-	-
	$D_{rwt}(m \cdot \sqrt{t})$	1.83×10^{-2}	-	-
	τ_{top}	0.2	-	-
	RMSE (kg)	0.5278	-	-

RMSE - Root Mean Square Error

Figure 6.10 presents the estimated progression of the three moisture fronts, (i) drying, (ii) imbibition, and (iii) rewetting, calculated for the beam affected by moderate DEF, and the drying and imbibition fronts during "phase a" for the beams affected by severe DEF and DEF+ASR, which experienced only this initial exposure phase.

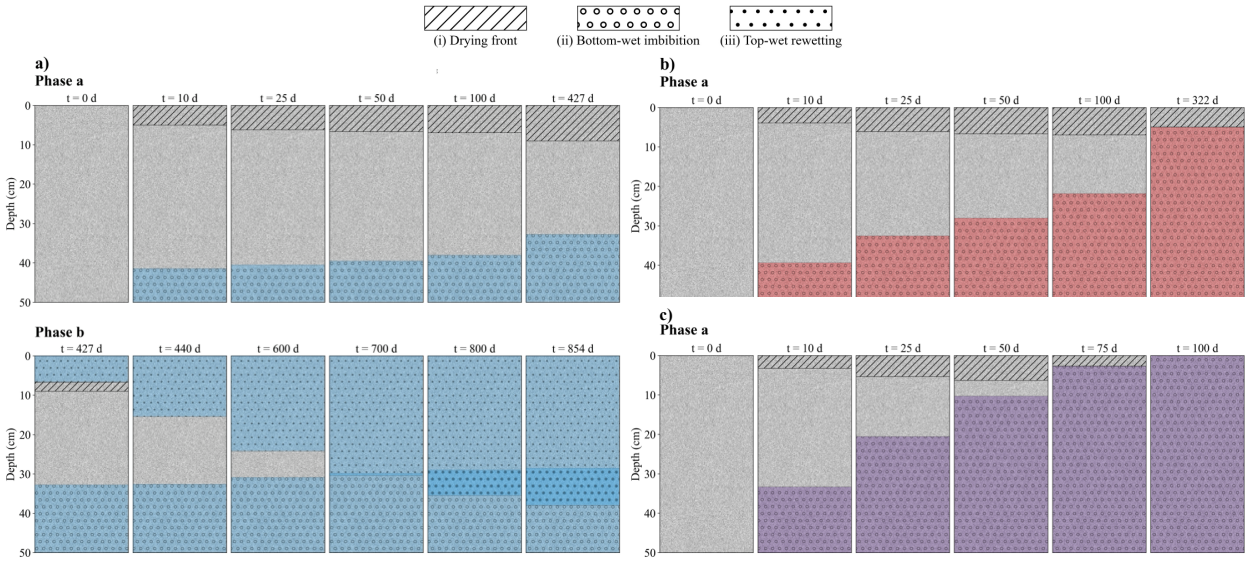


Figure 6.10 – Water transfer behavior. a) Moderate DEF, b) Severe DEF. c) DEF+ASR.

As observed in Figure 6.10a, the beam affected by moderate DEF exhibited gradual and limited water ingress over time. The drying front evolved slowly and stabilized at approximately 9 cm

below the top surface after approximately 427 days. This behavior indicates limited moisture loss and low permeability through the upper face. The imbibition front advanced gradually from the bottom of the member, reaching 8.6 cm (50 cm – 42 cm) at 10 days, 10.5 cm (50 cm – 39.5 cm) at 50 days, and 17.2 cm (50 cm – 32.8 cm) after 427 days. This relatively short penetration suggests reduced permeability and limited capillary absorption capacity, likely influenced by the limited DEF-induced swelling. During the initial stages, the development of the moisture profile is governed by drying from the top surface. At the same time, the important imbibition front differences at the bottom occur only after prolonged exposure (i.e., period between 100 days and 427 days). During phase b, once water was supplied to the upper surface, the previously established drying cap was progressively replaced by the advancing rewetting front. The rewetting front moved downward, from 6.7 cm at 427 days (approximately 2.3 cm of remaining drying) to 15.5 cm at 440 days, reaching near-complete homogenization of moisture conditions after about 700 days, when the rewetting and imbibition fronts converged. In parallel, the imbibition front continued its slow ascent from 17.2 cm (50 cm – 32.8 cm) at 427 days to 19.1 cm (50 cm – 30.9 cm) at 600 days, ultimately reaching the descending rewetting front according to the calculation. This interaction demonstrates the gradual recovery of saturation throughout the member while illustrating the low but progressive imbibition from the bottom of the moderate DEF-affected concrete during “phase b”. After approximately 600 days, the assumptions used for the calculation are no longer valid, as the equations above do not consider the possibility of convergence between the imbibition and rewetting fronts. At this stage, the entire cross-section is considered to be affected by water penetration, and it is not possible to differentiate between water from the bottom or the top.

In contrast, the severe DEF-affected beam (Figure 6.10b) developed greater water ingress height at a higher rate. Within the first 50 days, the imbibition front has already advanced more than 22.0 cm (50 cm – 28 cm), and by 300 days, it approaches the uppermost height of the cross-section, reaching 45 cm (50 cm – 5 cm). This rapid, steep imbibition suggests a more permeable material, possibly due to severe DEF-induced swelling and cracks induced by the structural test. As a result, this beam develops a near-linear moisture imbibition gradient that persists throughout the exposure period. The DEF+ASR-affected beam (Figure 6.10c) displayed an even steeper and earlier water uptake profile compared to the concrete affected by moderate and severe DEF. The moisture front

reached mid-height at 25 days, and after 76 days, water ingress was nearly uniform across the entire height. This behavior suggests that the combined action of DEF and ASR importantly increased the permeability of the material, facilitating water ingress. The synergistic interaction between the two mechanisms promotes early microcracking in the aggregate and cement paste, facilitating water movement compared to concrete affected by DEF. The progressive and rapid imbibition observed in this beam reflects the severe deterioration present throughout the cross-section. One must, however, keep in mind that these results are based on simplified calculations that consider multiple assumptions; yet, they allow for a semi-quantitative analysis of the water content of the specimens.

The moisture-front evaluation presented in Figure 6.10 provides further insight into the results illustrated in Figure 6.7, by cracks in the cement paste, and considering the similar drying front observed in all cases. In the moderate-DEF beam, the drying front stabilized near 9 cm early in "phase a", while the imbibition front rose slowly and reached about 17.2 cm at 427 days. After the onset of "phase b", the rewetting front descended from the top and progressively reduced the top–bottom contrast in moisture conditions. This sequence is consistent with the difference between the upper and lower sections, where the upper part exhibits a greater feature count, as shown in Figure 6.7. In the severe-DEF beam, the imbibition front crossed 22 cm within 50 days and approached the upper face by 300 days, which explains the higher feature counts and the greater concentration of distress in the lower section. The DEF+ASR beam exhibited the fastest imbibition kinetics, reaching mid-height by 25 days; calculations further suggest a pronounced reduction in the top–bottom moisture contrast by approximately 76 days. Given that the formulation does not couple imbibition and drying, this estimate is semi-quantitative and should not be taken as evidence of near-uniform moisture, which remains nevertheless consistent with the higher feature counts observed in Figure 6.7.

A comparison with Morenon's [70] modelling of the severe DEF beam provides an external consistency check for the trends inferred from the present semi-empirical reconstruction. Using a diffusion-based framework with transport properties evolving with local water state and damage, the study showed that cracking accelerates apparent moisture uptake, consistent with the steeper imbibition kinetics obtained here for the most severely damaged beams and supporting use of the reconstructed fronts as semi-quantitative indicators of water availability. It also reported that rapid

DEF precipitation requires high humidity (i.e., < 92 RH [72]), reinforcing the focus on zones likely to remain above the expansion-onset saturation threshold adopted in the reconstruction.

To examine the influence of these moisture fronts more explicitly across the member height, the beams were stratified into five layers in the next section. This layered analysis links the timing and extent of front arrival to the distribution of distress features, crack density, and maximum crack width and length.

6.6.2 Effect of water imbibition on the "stratified" DEF- and DEF+ASR-induced damage

The water imbibition behavior described in the previous section demonstrated a layered pattern of water ingress, which directly influenced the development and distribution of DEF- and DEF+ASR-induced deterioration across the height of the concrete members. This stratified water uptake was observed in the microscopic assessment through the distribution of distress features (Figure 6.5), crack density (Figure 6.6), and maximum crack widths and lengths (Figure 6.7). Altogether, these results indicate that water gradients drive the type, intensity, and extent of distressing features observed across the cross-section of each member: the higher and steeper the water ingress front, the greater the crack counts and the crack density, while longer and wider cracks are also observed. To better visualize this effect, Figure 6.11 presents the overall DRI values stratified into five depths (0–10, 10–20, 20–30, 30–40, and 40–50 cm), with the upper face considered as zero and the bottom face as 50 cm (Figure 6.3a). The surface analyzed (1250 cm² per slice) was subdivided into five equal zones of 250 cm² each, which is greater than the minimum representative area recommended for DRI analysis [12,56,65]. These profiles provide a detailed view of the vertical development of DEF- and DEF+ASR-related deterioration under varying exposure and moisture conditions.

In the concrete affected by moderate DEF, the distribution of deterioration features followed a stratified pattern that reflects the water imbibition profile described in Section 6.6.1. As the imbibition front advanced slowly and reached approximately 17.2 cm after 427 days, the lower portion of the member remained continuously exposed to moisture during "phase a", while the upper section became saturated only after the late addition of water during "phase b". This exposure sequence is reflected in the quantitative assessment through the conventional DRI. In the bottommost section (40–50 cm), a total DRI of 562 was recorded, marked by notable weighted counts of CCP (170), CCP_RP (323), and Debon (52). The mid-height layers (30–40 and 20–30

cm), which were reached the latest by both the imbibition and rewetting fronts, exhibited lower deterioration levels (DRI = 435 and 342, respectively), which demonstrates the impact of the delayed water ingress fronts. In contrast, the upper sections (10–20 cm and 0–10 cm) exhibited higher deterioration (DRI = 613 and 632, respectively), characterized by elevated CCP_RP and OCA counts (the stratified unweighted microscopic distressing features are further discussed in section 6.6.4). This behavior highlights the impact of the two-phase exposure to water. While the early drying phase limited DEF development in the top, it likely induced shrinkage-related cracking that later facilitated moisture ingress when water was added to the upper face, "phase b". Zhu [73] showed that decreasing relative humidity increases the number of cracks in the cement paste (CCP) and raises DRI values in concrete not affected by internal swelling reactions, with the evolution of DRI closely following measured shrinkage strains. This confirms that DRI is sensitive to shrinkage-related cracking and supports the interpretation that the upper 0–20 cm zone first developed a shrinkage crack network.

Additionally, the late water supply induced highly differential strains in the top part, as the wet concrete tended to expand while the still-dry concrete continued to shrink, generating restrained deformations. As a result, the DEF deterioration in this section appears to follow a distinct progression, with a higher proportion of CCP relative to CCP_RP.

In the concrete affected by severe DEF, the stratified DRI number showed a consistent increase in deterioration with depth, consistent with the continuous bottom-face immersion imposed during "phase a". DRI values rose from 324 at the top (0–10 cm) to 1350 (20–30 cm), reaching a maximum value of 1969 in the most saturated section (40–50 cm). The deterioration in the lower depth was characterized by high CCP (1025), CCP_RP (784), and increasing Debon (140), indicating significant microscopic deterioration of the bulk cement paste and progressive loss of aggregate–paste bond. The mid-depth layer showed similar features, while the top section remained less affected due to limited water exposure and the drying regime. The progression of damage along the height of this member illustrates how water availability enhances DEF development, reflecting a severe microscopic deterioration in the most saturated sections.

In the concrete affected by DEF in combination with ASR, the stratification of the beam cross-section into 5 depths revealed an exceptionally high DRI value of 2152 at bottommost (40–50 cm), the highest among all members, which represented 2.5 times higher DRI number compared to the

uppermost section (0–10 cm – DRI number 851). The deterioration was driven by extensive CCP (898) and CCP_RP (806), as well as severe deterioration of the ITZ (Debon = 103) and open cracks in aggregates (OCA = 109 and OCA_RP = 233), indicating an important ASR contribution (the stratified unweighted features count is further discussed in 6.6.4). The early and steep water ingress described in Section 6.6.1 likely intensified the damage in this section, as microcracking initiated by ASR may have facilitated sulfate migration, promoting intense DEF-induced damage. The variety and intensity of damage features observed indicate that DEF and ASR evolved in a highly interdependent manner, contributing to relatively severe deterioration.

Although the beams affected by severe DEF and DEF+ASR failed prematurely during the initial water exposure phase, this outcome allowed for a distinct interpretation of the effects of water imbibition on the resulting deterioration profiles. The absence of a second water exposure phase in these members preserved the signatures of deterioration driven solely by early-age water uptake from the bottom while the upper surface is exposed to drying conditions. This enabled a more focused evaluation of how early and unidirectional moisture gradients shape DEF- and DEF+ASR-induced damage; an effect that would have been masked by homogenization if "phase b" had occurred in these beams.

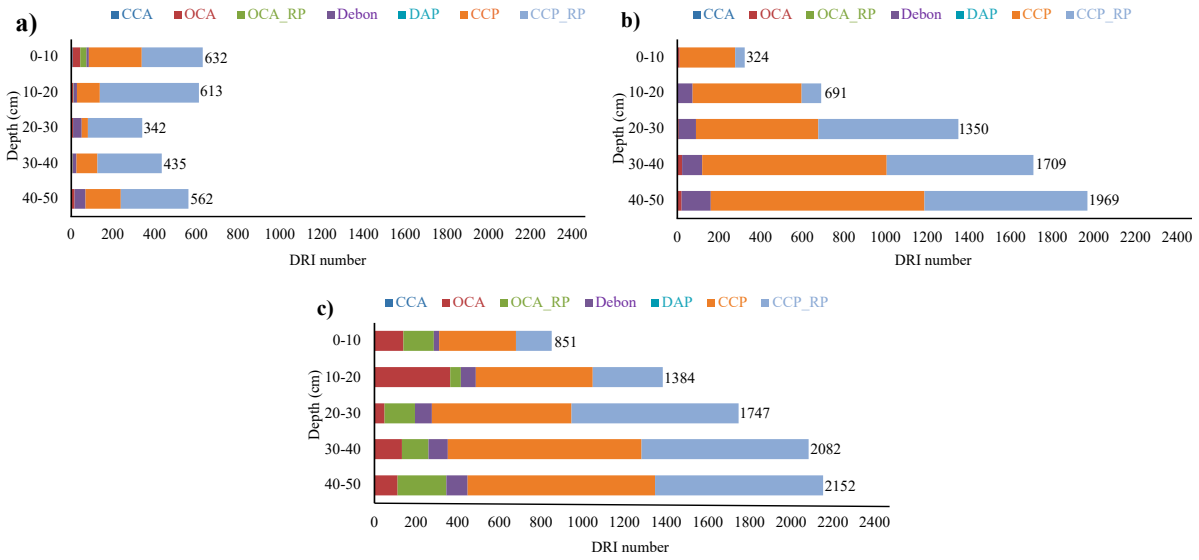


Figure 6.11 – DRI chart of all beams. a) Moderate DEF, b) Severe DEF. c) DEF+ASR.

The heatmap of the DRI number for the full cross-sections (Figure 6.12) reveals clear differences in the distribution and intensity of deterioration along the height of beams affected by moderate

DEF, severe DEF, and DEF in combination with ASR. These variations correspond to (i) the distinct water imbibition behavior observed in each member, (ii) the presence or absence of late water supply from the top surface, and (iii) the swelling potential of the mechanisms involved.

In concrete affected by moderate DEF (Figure 6.12a), the DRI number distribution remained relatively uniform throughout the cross-section, with slightly higher values in the upper sections (0–10 cm and 10–20 cm). This profile reflects the combined effect of the initial drying exposure "phase a" and the subsequent water ingress from the top during "phase b". The distress in the lower section (40–50 cm) suggests limited DEF development, consistent with the reduced ettringite-forming potential associated with the cement used (Figure 6.3).

The beam affected by severe DEF displayed a more pronounced and vertically layered deterioration pattern, with a progressive increase in DRI values from top to bottom. Maximum damage is observed between 20 and 50 cm, consistent with the steep water ingress profile developed under continuous bottom-surface exposure during "phase a". The heatmap (Figure 6.12b) highlights this behavior, with deterioration extending deeply and vertically through the central portion of the cross-section. Interestingly, a distinct arrow-shaped pattern is visible between 20–40 cm, where deterioration is more concentrated along the central transverse axis and gradually decreases toward the outer edges. The origin of this pattern remains uncertain. Possible contributors include edge effects at the aluminum sealing, minor water ingress at the side interfaces, or sampling biases; available evidence is insufficient to discriminate among these possibilities. The pattern is reported here to document the geometry of deterioration and to motivate targeted follow-up measurements.

Concrete affected by DEF in combination with ASR presented the most severe deterioration among all beams. As shown in Figure 6.12c, DRI values were markedly higher in the lower sections (40–50 cm and 30–40 cm), gradually decreasing toward the top. This vertical pattern reflects the early and nearly complete saturation observed in Section 6.6.1, where water ingress reached the upper face within only 76 days. Compared to the severe DEF beam, deterioration extended further upward, indicating both enhanced water transport and the more aggressive nature of the combined mechanisms. An arrow-shaped pattern is also apparent. Its origin remains uncertain. Self-weight bending produces longitudinal stresses that are approximately uniform along a horizontal line at a given depth and therefore does not readily explain a transverse gradient

in damage. Potential contributors include side-edge sealing effects, minor lateral ingress at the side interfaces, or sampling biases; current evidence is insufficient to attribute causality. The observation is documented to guide targeted verification in future measurements.

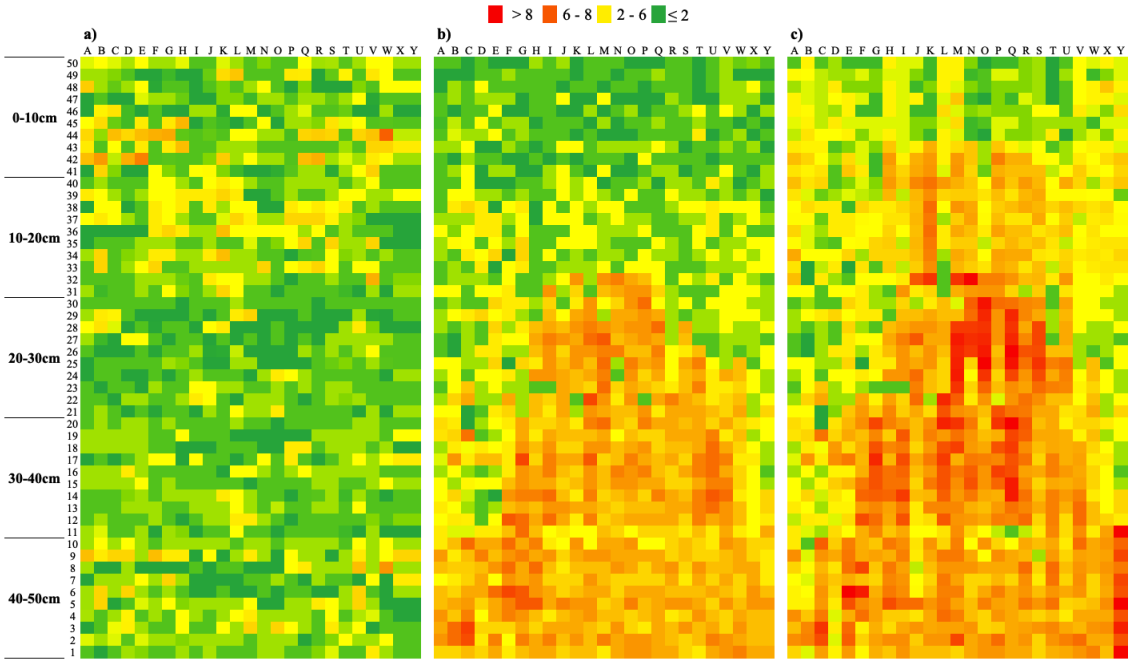


Figure 6.12 – Heatmap of damage distribution over the cross-section. a) Moderate DEF, b) Severe DEF. c) DEF+ASR.

6.6.3 Understanding DEF- and DEF+ASR-induced deterioration

Previous sections discussed the use of "overall damage values" for appraising the stratified deterioration distribution of DEF- and DEF+ASR-affected concrete, along with the importance of combining mechanism-induced damage potential and distinct water transport behavior, which results in specific damage distributions throughout the beams' height. Further exploring this previous understanding, the current section aims to describe and compare DEF- and DEF+ASR-induced damage development (i.e., crack generation and propagation) of concrete exposed to distinct moisture gradients.

- DEF-induced deterioration

Cracks associated with DEF-induced deterioration exhibit distinct crack density (counts/cm²) and crack dimensions (i.e., maximum width and length) depending on the severity of the mechanism and the exposure conditions.

The concrete affected by moderate DEF exhibited low crack density values (Figure 6.13) along the entire section, ranging from 1.21 to 2.48 counts/cm². The highest densities were observed near the top of the member (0–10 cm and 10–20 cm), likely due to drying-induced cracking during "phase a" and late DEF development during "phase b". Maximum crack widths (Figure 6.14) in this member remained narrow across all depths (0.01–0.02 mm), reflecting the scattered deterioration distribution across the analyzed cross-section. Similarly, crack lengths were short, with values ranging from 4.20 to 6.70 mm. These findings indicated limited DEF development, consistent with the analysis of the stratified DRI number, which is explained by the moderate potential of the cement used to generate ettringite and the layered water exposure conditions (i.e., "phase a" and "phase b").

In contrast, severe DEF resulted in extensive cracking throughout the lower half of the member. Crack density increased progressively with depth, from 1.13 counts/cm² in the top (0–10 cm) to 6.61 counts/cm² in the bottommost section (40–50 cm). The maximum crack widths followed a similar trend, increasing from 0.07 mm at the top to 0.31 mm in the bottom layer. Crack length values reached 31.40 mm at 40–50 cm, decreasing gradually toward the top, and ultimately reached only 5.70 mm (0–10 cm). The observed higher crack density and maximum width and length of cracks, compared to moderate DEF affected beam, reflects extensive DEF development in the beam affected by severe DEF, which is explained by the higher ettringite formation potential of the cement used in this concrete, estimated via thermodynamic modelling (Figure 6.3) to be 31% greater than that of the cement used in the moderate DEF concrete, combined with the uninterrupted water exposure from the bottom face during "phase a".

- DEF+ASR-induced deterioration

Distress features associated with DEF+ASR-induced deterioration consistently exhibited high crack density values, as well as greater maximum width and length along the height of the beam, reflecting the severity and extent of deterioration due to the combined mechanisms. Crack density (Figure 6.13) ranged from 3.34 to 7.86 counts/cm², with the highest values observed in the bottommost section (40–50 cm). Maximum crack widths (Figure 6.14a) reached 0.35 mm at 40–50 cm and remained relatively elevated throughout the section. Crack lengths varied from 6.10 to 31.10 mm, also showing a tendency for greater values in the lower layers (Figure 6.14b).

These findings revealed severe deterioration throughout the entire cross-section, which is explained by the synergistic action of DEF and ASR, as well as the rapid water imbibition that saturated the member during the early exposure period. Early ASR-induced microcracking likely facilitated water ingress and ion migration, accelerating ettringite formation and contributing to widespread internal swelling. Compared to the beam affected by severe DEF, the concrete affected by DEF+ASR showed greater values of crack parameters analyzed along the beam height, with a similar trend of decreasing values from the lower to the upper layer. The interaction between DEF and ASR appears to have intensified the deterioration process, leading to higher crack connectivity, wider openings, and longer propagation paths throughout the cross-section.

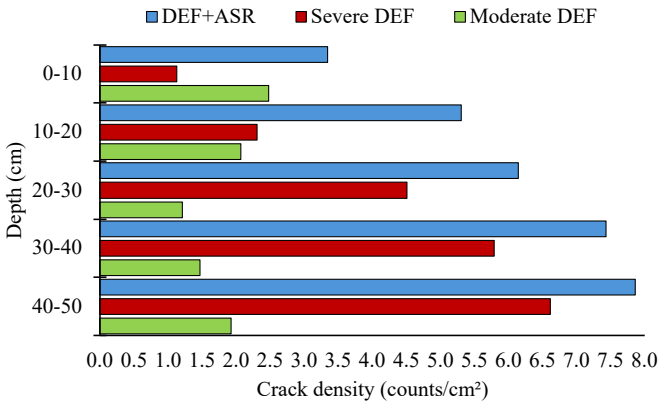


Figure 6.13 – Crack density as a function of depth of Moderate DEF, Severe DEF, and DEF+ASR-affected concrete.

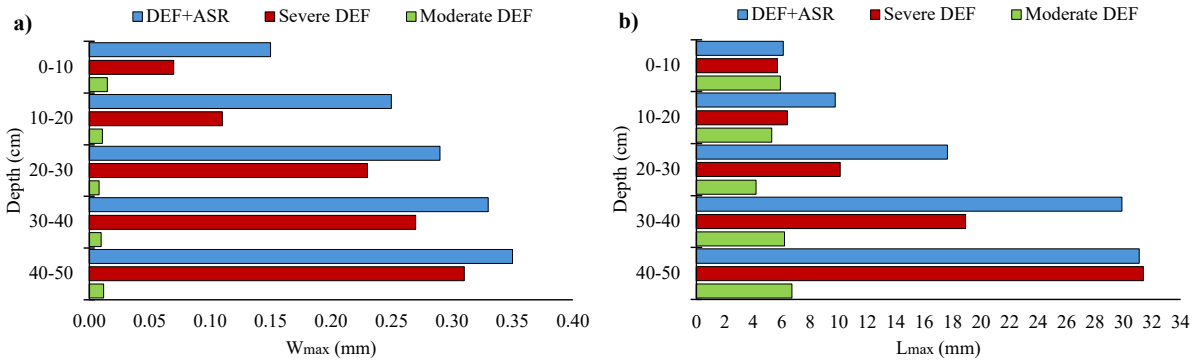


Figure 6.14 – Maximum a) width and b) length as a function of depth of Moderate DEF, Severe DEF, and DEF+ASR-affected concrete.

- Potential non-ISR contributions to cracking and transport connectivity

Additional microcracking sources may have contributed to the observed distress independently of ISR development. The imposed heat treatment and subsequent cooling can generate microcracking due to differential thermal dilation between aggregate and paste and transient thermal gradients, which may create local tensile stresses during temperature changes. During the long-term exposure, deadweight-induced flexure and the evolving stiffness degradation may further amplify cracking, particularly once localized deterioration reduces section rigidity. These effects can increase transport connectivity and may partially superimpose mechanically induced cracking on ISR-related features; one therefore interprets DRI and crack metrics as the combined outcome of moisture availability, reaction-induced swelling, and structurally induced stress states.

6.6.4 Evaluating DEF- and DEF+ASR-induced distressing features as a function of the depth

The microscopic analyses conducted in this study enable the evaluation of distress features associated with moderate DEF, severe DEF, and DEF+ASR-induced deterioration as a function of depth. The results are presented in Figure 6.15 (i.e., the absolute counts of microscopic features normalized to 100 cm²) and Figure 6.16 (i.e., the corresponding proportions), providing a complementary understanding of the proportion of distressing features generated by each mechanism across the beam depth.

In the member affected by moderate DEF, the damage was predominantly characterized by the presence of Group III features (cracks in the cement paste with or without reaction products), with values ranging from 97 to 195 across the height. A higher count of Group III was observed in the 10–20 cm section (195), followed by the top 0–10 cm (182). Group I (closed cracks in aggregates) and Group II (open cracks in aggregates) were also more frequent in the upper section, with values of 29 and 33, respectively. This distribution reflects the influence of early drying in the upper layers during “phase a”, which has limited DEF-induced development in the early aging period, while likely activating minor ASR-like-induced distressing features, further intensified by the water supply of “phase b”. Although the aggregate used is classified as non-reactive (silicious aggregate – Section 4), rather minimal and isolated signs of ASR reaction production were previously observed by Martin [7] using a uranyl acetate solution, which is adsorbed to the ASR

gel surface, and upon exposure to ultraviolet light, reveals a greenish-yellow fluorescence of the uranyl ion. Group IV (debonding at the aggregate–paste interface) remained comparatively low throughout the layers, with slightly elevated values in the lower depths (14–17), indicating localized ITZ degradation where early DEF swelling occurred. Although low values of Group IV were observed, this distress feature indicates the impact of the bond between aggregate particles and cement paste, which is likely reflected in the mechanical performance of the affected material. The severe DEF-affected member showed a progressive increase in Group III feature counts with depth. The lower three layers (20–30, 30–40, and 40–50 cm) presented values of 420, 530, and 603, respectively, while the upper layers displayed lower counts (206 and 104). Group IV also increased from 0 (i.e., 0-10 cm) to 47 (i.e., 40-50 cm), indicating a progressive deterioration of the aggregate-paste bond with depth. Groups I and II remained relatively low across all depths, consistent with the hypothesis of minimal ASR-related induced distress in the moderate DEF-affected beam. In the member affected by severe DEF, it was even lower since there was no "phase b" of water exposure. These results align with the bottom-up water ingress (Figure 6.10) and the severity of the DEF reaction induced by the cement composition (Figure 6.3).

In the DEF+ASR-affected member, the distribution of microscopic features was quite spread along the height, marked by a variety of distressing features identified. Group III features remained high across all depths, ranging from 180 in the top layer to 576 at 30–40 cm. Notably, the feature counts of Group II were substantial across all regions, reaching 207 in the 10–20 cm section and 171 in the 0–10 cm layer. These features count demonstrate the simultaneous deterioration in the cement paste and aggregate particles, promoted by the synergy of DEF and ASR, which is shaped by rapid saturation.

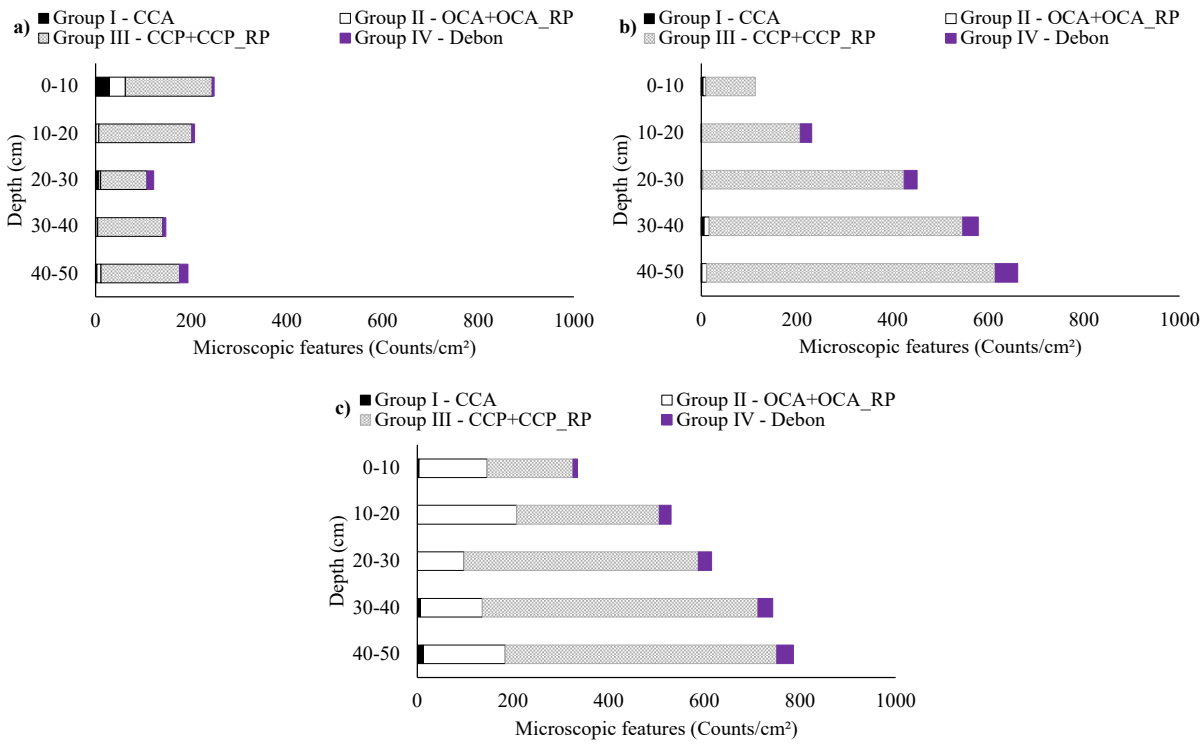


Figure 6.15 – Microscopic features of deterioration as counts normalized for 100 cm² as a function of depth of a) Moderate DEF, b) Severe DEF, and c) DEF+ASR-affected concrete.

The normalized proportions of distress features across depth (Figure 6.16) provide further insight into the deterioration profiles previously described using absolute counts (Figure 6.15). These relative values depict the proportional contribution of each group of features to the attained extent of deterioration of moderate DEF, severe DEF, and DEF+ASR-affected concrete.

In the member affected by moderate DEF, Group III accounted for the majority of features at all depths, ranging from 73% to 94%, confirming the predominant deterioration of the cement paste. The upper layer (0–10 cm) displayed the highest relative presence of Group II (13%), while the remaining sections presented 3% to 4%, reinforcing the interpretation that limited ASR-induced distress may have occurred in this region following early drying during “phase a” and subsequent rewetting during “phase b”. Although Group II appeared only modestly in absolute counts, their proportion was evident locally, indicating localized aggregate distress. Group IV remained below 11% at all depths, with the highest values in the mid-height section (20–30 cm), indicating that an important portion of the aggregate particles had a weakened bond with the cement paste.

For the concrete affected by severe DEF, Group III represented the greater contribution to observed damage throughout the section, exceeding 89% across all depths and reaching up to 93% in the middle and lower layers. This supports the earlier analysis of a widespread and vertically progressive deterioration profile related to DEF, concentrated in the bulk cement paste. The contribution of Group IV varied along the height, ranging from 6 to 10%, indicating a pronounced deterioration of the aggregate–paste bond. Group II contributed marginally to the overall deterioration at all depths, remaining below 5%, consistent with the minimal ASR-related deterioration potential from this aggregate type. These proportions confirm that the microscopic damage in severe DEF is concentrated in the ITZ and propagates into the bulk cement paste, with intensified effects observed in the deeper saturated layers. Such behavior clearly demonstrates the DEF damage progress, with deterioration of the ITZ further extending into the bulk cement paste, similarly observed by [7,8,48].

In the member affected by DEF in combination with ASR, the proportion of distress features was notably more heterogeneous. Group III continued to be the predominant group (54% to 80%) across all layers, while Group II represented a significant contribution, particularly in the top two layers (42% and 39% in the 0–10 and 10–20 cm layers, respectively). These values align with the high absolute counts of Group II observed in Figure 6.14 and confirm the important role of ASR-induced cracking in the upper section of the beam. Group IV remained relatively constant along the height (3–5%), demonstrating a reduced yet important contribution of ITZ deterioration to the overall damage observed. These results demonstrate that DEF+ASR induces deterioration in the main macroscopic phase of the concrete (i.e., bulk cement paste, aggregate particles, and the ITZ).

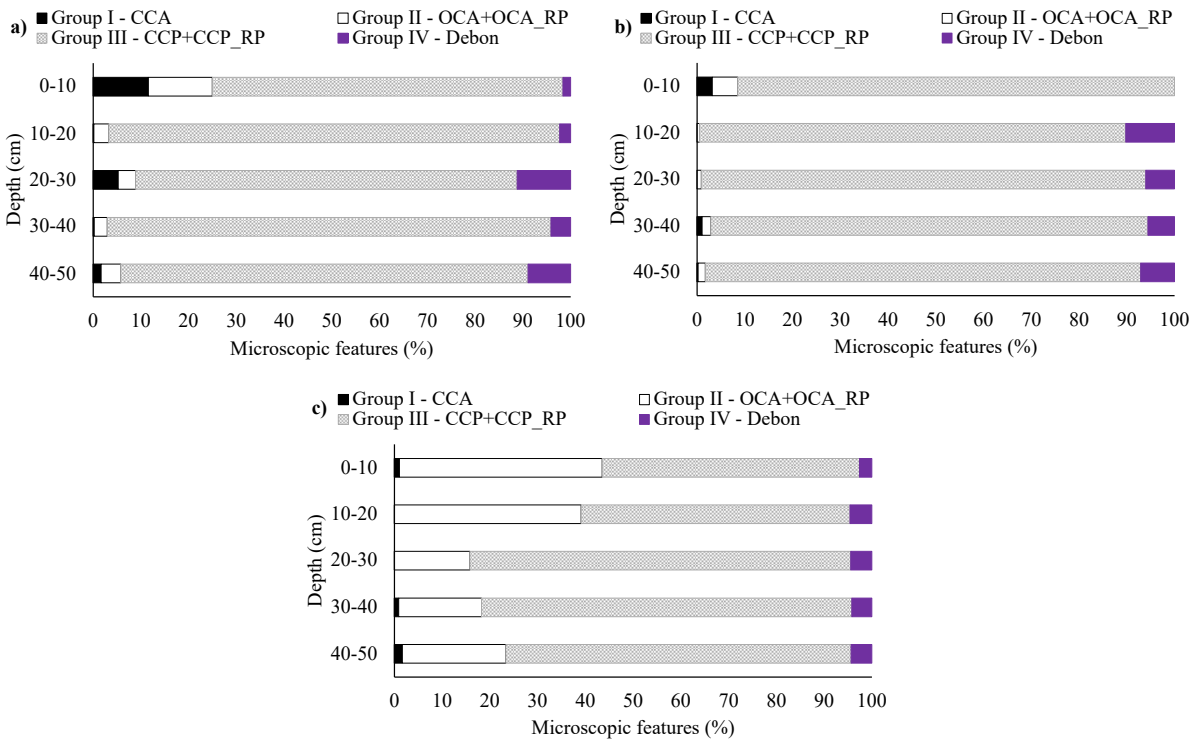


Figure 6.16 – Microscopic features of deterioration as percentage as a function of depth of a) Moderate DEF, b) Severe DEF, and c) DEF+ASR-affected concrete.

6.6.5 Estimating the contribution of DEF and ASR to the overall deterioration

As discussed in the previous sections, the extent and distribution of deterioration features observed in concrete affected by DEF and DEF+ASR result from differences in material reactivity, moisture exposure, and the interaction between ISR mechanisms. Although DEF and ASR may develop simultaneously, distinct types of distressing features associated with each ISR mechanism can be observed in different phases of the affected material, including bulk cement paste, the interfacial transition zone (ITZ), and aggregate particles. To support the interpretation of the deterioration pattern observed in the DEF+ASR-affected concrete, the microscopic features were grouped according to the ISR mechanism primarily associated with their development.

Under DRI assessment, DEF-related deterioration is typically represented by cracks in the cement paste (CCP), cracks in the cement paste with reaction products (CCP_{RP}), and ITZ deterioration, which is represented either by CCP or by debonding of aggregate particles (Debon), depending on crack extent [15]. ASR-related deterioration is more often identified through open cracks in coarse aggregates (OCA), open cracks with reaction products (OCA_{RP}), and, in specific aggregate types,

signs of aggregate disaggregation or corrosion (DAP). At moderate and high expansion levels, ASR-related cracks initiated within aggregate particles extend into the cement paste, forming CCP or CCP_{RP} features [12], which were observed in this work to display a remaining connection to the cracks within the aggregate particles. In contrast, cracks associated with DEF generally initiate in the cement paste and do not display such connections. Based on such distinctions, each distressing feature was attributed to either ASR or DEF for quantitative comparison. Closed cracks in aggregates (CCA), typically unrelated to ISR mechanisms, are attributed to pre-existing flaws or aggregate processing.

Figure 6.17 presents the grouped feature counts for ASR- and DEF-related distress. Group I (CCA) is excluded from interpretation. Group V includes ASR-related features (i.e., OCA, OCA_RP, $CCP_{\_ag}$, and CCP_{RP_ag}), while Group VI includes DEF-related features (i.e., Debon, $CCP_{\_paste}$, and CCP_{RP_paste}).

The count-based results (Figure 6.17a) indicate that ASR-related features (Group V) were mainly concentrated in the upper part of the cross-section, with 299 and 222 counts in the 10–20 cm and 0–10 cm layers, respectively. In contrast, DEF-related features (Group VI) became more frequent with depth, reaching 567 counts in the 30–40 cm section and 511 in the 40–50 cm section. This depth-dependent distribution is consistent with the water transport behavior discussed in Section 6.6.1. ASR was triggered early in the upper portion of the beam due to early and localized low saturation, whereas DEF developed progressively in the lower part, where water remained available for a longer period.

The percentage-based distribution (Figure 6.17b) reinforces this shift across depth. ASR-related features (Group V) accounted for 66% of the observed damage in the top 10 cm and 56% in the 10–20 cm layer. Below this section, DEF-related features became more frequent, reaching 76% in the 30–40 cm section and 65% in the bottommost layer. This transition reflects the layered deterioration profile induced by the different ISR mechanisms, with ASR prevailing in the upper layers and DEF in the lower sections of the cross-section.

The proposed approach demonstrates that in concrete affected by severe DEF and ASR, ASR triggers early deterioration, thereby fostering DEF distress. This behavior has been discussed by Martin [7]; yet, it has not been previously captured through mesoscale microscopic analyses, which provide an important contribution to further understanding the mechanical behavior of concrete

affected by coupled ISR mechanisms. Understanding and quantitatively estimating the contribution of each mechanism (i.e., ASR and DEF) provides important information for managing DEF+ASR-affected structures, as both mechanisms induce distinct yet interrelated effects on the mechanical properties of the affected material [66] and residual structural capacity [7,30].

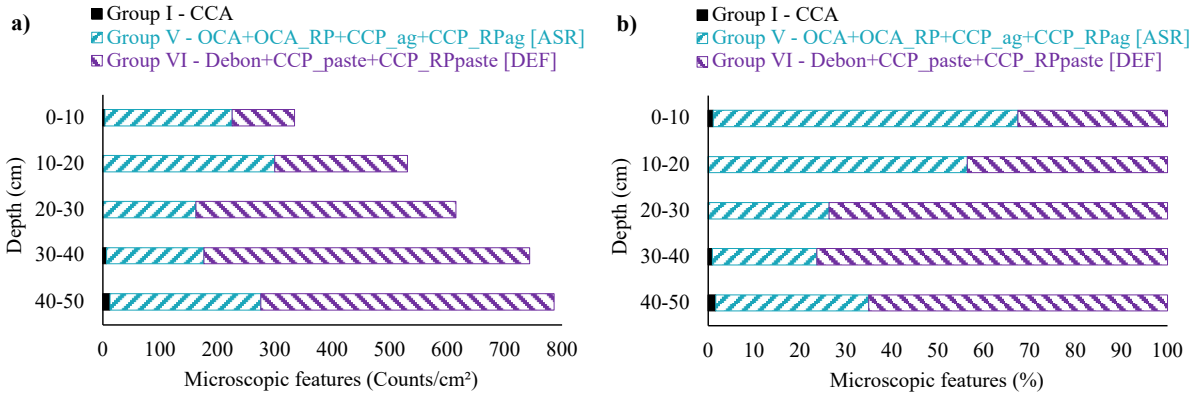


Figure 6.17 – Estimation of the contribution of DEF and ASR to the overall deterioration (a) counts (b) percentage as a function of depth of Moderate DEF, Severe DEF, and DEF+ASR-affected concrete.

6.6.6 Qualitative descriptive models to describe ASR, DEF, and DEF+ASR-induced damage initiation and propagation

The progression of deterioration in concrete affected by DEF and DEF+ASR was found to depend strongly on the distressing mechanism involved and the internal moisture gradients. The depth-wise microscopic assessment carried out in this study helps to clarify how distress features associated with each mechanism (i.e., DEF and ASR) initiate and propagate. Figure 6.18 presents representative micrographs from non-reinforced beams affected by moderate DEF, severe DEF, and DEF in combination with ASR, illustrating the vertical development of distress features across the section.

The deterioration of concrete affected by moderate DEF was primarily characterized by Group III features (CCP and CCP_RP), followed by the presence of Group IV (Debon), indicating degradation of the aggregate–paste bond. These features were relatively evenly distributed throughout the cross-section, with slight intensification near the continuously wet (i.e., 40-50 cm) and rewetting (i.e., 0-10 cm) zones. The presence of CCP with limited reaction products suggests a reduced ettringite recrystallization, consistent with the limited potential of the cement used to

generate ettringite and the delayed availability of moisture. Cracks remained mostly isolated and showed limited interconnection, particularly in the mid-depth layers where moisture imbibition was insufficient to sustain DEF development.

The deterioration of concrete affected by severe DEF was markedly advanced and vertically stratified. The most pronounced damage was concentrated in the lower portion of the cross-section, where sustained moisture availability promoted intense recrystallization of ettringite. Micrographs revealed a high presence of CCP and CCP_RP features in the interfacial transition zone, which eventually extend, outlining aggregate particles and evolving into Debon-type features. As deterioration progressed, these cracks extended into the surrounding cement paste, forming interconnected cracking networks that linked the ITZs of multiple aggregate particles throughout the cross-section.

The deterioration of DEF+ASR-affected concrete revealed the presence of both Group III (CCP and CCP_RP) and Group II (OCA and OCA_RP) features, characterized by widespread cracking in both paste and aggregates, as well as clear signs of ITZ deterioration, as represented by the Group IV (Debon) feature. The micrographs of DEF+ASR-affected concrete unveil the presence of ASR-induced cracks, predominantly of the onion-skin type, and a modest presence of sharp cracks, in the upper layer. These cracks initiate and grow into the aggregate particles, without extending into the bulk cement paste. The relatively early water imbibition in the sections 10-20cm and 20-30cm resulted in the presence of sharp cracks, which usually extend into the cement paste, maintaining the connection with the initial crack within the aggregate particle. In the section 20-30cm, sharp cracks initiate within the aggregate particle and extend into the cement paste, likely enhanced by the availability of moisture. The deterioration of the bottommost sections (i.e., 30-40 cm and 40-50 cm) indicated the presence of cracks in the cement paste, with quite limited connection to cracks in the aggregate particles. This observation demonstrates that the reactivity potential of the aggregate to ASR and the cement to DEF is limited or intensified by the availability of water.

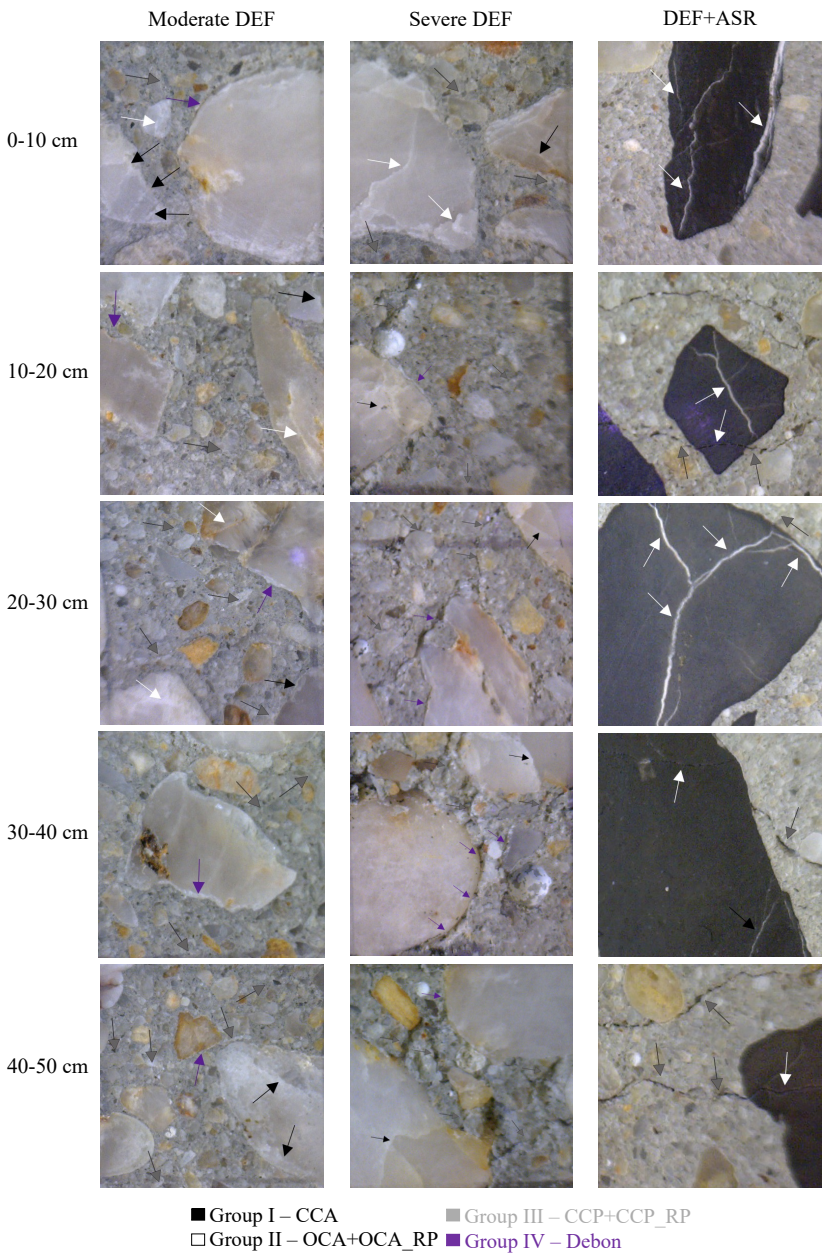


Figure 6.18 – Micrographics highlighting features of deterioration across the depths of Moderate DEF, Severe DEF. DEF+ASR affected concrete.

Based on these observations and supported by DRI analyses of ISR-affected concrete reported in the literature [12,13,15], Figure 6.19 presents qualitative models describing the progression of damage associated with ASR, DEF, and DEF+ASR under various exposure and material conditions at the mesoscale.

The development of ASR under conditions prone to high deterioration is typically marked by a greater number of sharp cracks than onion-skin cracks. This behavior was described by Sanchez et al. [12], based on the analysis of highly reactive aggregates subjected to exposure conditions that enhanced their maximum expansion potential (Figure 6.19a). In contrast, the ASR deterioration observed in this study, where the aggregate presented a limited reactivity potential (i.e., maximum expansion of 0.16%) and the exposure conditions restricted ASR development, was characterized by a higher occurrence of onion-skin cracks compared to sharp cracks (Figure 6.19b). As discussed by Sanchez et al. [12], both the nature of the aggregate and the concrete characteristics, including the exposure conditions, influence the type of cracks that form and whether they remain within the aggregate or extend into the surrounding cement paste.

The deterioration induced by DEF initiates with the formation of cracks in the interfacial transition zone (ITZ), while only a few isolated cracks are observed in the bulk cement paste throughout the initial and moderate levels of deterioration. As damage progresses (i.e., high level of deterioration), new cracks are generated in both the ITZ and bulk cement paste, while preexisting ones continue to extend. In more advanced damage levels, cracking becomes more pronounced, outlining the aggregate particles (i.e., Debon features) and propagating into the surrounding paste, eventually linking with preexisting cracks to form initial networks. A very high deterioration level is characterized by an extensive cracking network, and aggregate particles may become detached from the surrounding paste due to the substantial loss of bond strength. The higher incidence of cracking around the ITZ compared to the bulk paste at moderate deterioration levels is consistent with the damage patterns induced by DEF described by [47]. However, it is worth noting that in the DRI protocol [12,57,58], an aggregate particle is classified as debonded only when the crack outlines more than 70% of its perimeter [74], which accounts for the impact on mechanical properties [66]. Prior to this threshold, the damage in the ITZ is classified as a crack in the cement paste (CCP or CCP_RP). This interpretation aligns with the gradual deterioration process described by the British Cement Association and Poole & Sims [49,50], and more recently observed by Sanchez [15].

In DEF+ASR-affected concrete, deterioration involves the formation of cracks within reactive aggregates, marking the initiation of ASR-related distress, along with a minor presence of cracks in the cement paste, particularly around the ITZ, indicating the presence of DEF activity. At a

moderate level of deterioration, cracks begin to grow both toward the ITZ and into the bulk cement paste, while continuing to develop within the aggregate particles. As deterioration advances, preexisting cracks propagate and new cracks emerge inside the aggregate particles, along the ITZ, and within the bulk cement paste. At higher damage levels, cracks in the ITZ increasingly outline the aggregate particles and extend into the surrounding cement paste. Sharp cracks that originate within the aggregate particles propagate into the cement paste. In contrast, the onion skin cracks propagate parallel to the boundaries of the aggregate particles, eventually propagating into the surrounding cement paste. This progression leads to the formation of a critical cracking network resulting from the combined action of DEF and ASR. It is essential to note that the cracks induced by DEF were not found to be connected to those associated with ASR. This behavior is consistent with the high alkali concentration in ASR gel, which could limit the recrystallization of ettringite. The limitation of ettringite formation due to the presence of alkalis has been previously described and demonstrated in the literature [7,11,19–22]. Nevertheless, it is worth noting that this behavior was observed under the limitations of this study, including the type of aggregate, concrete characteristics, and exposure conditions.

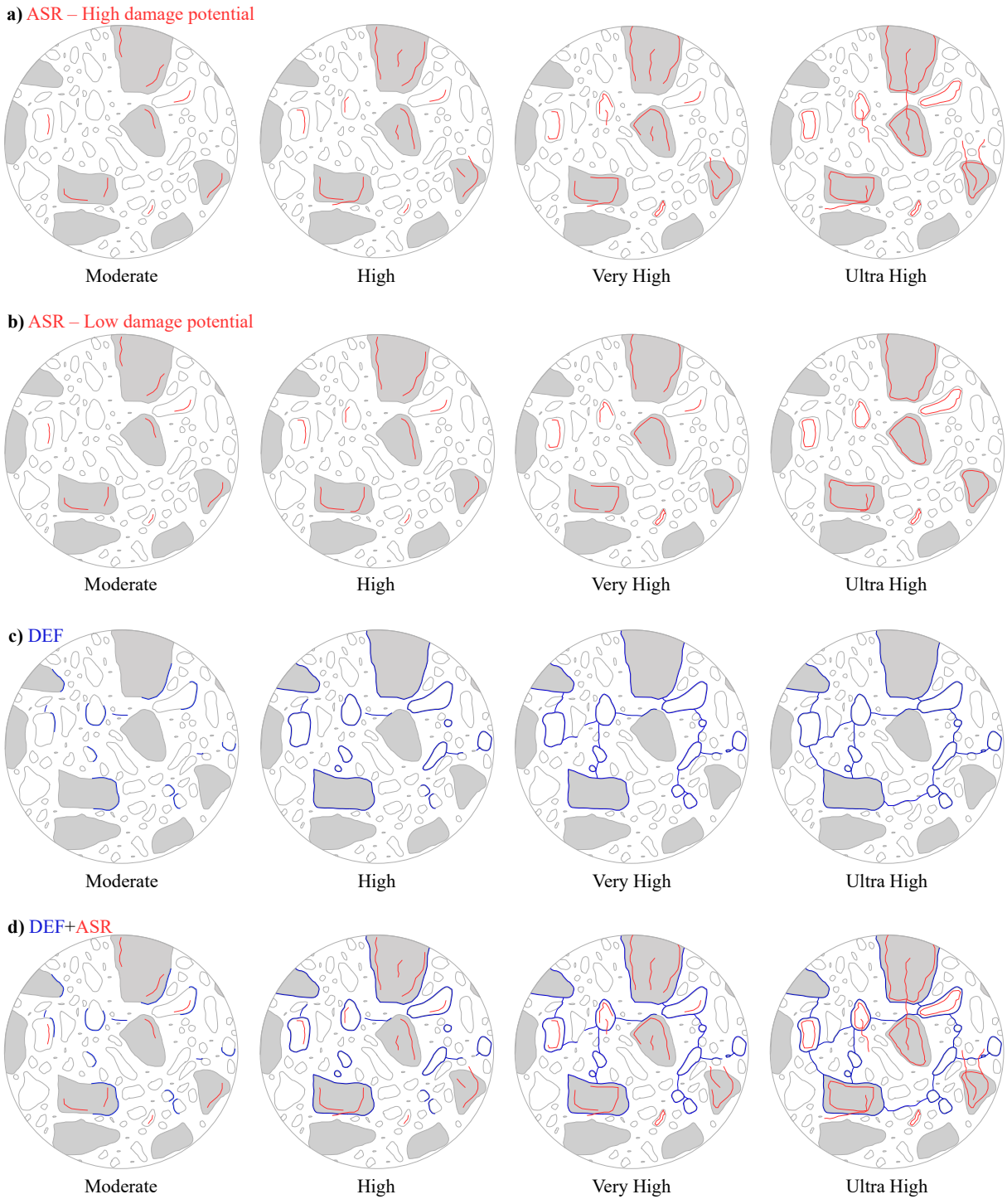


Figure 6.19 – Qualitative descriptive model of a) ASR low damage potential, b) ASR high damage potential, c) DEF, and d) DEF+ASR-induced damage.

6.7 Conclusion

Microscopic investigations were performed on large cross-sections of non-reinforced concrete beams affected by DEF and DEF+ASR, aged under severe moisture gradients. The moisture profile of beams exposed to variable yet controlled water supply conditions was evaluated through a simplified 1D model. The Damage Rating Index (DRI) methodology was applied in both its conventional and extended forms to assess and quantify deterioration. Based on the findings of this study, the following conclusions can be drawn:

- The deterioration pattern in all members was strongly influenced by the imposed moisture gradient. Water imbibition from the bottom face and late re-saturation from the top surface shaped and intensified the development and progression of DEF and DEF+ASR-induced damage.
- The member affected by moderate DEF showed limited deterioration, with pronounced cracks in the cement paste and ITZ deterioration in the wetting zones. There was no significant cracking network, which is explained by the limited DEF development due to the lower potential for ettringite formation and reduced moisture availability.
- Severe DEF-induced damage resulted in an extensive and stratified crack network in the cement paste, concentrated in the bottom region. Sustained moisture exposure promoted the formation of reaction products and progressive deterioration at the aggregate–paste interface.
- The DEF+ASR-affected concrete exhibited the most advanced state of damage, characterized by distributed cracking in both aggregates and paste. Aggregate cracking associated with ASR was observed across the height, while DEF-related features concentrated in the lower section, where moisture imbibition was high since the early exposure period.
- Stratified DRI number mapping confirmed the depth-wise pattern of deterioration. Cracking density, maximum width and length, and DRI numbers increased with depth in DEF-affected members, while a more homogeneous but intense pattern was found in DEF+ASR-affected concrete.

- An approach was developed to estimate the contributions of DEF and ASR to the overall damage. The DRI-based partitioning indicates that ASR-related features are more prevalent in the upper section, whereas DEF-related features dominate in the lower zones, in agreement with the reconstructed moisture availability.

Based on the microscopic evidence, a qualitative model of DEF- and DEF+ASR-induced damage propagation was proposed, distinguishing typical damage features, deterioration distribution, and interaction mechanisms across deterioration scenarios. The microscopic analysis, combined with the analysis reported in the literature, enhanced important insights for the established ASR distress model.

6.8 References

[1] B. Fournier, M.-A. Bérubé, Alkali-aggregate reaction in concrete: a review of basic concepts and engineering implications, Canadian Journal of Civil Engineering 27 (2000) 167–191. https://doi.org/10.1139/l99-072.

[2] P. Fasseu, B. Mahut, Aide à la gestion des ouvrages atteints de réactions de gonflement interne : Guide méthodologique, GUIDES TECHNIQUES, Laboratoire Central des Ponts et Chaussées (LCPC), Paris, 2003.

[3] L.F.M. Sanchez, Internal Swelling Reactions in Concrete: Mechanisms and Condition Assessment, 1st ed., CRC Press, Boca Raton, 2024. https://doi.org/10.1201/9781003188155.

[4] F. Toutlemonde, Structural implications and management of infrastructure assets affected by ISR: example of French experience on road bridges, Canadian Journal of Civil Engineering 52 (2025) 1843–1851. https://doi.org/10.1139/cjce-2025-0120.

[5] B. Godart, J. Wood, Interaction of DEF and AAR, a review, Revista Portuguesa de Engenharia de Estruturas. Ed. LNEC. 3 (2021) 25–34.

[6] K. Scrivener, J.P. Skalny, eds., Internal sulfate attack and delayed ettringite formation: Proceedings of the International RILEM TC 186-ISA Workshop, Villars, Switzerland, 4–6 September 2002, RILEM Proceedings PRO 35, RILEM publications, in: 2004.

[7] R.P. Martin, Analyse sur structures modèles des effets mécaniques de la réaction sulfatique interne du béton, PhD thesis, Université Paris Est., 2010. https://theses.hal.science/tel-00558200.

[8] H.F.W. Taylor, C. Famy, K.L. Scrivener, Delayed ettringite formation, Cem Concr Res 31 (2001) 683–693. https://doi.org/10.1016/S0008-8846(01)00466-5.

[9] R.P. Martin, J.C. Renaud, F. Toutlemonde, Experimental investigations concerning combined delayed ettringite formation and alkali aggregate reaction, in: P. Castro-Borges, E.I. Moreno, K. Sakai, O.E. Gjørv, N. Banthia (Eds.), 6th International Conference on Concrete under Severe Conditions (CONSEC10), CRC Press, Mérida, Yucatán, Mexico, 2010: pp. 287–295. https://hal.science/hal-00904253.

[10] S.O. Ekolu, M.D.A. Thomas, R.D. Hooton, Implications of pre-formed microcracking in relation to the theories of DEF mechanism, Cem Concr Res 37 (2007) 161–165. https://doi.org/10.1016/j.cemconres.2006.10.014.

[11] M. Collepardi, A state-of-the-art review on delayed ettringite attack on concrete, Cem Concr Compos 25 (2003) 401–407. https://doi.org/10.1016/S0958-9465(02)00080-X.

[12] L.F.M. Sanchez, B. Fournier, M. Jolin, J. Duchesne, Reliable quantification of AAR damage through assessment of the Damage Rating Index (DRI), Cem Concr Res 67 (2015) 74–92. https://doi.org/10.1016/j.cemconres.2014.08.002.

[13] A. Zahedi, C. Trottier, L.F.M. Sanchez, M. Noël, Microscopic assessment of ASR-affected concrete under confinement conditions, Cem Concr Res 145 (2021) 106456. https://doi.org/10.1016/j.cemconres.2021.106456.

[14] L.F.M. Sanchez, B. Fournier, D. Mitchell, J. Bastien, Condition assessment of an ASR-affected overpass after nearly 50 years in service, 236 (2020) 117554. https://doi.org/10.1016/j.conbuildmat.2019.117554.

[15] L.F.M. Sanchez, T. Drimalas, B. Fournier, Assessing condition of concrete affected by internal swelling reactions (ISR) through the Damage Rating Index (DRI), Cement 1–2 (2020) 100001. https://doi.org/10.1016/j.cement.2020.100001.

[16] R.-P. Martin, L. Sanchez, B. Fournier, F. Toutlemonde, Evaluation of different techniques for the diagnosis & prognosis of Internal Swelling Reaction (ISR) mechanisms in concrete, Constr Build Mater 156 (2017) 956–964. https://doi.org/10.1016/j.conbuildmat.2017.09.047.

[17] F. Toutlemonde, B. Kchakech, O. Omikrine Metalssi, R.-P. Martin, DEF coupled to thermal history: Recent Advances, in: Concrack 5, JCI-Rilem International Workshop, Tokyo, Japan, 2017: pp. 175–188.

[18] B. Kchakech, R.-P. Martin, O. Omikrine Metalssi, J.-C. Renaud, L. Baron, Effect of temperature and curing duration of early heat treatments on the risk of expansion associated with delayed ettringite formation, in: 15th International Conference on Alkali Aggregate Reaction (ICAAR), São Paulo (Brazil), 2016.

[19] R.-P. Martin, A. Bonnet, J.-C. Renaud, R. Chlela, F. Toutlemonde, C. Sauvaget, Influence of moisture on the development of delayed ettringite formation, Magazine of Concrete Research 75 (2023) 747–754. https://doi.org/10.1680/jmacr.22.00282.

[20] H.F.W. Taylor, Sulfates in Portland clinker and cement, in: S. Karen, J. Skalny (Eds.), International RILEM Workshop on Internal Sulfate Attack and Delayed Ettringite Formation, RILEM, 2002: pp. 3–17.

[21] K.L. Scrivener, J.P. Skalny, Conclusions of the International RILEM TC 186-ISA workshop on Internal Sulfate Attack and Delayed Ettringite Formation (4–6 September 2002, Villars, Switzerland), Materials and Structures/Materiaux et Constructions 38 (2005) 659–663. https://doi.org/10.1617/14111.

[22] G. Escadeillas, J.-E. Aubert, M. Segerer, W. Prince, Some factors affecting delayed ettringite formation in heat-cured mortars, Cem Concr Res 37 (2007) 1445–1452. https://doi.org/10.1016/j.cemconres.2007.07.004.

[23] S. Chatterji, A.D. Jensen, N. Thaulow, P. Christensen, Studies of alkali-silica reaction. Part 3. Mechanisms by which NaCl and Ca(OH)2 affect the reaction, Cem. Concr. Res. 16 (1986) 246–254. https://doi.org/https://doi.org/10.1016/0008-8846(86)90141-9.

[24] L.J. Struble, S. Diamond, Swelling properties of synthetic alkali silica gels, Am. Ceram. Soc. 64 (1981) 652–655. https://doi.org/https://doi.org/10.1111/j.1151-2916.1981.tb15864.x.

[25] A. Leemann, M. Góra, B. Lothenbach, M. Heuberger, Alkali silica reaction in concrete - Revealing the expansion mechanism by surface force measurements, Cem Concr Res 176 (2024) 107392. https://doi.org/10.1016/j.cemconres.2023.107392.

[26] Y. Kawabata, C. Dunant, K. Yamada, K. Scrivener, Impact of temperature on expansive behavior of concrete with a highly reactive andesite due to the alkali–silica reaction, Cem Concr Res 125 (2019) 105888. https://doi.org/10.1016/j.cemconres.2019.105888.

[27] W. Chen, H.J.H. Brouwers, Alkali binding in hydrated Portland cement paste, Cem Concr Res 40 (2010) 716–722. https://doi.org/10.1016/j.cemconres.2009.12.007.

[28] B. Godart, O. Omikrine-Metalssi, B. Kchakech, S. Lavaud, The effects of delayed ettringite formation on the expansion of a massive bridge pier and a precast prestressed concrete beam of a bridge, in: International Conference on Alkali Aggregate Reaction (ICAAR), São Paulo (Brazil), 2016.

[29] M. Jebli, F. Jamin, C. Pelissou, E. Lhopital, M.S. El Youssoufi, Characterization of the expansion due to the delayed ettringite formation at the cement paste-aggregate interface, Constr Build Mater 289 (2021) 122979. https://doi.org/10.1016/j.conbuildmat.2021.122979.

[30] S. Multon, F. Toutlemonde, Effect of moisture conditions and transfers on alkali silica reaction damaged structures, Cem Concr Res 40 (2010) 924–934. https://doi.org/10.1016/j.cemconres.2010.01.011.

[31] Y. Kawabata, R.-P. Martin, J.-F. Seignol, F. Toutlemonde, Modelling of evolution of transfer properties due to expansion of concrete induced by internal swelling reaction, in: H.M. Bernardes, N.P. Hasparyk (Eds.), 15th International Conference on Alkali-Aggregate Reaction in Concrete (ICAAR), São Paulo, Brazil, 2016: pp. 287–295. https://icaarconcrete.org/wp-content/uploads/2020/11/15ICAAR-KawabataY-2.pdf.

[32] R.-P. Martin, F. Toutlemonde, C. Sauvaget, Effects of Alternative Wetting and Drying on the Development of Delayed Ettringite Formation, in: L.F.M. Sanchez, C. Trottier (Eds.), 17th International Conference on Alkali-Aggregate Reaction in Concrete (ICAAR), RILEM Bookseries, Volume 49, Springer, Ottawa, 2024: pp. 176–183. https://doi.org/10.1007/978-3-031-59419-9_21.

[33] L. Divet, R. Randriambololona, Delayed Ettringite Formation: The Effect of Temperature and Basicity on the Interaction of Sulphate and C-S-H Phase 11Communicated by M. Moranville-Regourd., Cem Concr Res 28 (1998) 357–363. https://doi.org/10.1016/S0008-8846(98)00006-4.

[34] P.K. Sarkar, N. Mitra, D. Prasad, Molecular level deformation mechanism of ettringite, Cem Concr Res 124 (2019) 105836. https://doi.org/10.1016/j.cemconres.2019.105836.

[35] L.G. Baquerizo, T. Matschei, K.L. Scrivener, Impact of water activity on the stability of ettringite, Cem Concr Res 79 (2016) 31–44. https://doi.org/10.1016/j.cemconres.2015.07.008.

[36] M. Malbois, B. Nedjar, S. Lavaud, C. Rospars, L. Divet, J.-M. Torrenti, On DEF expansion modelling in concrete structures under variable hydric conditions, Constr Build Mater 207 (2019) 396–402. https://doi.org/10.1016/j.conbuildmat.2019.02.142.

[37] O.D. Olajide, M.R. Nokken, L.F.M. Sanchez, Alkali–Silica Reactions: Literature Review on the Influence of Moisture and Temperature and the Knowledge Gap, Materials 17 (2023) 10. https://doi.org/10.3390/ma17010010.

[38] L.-O. Nilsson, O. Peterson, Alkali-silica reactions in Scania, Sweden: a moisture problem causing pop-outs in concrete floors, Lund, Sweden, 1983. https://portal.research.lu.se/files/4604450/1594285.pdf.

[39] H. Ólafsson, The Effect of Relative Humidity and Temperature on Alkali Expansion of Mortar Bars, in: P.E. Grattan-Bellew (Ed.), Concrete Alkali-Aggregate Reactions: Proceedings of the 7th International Conference, 1986, Ottawa, Canada, Noyes Publications, Ottawa, ON, Canada, 1987: pp. 461–465. https://icaarconcrete.org/wp-content/uploads/2024/04/7ICAAR-OlafssonH-1.pdf.

[40] O.D. Olajide, Multilevel Assessment of The Role of Moisture and Temperature in ASR-Induced Expansion and Deterioration, PhD, Concordia University, 2025.

[41] A. Saccani, V. Bonora, P. Monari, Laboratory short-term evaluation of ASR, Cem Concr Res 31 (2001) 739–742. https://doi.org/10.1016/S0008-8846(01)00477-X.

[42] D. Lenzner, Influence of the Amount of Mixing Water on the Alkali-Silica Reaction, in: Proceedings of the 5th International Conference on Alkali-Aggregate Reaction, Cape Town, South Africa, 1981: pp. 1–6.

[43] S. Multon, J.F. Seignol, F. Toutlemonde, Structural Behavior of Concrete Beams Affected by Alkali-Silica Reaction, ACI Mater J 102 (2005) 67–76. https://doi.org/10.14359/14299.

[44] S. Poyet, A. Sellier, B. Capra, G. Thèvenin-Foray, J.-M. Torrenti, H. Tournier-Cognon, E. Bourdarot, Influence of Water on Alkali-Silica Reaction: Experimental Study and Numerical Simulations, Journal of Materials in Civil Engineering 18 (2006) 588–596. https://doi.org/10.1061/(ASCE)0899-1561(2006)18:4(588).

[45] J. Lindgård, M.D.A. Thomas, E.J. Sellevold, B. Pedersen, Ö. Andiç-Çakır, H. Justnes, T.F. Rønning, Alkali–silica reaction (ASR)—performance testing: Influence of specimen pre-treatment, exposure conditions and prism size on alkali leaching and prism expansion, Cem Concr Res 53 (2013) 68–90. https://doi.org/10.1016/j.cemconres.2013.05.017.

[46] J. Lindgård, E. Rodum, B. Pedersen, Alkali-Silica Reactions in Concrete - Relationship between Water Content and Observed Damage on Structures, in: SP-234: Seventh CANMET/ACI International Conference on Durability of Concrete, American Concrete Institute, 2006. https://doi.org/10.14359/15934.

[47] P. Goltermann, Mechanical Predictions of Concrete Deterioration; Part 2: Classification of Crack Patterns, ACI Mater J 92 (1995) 58–63. https://doi.org/10.14359/1177.

[48] R.J. Detwiler, P.C. Taylor, Specifier's guide to durable concrete: Engineering Bulletin 221, Portland Cement Association, Skokie, IL, USA, 2005.

[49] British Cement Association (BCA), The Diagnosis of Alkali Silica Reaction – Report of a Working Party, England, 1992.

[50] A.B. Poole, I. Sim, Concrete Petrography: A handbook of investigative techniques, 2nd ed., CRC Press, Boca Raton, FL, 2016. https://doi.org/10.1201/b18688.

[51] J.M. Ponce, O.R. Batic, Different manifestations of the alkali-silica reaction in concrete according to the reaction kinetics of the reactive aggregate, Cem Concr Res 36 (2006) 1148–1156. https://doi.org/10.1016/j.cemconres.2005.12.022.

[52] F. Rajabipour, H. Maraghechi, G. Fischer, Investigating the Alkali-Silica Reaction of Recycled Glass Aggregates in Concrete Materials, Journal of Materials in Civil Engineering 22 (2010) 1201–1208. https://doi.org/10.1061/(ASCE)MT.1943-5533.0000126.

[53] L.F.M. Sanchez, B. Fournier, M. Jolin, D. Mitchell, J. Bastien, Overall assessment of Alkali-Aggregate Reaction (AAR) in concretes presenting different strengths and incorporating a wide range of reactive aggregate types and natures, Cem Concr Res 93 (2017) 17–31. https://doi.org/10.1016/j.cemconres.2016.12.001.

[54] D. Siegert, S. Multon, F. Toutlemonde, Resonant frequencies monitoring of alkali aggregate reaction (AAR) damaged concrete beams, Exp Tech 29 (2005) 37–40. https://doi.org/10.1111/j.1747-1567.2005.tb00245.x.

[55] P.A. Dunbar, P.E. Grattan-Bellew, Results of damage rating evaluation of condition of concrete from a number of structures affected by AAR, in: B. Fournier (Ed.), Proceedings of the CANMET/ACI International Workshop on Alkali-Aggregate Reactions in Concrete, CANMET/ACI, Dartmouth (Nova Scotia), 1995: pp. 257–265.

[56] P.E. Grattan-Bellew, A. Danay, Comparison of laboratory and field evaluation of alkali-silica reaction in large dams, in: Proceedings of the International Conference on Concrete Alkali–Aggregate Reactions in Hydroelectric Plants and Dams, Canadian Electrical Association; Canadian National Committee of the International Commission on Large Dams, Fredericton, New Brunswick, Canada , 1992: p. 23.

[57] V. Villeneuve, B. Fournier, J. Duchesne, Determination of the Damage in Concrete Affected by ASR—The Damage Rating Index (DRI), in: T. Drimalas, J. H. Ideker, B. Fournier (Eds.), 14th International Conference on Alkali-Aggregate Reaction (ICAAR), University of Texas at Austin, Austin, Texas, USA, 2012: p. 10. https://icaarconcrete.org/wp-content/uploads/2022/10/14ICAAR-VilleneuveV-1.pdf.

[58] V. Villeneuve, Détermination de l'endommagement du béton par méthode pétrographique quantitative, Master's thesis (Mémoire de maîtrise), Université Laval, 2011. https://www.collectionscanada.gc.ca/obj/thesescanada/vol2/QQLA/TC-QQLA-27962.pdf.

[59] R. Medeiros, L. Sanchez, A.C. dos Santos, Assessing Alkali-Carbonate Reaction-Induced Damage in Critical Concrete Infrastructure: The First ACR-Affected Field Structure Reported in Brazil, in: L.F. Sanchez, C. Trottier (Eds.), Proceedings of the 17th International Conference on Alkali-Aggregate Reaction in Concrete. ICAAR 2024.RILEM Bookseries, Springer, 2024: pp. 445–452. https://doi.org/10.1007/978-3-031-59349-9_51.

[60] L. Sanchez, B. Fournier, M. Jolin, M.A.B. Bedoya, J. Bastien, J. Duchesne, Use of Damage Rating Index to Quantify Alkali-Silica Reaction Damage in Concrete: Fine versus Coarse Aggregate, ACI Mater J 113 (2016) 395–407. https://doi.org/10.14359/51688983.

[61] R.-P. Martin, F. Toutlemonde, Theoretical and experimental validation of a simple method to reproduce representative DEF-prone conditions in laboratory, Mater Struct 46 (2013) 1245–1255. https://doi.org/10.1617/s11527-012-9967-2.

[62] ASTM International, ASTM C1778-22: Standard Guide for Reducing the Risk of Deleterious Alkali-Aggregate Reaction in Concrete, West Conshohocken, PA, 2022. https://doi.org/10.1520/C1778-22.

[63] D.P. Prentice, B. Walkley, S.A. Bernal, M. Bankhead, M. Hayes, J.L. Provis, Thermodynamic modelling of BFS-PC cements under temperature conditions relevant to the geological disposal of nuclear wastes, Cem Concr Res 119 (2019) 21–35. https://doi.org/10.1016/j.cemconres.2019.02.005.

[64] R. Loser, B. Lothenbach, A. Leemann, M. Tuchschmid, Chloride resistance of concrete and its binding capacity – Comparison between experimental results and thermodynamic modeling, Cem Concr Compos 32 (2010) 34–42. https://doi.org/10.1016/j.cemconcomp.2009.08.001.

[65] P.E. Grattan-Bellew, L.D. Mitchell, Quantitative petrographic analysis of concrete –The Damage Rating Index (DRI) method, a review, in: Proc. Marc-André Bérubé Symposium on AAR in Concrete, CANMET/ACI Advances in Concrete Technology Seminar, CANMET/ACI, Montréal, Canada, 2006: pp. 321–334.

[66] L.F.M. Sanchez, T. Drimalas, B. Fournier, D. Mitchell, J. Bastien, Comprehensive damage assessment in concrete affected by different internal swelling reaction (ISR) mechanisms, Cem Concr Res 107 (2018) 284–303. https://doi.org/10.1016/j.cemconres.2018.02.017.

[67] C. Trottier, Advancing the use of the damage rating index (DRI) for evaluation of concrete affected by internal swelling reactions (ISR), PhD, University of Ottawa, 2025.

[68] S. Multon, F. Toutlemonde, Water distribution in concrete beams, Mater Struct 37 (2004) 378–386. https://doi.org/10.1007/BF02479634.

[69] S. Multon, Évaluation expérimentale et théorique des effets mécaniques de l'alcali-réaction sur des structures modèles (Études et recherches des Laboratoires des Ponts et Chaussées, Série Ouvrages d'art, OA 46), Laboratoire Central des Ponts et Chaussées - LCPC., Paris, France, 2004.

[70] P. Morenon, Modélisation des réactions de gonflement interne des bétons avec prise en compte des couplages poro- mécaniques et chimiques, PhD thesis, Université Toulouse III – Paul Sabatier, 2017.

[71] R.-P. Martin, C. Khetib, Étude expérimentale de l'influence de l'hygrométrie du béton sur le risque d'expansions associées à la RSI, Paris, 2024.

[72] L. Graf, Effect of relative humidity on expansion and microstructure of heat- cured mortars, Skokie, Illinois, USA: RD139, 2007.

[73] X. Zhu, Assessing Drying Shrinkage Induced Deterioration of Concrete Stored at Distinct Exposure Conditions, Master of applied science, University of Ottawa, 2024.

[74] B. Fournier, P.-L. Fecteau, V. Villeneuve, S. Tremblay, L. Sanchez, Description of petrographic features of damage in concrete used in the determination of the Damage Rating Index (DRI), Laval, Québec, Canada, 2015.

Chapter 7: Paper II - Impact of moisture gradients on the current condition and future deterioration potential of non-reinforced beams affected by DEF

Rennan Medeiros [1]; Leandro Sanchez [2]; Renaud-Pierre Martin[3]; François Toutlemonde [4]

[1]PhD Candidate – University of Ottawa, Department of Civil Engineering
[2]Full Professor – University of Ottawa, Department of Civil Engineering
[3]Univ Gustave Eiffel, MAST-EMGCU, F-77454 Marne - la- Vallée, France
[4] Univ Gustave Eiffel, MAST-EMGCU, F-77454 Marne - la- Vallée, France

ABSTRACT

Delayed ettringite formation (DEF) induces progressive swelling and cracking in concrete, strongly influenced by moisture exposure. While DEF behaviour under uniform wetting is well documented, the effect of moisture gradients on current and future conditions remains insufficiently characterized. This study evaluates non-reinforced beams with moderate and severe DEF potential subjected to long-term conditioning under moisture gradients using a multi-level assessment combining the Damage Rating Index (DRI), the Stiffness Damage Test (SDT), residual expansion, and moisture-transfer modelling. Results demonstrate that moderate DEF displayed variable deterioration, with intensified damage in upper and lower regions and relative reduction at mid-depth, whereas severe DEF developed stratified profiles with advanced damage at the bottom and significant residual potential at the top. An integrated diagnosis-to-prognosis framework combined current-induced expansion with Bayesian modelling of residual swelling potential at each depth. Finally, the need to account explicitly for moisture-transfer history when appraising DEF-affected concrete members is emphasised.

Keywords: Delayed ettringite formation (DEF), moisture gradient, DEF-induced damage potential, current deterioration condition, expansion attained, future deterioration potential.

7.1 Introduction

Delayed ettringite formation (DEF) is a complex deterioration mechanism that progressively damages concrete, reducing long-term durability and structural performance [1,2]. The initiation and evolution of DEF-induced deterioration are influenced by several factors, including peak (e.g., > 65 °C) and duration of exposure temperature during early hydration [3,4], sulfate and aluminate

availability [5,6], alkali content [6,7], pre-existing microcracking [8–10], wetting-drying cycles, and internal moisture conditions [11,12]. Among these factors, moisture plays a decisive role. It facilitates ionic transport and dissolution–precipitation reactions while providing the necessary amount of water for the recrystallization of ettringite [6,7,12]. Although DEF behaviour under constant moisture exposure has been extensively studied [8,12–14], much less attention has been given to non-uniform conditions. Moisture gradients, arising from partial immersion or environmental exposure, alter internal transport and recrystallization patterns, leading to heterogeneous induced expansion and damage [1,9,13,15]. These effects complicate the estimation of a representative "overall damage" when conducting a condition assessment of DEF-affected members.

To address this limitation, the present study investigates the influence of moisture gradients on DEF-induced damage in non-reinforced concrete members with distinct potentials (i.e., moderate vs high). A multi-level protocol combining semi-quantitative petrography (i.e., Damage Rating Index - DRI), mechanical testing (i.e., Stiffness Damage Test - SDT), and residual expansion analysis is employed to diagnose and prognose the affected members.

7.2 DEF-induced damage in concrete

7.2.1 DEF mechanism

DEF is a specific type of internal sulfate attack in which ettringite recrystallizes within hardened concrete, leading to induced expansion and damage. Unlike external sulfate attack, DEF does not involve sulfate ingress from the environment; rather, it results from the transformation of sulfate-bearing hydration products that originally formed during early hydration and are later destabilized by thermal exposure. Two conditions are necessary for DEF to develop: (i) exposure of the concrete to elevated temperatures during the early stages of hydration (i.e., > ~65 °C) for a sufficiently long duration (e.g., 24h to 120h) [3] and (ii) sustained moisture availability over time [7,14,16].

Temperature conditions typically experienced by massive and steam-cured structural members can decompose primary ettringite into monosulfate or other intermediate sulfate-bearing compounds, often referred to as "ettringite precursors" [7]. Upon subsequent cooling and under conditions of

sufficient internal moisture, these precursors recrystallize as late ettringite within the hardened concrete, leading to expansion and cracking [7,17,18]. The effect of the thermal history on DEF, encompassing the combined influence of temperature level and exposure duration, can be quantified by an effective thermal energy (ETE) [3]. This quantity is defined as the time integral of the temperature above a critical threshold (generally 65°C) during the heating period. For a given concrete mixture, DEF-induced expansion initially increases with ETE; above a certain pessimum value, experimental results indicate a decrease in expansion [3]. This decrease has been attributed to reduced aluminate availability during the hot phase, as aluminates become stabilized in more stable products such as calcium aluminate–silicate hydrates (C-A-S-H) and hydrogarnets (e.g., katoite), which limits late ettringite recrystallization despite sulfate availability [3].

Moisture availability plays a major role in the recrystallization and progression of DEF-induced expansion. It enables ion transport, supports dissolution–precipitation reactions, providing the chemical environment required for ettringite reformation [19,20]. Moisture gradients, including those arising from drying–wetting exposure or partial immersion, have been experimentally shown to affect the rate and distribution of DEF-induced expansion throughout the affected concrete member [21–24]. Under such conditions, internal moisture gradients may drive localized variations in sulfate, aluminum, and calcium ion availability and saturation state, all of which influence the location and intensity of ettringite recrystallization. Furthermore, the alkali concentration in the pore solution also influences DEF development. High concentrations can suppress ettringite precipitation by stabilizing sulfate in solution; however, prolonged exposure to water can reduce this stabilizing effect through alkali leaching, thereby fostering late ettringite formation [7,25,26].

Two main theories have been proposed to explain the resulting expansion and damage: (a) localized crystallization in the interfacial transition zone (ITZ), where ettringite growth induces stress concentration and cracking at the aggregate–paste interface; and (b) homogeneous swelling of the cement paste, driven by ettringite formation in confined micropores within the outer calcium silicate hydrate (C–S–H), particularly near the boundary with inner C–S–H [7,17,18]. Although both mechanism theories involve crystallization pressure in constrained spaces, their relative contributions to the observed behaviour remain subject to experimental interpretation [6,7].

Microstructural damage caused by DEF has direct implications for the mechanical performance of concrete. A qualitative descriptive model indicates that DEF-induced cracking initiates within the cement paste at the ITZ, often outlining aggregates and propagating into the bulk paste, creating an extensive crack network as expansion progresses (Paper I – Chapter 6). This progressive loss of continuity within the bulk cement paste and at the aggregate–paste interface initially reduces the modulus of elasticity and tensile strength and later affects the compressive strength as cracking advances [27]. The resulting loss of mechanical integrity compromises serviceability and accelerates deterioration under continuous or cyclic environmental exposure [8,12].

7.2.2 Advanced Appraisal of DEF-Induced Current Deterioration (Diagnosis)

DEF leads to progressive deterioration in concrete, characterized by cracking in the cement paste and at the interfacial transition zone (ITZ). These cracks reduce stiffness, tensile and compressive strength, and increase permeability [27,28]. At the materials scale, deterioration in concrete due to internal swelling reactions (ISR), including DEF, is characterized by (i) stiffness reduction, (ii) loss of mechanical properties, and (iii) compromised durability, all related to the extent and distribution of cracking [27,29].

Diagnosis of DEF requires methods that identify the mechanism leading to damage (i.e., cause) and quantify the severity of deterioration (i.e., extent) [30,31]. The combined use of the Damage Rating Index (DRI) and the Stiffness Damage Test (SDT) has proven to be efficient in diagnosing ISR-induced damage in concrete via a multi-level protocol that relates microscopic damage features to mechanical properties reduction [27,31].

7.2.2.1 Damage Rating Index (DRI)

The DRI is a semi-quantitative microscopic method developed to assess microstructural deterioration in concrete affected by ISR. Proposed initially by Grattan-Bellew, Dunbar, and Danay [32,33] for assessing alkali–silica reaction (ASR)-affected concrete, the method involves identifying and counting microscopic damage features within a 1 × 1 cm grid on polished concrete sections. Observations are conducted using a stereomicroscope at 15–16× magnification under white-light.

Each feature count is multiplied by a weighting factor that reflects its relative contribution to damage progression, as defined in the revised protocol by Villeneuve and Fournier [34,35]. The weighted counts are then summed and normalized to a reference area of 100 cm², enabling comparisons between specimens of different sizes (Figure 7.1) [36].

Typical damage features include closed cracks in aggregate particles (CCA), open cracks in aggregate particles without (OCA) and with reaction products (OCA-RP), cracks in the cement paste without (CCP) and with reaction products (CCP-RP), disaggregated aggregate particles (DAP), and aggregate particles debonding (Debon). Among these, CCA, often linked to natural flaws or pre-existing conditions, receives the lowest weighting (0.25). OCA and OCA-RP are commonly associated with ASR and weighted at 2, while CCP and CCP-RP, associated with advanced ASR deterioration and DEF, are weighted at 3. DAP and Debon are assigned weights of 2 and 3, respectively (Figure 7.1).

Sanchez et al. [36,37] proposed the extended version of the DRI to better understand the deterioration and further applied the method to assess concrete affected by other ISR mechanisms, including DEF. The technique was also applied to relate microscopic features to changes in mechanical performance. The DRI quantifies the distribution and severity of deterioration features in aggregate particles, cement paste, and interfacial transition zones.

a)

Features of deterioration		Weighing factor
Aggregate	Closed crack (CCA)	0.25
	Opened crack (OCA)	2
	Opened crack with reaction product (OCA_RP)	2
Cement paste	Crack in the cement paste (CCP)	3
	Crack in the cement with reaction product (CCP_RP)	3
Disaggregate/corroded aggregate particle (DAP)		2
Coarse aggregate debonded (Debon)		3
$\boldsymbol{DRI_{number}} = \left[\frac{\sum_{i=1}^{i=n} 0.25(CCA)+2(OCA+OCA_{RP}+DAP)+3(CCP+CCP_{RP}+Debon)}{n\ of\ analyzed\ \ 1\ cm\ by\ 1\ cm\ squares}\right] \times 100\ cm^2$		

b)

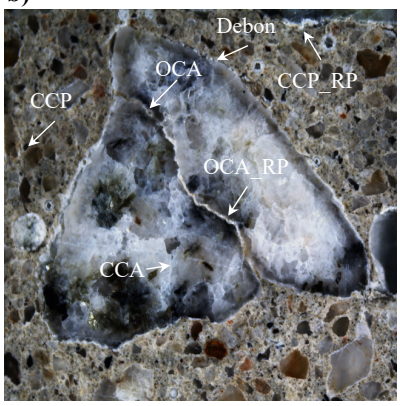


Figure 7.1 – Damage Rating Index method. a) Damage features classified in DRI analysis [34]. b) Micrograph section (1x1 cm) illustrating most of the damage features [38].

7.2.2.2 Stiffness Damage test (SDT)

The SDT is a cyclic mechanical test developed to quantify internal damage in concrete by analyzing its stress-strain response under controlled loading conditions. Walsh [39] originally proposed the method for characterizing microcrack development in rocks and was later adapted by Crouch [40] and Crisp et al. [41,42] for assessing ASR-affected concrete.

The SDT protocol involves subjecting core or laboratory-made concrete specimens to five cycles of uniaxial loading-unloading, reaching a maximum stress corresponding to 40% of the design compressive strength or of the soundest location in the structure under assessment. Sanchez et al. [43–45] demonstrated that adopting this normalized stress threshold enhances the reproducibility of SDT outcomes across concrete mixtures with different compressive strengths. However, severely damaged concrete may not withstand the most diagnostic load (i.e., 40%); thus, the test can be conducted under 30% of the corresponding compressive strength in this case [29].

Four parameters are obtained from the stress–strain curves: the stiffness damage index (SDI), the plastic deformation index (PDI), the modulus of elasticity (E_{SDT}), and the non-linearity index (NLI) (Figure 7.2). The SDI quantifies the energy dissipated ($\sum_{i=1}^{5} SI_i$) relative to the total applied energy over the five cycles ($\sum_{i=1}^{5} SI_i + SII_i$). The PDI represents the ratio of plastic deformation (DI) to the total deformation (DII). The NLI is calculated as the ratio of secant moduli determined at different stages of the first loading cycle (i.e., $Sec\ 1$ is obtained at half of the maximum load, $Sec\ 2$ at the maximum load), providing information on crack orientation (i.e., NLI >1 denotes cracks perpendicular to the load axis, and NLI <1 denotes parallel cracks). The modulus of elasticity (E_{SDT}) is calculated as the average secant modulus from the second and third loading cycles. Although initially validated for ASR-affected concrete, the SDT has been successfully applied to deterioration induced by DEF [27,29,46].

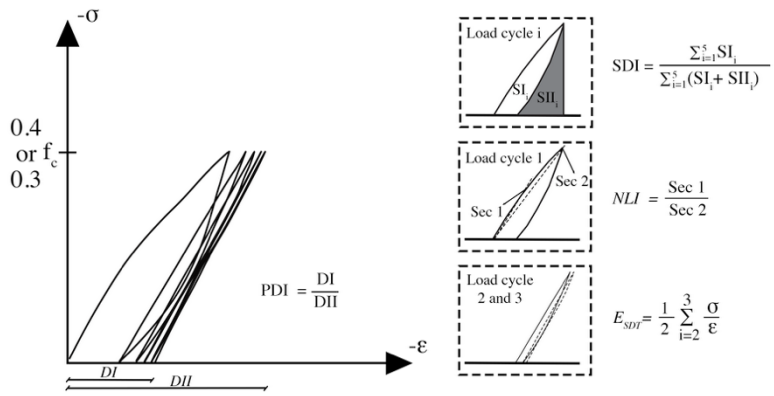


Figure 7.2 – SDT outcomes definition. Stiffness damage index (SDI). Plastic deformation index (PDI). Non-linear index (NLI). Modulus of elasticity (E_{SDT}).

7.2.2.3 Multi-level assessment

The combined use of DRI and SDT results is the cornerstone of a multi-level damage assessment protocol. Building on this approach, Sanchez et al. [27] developed a benchmark database encompassing microscopic and mechanical indicators for evaluating the current condition of ISR-affected concrete. Table 7.1 illustrates established correlations between induced expansion (in free conditions), stiffness loss, reductions in compressive and tensile strength, and microscopic features (i.e., DRI values), providing a robust framework for assessing the condition of ISR-affected concrete and supporting more informed decisions on maintenance and rehabilitation.

In practice, the damage degree is estimated by positioning the measured DRI, Stiffness Damage Index (SDI), and strength- and stiffness-loss values within the diagnostic intervals of Table 7.1, and the associated reference induced expansion level is then inferred from the corresponding benchmark range [27]. Values outside the tabulated domains require interpretation anchored to the underlying dataset for DEF and DEF+ASR [27]. When applied to existing structures, the interpretation must further account for restraint of expansion, stress release during coring, and differences in in situ moisture and thermal histories relative to the free-expansion laboratory basis of the benchmark [27,47–49].

Table 7.1 – Benchmark table of ISR-induced development on affected concrete [27]

Distress Mechanism	Classification of damage degree	Reference level of expansion (%) [a]	Damage results				
			Stiffness loss (%)	Compressive strength loss (%)	Tensile strength loss (%)	SDI	DRI
DEF and DEF + ASR	Negligible	0.00–0.03	–	–	–	0.11	110–147
	Marginal	0.04 ± 0.01	–	–	–	–	–
	Moderate	0.11 ± 0.01	35–56	9–34	–	0.17–0.20	355–599
	High	0.20 ± 0.01	–	–	–	–	–
	Very high	0.30 to 0.50 ± 0.01	55–62	29–43	–	0.19–0.28	623–710
	Ultra-high	0.50 to 1.00 ± 0.01	56–77	40–47	–	0.27–0.43	828–1022
	–	≥1.00 ± 0.01	60–86	40–50	–	0.30–0.54	841–1363

[a] These levels of expansion should not be considered as strict limits among the various damage degrees, but rather indicators/reference levels.

7.2.3 Assessing the potential for future DEF-induced expansion (Prognosis)

DEF is a progressive damage mechanism that usually continues evolving after damage becomes detectable, as long as sulfate- and aluminate-bearing phases remain under sufficient moisture [18,29]. Prognosis aims to estimate the potential for further DEF-induced expansion and deterioration, which is assessed through experimental testing and numerical analysis [15,18,24,50].

7.2.3.1 Laboratory testing – Residual expansion (RE)

Two main types of protocols have been developed for DEF residual expansion tests. In one French method, cores are immersed in water at 20 ± 2 °C. Length measurements begin after 24 h of conditioning to homogenize moisture and temperature and continue at the same temperature until expansion stabilizes, revealing the residual swelling potential due to DEF [15,50]. In one North American method, cores are stored in lime-saturated water at 23 °C, which preserves the chemical stability of calcium and sulfate while promoting alkali leaching. This condition favors DEF-related expansion, particularly when ASR-reactive aggregates are present [51–53].

Residual expansion tests provide a practical means of quantifying the remaining swelling potential of DEF-affected concrete, but the measured expansions reflect several concurrent processes that must be considered during interpretation. These include differences between the stress state of the cored specimens and that of the structural concrete, initial hygric swelling during re-saturation of partially desaturated cores, possible leaching of alkalis and sulfates into the immersion water, and variability in pre-existing damage and swelling history between cores and sampling locations [15,50,54].

7.2.3.2 Analyzing residual expansion outcomes

The interpretation of residual expansion outcomes generally relies on semi-empirical parametric models that describe the time-dependent swelling process of concrete affected by ISR, including DEF.

Larive [55] introduced a three-parameter sigmoidal law (Equation 7.1) that captures the initiation, acceleration, and stabilization of expansion to describe ASR-induced full expansion; the proposed approach was later extended to DEF [18,56,57].

$$\varepsilon(t) = \varepsilon_{\infty} \cdot \frac{1 - e^{-\frac{t}{\tau_C}}}{1 + e^{-\frac{t-\tau_L}{\tau_C}}} \tag{7.1}$$

Where $\varepsilon(t)$ is the expansion at time (t), ε_{∞} is the ultimate expansion at long times under the imposed conditions, τ_L is the latency time associated with the dormant period and equal to the inflection time, and τ_C is the characteristic time governing the expansion rate during the main expansion phase.

Residual expansion reconstruction interprets post-coring induced expansion as the continuation of a free-expansion curve calibrated under favourable moisture conditions [58,59]. Equation 7.1 is first calibrated on laboratory specimens stored at high relative humidity, defining a reference curve that represents the mixture's swelling potential under near-saturated conditions. Cores extracted from an affected member are then tested in residual expansion, and the measured post-coring induced expansion is assumed as a segment of the same reference curve starting from a non-zero expansion state at the time of coring. The expansion history can be reconstructed by aligning post-coring-induced expansion results with the calibrated reference curve when the latter is available [58].

This approach was first implemented for alkali–silica reaction (ASR) and later extended to delayed ettringite formation (DEF) and combined DEF+ASR by introducing time and expansion offsets, jointly fitted with the free-expansion parameters, to align residual-expansion curves with the free-swelling reference [18,58]. The reconstruction relies on four assumptions: (i) the affected material follows a parametric free-expansion law (Equation 7.1) calibrated on laboratory free-swelling specimens under well-defined high-humidity conditions; (ii) residual expansion of cores represents the continuation of that law from an advanced reaction state; (iii) the combined pre-coring and

residual expansion converges toward a common ultimate swelling potential under favourable moisture; and (iv) restraint effects at the core scale remain negligible or secondary.

Although important advances have been made in diagnostic and prognostic tools, the extent to which moisture gradients shape the development and progression of DEF-induced deterioration, having distinct potentials (i.e., moderate vs high) in affected structural members, remains insufficiently characterized and requires further investigation.

7.3 Scope of the work

To investigate the effect of moisture gradients on the development and distribution of DEF-induced deterioration, an experimental program was conducted on two non-reinforced concrete beams manufactured with concrete mixtures of different potential for DEF-induced expansion. Both beams were subjected to long-term conditioning designed to promote DEF while establishing a vertical gradient in internal moisture. Throughout conditioning, the lateral faces were sealed to restrict transverse water movement. During the first 14 months, the bottom surface was immersed to a depth of 7 cm, while the top surface was maintained at 30% relative humidity. During the subsequent 14 months, water was also applied to the top surface to assess the effect of delayed water supply. After 28 months, the beams were stored under ambient laboratory conditions (22 ± 4 °C; 50–70% relative humidity) for an extended period (see Chapter 4). Cylindrical cores were extracted from multiple heights, as well as cross-sectional slices. These samples were evaluated using a multi-level diagnostic and prognostic protocol that included microscopic analysis through the Damage Rating Index (DRI), mechanical testing through the Stiffness Damage Test (SDT), and residual expansion measurements.

The objective of the study is to assess the influence of moisture gradients on the local DEF-induced deterioration, associated mechanical degradation, and residual expansion potential in structural members. Comparisons were drawn between locations with moderate and severe deterioration to evaluate the role of moisture exposure. Results were interpreted in conjunction with semi-empirical modeling of water transfer and cement chemistry to provide a broader understanding of moderate and severe DEF development under non-uniform moisture exposure. Moreover, the joint interpretation of SDT, DRI, and residual expansion is examined.

7.4 Materials and Methods

7.4.1 Description of the specimens

Two non-reinforced concrete beams were fabricated at the former *Laboratoire Central des Ponts et Chaussées* (LCPC), now the *Laboratoire Expérimentation et Modélisation pour le Génie Civil et Urbain* (EMGCU) at *Université Gustave Eiffel* in Paris, France, as part of the program reported by Martin [18]. Each beam measured 0.25 m × 0.50 m × 3.00 m with a supported span of 2.8 m (Figure 7.3a) and was cast with mixtures proportioned to develop, respectively, moderate and severe delayed ettringite formation (DEF) [18]. The concrete mixtures targeted a 28-day average compressive strength of approximately 40 MPa with a water-to-cement ratio of 0.46; the measured 28-day compressive strengths were 39.3 MPa (moderate DEF mix) and 38.7 MPa (severe DEF mix), with corresponding 28-day elastic moduli of 32.8 GPa and 30.8 GPa, respectively. To replicate conditions that lead to massive-element cast-in-place curing and trigger DEF, the beams were placed 2 hours after casting into a temperature-controlled water bath with a specific thermal cycle: an initial heating matching the mix's adiabatic temperature rise, a steady plateau at 81°C for 72 hours, and an controlled cooling at about 1°C per hour over roughly 6 days [18,60]. Afterwards, a vertical moisture gradient was created in two stages: for the first 14 months, the bottom 7 cm was partially immersed while the top surface stayed at 30% RH; then, for the next 14 months, water was also applied to the top to assess the impact of late water supply. During these phases, the beams were kept at 38 ± 1°C and 30% RH, with lateral faces sealed with aluminum foil to prevent transverse water exchange (Figure 7.3b). Outside these phases, they were maintained at 22 ± 4°C and 50–70% RH under lab conditions. The moderate-DEF beam underwent both phases and was then tested with a 4-point bending test to measure residual load capacity, while the severe-DEF beam failed early (i.e., 330 days) during phase (a) due to self-weight and deterioration [18]; additional details are given in Section 7.6. This exposure setup may have promoted leaching, potentially altering the initial alkali content of the mixtures. However, the effect was considered negligible and assumed to be comparable for both beams.

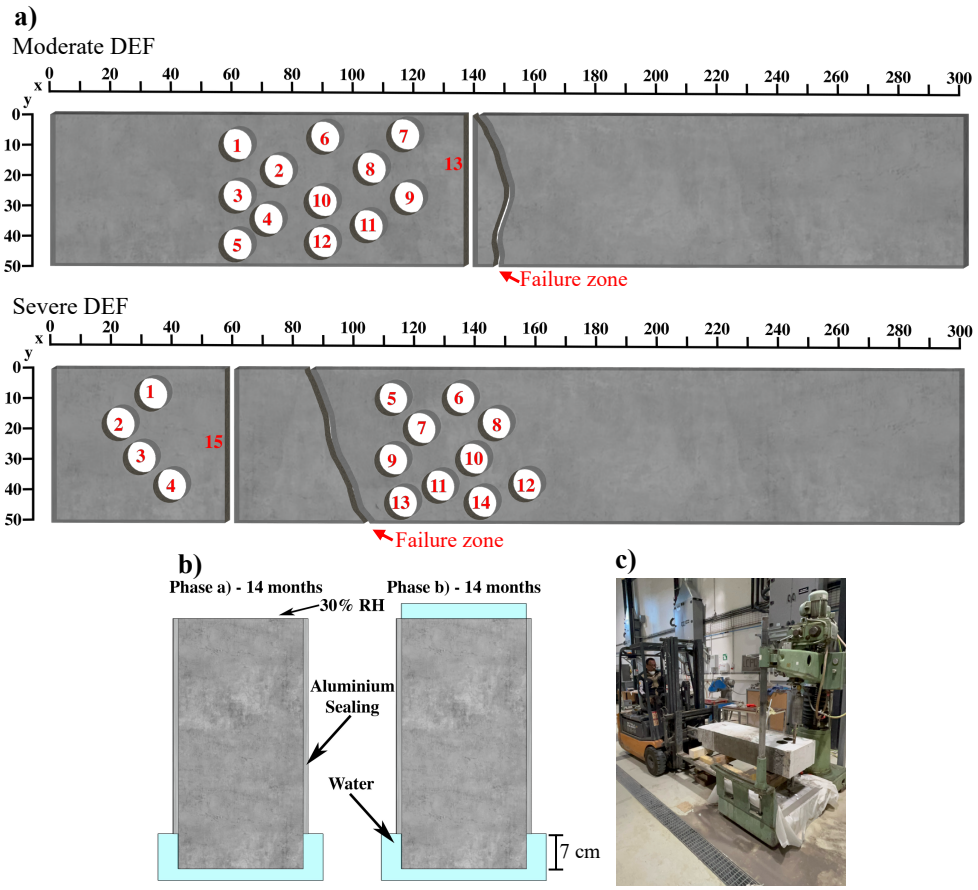


Figure 7.3 – Schematic illustration of a) the dimensions of the beams (cm), and the locations where the slices and cylindrical cores were extracted. b) the water exposure setup. c) Coring process.

To achieve distinct levels of DEF-induced development, two cements with different sulfate and aluminate content were used, and the alkali content was increased in the concrete mixture. The moderate DEF-affected member was manufactured with a cement bearing 2.35% C_3A, 2.61% SO_3, and 0.44% Na_2O_{eq}. In contrast, the severe DEF-affected member was manufactured with a cement containing 4.97% C_3A, 3.46% SO_3, and 0.83% Na2Oeq. Additionally, the alkali content in the severe DEF mix was increased to 1.1% Na_2O_{eq} by adding 1.745 kg of KOH per cubic meter, to enhance primary ettringite decomposition.

To support the interpretation of the contrasted DEF-induced swelling capacities of the two cements, hydrate phase assemblages were simulated using the Gibbs Energy Minimization Software (GEMS), which determines equilibrium phases in a closed system from the imposed

temperature, pressure, and bulk chemical composition [61]. Oxide compositions and clinker phase proportions were taken from Martin [18] and used as model inputs. The computed evolution of hydrate masses for Cements A and B is reported in Figure 7.4 for a 1000-day period at 38 °C, assuming 100 g of cement and a water-to-cement ratio of 0.46. In both systems, hydration proceeded rapidly, with most clinker phases largely depleted within the first day. The severe DEF binder (Cement B) yielded a higher ettringite mass than Cement A (18.43 g versus 14.06 g), in agreement with its greater sulfate availability. At the imposed temperature, the calculations also indicate reduced stability of monosulfate and monocarbonate compared with ambient conditions, favouring the formation of siliceous hydrogarnet, especially for temperatures exceeding 50 °C [62]. In addition, the low C_3A contents of the binders (approximately 2% to 5%) constrain the formation of carbonate-bearing aluminate hydrates, consistent with the simulated shift in hydrate assemblage (about 3% to 8%) [61]. Overall, the simulations indicate that sulfate and aluminate supply, coupled with temperature-controlled phase stability, governs the higher DEF swelling potential associated with Cement B.

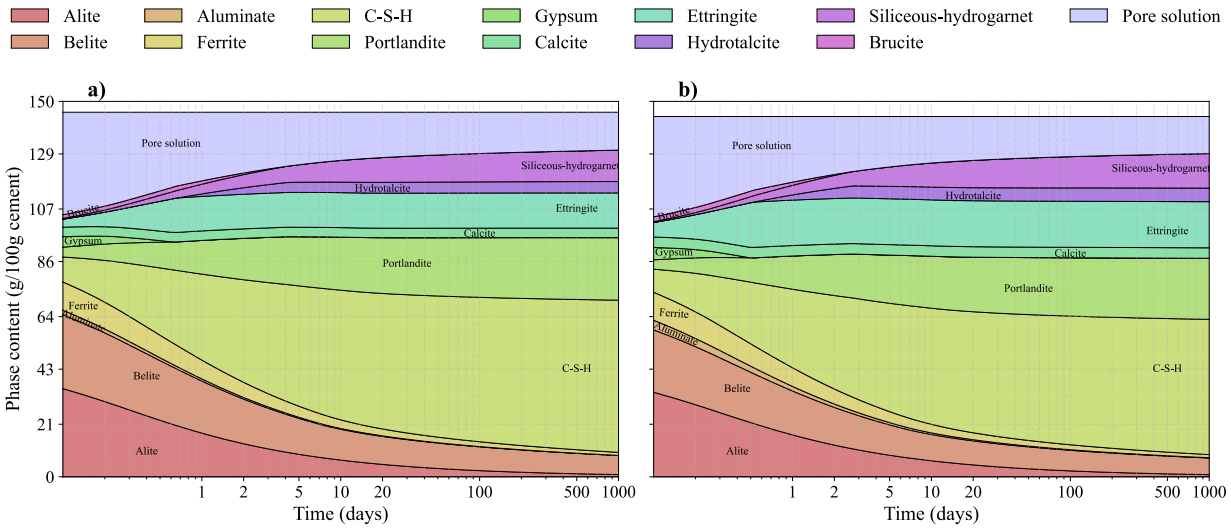


Figure 7.4 – Calculated mass of hydrates in moderate DEF Cement and severe DEF Cement as a function of time.

The two beams were saw-cut perpendicular to the longitudinal direction to obtain slices of the cross-section (Figure 7.3). One slice (i.e., 500 x 250 x 50 mm) from each beam was then prepared for the microscopic analysis. Cylindric cores (i.e., 110 x 250) were extracted from different heights of both beams for SDT and residual expansion testing. An effort was made to avoid zones with

major cracks generated during aging while retrieving the specimens investigated herein. Table 7.2 summarizes the specimens extracted from beams affected by moderate and severe DEF, categorized by depth and testing method.

Table 7.2 – Location and identification of cores and slices extracted from beams affected by moderate and severe DEF, including nominal coring depth, spatial coordinates, and associated testing program (DRI, SDT, and RE)

Beam	Sketch_ID (Figure 7.3a)	Sample_ID	Location of coring			Testing 1			Testing 2
			Nominal location	Coordinate (x) [cm]	Coordinate (y) [cm]	DRI	SDT	RE	RE
Moderate DEF	1	P1_0,08 (2)	0-10cm	60.7	10.2		✓		✓
	2	P1_0,17 (2)	10-20cm	74.2	18.6		✓		✓
	3	P1_0,27 (2)	20-30cm	60.7	27.1		✓		✓
	4	P1_0,37 (2)	30-40cm	70.8	34.7		✓		✓
	5	P1_0,44 (2)	40-50cm	60.7	43.2		✓		✓
	6	P1_0,08 (3)	0-10cm	89.5	7.6			✓	
	7	P1_0,08 (4)	0-10cm	115.8	6.8			✓	
	8	P1_0,17 (3)	10-20cm	104.7	17.8			✓	
	9	P1_0,23 (2)	20-30cm	17.0	27.5			✓	
	10	P1_0,27 (3)	20-30cm	88.6	28.8			✓	
	11	P1_0,34 (1)	30-40cm	103.7	36.8			✓	
	12	P1_0,44 (3)	40-50cm	88.7	42.4			✓	
	13	P1_S1	Cross-section	137.6	-	✓			
Severe DEF	1	P2_0,08 (2)	0-10cm	32.8	7.1			✓	
	2	P2_0,17 (2)	10-20cm	22.0	18.0			✓	
	3	P2_0,27 (2)	20-30cm	29.0	29.0			✓	
	4	P2_0,37 (2)	30-40cm	39.0	38.0			✓	
	5	P2_0.08_1	0-10cm	116.1	8.0		✓		
	6	P2_0.08_2	0-10cm	135.0	7.9		✓		
	7	P2_0.17_1	10-20cm	121.0	17.8		✓		
	8	P2_0.17_2	10-20cm	148.0	18.0		✓		
	9	P2_0.27_1	20-30cm	116.2	27.2		✓		
	10	P2_0.27_2	20-30cm	139.0	27.1		✓		
	11	P2_0.37_1	30-40cm	128.0	37.3		✓		
	12	P2_0.37_2	30-40cm	157.0	37.4		✓		
	13	P2_0.44_1	40-50cm	117.1	44.3		✓		
	14	P2_0.44_2	40-50cm	141.0	44.1		✓		
	15	P2_S1	Cross-section	59.7	-	✓			

Obs.: The specimens from the beam affected by severe DEF tested for SDT were extracted and tested in 2015. Testing method 2 was applied after testing method 1 for a given core, considering the non-destructive aspect of the SDT [43–45].

7.4.2 Experimental procedures

7.4.2.1 Damage rating index (DRI)

The DRI was performed on slices of the cross-section of the beams. After cutting (Figure 7.3), the slices were polished using a handheld polishing device with diamond-impregnated pads applied in a sequential grit order: no. 50 (coarse), 100, 400, 800, 1500, and 3000 (very fine) [36]. DRI analysis was conducted on polished specimens with a surface area of 1,250 cm². The DRI number was computed by summing the total counts of each deterioration feature, multiplying these counts by their respective weighting factors (Figure 7.1), and normalizing the results to 100 squares.

7.4.2.2 Stiffness damage test (SDT)

Specimens extracted from different depths of the beams (Table 2) were submitted to the stiffness damage test (SDT) protocol proposed by Sanchez et al. [45]. The cross-sections of the specimens were finished using an automatic grinding machine to ensure uniformity. Then, the specimens were conditioned in a moist curing room at 20 ± 2°C for 48 hours to restore moisture conditions, yielding more consistent results [45]. The SDT protocol establishes that the maximum load must be 40% of the reference compressive strength applied at a rate of 0.10 MPa/s over five loading-unloading cycles; however, considering the advanced deterioration, the maximum load was adjusted to 30% of the reference compressive strength (i.e., 40 MPa). This adapted approach has been validated by Martin et al. [29]. The analysis of the test focuses on the parameters: stiffness damage index (SDI), plastic deformation index (PDI), and modulus of elasticity (E).

7.4.2.3 Residual expansion (RE)

RE testing was performed on cylindrical concrete cores with nominal dimensions of 110 mm in diameter and 250 mm in height, following the experimental protocol previously described by Martin et al. [29]. Stainless-steel measurement pins were installed along the vertical axis of each specimen at 120° intervals, allowing longitudinal expansion to be monitored with a digital extensometer having a gauge length of 100 mm. After drilling and pin installation, all specimens were immersed in water at 38°C for 24 hours to restore moisture conditions and reach temperature equilibrium before zero reading. Length readings were then taken to establish a zero-measurement

reference. This procedure reduces the influence of hygric swelling on the measured expansion, thereby improving the appraisal of swelling primarily caused by DEF. Following the initial measurement, the specimens were stored in water at 38 °C for a prolonged period (approximately 406 days). Axial expansion and mass gain were periodically monitored throughout the test duration. The storage conditions of the samples were determined to represent the beams' storage conditions during the aging phases.

7.5 Results

7.5.1 Damage rating index (DRI)

The results of the microscopic assessment of DEF-affected beams presented in this section are organized into five depths (i.e., 0-10, 11-20, 21-30, 31-40, and 41-50 cm) of the beams, with the upper part considered as zero and the bottom as 50 cm (Figure 7.3a). The analyzed surface (i.e., slice of 1,250 cm²) was then divided into five areas (i.e., 250 cm² each) across the depth of interest, considering that 200 cm² is recommended as representative for DRI analysis, as per [36,63]. Figure 7.5 presents the DRI number as a function of depth for beams affected by a) moderate and b) severe DEF.

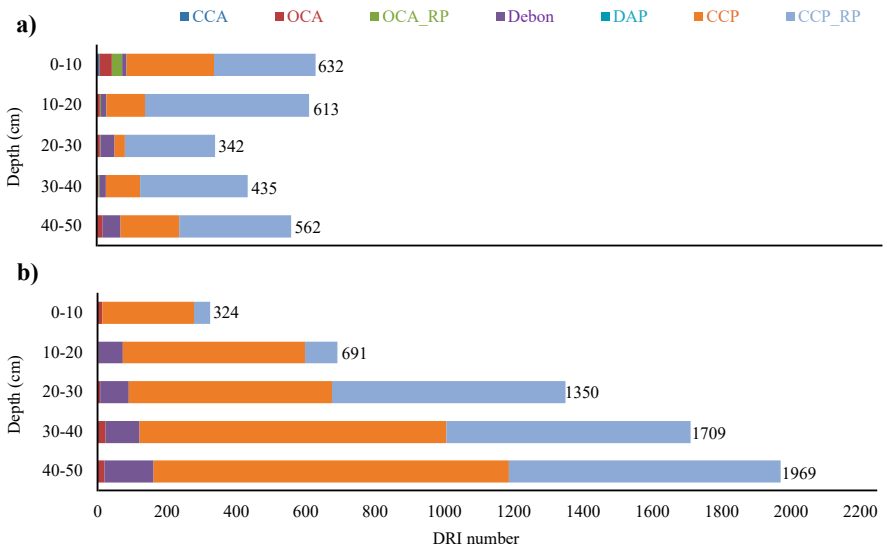


Figure 7.5 – DRI number as a function of the depths. a) Moderate DEF- and b) Severe DEF-affected beam.

In moderate DEF-affected concrete, the DRI number varied non-progressively: the highest value was recorded in the uppermost location (i.e., 0–10 cm, DRI number 632), followed by a reduction toward mid-depth (i.e., DRI number 342 at 20–30 cm), and a subsequent increase at the bottom levels, reaching 562 at 40–50 cm. In contrast, severe DEF-affected concrete exhibited a progressive increase in DRI number depth-wise. The lower DRI number (i.e., 324) was observed at depths of 0–10 cm; the values rose steadily to a maximum of 1969 at a depth of 40–50 cm, giving an amplitude of 1645. When averaged over the full cross-section, the DRI number reached 517 for moderate DEF (standard deviation 118; range 342–632) and 1209 for severe DEF (standard deviation 719; range 324–1969). This variation indicates the pronounced heterogeneity of damage throughout the height of the affected members.

7.5.2 Stiffness damage test

Figure 7.6 presents the results of the SDT, including the Stiffness Damage Index (SDI), Plastic Deformation Index (PDI), and modulus of elasticity (E) as a function of depth for beams affected by moderate and severe DEF. The bars represent the average values, while the error bars represent the maximum and minimum values obtained from the available samples, as described in Table 7.2. In the moderate DEF-affected beam, SDI and PDI values remained relatively low and consistent along the height of the beam, ranging from 0.17 to 0.23 and 0.12 to 0.18, respectively. The modulus of elasticity varied slightly with depth, reaching its highest value of 24.7 GPa at 30–40 cm depth and its lowest at 17.7 GPa at 40–50 cm depth. The results of moderate DEF at 0- 10 cm are not reported in Figure 7.6 due to technical issues during the test. In contrast, the severe DEF-affected beam exhibited a pronounced gradient in all SDT parameters. The SDI increased from 0.14 at the top (i.e., 0–10 cm) to 0.57 at the bottom (i.e., 40–50 cm), while PDI rose from 0.10 to 0.35 over the beam depth. The modulus of elasticity decreased steadily depth-wise, from 28.8 GPa at the top to 5.3 GPa at the bottom.

When averaged over the full cross-section, the moderate DEF-affected beam exhibited an SDI of 0.20, a PDI of 0.14, and a modulus of elasticity of 21.4 GPa, whereas the severe DEF-affected beam showed higher average SDI and PDI values of 0.36 and 0.23, respectively, and a lower average modulus of elasticity of 14.0 GPa. These global values provide an overall mechanical degradation but do not fully reflect the pronounced gradients described above.

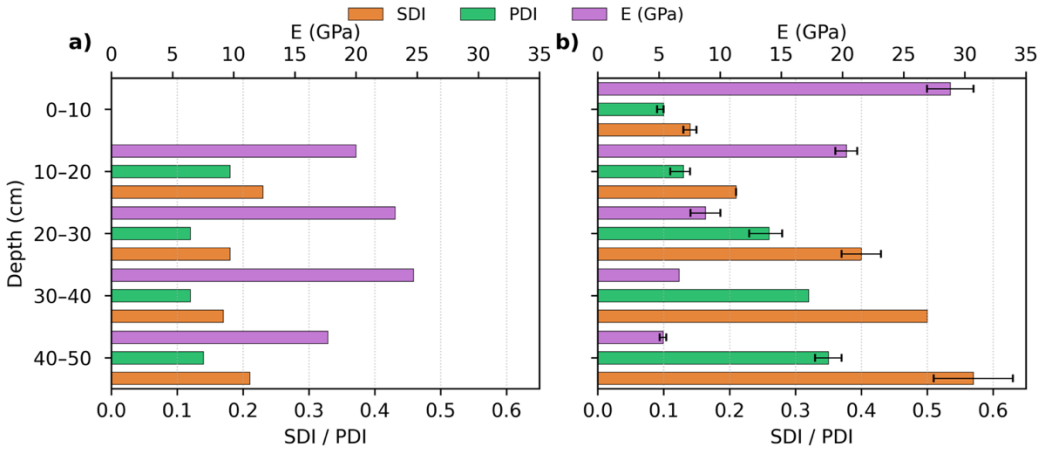


Figure 7.6 – SDT outcomes as a function of the depths. a) Moderate DEF- and b) Severe DEF-affected beam.

7.5.3 Residual expansion (RE)

The results of the residual expansion tests are presented in Figure 7.7, which depicts the remaining expansion potential profiles over time for concrete mixtures affected by moderate and severe DEF as a function of depth. The averages are represented by the markers, while the error bars represent the amplitude (i.e., maximum and minimum). The average maximum expansion measured across the depth was 0.13% for moderate DEF and 0.45% for severe DEF.

In moderate DEF, the maximum expansion reached ranged from 0.15% at 10–20 cm to 0.18% at 20–30 cm. The variation did not follow a consistent pattern of either ascending or descending along the beam depth. In contrast, severe DEF exhibited higher values in the upper location, with the highest expansion observed at 0–10 cm (i.e., 0.61%). At 40–50 cm, residual expansion and mass variation measurements could not be obtained due to extreme deterioration (i.e., DRI number of 1969, SDI of 0.57, and E of 5.3 GPa), which caused cores to break during extraction. Measurements at 10–20 cm depth were discontinued at 83 days to allow further analysis in another stream of the project. It is important to highlight that not all residual expansion curves are considered stabilized; the samples are still under measurement. When averaged over the investigated depths, the maximum residual expansion reached 0.13% for moderate DEF and 0.45% for severe DEF. These global values depict an overall remaining swelling potential but do not fully reflect the pronounced depth-wise differences described above.

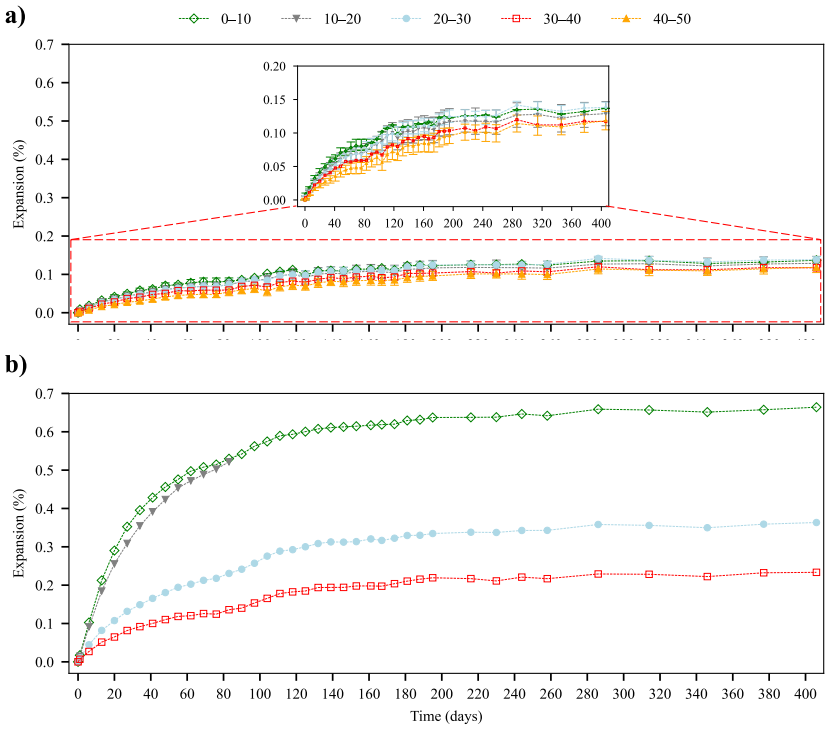


Figure 7.7 – Residual expansion results. a) Moderate DEF- and b) Severe DEF-affected beam.

The results of the mass gain measurements are presented in Figure 7.8, showing the cumulative water-uptake profiles for beams affected by moderate and severe DEF as a function of depth. The average mass gain at 406 days was 0.33% for moderate DEF and 0.83% for severe DEF. In moderate DEF-affected concrete, the values remained relatively uniform along the beam height, ranging from 0.42% at 0–10 cm to 0.28% at 10–20 cm. No clear progressive trend of mass gain with depth was observed. In contrast, severe DEF-affected concrete exhibited significantly higher mass gain in the upper regions, with a maximum value of 1.33% at 0–10 cm and a minimum value of 0.55% at 30-40 cm. When averaged over the cross-section, the mass gain at 406 days was 0.33% for moderate DEF and 0.83% for severe DEF. These average values provide a convenient global indicator of moisture uptake but only partially capture the pronounced gradients observed in Figure 7.8.

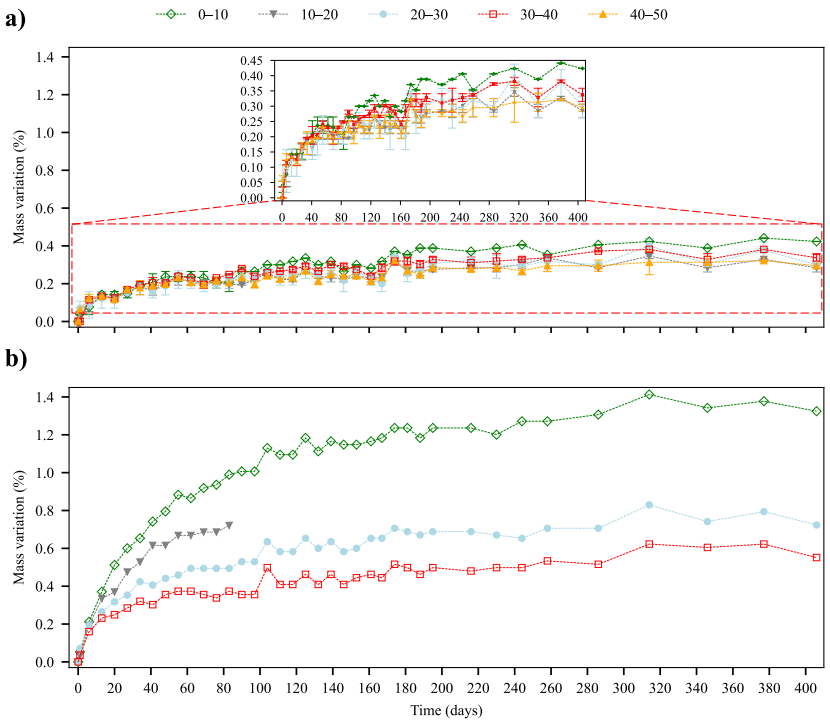


Figure 7.8 – Mass variation during residual expansion testing. a) Moderate DEF- and b) Severe DEF-affected beam.

7.6 Discussion

7.6.1 Understanding the impact of water saturation gradients on DEF-induced deterioration

- Evaluation of the moisture profiles

The condition assessment conducted in this study, integrating microscopic evidence from the DRI (Figure 7.5), mechanical response from SDT outcomes (Figure 7.6), and residual expansion results (Figure 7.7), provided important insights into the deterioration of concrete induced by moderate and severe DEF under distinct moisture gradients.

To further investigate the role of moisture in the observed deterioration pattern, the moisture transfer experienced by the beams was estimated following the framework illustrated in Figure 7.9. This reconstruction accounted for beam weighing combined with automated γ-densimetry and companion cylinders subjected to identical thermal and hydric histories, supplying material parameters, such as saturation thresholds and free-expansion kinetics, obtained by Martin [18]. The moisture transfer within the beams is described by three governing fronts that control water

availability and swelling kinetics: a) a top-drying front, b) a bottom imbibition front, and c) once the top is wetted, a top-rewetting front. During "phase a", drying from the top and imbibition from the bottom act concurrently (Equation 7.2); during "phase b", bottom imbibition continues while the prior dry cap is overtaken by a top-rewetting front (Equation 7.7). The global mass variation is obtained as the sum of the active front contributions, with t_b marking the start of "phase b"; mass gains are positive, drying is negative, and imbibition is cumulative from $t = 0$ throughout both phases.

The drying front is defined as the depth where the local relative mass loss reaches the iso-loss (Equation 7.3) corresponding to a reduction in saturation from the post-curing saturation S_0 to an expansion-onset threshold S_{onset} (Equation 7.5), linking relative mass loss to the saturation drop through the material balance, where p is the open porosity, $\rho_{concrete}$ is the concrete bulk density, and $\beta = \frac{\rho_{\text{water}} \cdot p}{\rho_{\text{concrete}}}$. The depth-dependent drying kinetics during "phase a" is obtained via Equation 7.4, with $A(z)$ and $\tau(z)$ identified by fitting the γ-densimetry measurements from the top of the moderate DEF beam, and this calibrated profile is applied to both beams, given their comparable mixture and transport properties and the lack of reliable γ-densimetry measurements for the severe DEF-affected beam. To respect γ-densimetry instrument repeatability ($\pm 0.18\%$), a 0.20% floor is imposed when the computed iso-loss is smaller, which leads to 0.20% for the moderate and severe DEF beams. At any time $t, h_{\text{dry}}(t)$ is taken as the first depth where $\Delta m/m(z,t)$ equals the iso-loss, using linear interpolation between instrumented depths, providing a physically based evolution of the advancing dry cap during Phase a that is consistent with Martin's [18] observations.

The ascent of the capillary imbibition front follows a square-root-in-time law with the absorption coefficient D (Equation 7.6), giving the imbibition rise $h_{\text{imb}}(t) = 0.07 + \zeta(t)$, A_{imm} cross-section, and ρ_{concrete} concrete bulk density. The contribution of DEF kinetics to the observed water uptake is accounted for by a modified relative mass-variation function with sigmoidal kinetics, obtained from the companion cylinders studied in [18]. The drying contribution to the global mass variation is obtained by integrating the γ-densimetry-based local mass change over the drying zone (Equation 7.6). The coefficient D_{imb} is identified by minimizing the misfit between modeled and measured masses [18].

The rewetting front accounts for the rapid mass gain at the start of "phase b" and the subsequent diffusion-controlled advance while bottom imbibition continues; the drying front is taken as fixed at the transition time t_b because the top dry cap ceases to evolve once the top surface is wetted. The global mass variation in "phase b" is represented as the sum of three contributions (Equation 7.8): an instantaneous rewetting term that captures the immediate capillary surge parameterized by H_{inst} and a diffusion-controlled rewetting term governed by the coefficient D_{rwt} and the time constant τ. These parameters are estimated by minimizing the misfit between modeled and measured beam masses, while the continuous imbibition term D_{imb} that persists from the bottom was determined in "phase a" analysis.

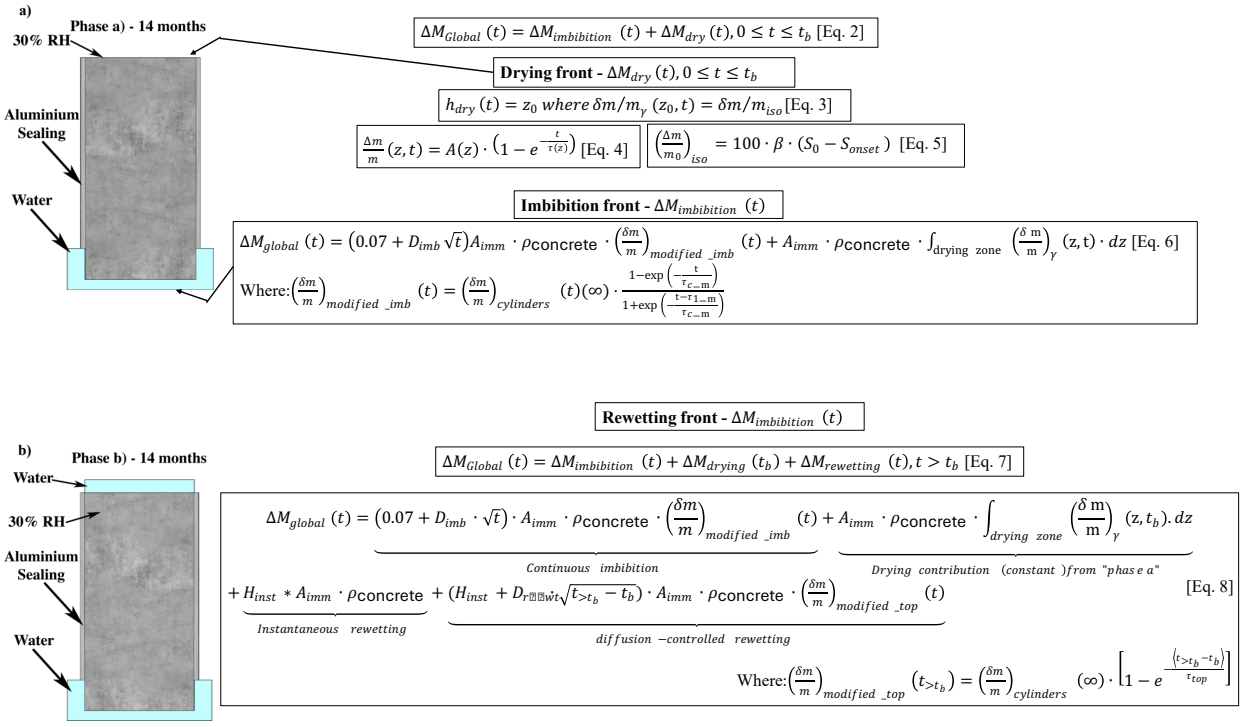


Figure 7.9 – Estimating moisture-transfer behaviour. a) Phase a, b) Phase b.

Where t_b is the start of "phase b" (427 days), H_{inst} represents the thickness that gets back to initial saturation

S_0 when water is added to the top, D_{imb} is the diffusion imbibition coefficient determined in "phase a", $\left(\frac{\delta m}{m}\right)_{modified\_top}$ is the asymptotic mass variation obtained in the material characterization in [18], and τ_{top} top time constant. The H_{inst}, D_{rwt}, and τ_{top} were determined by minimizing the difference between the modeled global mass variation and the measured weighing data. This formulation

provides a consistent description of how the capillary front progresses and how the corresponding mass gain contributes to the overall moisture balance of the structure. The absolute position of the rewetting front from the top surface is then expressed as $h_{rwt} = H_{inst} + D_{rwt} \cdot \sqrt{t_{>t_b} - t_b}$.

Table 7.3 presents the Parameters used to estimate the water-transfer behaviour, and Figure 7.10 illustrates the global mass variation of moderate DEF and severe DEF-affected concrete beams.

Table 7.3 – Parameters used to estimate the water-transfer behaviour of moderate DEF and severe DEF-affected concrete beams.

		Moderate DEF	Severe DEF
Drying	$\rho_{concrete}$(kg/m³) [18]	2328	2320
	p (%) [18]	14.6	14.6
	S_0 [18]	0.92	0.93
	β	2328	0.06293
	ΔS	-0.020	-0.030
	Iso-loss (raw) %	-0.125	-0.189
	Iso-loss used %	-0.200	-0.200
Imbibition	$(\delta m/m)\ \infty$	0.0085	0.0241
	$\tau_{c\,m}\ (days)$ [18]	150	50
	$\tau_{l\,m}\ (days)$ [18]	170	290
	$D_{imb}\ (m \cdot \sqrt{t})$ [18]	4.95×10^{-3}	2.12×10^{-2}
	RMSE (kg)	0.6322	0.1588
Rewetting	H_{inst} (m)	9.65×10^{-4}	-
	$D_{rwt}(m \cdot \sqrt{t})$	1.83×10^{-2}	-
	τ_{top} (days)	0.2	-
	RMSE (kg)	0.5278	-

RMSE - Root Mean Square Error.

Figure 7.10 illustrates the moisture transfer behaviour estimated for the moderate DEF- and severe DEF-affected beams. In Figure 10a, the beam with moderate DEF presents limited, gradual water ingress through the cross-section. The drying zone at the top advances slowly and levels off near 9 cm below the upper surface by approximately 427 days, which indicates small moisture loss and low permeability at the top boundary. The imbibition front rises modestly from the base, reaching about 8.6 cm at 10 days, 10.5 cm at 50 days, and 17.2 cm at 427 days. When “phase b” begins and water is supplied at the top surface, the pre-existing dry cap is progressively replaced by a descending rewetting front that moves from 6.7 cm at 427 days to 15.5 cm at 440 days, and moisture conditions approach uniformity by about 700 days as this rewetting front meets the slowly advancing imbibition front. Over the same interval, the imbibition front continues its gradual rise from 17.2 cm at 427 days to 20.1 cm at 700 days, culminating in the convergence of the two fronts and a slow recovery of saturation throughout the member during “phase b”.

In Figure 7.10b, the severe DEF beam exhibits a steeper, faster rise in the imbibition front. Within 50 days, the imbibition height exceeds 22.0 cm, and by 322 days, the front approaches the upper face near 45 cm. This steep, rapid progression is consistent with a more permeable internal state associated with a higher swelling potential, producing a near-linear imbibition gradient that persists over the exposure period.

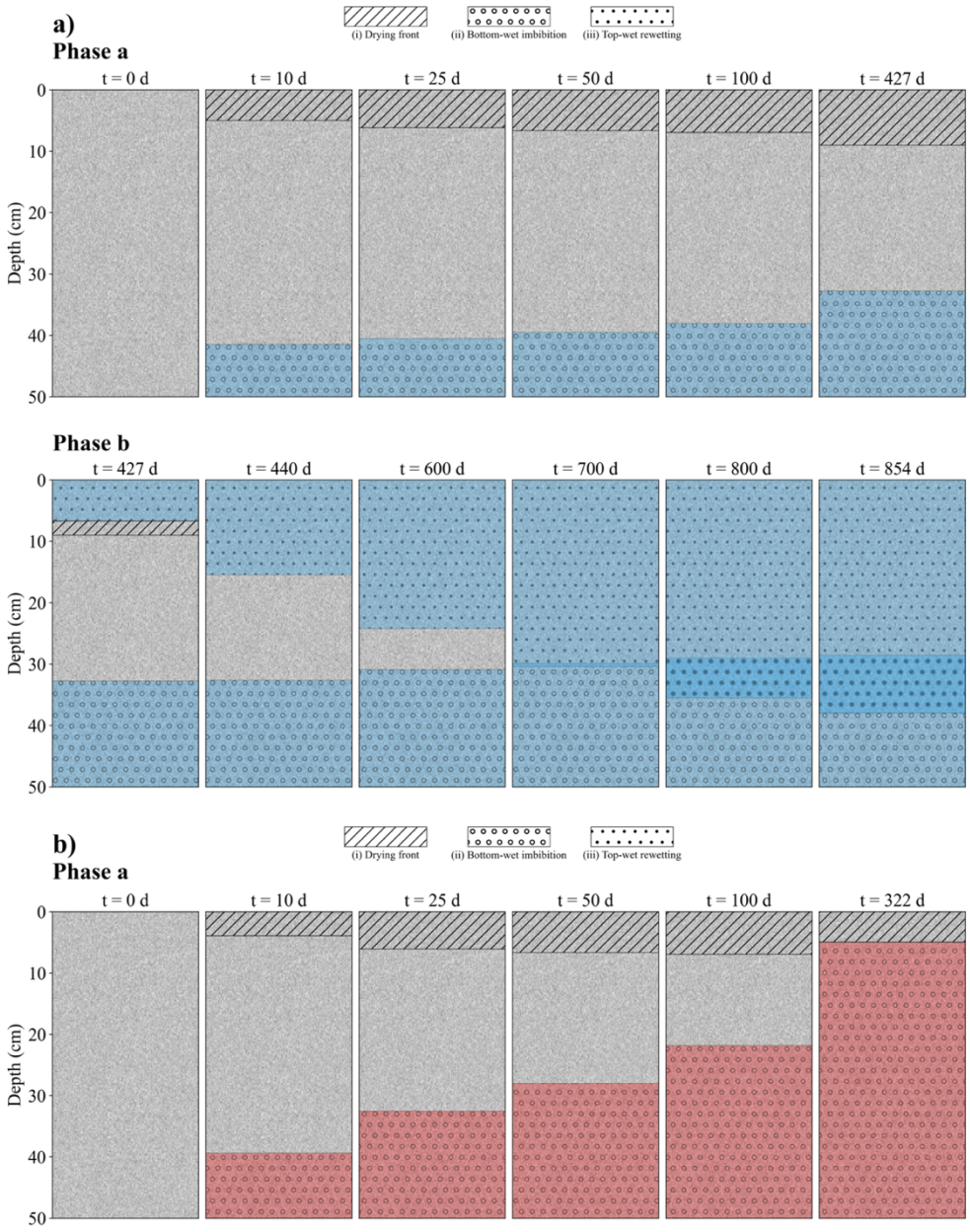


Figure 7.10 – Moisture-transfer estimated behaviour. a) Moderate DEF- and b) Severe DEF-affected beam.

- Microscopic assessment

The DRI mapping results (Figure 7.5) reveal a clear difference in the distribution and intensity of deterioration throughout the cross-section of beams affected by both moderate and severe DEF. These differences reflect both in water transfer behaviour (i.e., (i) Drying front, (ii) Bottom-wet imbibition, (iii) Top-wet rewetting), and the DEF swelling potential of the respective cements (see section 7.4.1).

For the moderate DEF-affected beam (Figure 7.5a), DRI numbers were moderate at all depths, with slightly higher values in the 0–10 cm and 10–20 cm layers. This gradient is consistent with the moisture exposure history. During "phase a", the upper part of the beam was exposed to 30% relative humidity, and the semi-empirical moisture-transfer modelling results (Figure 10a) indicate a drying front of 9 cm. The 0–10 cm layer can therefore be considered roughly dried, whereas the 10–20 cm layer, located immediately beneath the drying front, was partially desaturated. Although the extent of drying in this intermediate layer is constrained by the discrete γ-desimetry measurements, the clear evidence of drying at the upper surface and the similar DRI numbers across 0–20 cm support the inference that both layers developed pronounced drying-shrinkage-induced cracking, with more intense desiccation in the 0–10 cm zone. Zhu [64] showed that decreasing relative humidity increases the number of cracks in the cement paste (CCP) and raises DRI values in concrete not affected by internal swelling reactions, with the evolution of DRI closely following measured shrinkage strains. This confirms that DRI is sensitive to shrinkage-related cracking and supports the interpretation that the upper 0–20 cm zone first developed a shrinkage crack network.

During "phase b", water was supplied from the top surface while continuing from the bottom. The moisture-transfer analysis indicates that the imbibition front from the bottom reached 8.7 cm at 10 days, 11.2 cm at 50 days, 17.1 cm at 427 days, and met the top-wet front after about 600 days (Figure 10a). Thus, the lower 30–50 cm experienced a long-term high-water supply early in the exposure, favouring DEF development, whereas the upper 0–20 cm remained relatively dry for a longer period and was later rewetted through an already cracked cement paste. This exposure sequence implies that the upper 0–20 cm zone remained desaturated for a longer period during "phase a" and was subsequently rewetted from the top during "phase b", after a shrinkage crack

network had already formed. This interpretation is consistent with the boundary conditions and with the rapid mass gain captured at the start of "phase b" by the rewetting term; however, the front-based reconstruction remains a simplified representation of the rewetting stage. Kawabata et al. [65] developed a coupling approach in which ISR-induced microcracking enhances moisture transfer and, in turn, modifies the internal moisture field governing subsequent expansion. Their approach updates the moisture diffusion coefficient as a damage-type function of accumulated expansion above a threshold, providing interpretations that are not captured by the present parameterization. Consequently, the fitted rewetting parameters (D_{imb} and D_{rwt}) support the drying–rewetting chronology, but they cannot be used to quantify crack-enhanced ingress relative to a stationary-transport baseline.

In addition, shrinkage-induced cracking can have an antagonistic influence on DEF-induced deterioration. While pre-existing cracks can increase local water accessibility and facilitate transport of dissolved species, they can also provide accommodation volume for precipitation within the paste and interfacial transition zone (ITZ), thereby reducing crystallization pressure for a given amount of expansive product. The higher number of cracks in the cement paste (CCP) and the lower coarse aggregate debonding (CAD) in the upper 0–20 cm relative to the lower 30–50 cm are therefore interpreted as the combined outcome of early shrinkage microcracking and subsequent DEF-related damage developing within a paste that was already cracked, rather than evidence of a single mechanism acting in isolation. The overall moisture-transfer behaviour remains consistent with the redistribution of microscopic damage across the beam height (Figures 5a and 11a), while the limitations of the rewetting reconstruction constrain the extent to which crack-assisted ingress can be inferred from the fitted transport parameters alone.

The severe DEF beam (Figure 7.5b) exhibited a markedly different damage profile, with DRI numbers increasing progressively with depth and reaching their highest values (1350–1969) between 20 and 50 cm. The corresponding heatmap (Figure 7.11b) illustrates this depth-dependent accumulation of damage, with high-density deterioration primarily located in the lower half of the beam. This more severe damage profile is consistent with the greater ettringite formation potential of the cement used in severe DEF concrete, estimated to be 31% higher than that of the cement used in moderate DEF concrete (Figure 7.4). However, microstructural factors must also be considered: even if ettringite forms, the associated swelling depends on the available space for

precipitation within the paste and ITZ. Given the intentional similarities in the concrete microstructure between the two beams, the higher ettringite yield of the cement used in severe DEF concrete likely imposed greater crystallization pressures, thus amplifying deterioration. Free-expansion tests on cylinders made with the same concretes confirm this difference in potential: the maximum expansion of the moderate DEF mixture was about 0.35%, whereas the severe DEF mixture reached approximately 1.79% [18]. This fivefold increase in free-swelling capacity is consistent with the higher ettringite-formation potential of the cement used in the severe DEF concrete and with the much larger DRI values and more advanced deterioration observed in that beam for similar moisture exposure histories.

The water-transfer estimation corroborates this behavior. In the severe DEF beam, the imbibition front reached 25 cm within 25 days and exceeded 46.5 cm after 300 days, indicating that high water content extended over most of the member height early during exposure. This evolution is consistent with the rapid rise of the imbibition front (Figure 7.10b) and with the increase in DRI values toward the lower half of the cross-section (Figures 7.5b and 7.11b). Monitoring of the severe DEF beam ended prematurely due to structural failure before Phase (b), which nevertheless provides a contrast with the more gradual deterioration observed in the moderate DEF beam under staged moisture supply.

In the severe DEF beam, the DRI heatmap also shows an arrow-shaped pattern in the 20–30 and 30–40 cm layers (Figure 7.11b), characterized by a damage core along the transverse axis tapering toward the sides. This geometry may reflect the combined influence of internal swelling and member-level deformation under self-weight in a simply supported configuration, together with boundary-condition effects associated with side sealing. The available evidence remains insufficient for a definitive attribution, and the observation is reported to guide targeted verification in future work.

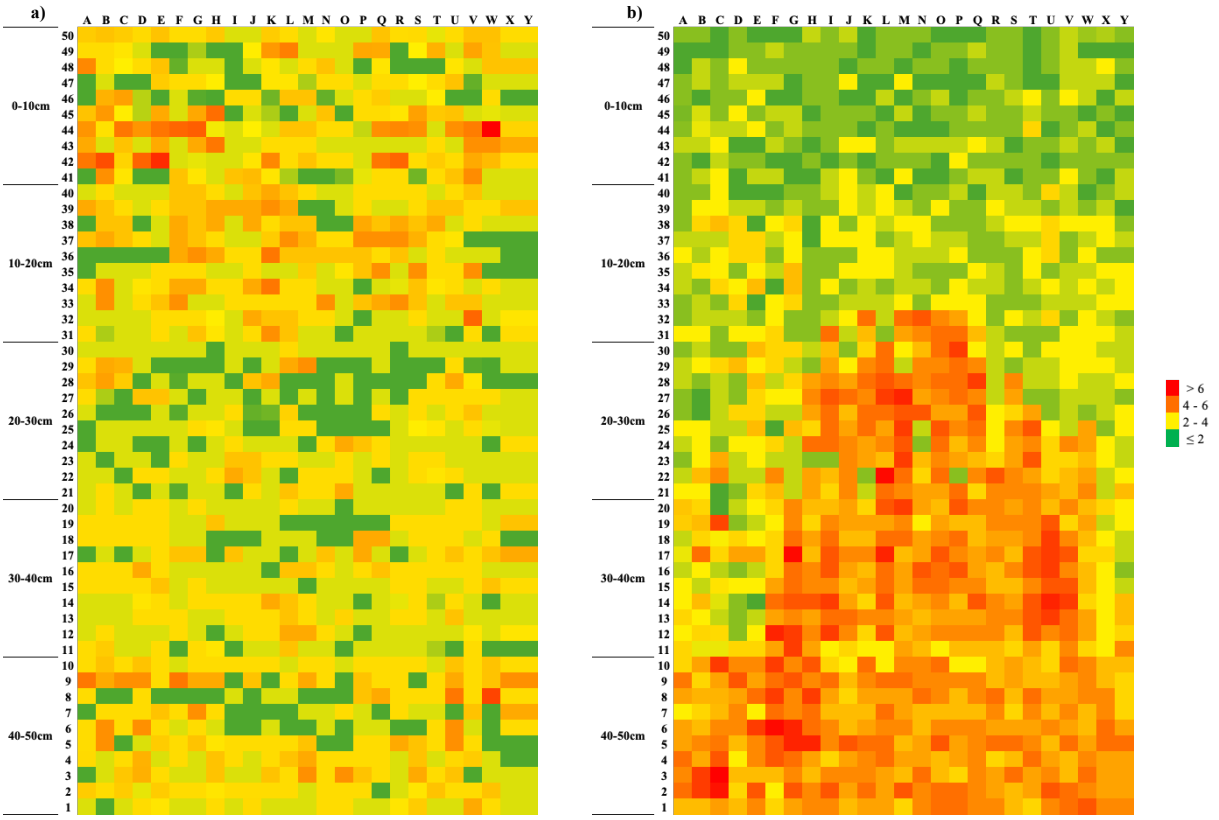


Figure 7.11 – Heatmap of damage distribution over the cross-section. a) Moderate DEF, b) Severe DEF.

- Mechanical assessment

The mechanical response of the cores extracted from beams affected by moderate and severe DEF reflects the depth-dependent deterioration pattern driven by water transfer and material reactivity. Stiffness degradation was assessed through the residual modulus of elasticity, defined as the ratio between the modulus of elasticity obtained from SDT testing and the reference modulus at 28 days (i.e., 32.8 GPa for the moderate DEF concrete and 30.8 GPa for the severe DEF concrete [18] detailed in section 7.4.1).

For the moderate DEF beam, the 10–20 cm layer did not exhibit lower stiffness than the 40–50 cm layer, despite its relatively elevated DRI number. This apparent mismatch is consistent with the earlier evidence of drying during "phase a" in the upper zone and with the antagonistic role that pre-existing drying-shrinkage cracks can play in DEF-induced mechanical degradation. Drying shrinkage cracking tends to be distributed within the bulk cement paste, increasing the crack counts captured by DRI, while preserving the aggregate–paste load-transfer paths to a greater extent than

deterioration dominated by ITZ debonding. In addition, once the upper zone is rewetted during "phase b", shrinkage-induced cracks may facilitate water ingress and promote ettringite precipitation, yet part of this precipitation can occur within the existing crack volume, which limits crystallization pressure and reduces the severity of stiffness loss compared with regions where expansive products must generate new cracks and debonding to accommodate volume change.

This behaviour is consistent with the distribution of deterioration features at this damage level. The DRI results show that the 10–20 cm layer contains fewer coarse aggregate debonding weighted features (CAD = 14) but more cracks in the cement paste with and without reaction products (CCP + CCP_RP = 546) than the 40–50 cm layer (CAD = 52; CCP + CCP_RP = 493) (Figure 5a). In other words, cracking in the upper zone is predominantly located within the bulk cement paste, consistent with drying-shrinkage during "phase a", whereas cracking toward the bottom involves a larger proportion of aggregate–paste interfaces. This distinction is mechanically important because aggregate interlock and stress redistribution are less compromised in the 10–20 cm layer, and coarse aggregates remain more effectively engaged in load transfer. The SDT results corroborate this interpretation. SDI and PDI values are higher at 10–20 cm (0.23 and 0.18) than at 40–50 cm (0.21 and 0.14) (Figure 7.6), indicating a greater number of cracks in the upper layer.

The residual modulus of elasticity does not follow a simple progressive trend with depth, which is consistent with the water supply history corresponding to moisture ingress both in the bottom (phases a and b) and in the top (phase b) of the beam. The modulus at 10–20 cm is 20.0 GPa, corresponding to 60.9% of the reference value E_0, while the 20–30 cm and 30–40 cm layers show higher residual moduli of 23.2 GPa and 24.7 GPa, representing 70.9% and 75.3% of E_0, respectively. The lowest residual modulus occurs at 40–50 cm (17.7 GPa, 54.0% of E_0), reflecting a greater influence of DEF deterioration, as evidenced by greater coarse aggregate debonding in this region (Figure 12). Across the depth, SDI ranges from 0.17 to 0.23, and PDI from 0.12 to 0.18, indicating limited energy dissipation and a relatively limited reduction of stiffness. Overall, debon features associated with loss of aggregate–paste bond remain below 52 counts at all depths, without a clear vertical trend related to the water supply history (Figure 7.5a). This limited interface damage suggests that aggregate interlock was partially preserved, allowing coarse aggregates to remain mechanically engaged and to contribute to stiffness.

In contrast, the severe DEF-affected beam exhibited a pronounced deterioration gradient along its height. Near the top (0–10 cm), the residual modulus of elasticity remained relatively high at 87.8% of E_0, corresponding to an effective modulus of 28.8 GPa (Figure 7.6), and SDI and PDI values were low (0.14 and 0.10), with negligible Debon counts. This response indicates limited stiffness loss and, when interpreted with the microscopic observations, suggests that the limited cracking near the top is primarily associated with shrinkage rather than DEF-induced deterioration. With increasing depth, stiffness loss, and SDT indices increased progressively. At 40–50 cm, the residual modulus dropped to 16.3% of E_0, corresponding to 5.3 GPa, while SDI and PDI increased to 0.57 and 0.35, and Debon counts reached 140. This combination indicates severe cracking and debonding in the interfacial transition zone, where coarse aggregates become mechanically disconnected from the surrounding cement paste and lose their capacity to redistribute internal stresses. Intermediate layers show a gradual transition between these two states, consistent with the rapid water imbibition along the beam height (22 cm in 50 days) that accelerated DEF development. The correspondence between the accumulation of Debon features and the steep reduction in E/E_0 highlights the central role of ITZ degradation in driving stiffness loss in concrete severely affected by DEF. Overall, the residual modulus of elasticity averaged 48.0% over the beam height (Figure 7.12), confirming that this deterioration gradient results in a substantial loss of global stiffness. However, this global indicator does not reflect the local mechanical properties

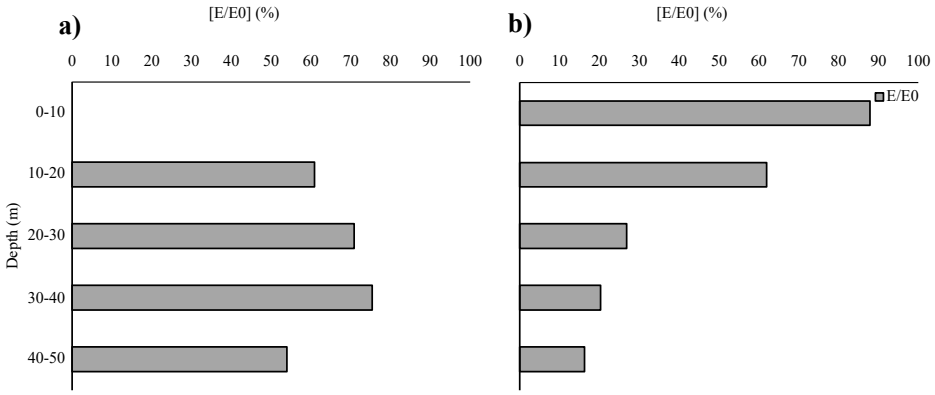


Figure 7.12 – Residual modulus of elasticity (E/E_0). a) Moderate DEF, b) Severe DEF.

- Ultimate residual expansion potential

The RE results must be interpreted considering the different pre-test exposure histories: the moderate DEF beam completed Phases (a) and (b) (i.e., 854 days), whereas the severe DEF beam

was limited to Phase (a) due to premature failure (i.e., 330 days), while the RE monitoring duration was 406 days for both concretes.

Figure 7.13a illustrates the ultimate maximum residual expansion of the different depths of the DEF-affected beam. The potential for further expansion remained relatively low at all depths, averaging 0.13% (0.12%-0.15%). Exposure to both phases of water supply promoted, and the induced deterioration patterns identified through microscopic and mechanical assessment, resulted in a narrow range of residual expansion.

The severe DEF-affected beam (Figure 7.13b) exhibited important depth-dependent residual expansion, with an average of 0.45% across the height, ranging from 0.23% in the 30–40 cm layer to 0.66% in the 0–10 cm layer. Residual expansion at 40–50 cm could not be measured because the severe deterioration at this depth (DRI = 1969, SDI = 0.57, and E = 5.3 GPa) caused the cores to fracture during extraction. The high residual expansion measured near the top suggests that DEF development in these upper layers was delayed during “phase a”, preserving a larger fraction of the ettringite formation potential that would have been later mobilised under renewed moisture supply if this beam had experienced “phase b”. This behaviour is consistent with the high-DEF potential of the severe DEF concrete and indicates that, under the combined effects of high material reactivity and non-uniform water supply, DEF progression in some heights of the beam was limited, thereby explaining the substantial residual swelling capacity detected, particularly in the upper part of the severe DEF-affected beam.

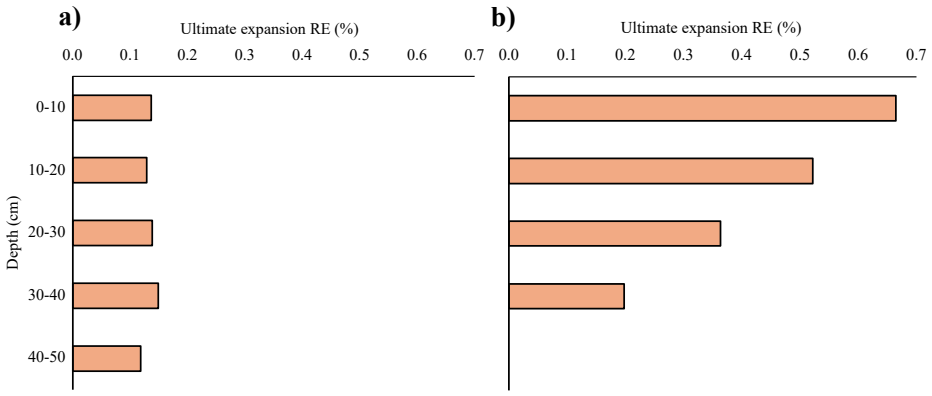


Figure 7.13 – Ultimate expansion measured after 406 days of RE testing (moderate: Phases (a)+(b) - 854 days; severe: Phase (a) until 330 days only due to premature failure). a) Moderate DEF and b) Severe DEF.

It is also noted that residual expansion is not solely governed by potential development of the reaction; it is influenced by the capacity of the existing crack network to accommodate reaction products during the residual expansion test. Early shrinkage cracking can reduce the extent to which expansive products translate into measurable expansion by providing available space, even when DEF precipitation proceeds (further discussion in 7.6.4).

7.6.2 Current damage extent – multi-level assessment

The current damage condition of the beams was assessed by combining microscopic (DRI) and mechanical (SDT) indicators and interpreting them against a dataset developed for condition assessment of concrete affected by DEF. Figure 7.14 displays, for each depth, the triplets (DRI, SDI, stiffness loss) in a polar chart, while Figure 7.15 presents the corresponding depth-wise estimates of current-induced expansion.

The multi-level assessment protocol employed in this study aims to characterize the current deterioration state of concrete affected by DEF and to estimate the expansion induced at the time of coring, following the framework proposed by Sanchez et al. [27]. This damage extent, represented as $\varepsilon_{ML}(t_{coring})$, indicates the level of induced expansion inferred from the combined microscopic and mechanical indicators measured on the extracted cores. It corresponds to the unrestrained expansion that would result in a similar degree of damage under the benchmark calibration of the multi-level database.

The qualitative bands in Figure 7.14 were derived from the DEF ranges in Sanchez et al. [27] (Table 7.1) and from the Tx+MM-DEF dataset, obtained from non-air-entrained concrete manufactured with a conventional CSA Type GU/ASTM Type I Portland cement ($Na_2O_{eq} \approx 0.90$ %), with total alkalis adjusted to 1.25% by cement mass, incorporating a limestone coarse aggregate from San Antonio, Texas (USA), non-reactive to ASR. DEF was triggered by a controlled thermal cycle (i.e., the temperature was raised to 95 °C over 4 h, held at 95 °C for 12 h, then lowered to 23 °C over 12 h) after which specimens were stored in water at 23 °C [27]. From these data, non-overlapping bands were defined by slightly shifting the limits, centring each class on one damage level, and resolving overlaps on the safe side. For DRI, the ranges 355–599, 623–710, 828–1022, and >1022 correspond to the “moderate”, “very high”, “ultra-high”, and “beyond ultra-high” qualitative damage levels, respectively. For SDI, the four classes are defined as

SDI≤0.20, 0.20<SDI 0.28, 0.28 <SDI ≤0.43, and SDI>0.43; for stiffness loss, the corresponding limits are 35%≤ΔE≤56%, 56%< ΔE≤62%, 62%<ΔE ≤ 77%, and 77%<ΔE≤90%, respectively. In parallel, following Sanchez et al. [27], induced expansion up to about 0.11% were associated with "moderate" damage, 0.30–0.50% with "very high" damage, 0.50–1.00% with "ultra-high" damage, and values above 1.00% with "beyond ultra-high" damage, whereas values below 0.10% were considered negligible to low.

For each depth, the measured DRI, SDI, and stiffness-loss values were first located within these bands and then projected onto induced expansion. When the indicators fell inside a single band, the corresponding induced expansion class from Sanchez et al. [27] and the Tx+MM-DEF dataset was assigned. When indicators fell between two bands, or DRI and SDI were not in the same band, the estimated induced expansion was obtained by linear interpolation between the two nearest reference levels, using DRI and SDI to define the damage level and stiffness loss as a consistency check. When indicators were in the "beyond ultra-high" band and exceeded the Tx+MM-DEF values, the estimated induced expansion was obtained by extrapolating along the SDI–expansion trend and bounding the result by the free-expansion potential of the corresponding concrete. The resulting depth-wise values are shown in Figure 7.15.

For the moderate DEF-affected beam (Figure 7.14a), the multi-level indicators place all depths between the negligible and high bands. The mid-depth layers (20–30 and 30–40 cm) fall at or below the "moderate" bands for DRI, SDI, and stiffness loss, and are therefore associated with low current-induced expansion, respectively 0.10% and 0.12% (Figure 7.15a). The bottom layer (40–50 cm) lies between the moderate and very-high bands, which, by interpolation, yield an estimated induced expansion of 0.20%, indicating a more advanced deterioration condition.

At the top (0–10 and 10–20 cm), DRI and SDI fall between the moderate and very-high bands, whereas stiffness loss remains close to the moderate threshold. These layers are placed at the upper end of the moderate induced expansion range, with an estimated induced expansion of 0.25%. In the upper layers, especially at 0–10 cm, microscopic observations indicate that part of the DRI signal arises from drying shrinkage cracking; the estimated induced expansion of 0.25% should therefore be regarded as a conservative upper bound of the DEF-related induced expansion.

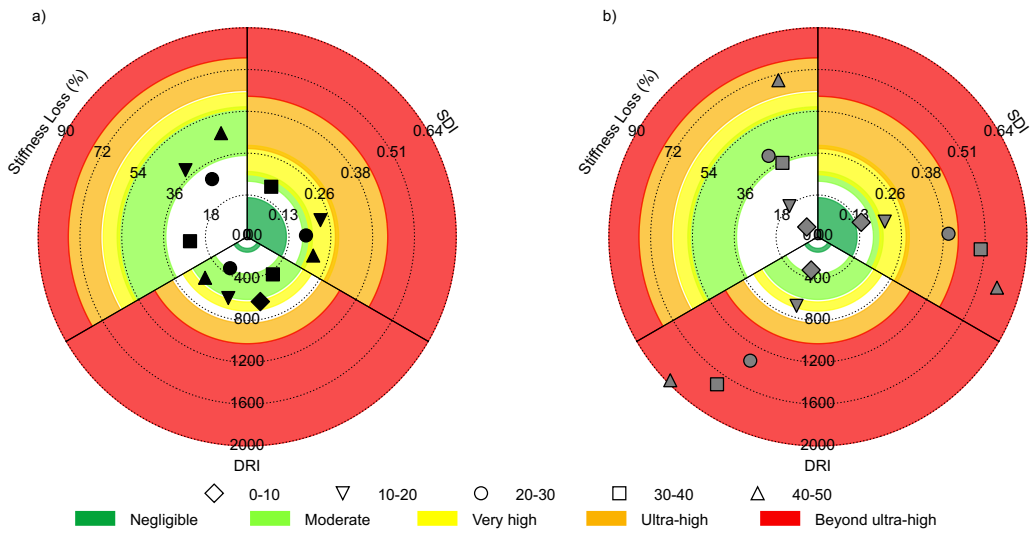
Overall, moderate DEF exhibits a current-induced expansion of 0.10% to 0.25% and average indicators that remain within the moderate bands, confirming that this beam is globally at a

moderate DEF damage level; however, this “average induced expansion” does not reflect the variation observed along the beam (Figure 7.15a).

For the severe DEF-affected beam (Figure 7.14b), the multi-level indicators reveal a pronounced vertical gradient. At 0–10 cm, the DRI value lies very close to the lower limit of the moderate band, whereas SDI and stiffness loss fall in the interval between the negligible–marginal and moderate ranges, for which no explicit qualitative damage level is defined. Given the low impact on stiffness, which, when interpreted with the microscopic results, indicates primarily shrinkage, the induced expansion was estimated as 0.05% (Figure 7.15b). At 10–20 cm, DRI enters the very-high band, and SDI lies between the moderate and very-high bands, while stiffness loss remains modest. Projection onto the induced expansion classes yields an estimated induced expansion of 0.40%, placing this layer in the “very high” damage level.

In the lower half of the beam, the indicators move into the ultra-high and beyond ultra-high bands. At 20–30 cm, DRI falls in the beyond-ultra-high band and SDI lies between the very-high and ultra-high bands, while stiffness loss approaches the lower limit of the ultra-high range; interpolation of the Tx+MM-DEF dataset between the 1.16% and 1.87% reference levels, using stiffness loss as a consistency check, yields an estimated induced expansion of 1.25%, which falls within the beyond-ultra-high range. At 30–40 cm, DRI exceeds the highest value, SDI approaches the upper bound, and stiffness loss remains moderate with respect to the Tx+MM-DEF calibration. The induced expansion at this depth is therefore obtained by a limited extrapolation of the DRI–expansion trend above 1.16%, constrained by the mechanical response, leading to an estimated induced expansion of 1.60%. At 40–50 cm, DRI and SDI fall in the beyond-ultra-high bands while stiffness loss fall in the upper band of ultra-high, thus the induced expansion is taken as 1.80%, corresponding to a further extrapolation of the calibration curve that is explicitly bounded by the measured free-expansion capacity of the severe DEF concrete (1.79%) and accounts for additional cracking from structural effects in this region.

Overall, the lower 30 cm of severe DEF-affected beam are therefore classified as “beyond ultra-high” damage, while the top 20 cm remain in the low and very-high classes. The average current-induced expansion of the beam is estimated at 1.02%, which is near the upper limit of the “ultra-high” range. This single average value confirms that the concrete is severely affected by DEF but masks the pronounced height-related differences revealed by the layered analysis (Figure 7.15b).



Obs.: There is no threshold values defined to estimate the damage level for the regions left in white.

Figure 7.14 – Global analysis of damage degree. a) Moderate DEF and b) Severe DEF.

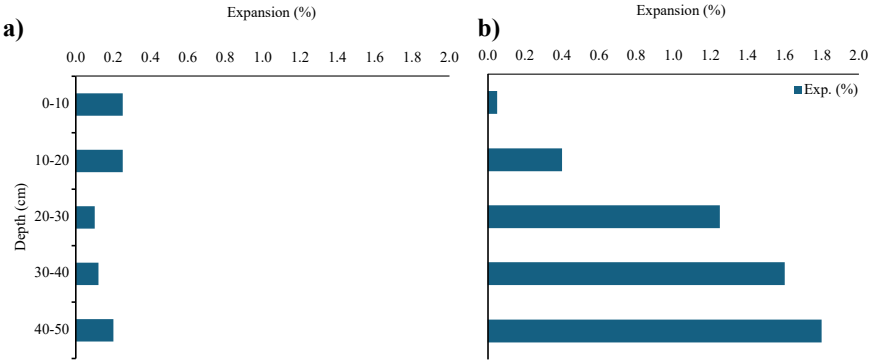


Figure 7.15 – Estimated current damage extent through the multi-level protocol. a) Moderate DEF and b) Severe DEF.

7.6.3 DEF-induced residual expansion potential and Bayesian inference

This section evaluates the residual DEF-induced swelling capacity at each depth and characterises its uncertainty, based solely on the residual expansion tests conducted on cores under free, favourable moisture conditions. A Larive-type sigmoidal law is used in a residual form within a Bayesian framework, yielding posterior distributions of residual parameters and credible envelopes for the residual curves. This residual expansion analysis complements the multi-level diagnosis in Section 7.6.2 and provides input for discussion with the reconstruction approach in Section 7.6.4, which uses free-expansion references and offsets.

The residual expansion behaviour at each depth is described using the semi-empirical law originally proposed by Larive [55] for ASR, later extended to DEF [18,56,57]. In its classical formulation (Equation 7.1), this law represents the full free-expansion curve $\varepsilon(t) = \varepsilon_{full}(t)$ with three parameters: an asymptotic free expansion (ε^{∞}), a latency time (τ_L), and a characteristic time (τ_C). In the present context, the same sigmoidal function is applied to the residual expansion curves measured on cores, with time t measured from the start of the residual expansion test rather than in the early ages of the concrete, when the full free expansion is obtained. The deterministic residual expansion $\varepsilon_{res}(t)$ is obtained through Equation 7.9, with a time origin at the start of the residual expansion test and three residual parameters: the asymptotic residual expansion $(\varepsilon_{\infty,res})$, an apparent residual latency parameter $(\tau_{L,res})$, and an apparent residual characteristic time $(\tau_{C,res})$. Here, $\tau_{L,res}$ is an apparent time-shift parameter that governs the timing of the transition toward expansion rather than a strict dormant period, while $\tau_{C,res}$ controls the rate at which the residual expansion approaches its asymptote. These parameters describe the residual expansion response of each core under the conditions of the residual expansion test. They are not interpreted as free-expansion parameters and are distinct from the free-expansion quantities used later in Section 7.6.4 for reconstruction.

For each residual expansion time-series, $(\varepsilon_{meas}(t))$ denote the measured axial expansion of the core at time t, since the start of the residual test, with (t_0) the time of the first finite reading. The observed residual expansion increment is defined as $\varepsilon_{res,i}^{obs} = \varepsilon_{meas}(t_i) - \varepsilon_{meas}(t_0)$, so that $\varepsilon_{res,i}^{obs}$ represents only additional swelling that develops during the residual expansion test. In practice, the measurements are baseline-corrected at t_0 by taking $\varepsilon_{meas}(t_0)$, as the reference value (equivalent to setting $\varepsilon_{meas}(t_0) = 0$ for the residual test), and all subsequent readings are expressed relative to this reference. The statistical model for the observed residual expansion increments is obtained through Equation 7.10.

To incorporate the uncertainty associated with the residual model parameters and the predicted residual expansions, a Bayesian framework was adopted. In this framework, the residual parameters $\theta = (\varepsilon_{\infty,res}, \tau_{L,res}, \tau_{C,res}, \sigma_{res})$ are treated as probability distributions rather than fixed values, thereby propagating uncertainty from both the experimental data and the fitting process. Here (σ_{res}) represents the within-test scatter of the residual expansion measurements around the

fitted residual curve for a given core, including measurement noise and model discrepancy, and is inferred from the time-series residuals used in the Gaussian likelihood (Equations 7.10 and 7.13). Weakly informative priors were adopted, consistent with ranges reported in the literature for DEF [3,18,57] and with the time scales of the present tests (Equation 7.11). The probability of the residual parameters given the observed residual expansions follows Bayes' theorem (Equation 7.12), where the likelihood is defined as a Gaussian (Equation 7.13). Posterior sampling was performed using Markov chain Monte Carlo (MCMC) with four chains, 1 000 warm-up and 1 000 retained draws per chain. For each posterior sample, the residual expansion equation (Equation 7.9) was evaluated, along with the statistical model, priors, Bayes formulation, and likelihood (Equations 7.10–7.13), on a uniform time grid up to 410 days. At each time t, a 95% highest-density interval (HDI) was computed by evaluating Equation 7.9 over the posterior samples of the residual parameters, yielding a credible envelope for the model-predicted residual expansion curve $\varepsilon_{res}^{pred}(t)$ (Equation 7.14). The resulting HDI bands summarize posterior uncertainty in the fitted residual expansion response; a 95% level was selected as a conventional reporting standard to capture the dominant credible range while retaining sensitivity to tail behaviour, even though the number of tested cores per depth is limited. In this study, the HDI is constructed on the distribution of the model-predicted mean response obtained from posterior parameter samples, rather than on posterior predictive realizations that would additionally propagate σ_{res} through simulated observations. For this reason, the 95% HDI is retained as the primary reporting level, while the interpretation emphasizes posterior medians and interval widths rather than tail-driven comparisons.

$$\varepsilon_{res}(t \mid \varepsilon_{\infty,res}, \tau_{L,res}, \tau_{C,res},) = \varepsilon_{\infty,res} \frac{1 - exp\left(-\frac{t}{\tau_{C,res}}\right)}{1 + exp\left(-\frac{t - \tau_{L,res}}{\tau_{C,res}}\right)} \tag{7.9}$$

$$\varepsilon_{res,i}^{obs} \backsim N\left(\mu_{res,i}, \sigma_{res}^2\right), \quad \mu_{res,i} = \varepsilon_{res}\left(t_i \mid \varepsilon_{\infty,res}, \tau_{L,res}, \tau_{C,res}\right), \tag{7.10}$$

$$\varepsilon_{\infty,res} \backsim Uniform\left(0, 2.0 \max \varepsilon_{res,i}^{obs}\right), \tau_{C,res} \backsim Uniform(1, 200), \tau_{L,res} \backsim Uniform(0, 200),$$
$$\sigma_{res} \backsim HalfUniform(0.01), \tag{7.11}$$

$$p\left(\varepsilon_{\infty,res}, \tau_{L,res}, \tau_{C,res}, \sigma_{res} \mid \varepsilon_{res}^{obs}\right) \propto p\left(\varepsilon_{res}^{obs} \mid \varepsilon_{\infty,res}, \tau_{L,res}, \tau_{C,res}, \sigma_{res}\right) p(\varepsilon_{\infty,res})\, p\left(\tau_{L,res}\right) p\left(\tau_{C,res}\right) p(\sigma_{res}) \tag{7.12}$$

$$p\left(\varepsilon_{res}^{obs} \mid \varepsilon_{\infty,res}, \tau_{L,res}, \tau_{C,res}, \sigma_{res}\right) = \prod_{i} N\left(\varepsilon_{res,i}^{obs} \mid \varepsilon_{res}\left(t_i \mid \varepsilon_{\infty,res}, \tau_{L,res}, \tau_{C,res}\right), \sigma_{res}^2\right), \tag{7.13}$$

$$HDI_{0.95}(t) = \left[\varepsilon_{low,res}(t), \varepsilon_{high,res}(t)\right] \tag{7.14}$$

Figure 7.16 presents the time-dependent modelling results for residual expansion as a function of depth in both beams. Experimental measurements are represented as discrete dots, while the shaded regions depict the 95% HDI envelopes derived from the posterior distributions. This representation captures both the most likely residual expansion behaviour and the range of credible uncertainty associated with the fitting process. Figure 7.16 illustrates the probabilistic confidence interval of residual expansion, and Figure 7.17 displays the probabilistic ranges of the apparent residual expansion parameters obtained through the Bayesian approach proposed.

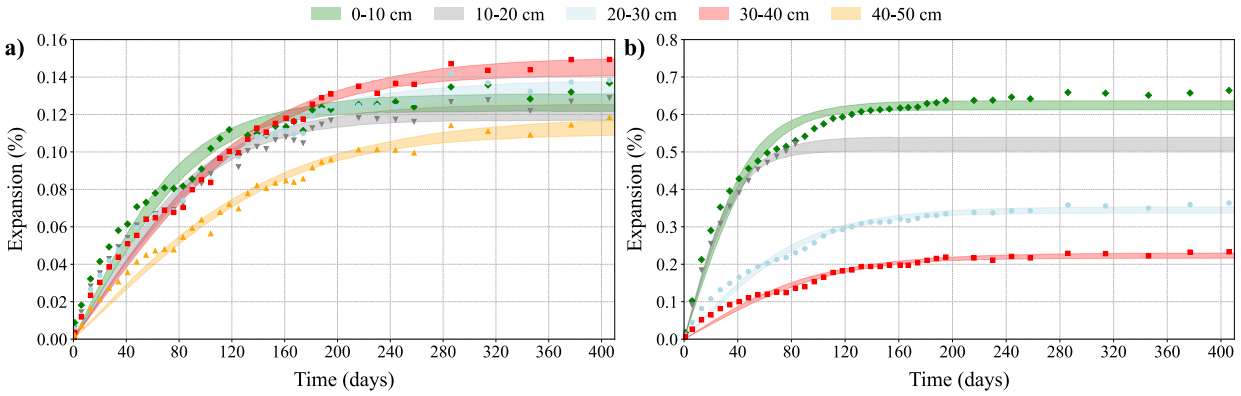


Figure 7.16 – Probabilistic confidence interval of residual expansion via Bayesian modeling. a) Moderate DEF and b) Severe DEF.

For the moderate DEF-affected beam (Figure 7.16a), residual expansions remain limited across all depths. The highest values are recorded in the 30-40 cm layer, with no clear trend along the height. This profile agrees qualitatively with the estimates from the multi-level deterioration assessment (Section 7.6.2) and reflects the limited residual swelling capacity of this beam. The posterior distributions of the residual parameters (Figure 7.17a) capture this uniformity: $\varepsilon_{\infty,res}$ ranges between about 0.11% and 0.15%, $\tau_{C,res}$ varies between 38 and 85 days, and $\tau_{L,res}$ lies between 0 and about 17 days. The limited ability to constrain $\tau_{L,res}$ is expected, because residual expansion testing does not capture the early stages of swelling where latency is most influential; by contrast, $\varepsilon_{\infty,res}$ and $\tau_{C,res}$ are less affected by this limitation and provide more robust estimates of the residual swelling capacity and residual kinetics.

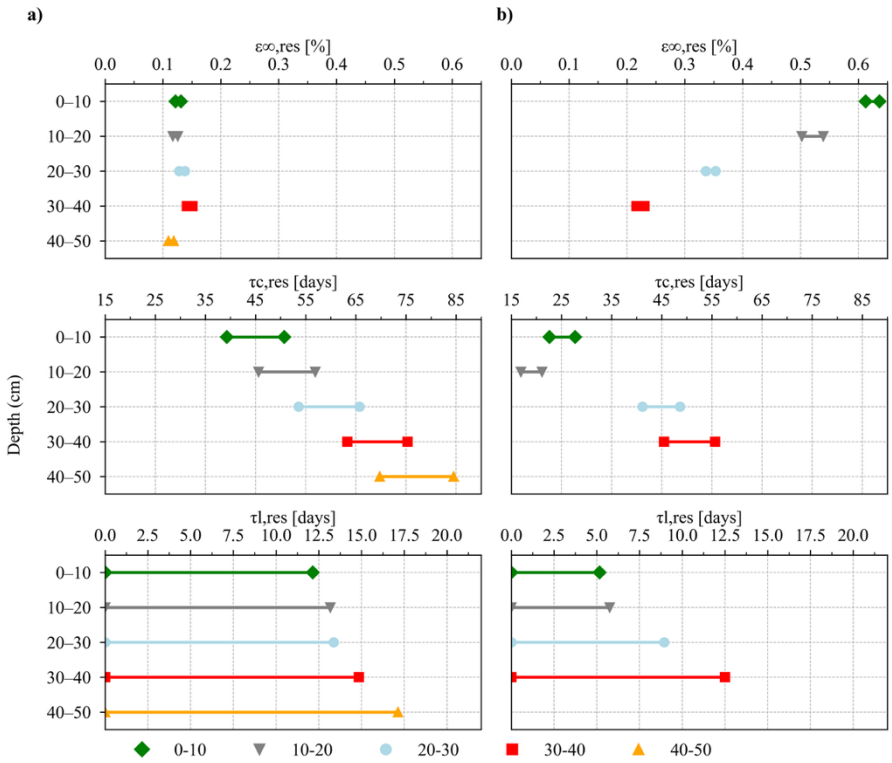


Figure 7.17 – Probabilistic ranges of the apparent parameters of the residual expansion obtained via Bayesian modeling. a) Moderate DEF and b) Severe DEF.

For the severe DEF-affected beam (Figure 7.16b), residual expansions are substantially higher and present a more pronounced gradient. In the upper layers (0–10 cm and 10–20 cm), residual expansions reach values of the order of 0.62% and 0.52%, whereas below 20 cm, the residual expansions fall between about 0.22% and 0.35%. This gradient reflects the influence of the water-transfer history described in Section 7.6.1. The posterior distributions reflect this behaviour (Figure 7.17b): $\varepsilon_{\infty,res}$ ranges between about 0.52% and 0.62% in the top layers and between about 0.22% and 0.35% in the lower layers. $\tau_{C,res}$ was shorter in the upper layers (17–27 days) than in the lower layers (41–56 days), indicating a more rapid residual progression once moisture becomes available near the top. $\tau_{L,res}$ varies between 0 and about 12.5 days and is again weakly constrained, which confirms that latency is difficult to resolve from residual expansion data alone and should be interpreted as an apparent parameter of the residual curve.

Overall, the Bayesian fitting of the residual expansion function provides a consistent representation of the depth-dependent residual expansion capacity, with credible intervals capturing the combined effects of material reactivity and water-transfer history. The inferred $\varepsilon_{\infty,res}$ and $\tau_{C,res}$ quantify, for

each depth, how much additional swelling can still occur under favourable moisture, nearly free conditions, and how rapidly this residual swelling is likely to develop, while the 95% HDI envelopes in Figure 7.16 express the associated temporal uncertainty. The results demonstrate that the attained deterioration history primarily governs the capacity for further DEF-induced swelling: in regions with restricted moisture ingress, expansion was delayed and remains available for reactivation, whereas in regions with earlier water access, most of the swelling potential was already consumed prior to testing. Section 7.6.4 builds on these residual-capacity estimates and on the free-expansion reference to reconstruct the full expansion histories, estimating a current expansion at the beginning of residual expansion testing.

A secondary feature in Figure 7.17a is that the apparent kinetics accelerate towards the upper layers, as reflected by lower $\tau_{C,res}$ and $\tau_{L,res}$ values, even though $\varepsilon_{\infty,res}$ remains comparable across depths. This trend likely reflects depth-dependent differences in the initial microcrack network and moisture accessibility during the residual test, thereby shortening the apparent time scale of expansion without materially altering the ultimate residual capacity. Because $\tau_{L,res}$ and $\tau_{C,res}$ are apparent parameters inferred under test conditions, this observation is interpreted as supportive of the moisture history rather than as evidence of a different residual expansion potential.

7.6.4 Reconstruction of DEF-induced development

Multon et al. [58] proposed, for ASR-affected concrete, a reconstruction approach in which a parametric free-expansion law of Larive type is first calibrated on laboratory free-swelling specimens and then used as a reference to interpret residual expansion tests on cores. Martin [18] extended this method to DEF and DEF+ASR beams, using specific reference curves obtained from companion specimens cast with the same concretes as the beams and stored under uniform, favourable moisture conditions, while proposing the use of time and expansion offsets fitted simultaneously with the expansion law parameters. In the present study, the reconstruction follows this framework: for each of the two concrete mixtures investigated (moderate DEF and severe DEF), the free-expansion reference curve reported by Martin [18] and the residual expansion tests (Section 7.5.3) serve as the basis for reconstructing the free-expansion histories of the present beams.

The procedure assumes that, under favourable high-humidity conditions for a sufficiently long period, the concrete from the two beams follows the same type of Larive free-expansion law as the reference characterised by Martin [18]. Residual expansion curves measured on cores extracted from the beams and stored at 38 °C and high relative humidity are considered as segments of these same free-expansion curves, starting from an advanced reaction state. This is then associated to a "potential chemical advancement", defined as a normalised descriptor of potential reaction progress from 0 to 1, in which 1 corresponds to exhaustion of the free-expansion potential, representing the reaction advancement that would have been developed under favorable moisture and temperature and free swelling conditions. For each depth, the residual expansion curve from the present study is aligned with the corresponding reference curve by introducing a vertical offset, interpreted as the equivalent free expansion already attained at the start of the residual test, and a horizontal offset, interpreted as an equivalent reaction-age shift. This alignment assumes that moisture conditions during the residual tests are sufficiently favourable to mobilise the remaining swelling potential, and that mechanical restraint at the core scale did not affect (in a very significant way) the "potential chemical advancement" of the reaction, such that the sum of pre-coring imposed chemical expansion and residual expansion converges toward the same asymptotic free expansion as the reference.

In Martin's original implementation, the offsets and Larive parameters were identified deterministically, yielding a single reconstructed curve at each depth [18]. In the present work, this reconstruction is embedded in the Bayesian framework introduced in Section 7.6.3 to obtain probabilistic ranges rather than single values for the asymptotic free expansion (ε^{∞}), latency time (τ_L), and characteristic time (τ_C), with boundaries defined in Equation 7.11. The time and expansion offsets are treated as additional parameters, and the free-expansion Larive law (Equation 7.1) is fitted jointly with the offsets to the combined dataset consisting of Martin's reference curves and the residual expansion data (Figure 7.7). For each depth, posterior sampling yields families of reconstructed free-expansion histories and corresponding highest-density interval (HDI) envelopes, which express the most credible range of free-expansion trajectories consistent with both the reference behaviour and the residual response of the cores (Figure 7.18).

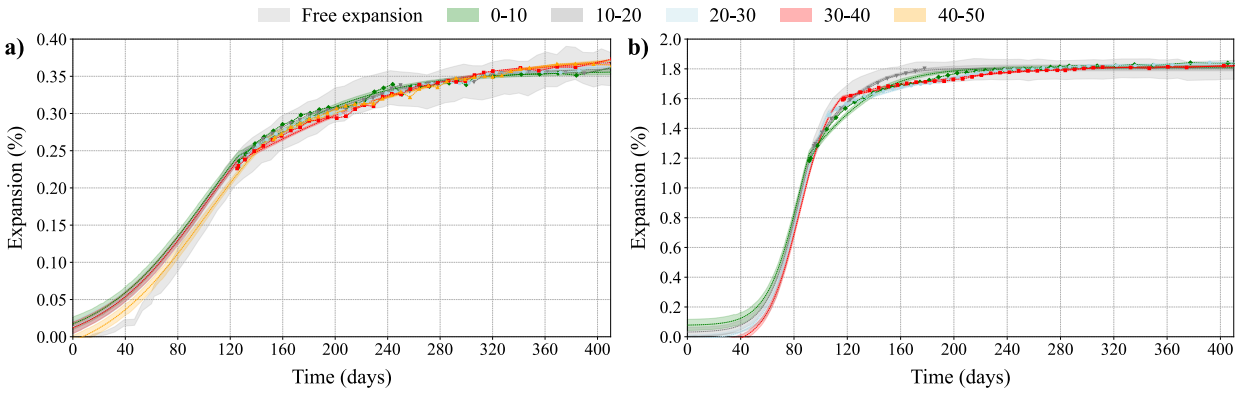


Figure 7.18 – DEF-induced expansion over time for each height in beams affected by a) moderate and b) severe DEF, obtained through the reconstruction approach combined with the Bayesian modeling.

For the moderate DEF-affected beam, Figure 7.18a shows that the reconstructed free-expansion curves are grouped within a relatively narrow band across the height. The vertical offsets, which represent the equivalent free expansion at the time of coring, yielded values of 0.22–0.23% at 0–40 cm and 0.27% at 40–50 cm, corresponding to 0.63–0.77 of "potential chemical advancement". The corresponding posterior distributions of the free-expansion parameters (Figure 7.19a) show ultimate free expansions ε^{∞} between 0.33% and 0.38%, characteristic times τ_C that increase with depth (from about 60 days near the top to about 70 days near the bottom), and latency parameters τ_L between 60 and 64 days. The reference residual expansion curve for moderate DEF mix presented $\varepsilon^{\infty}$of 0.35% raging between 0.33% and 0.37%, τ_C yielded values from 103 to 110, averaging at 106 days, and τ_L between 36 and 38 days, with an average of 37 days.

In the severe DEF-affected beam, the reconstructed free-expansion histories reveal larger offsets and a marked depth dependence (Figure 7.18b). The equivalent free expansions at the time of coring are about 1.17% at 0–10 cm, 1.28% at 10–20 cm, 1.54% at 20–30 cm, and 1.67% at 30–40 cm, corresponding to a "potential chemical advancement" of 0.65, 0.72, 0.86, and 0.93, respectively. No offset could be obtained at 40–50 cm because the cores from this depth failed during extraction. These offsets indicate that, under free-expansion conditions, the concrete in the lower half of the beam has already reached a very advanced "chemical potential", approaching the maximum free expansions reported by Martin [18] for the same concrete stored under favorable water supply (i.e., 1.79±0.06%), while the "chemical potential" of the upper part remains less advanced and still potentially highly reactive. The posterior distributions of ε^{∞}, τ_C, and τ_L for the

severe DEF concrete (Figure 7.19b) show ultimate free expansions between 1.74% and 1.86%, characteristic times that are longer in the upper layers (about 19 days) and shorter at depth (13-15 days), and latency parameters of about 84 days. The reference residual expansion curve for severe DEF mix yielded an asymptotic expansion ε^{∞} of 1.79%, ranging from 1.73% to 1.85%. The characteristic time τ_C remained tightly grouped between 12.1 and 12.6 days, with a mean of 12.3 days, while the latency parameter τ_L varied from 84 to 86 days, averaging 85 days.

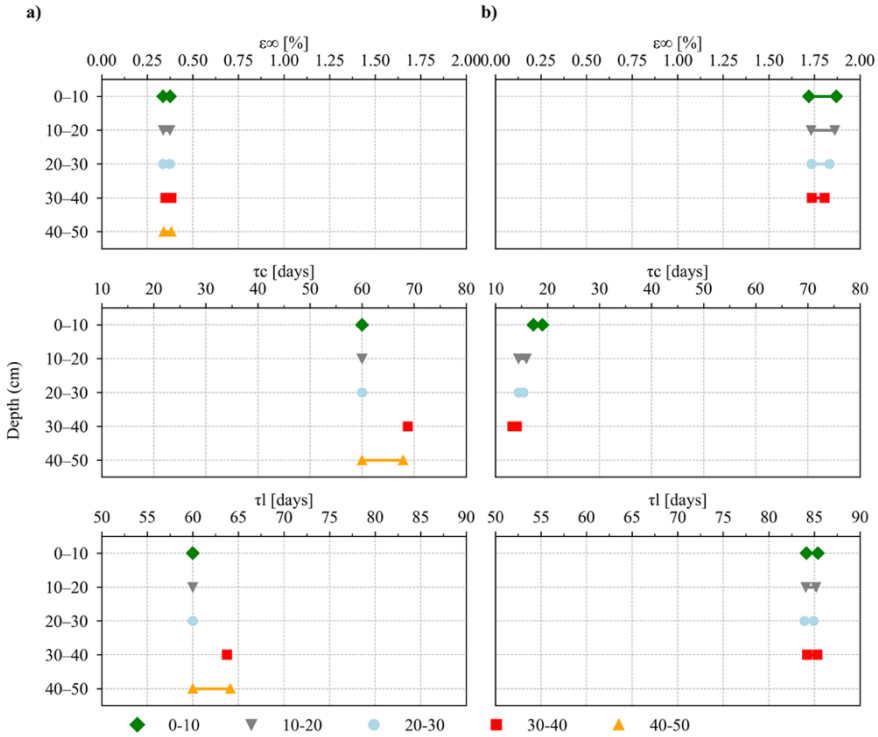


Figure 7.19 – Probabilistic ranges of the parameters of the sigmoidal expansion law for each height in beams affected by a) moderate and b) severe DEF, obtained from the reconstruction approach combined with Bayesian modelling.

The reconstructed offsets (which can be related to a "potential chemical advancement") can be qualitatively compared with the current-induced expansion estimated by the multi-level (ML) assessment in Section 7.6.2, keeping in mind that they refer to different physical quantities. The reconstruction offsets describe an equivalent free-expansion state that would be developed under idealised conditions of sufficient saturation and negligible restraint, inferred from the combination of reference curves and residual-expansion tests. The ML estimates, in contrast, represent equivalent induced expansion levels inferred from the combined microscopic and mechanical

indicators measured on the extracted cores, and correspond to the unrestrained expansion that would produce a comparable damage degree under the benchmark calibration of the multi-level database.

For the moderate DEF non-reinforced beam, ML-based current expansions range from about 0.10–0.12% at mid-depth (i.e., 20-40 cm) to about 0.25% near the top and 0.20% at the bottom (Section 7.6.2, Figure 7.15a). These values lie below the reconstructed offsets at 20–40 cm, remain slightly above at the top, and below at the bottom. This pattern suggests that, while the chemical swelling potential can be interpreted as advancing to a similar free-expansion state across the height, the actual induced expansion expressed in the concrete is reduced at 20–40 cm, likely influenced by the delayed wetting (Figure 7.10a), reflecting the lower damage indices (Figures 7.5a and 7.6a) observed in these layers.

In the severe DEF beam, the ML estimates indicate a pronounced vertical gradient, from about 0.05% at 0–10 cm and 0.40% at 10–20 cm to about 1.25–1.60% at 20–40 cm and 1.80% at 40–50 cm (Figure 15b). At 20–40 cm, reconstructed offsets yielded 1.54–1.67%, indicating that most of the chemical-free-expansion potential inferred for these depths has been transmitted to the concrete as induced expansion and severe damage, in agreement with the high DRI, SDI, and stiffness-loss values. Near the top, the reconstructed expansion offsets of about 1.17–1.28% contrast with ML estimates below 0.40%. This divergence shows that a significant portion of the chemical potential inferred under free, high-humidity conditions has not yet been fully expressed as induced expansion in the upper layers. This behaviour reflects the complex moisture history of the beam, in which the upper part experienced prolonged partial desaturation and remained below the moisture conditions required for full mobilisation of DEF expansion.

The divergence between the reconstructed free-expansion histories and the expansion estimated from the multi-level assessment reflects that the two approaches quantify different aspects of DEF development. The reconstruction method describes the potential advancement and remaining potential of the reaction under idealised free-expansion conditions, using residual expansion of cores to place each depth on an equivalent free-expansion curve calibrated on companion specimens exposed to continuously favourable moisture and temperature during a sufficient period. The multi-level assessment, in contrast, provides an equivalent induced expansion inferred from the microscopic and mechanical indicators comparable to the damage degree that would be

produced under unrestrained expansion. In non-reinforced beams subjected to vertical moisture gradients, the main limitation of expansion arises from non-uniform swelling between more saturated and drier zones, which generates self-equilibrated stress fields and internal self-restraint rather than uniform free expansion, as demonstrated in experimental and modelling results of non-reinforced DEF-affected concrete [66].

Moisture-controlled mobilisation of the DEF potential is central to this divergence. Tests on concrete mixtures equivalent to those used in the moderate- and severe-DEF beams have shown that the moisture sequence governs both the kinetics and the maximum expansion [11,13]. Under long wetting–drying cycles, moderate- and severe-DEF concretes reached ultimate expansions similar to those under continuous immersion, although with slower kinetics [11]. Under short wetting–drying cycles, designed with relatively brief immersion and long drying phases, the maximum expansions were reduced by approximately 54% and 36% for the moderate and severe DEF mixtures, respectively, when compared with continuously immersed specimens [13]. Residual expansion testing performed by Martin [18] on cores extracted from the severe DEF beam investigated herein yielded free-expansion capacities of about 2.00%, 1.27%, 0.90%, 0.48%, and 0.23% at 0–10 cm, 10–20 cm, 20–30 cm, 30–40 cm, and 40–50 cm, respectively, whereas the residual expansions measured in this programme (Figure 7.7) were about 0.66%, 0.52%, 0.36%, and 0.23% at 0–10 cm, 10–20 cm, 20–30 cm, and 30–40 cm. This comparison indicates that, for concretes of similar composition, the availability of water and the duration of wet and dry periods play an important role in the mobilisation of DEF expansion.

This distinction between "potential chemical advancement" and induced expansion forms the basis for the integrated diagnosis-to-prognosis approach.

7.6.5 Integrated diagnosis-to-prognosis approach

The integrated diagnosis-to-prognosis approach combines, at each depth, the multi-level estimate of the current induced expansion with the Bayesian residual-expansion model established in Section 7.6.3. In Section 7.6.3, the residual expansion potential is represented by the Larive-type sigmoidal law $\varepsilon_{res}(t \mid \varepsilon_{\infty,res}, \tau_{L,res}, \tau_{C,res})$ (Equation 7.9), calibrated on residual expansion increments measured during the residual expansion test. Specifically, for each core, the measured axial expansion series $\varepsilon_{meas}(t_i)$ is expressed as an increment relative to the beginning of the residual

expansion test, $\varepsilon_{res,i}^{obs} = \varepsilon_{meas}(t_i) - \varepsilon_{meas}(t_0)$ (Equation 7.10), where t_0 is the time of the first finite reading after test initiation. This baseline correction sets $\varepsilon_{meas}(t_0)$ as the reference value for calibration and ensures that the Bayesian model captures only the additional swelling occurring under favourable moisture conditions during the residual expansion test. The Bayesian formulation in Equations 7.11–7.13, together with the highest-density interval $HDI_{0.95}(t)$ (Equation 7.14), therefore yields, at each depth, a 95% credible envelope for the incremental residual expansion $\varepsilon_{res}^{pred}(t)$ referenced to t_0.

In the integrated framework, the zero-baseline convention used for residual expansion test calibration is replaced by an externally estimated offset representing the induced expansion already present in the beam at the time of coring $\varepsilon_{ML}(t_{coring})$, determined through the ML protocol (section 7.6.2). The Bayesian residual model from Section 7.6.3 then quantifies the additional swelling that may occur if the material is subsequently exposed to nearly free, favourable moisture conditions. For each posterior sample of the residual parameters, the incremental residual curve $\varepsilon_{res}^{pred}(t)$ is evaluated from Equation (7.9), and the corresponding diagnosis-to-prognosis induced expansion is written as $\varepsilon_{tot}(t) = \varepsilon_{ML}(t_{coring}) + \varepsilon_{res}^{pred}(t)$. Here, $\varepsilon_{res}^{pred}(t)$ remains an increment referenced to the residual expansion test starts (t_0), while $\varepsilon_{ML}(t_{coring})$ provides the current induced expansion level in the beam; their sum therefore represents a diagnosis-to-prognosis trajectory that begins at the diagnosed induced expansion extent and evolves according to the probabilistic residual swelling capacity under favourable moisture conditions. At each time t, the 95% highest-density interval of $\varepsilon_{tot}(t)$ is therefore obtained by shifting the 95% HDI of $\varepsilon_{res}^{pred}(t)$ by the deterministic offset $\varepsilon_{ML}(t_{coring})$.

Figure 7.20 presents the resulting depth-wise induced-expansion and the projected HDI envelopes of potential residual expansion for both beams. For the moderate DEF-affected beam (Figure 7.20a), the envelopes indicate moderate current expansion and a limited residual swelling capacity, whereas for the severe DEF-affected beam (Figure 7.20b), they show larger current expansion, particularly in the lower half of the beam, together with a significant remaining swelling potential when favourable moisture conditions become available.

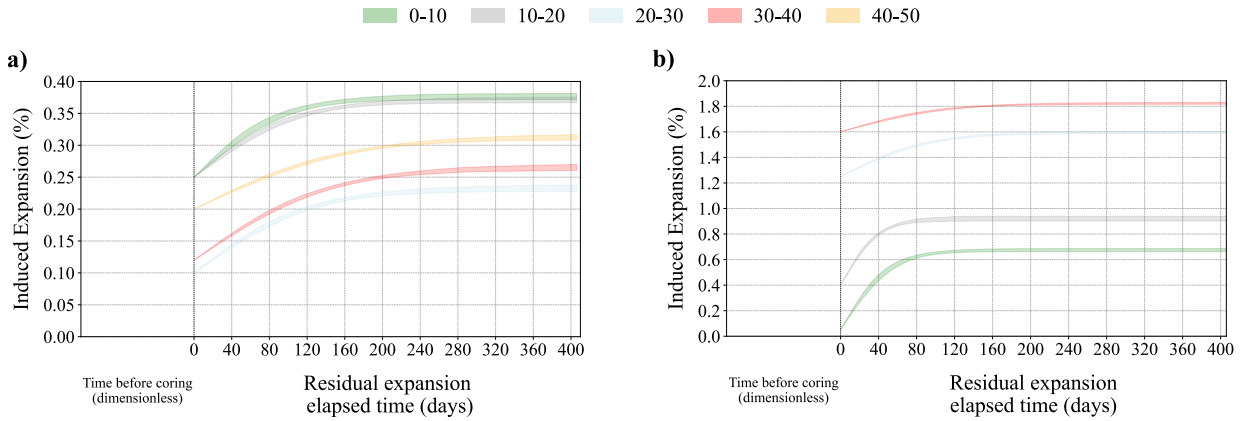


Figure 7.20 – Diagnosis-to-prognosis representation of a) moderate and b) severe DEF, obtained by combining the current induced-expansion estimated through the multi-level assessment protocol with the Bayesian modeling of residual expansion.

7.7 Conclusion

This study examined the role of moisture gradients on the current deterioration condition and remaining swelling potential of non-reinforced concrete beams affected by DEF. A combined diagnostic and prognostic protocol, integrating microscopic assessment (DRI), mechanical testing (SDT), residual expansion analysis supported by Bayesian modeling, and semi-empirical moisture-transfer analysis, was applied to beams with moderate and severe DEF potential.

- Moisture gradients governed the progression of DEF-related deterioration. In moderate DEF, deterioration was distributed across the beam height with localized intensification in the upper layers after late water supply. In severe DEF, water imbibition from the bottom boundary drove a stratified profile with progressive deterioration toward the bottom depths.
- Microscopic results (DRI), mechanical indicators (SDT), and current expansion estimates derived from the multi-level assessment were consistent with water-transfer modeling, highlighting the dependence of deterioration severity on both cement reactivity and moisture exposure history.
- Residual expansion tests, combined with Bayesian fitting, revealed that regions exposed later to water retained significant swelling potential, whereas zones subjected to early and sustained moisture had already consumed most of their expansion capacity, with credible HDI intervals, adding uncertainties to the analysis of residual expansion.

- Comparison with free-expansion reference curves showed that the chemical swelling potential under continuously favourable conditions can substantially exceed the induced expansion estimated for concrete when subjected to non-uniform humidity, because internal self-restraint between wetter and drier zones limits the expression of expansion at the member scale.
- The integrated diagnosis-to-prognosis approach, which superposes the multi-level estimate of current-induced expansion on the Bayesian residual envelopes, produces depth-wise induced-expansion fields that link current deterioration with remaining swelling potential under nearly free-moisture conditions.
- The combined use of multi-level diagnostics, probabilistic residual capacity, and moisture-transfer gradient history of different locations of the affected member, rather than relying on uniform free-expansion assumptions or single-location measurements, showed promising results for the diagnosis and prognosis of DEF-affected concrete members.

7.8 References

[1] B. Godart, L. Divet, Lessons learned from structures damaged by delayed ettringite formation and the French prevention strategy, in: Fifth International Conference on Forensic Engineering, Institution of Civil Engineers, London (UK), 2013: pp. 389–400.

[2] J. Skalny, Internal sulfate attack-Points of agreement and disagreement, in: K. Scrivener, J. Skalny (Eds.), International RILEM TC 186-ISA Workshop on Internal Sulfate Attack and Delayed Ettringite Formation, RILEM, Villars, Switzerland, 2002: pp. 265–276.

[3] F. Toutlemonde, B. Kchakech, O. Omikrine Metalssi, R.-P. Martin, DEF coupled to thermal history: Recent Advances, in: Concrack 5, JCI-Rilem International Workshop, Tokyo, Japan, 2017: pp. 175–188.

[4] M. Malbois, Analyse multi-echelle des déformations différées dans les matériaux cimentaires sous dessiccation ou réaction sulfatique interne, Doctoral thesis, Université Paris-Saclay, 2019. https://theses.fr/2019SACLN025.

[5] H.F.W. Taylor, Sulfates in Portland clinker and cement, in: S. Karen, J. Skalny (Eds.), International RILEM Workshop on Internal Sulfate Attack and Delayed Ettringite Formation, RILEM, 2002: pp. 3–17.

[6] H.F.W. Taylor, C. Famy, K.L. Scrivener, Delayed ettringite formation, 31 (2001) 683–693. https://doi.org/10.1016/S0008-8846(01)00466-5.

[7] K.L. Scrivener, J.P. Skalny, Conclusions of the International RILEM TC 186-ISA workshop on Internal Sulfate Attack and Delayed Ettringite Formation (4–6 September 2002,

Villars, Switzerland), Materials and Structures/Materiaux et Constructions 38 (2005) 659–663. https://doi.org/10.1617/14111.

[8] G. Escadeillas, J.-E. Aubert, M. Segerer, W. Prince, Some factors affecting delayed ettringite formation in heat-cured mortars, Cem Concr Res 37 (2007) 1445–1452. https://doi.org/10.1016/j.cemconres.2007.07.004.

[9] M. Collepardi, A state-of-the-art review on delayed ettringite attack on concrete, Cem Concr Compos 25 (2003) 401–407. https://doi.org/10.1016/S0958-9465(02)00080-X.

[10] S.O. Ekolu, M.D.A. Thomas, R.D. Hooton, Implications of pre-formed microcracking in relation to the theories of DEF mechanism, Cem Concr Res 37 (2007) 161–165. https://doi.org/10.1016/j.cemconres.2006.10.014.

[11] R.-P. Martin, A. Bonnet, J.-C. Renaud, R. Chlela, F. Toutlemonde, C. Sauvaget, Influence of moisture on the development of delayed ettringite formation, Magazine of Concrete Research 75 (2023) 747–754. https://doi.org/10.1680/jmacr.22.00282.

[12] M. Al Shamaa, S. Lavaud, L. Divet, G. Nahas, J.M. Torrenti, Influence of relative humidity on delayed ettringite formation, Cem Concr Compos 58 (2015) 14–22. https://doi.org/10.1016/j.cemconcomp.2014.12.013.

[13] R.-P. Martin, F. Toutlemonde, C. Sauvaget, Effects of Alternative Wetting and Drying on the Development of Delayed Ettringite Formation, in: L.F.M. Sanchez, C. Trottier (Eds.), 17th International Conference on Alkali-Aggregate Reaction in Concrete (ICAAR), RILEM Bookseries, Volume 49, Springer, Ottawa, 2024: pp. 176–183. https://doi.org/10.1007/978-3-031-59419-9_21.

[14] L. Divet, A. Pavoine, Delayed Ettringite Formation in massive concrete structures: an account of some studies of degraded bridges, in: K. and S.J.P. Scrivener (Ed.), International RILEM TC 186-ISA Workshop on Internal Sulfate Attack and Delayed Ettringite Formation, Villars, Switzerland, 2002: pp. 98–126.

[15] P. Fasseu, B. Mahut, Aide à la gestion des ouvrages atteints de réactions de gonflement interne : Guide méthodologique, GUIDES TECHNIQUES, Laboratoire Central des Ponts et Chaussées (LCPC), Paris, 2003.

[16] B. Godart, O. Omikrine-Metalssi, B. Kchakech, S. Lavaud, The effects of delayed ettringite formation on the expansion of a massive bridge pier and a precast prestressed concrete beam of a bridge, in: International Conference on Alkali Aggregate Reaction (ICAAR), São Paulo (Brazil), 2016.

[17] B. Godart, L. Divet, Recommendations for preventing disorders due to delayed ettringite formation: technical guide, Ifsttar, Techniques et Méthodes - Guide Technique - GTI5 (2018).

[18] R.P. Martin, Analyse sur structures modèles des effets mécaniques de la réaction sulfatique interne du béton, PhD thesis, Université Paris Est., 2010. https://theses.hal.science/tel-00558200.

[19] U. Ludwing, Effects of environmental conditions on alkali-aggregate reaction and preventive measures, in: 8th International Conference on Alkali-Aggregate Reaction, Kyoto (Japan), 1989: pp. 583–596.

[20] L.A. Graf, effect of relative humidity on expansion and microstructure of heat-cured mortars. research and development, 2007.

[21] P.K. Sarkar, N. Mitra, D. Prasad, Molecular level deformation mechanism of ettringite, Cem Concr Res 124 (2019) 105836. https://doi.org/10.1016/j.cemconres.2019.105836.

[22] L.G. Baquerizo, T. Matschei, K.L. Scrivener, Impact of water activity on the stability of ettringite, Cem Concr Res 79 (2016) 31–44. https://doi.org/10.1016/j.cemconres.2015.07.008.

[23] M. Jebli, F. Jamin, C. Pelissou, E. Lhopital, M.S. El Youssoufi, Characterization of the expansion due to the delayed ettringite formation at the cement paste-aggregate interface, Constr Build Mater 289 (2021) 122979. https://doi.org/10.1016/j.conbuildmat.2021.122979.

[24] Y. Thiebaut, Evaluation de structures en béton armé atteintes de réaction sulfatique interne, Doctoral thesis, Université Toulouse III – Paul Sabatier, 2018. https://theses.fr/2018TOU30271.

[25] D. Damidot, F.P. Glasser, Thermodynamic investigation of the CaO-Al2O3-CaSO4-H2O system at 50°C and 85°C, Cem Concr Res 22 (1992) 1179–1191. https://doi.org/10.1016/0008-8846(92)90047-Y.

[26] D. Damidot, F.P. Glasser, Thermodynamic investigation of the CaO-Al2O3-CaSO4-H2O system at 25°C and the influence of Na_2O, Cem Concr Res 23 (1993) 221–238. https://doi.org/10.1016/0008-8846(93)90153-Z.

[27] L.F.M. Sanchez, T. Drimalas, B. Fournier, D. Mitchell, J. Bastien, Comprehensive damage assessment in concrete affected by different internal swelling reaction (ISR) mechanisms, Cem Concr Res 107 (2018) 284–303. https://doi.org/10.1016/j.cemconres.2018.02.017.

[28] A. Pichelin, M. Carcassès, F. Cassagnabère, S. Multon, G. Nahas, Characterization of DEF affected concretes: detection and modification of properties, Materiales de Construcción 72 (2022) e284. https://doi.org/10.3989/mc.2022.17321.

[29] R.-P. Martin, L. Sanchez, B. Fournier, F. Toutlemonde, Evaluation of different techniques for the diagnosis & prognosis of Internal Swelling Reaction (ISR) mechanisms in concrete, Constr Build Mater 156 (2017) 956–964. https://doi.org/10.1016/j.conbuildmat.2017.09.047.

[30] M. Thomas, K. Folliard, T. Drimalas, T. Ramlochan, Diagnosing delayed ettringite formation in concrete structures, Cem Concr Res 38 (2008) 841–847. https://doi.org/10.1016/j.cemconres.2008.01.003.

[31] L.F.M. Sanchez, R.-P. Martin, Condition assessment of ISR-induced deterioration of concrete structures: connecting material analysis and structural-performance evaluation, Canadian Journal of Civil Engineering 53 (2026) 1–14. https://doi.org/10.1139/cjce-2025-0316.

[32] P.A. Dunbar, P.E. Grattan-Bellew, Results of damage rating evaluation of condition of concrete from a number of structures affected by AAR, in: B. Fournier (Ed.), Proceedings of the CANMET/ACI International Workshop on Alkali-Aggregate Reactions in Concrete, CANMET/ACI, Dartmouth (Nova Scotia), 1995: pp. 257–265.

[33] P.E. Grattan-Bellew, A. Danay, Comparison of laboratory and field evaluation of alkali-silica reaction in large dams, in: Proceedings of the International Conference on Concrete Alkali–Aggregate Reactions in Hydroelectric Plants and Dams, Canadian Electrical Association;

Canadian National Committee of the International Commission on Large Dams, Fredericton, New Brunswick, Canada , 1992: p. 23.

[34] V. Villeneuve, B. Fournier, J. Duchesne, Determination of the Damage in Concrete Affected by ASR—The Damage Rating Index (DRI), in: T. Drimalas, J. H. Ideker, B. Fournier (Eds.), 14th International Conference on Alkali-Aggregate Reaction (ICAAR), University of Texas at Austin, Austin, Texas, USA, 2012: p. 10. https://icaarconcrete.org/wp-content/uploads/2022/10/14ICAAR-VilleneuveV-1.pdf.

[35] V. Villeneuve, Détermination de l'endommagement du béton par méthode pétrographique quantitative, Master's thesis (Mémoire de maîtrise), Université Laval, 2011. https://www.collectionscanada.gc.ca/obj/thesescanada/vol2/QQLA/TC-QQLA-27962.pdf.

[36] L.F.M. Sanchez, B. Fournier, M. Jolin, J. Duchesne, Reliable quantification of AAR damage through assessment of the Damage Rating Index (DRI), Cem Concr Res 67 (2015) 74–92. https://doi.org/10.1016/j.cemconres.2014.08.002.

[37] L. Sanchez, B. Fournier, M. Jolin, M.A.B. Bedoya, J. Bastien, J. Duchesne, Use of Damage Rating Index to Quantify Alkali-Silica Reaction Damage in Concrete: Fine versus Coarse Aggregate, ACI Mater J 113 (2016) 395–407. https://doi.org/10.14359/51688983.

[38] R. Medeiros, L. Sanchez, A.C. dos Santos, Assessing Alkali-Carbonate Reaction-Induced Damage in Critical Concrete Infrastructure: The First ACR-Affected Field Structure Reported in Brazil, in: L.F. Sanchez, C. Trottier (Eds.), Proceedings of the 17th International Conference on Alkali-Aggregate Reaction in Concrete. ICAAR 2024.RILEM Bookseries, Springer, 2024: pp. 445–452. https://doi.org/10.1007/978-3-031-59349-9_51.

[39] J.B. Walsh, The effect of cracks on the compressibility of rock, J Geophys Res 70 (1965) 381–389.

[40] R.S. Crouch, Specification for the Determination of Stiffness Damage Parameters from the Low Cyclic Uniaxial Compression of Plain Concrete Cores, Revision A, Mott, Hay & Anderson, Special Services Division, Internal Technical Note. (1987).

[41] T.M. Crisp, J.G.M. Wood, P. Norris, Towards Quantification of Microstructural Damage in AAR Deteriorated Concrete, in: International Conference on Recent Developments on the Fracture of Concrete and Rock, 1993.

[42] T.M. Crisp, P. Waldron, J.G.M. Wood, Development of a non destructive test to quantity damage in deteriorated concrete, Magazine of Concrete Research 45 (1989).

[43] L.F.M. Sanchez, B. Fournier, M. Jolin, J. Bastien, Evaluation of the Stiffness Damage Test (SDT) as a tool for assessing damage in concrete due to alkali-silica reaction (ASR): Input parameters and variability of the test responses, Constr Build Mater 77 (2015) 20–32. https://doi.org/10.1016/j.conbuildmat.2014.11.071.

[44] L.F.M. Sanchez, B. Fournier, M. Jolin, J. Bastien, Evaluation of the stiffness damage test (SDT) as a tool for assessing damage in concrete due to ASR: Test loading and output responses for concretes incorporating fine or coarse reactive aggregates, Cem Concr Res 56 (2014) 213–229. https://doi.org/10.1016/j.cemconres.2013.11.003.

[45] L.F.M. Sanchez, B. Fournier, M. Jolin, J. Bastien, D. Mitchell, Practical use of the Stiffness Damage Test (SDT) for assessing damage in concrete infrastructure affected by alkali-silica reaction, Constr Build Mater 125 (2016) 1178–1188. https://doi.org/10.1016/j.conbuildmat.2016.08.101.

[46] E.R. Giannini, L.F.M. Sanchez, A. Tuinukuafe, K.J. Folliard, Characterization of concrete affected by delayed ettringite formation using the stiffness damage test, Constr Build Mater 162 (2018) 253–264. https://doi.org/10.1016/j.conbuildmat.2017.12.012.

[47] L.F.M. Sanchez, B. Fournier, D. Mitchell, J. Bastien, Condition assessment of an ASR-affected overpass after nearly 50 years in service, Constr Build Mater 236 (2020) 117554. https://doi.org/10.1016/j.conbuildmat.2019.117554.

[48] R. Medeiros, L. Sanchez, A.C. dos Santos, Exploring microscopic and mechanical tools to uncover the anisotropic damage evolution of prestressed concrete sleepers affected by internal swelling reactions, Magazine of Concrete Research 77 (2025) 891–902. https://doi.org/10.1680/jmacr.25.00060.

[49] R. Medeiros, D.J. De Souza, L.F.M. Sanchez, A.C. Santos, Condition assessment of pre-tensioning prestressed concrete sleepers distressed by internal swelling reactions (ISR), CEMENT 21 (2025) 100154. https://doi.org/10.1016/j.cement.2025.100154.

[50] A. Pavoine, L. Divet, Réaction sulfatique interne au béton : Essai d'expansion résiduelle sur carotte de béton extraite de l'ouvrage : Méthode d'essai n° 67, Techniques et méthodes des laboratoires des ponts et chaussées., Paris, 2009. https://doi.org/https://doi.org/10.3829/me67-fr.

[51] T. Ramlochan, P. Zacarias, M.D.A. Thomas, R.D. Hooton, The effect of pozzolans and slag on the expansion of mortars cured at elevated temperature, Cem Concr Res 33 (2003) 807–814. https://doi.org/10.1016/S0008-8846(02)01066-9.

[52] K.J. Folliard, M.D.A. Thomas, B. Fournier, Protocol for the Diagnosis and Prognosis of Concrete Structures Affected by Alkali-Silica Reaction and/or Delayed Ettringite Formation, Concrete Durability Center, The University of Texas at Austin, Austin, Texas, USA, 2007.

[53] E. Giannini, K. Folliard, J. Zhu, O. Bayrak, K. Kreitman, B. Hanson, Non-Destructive Evaluation of In-Service Concrete Structures Affected by Alkali-Silica Reaction (ASR) or Delayed Ettringite Formation (DEF)—Final Report, Part I, 2013.

[54] S. Multon, F.-X. Barin, B. Godart, F. Toutlemonde, Estimation of the Residual Expansion of Concrete Affected by Alkali Silica Reaction, Journal of Materials in Civil Engineering 20 (2008) 54–62. https://doi.org/10.1061/(ASCE)0899-1561(2008)20:1(54).

[55] C. Larive, Apports combinés de l'expérimentation et de la modélisation à la compréhension de l'alcali-réaction et de ses effets mécaniques, PhD, Ecole Nationale des Ponts et Chaussées, 1997. https://theses.hal.science/tel-00520676.

[56] X. Brunetaud, Étude de l'influence de différents paramètres et de leurs interactions sur la cinétique de l'amplitude de la réaction sulfatique interne au béton, Ph.D. thesis, Châtenay-Malabry, Ecole centrale de Paris, 2005. https://theses.fr/2005ECAP1025.

[57] A. Pavoine, X. Brunetaud, Développement et validation d'une méthode d'essai vis-à-vis de la formation différée de l'ettringite Application à l'étude d'impact de différents paramètres sur la cinétique et l'amplitude de gonflement, (2010). https://doi.org/10.3829/erlpc.oa65-fr.

[58] S. Multon, F.-X. Barin, B. Godart, F. Toutlemonde, Estimation of the Residual Expansion of Concrete Affected by Alkali Silica Reaction, Journal of Materials in Civil Engineering 20 (2008) 54–62. https://doi.org/10.1061/(asce)0899-1561(2008)20:1(54).

[59] F.-J. Ulm, O. Coussy, K. Li, C. Larive, Thermo-Chemo-Mechanics of ASR Expansion in Concrete Structures, J Eng Mech 126 (2000) 233–242. https://doi.org/10.1061/(ASCE)0733-9399(2000)126:3(233).

[60] R.-P. Martin, F. Toutlemonde, Theoretical and experimental validation of a simple method to reproduce representative DEF-prone conditions in laboratory, Mater Struct 46 (2013) 1245–1255. https://doi.org/10.1617/s11527-012-9967-2.

[61] R. Loser, B. Lothenbach, A. Leemann, M. Tuchschmid, Chloride resistance of concrete and its binding capacity – Comparison between experimental results and thermodynamic modeling, Cem Concr Compos 32 (2010) 34–42. https://doi.org/10.1016/j.cemconcomp.2009.08.001.

[62] D.P. Prentice, B. Walkley, S.A. Bernal, M. Bankhead, M. Hayes, J.L. Provis, Thermodynamic modelling of BFS-PC cements under temperature conditions relevant to the geological disposal of nuclear wastes, Cem Concr Res 119 (2019) 21–35. https://doi.org/10.1016/j.cemconres.2019.02.005.

[63] P.E. Grattan-Bellew, L.D. Mitchell, Quantitative petrographic analysis of concrete –The Damage Rating Index (DRI) method, a review, in: Proc. Marc-André Bérubé Symposium on AAR in Concrete, CANMET/ACI Advances in Concrete Technology Seminar, CANMET/ACI, Montréal, Canada, 2006: pp. 321–334.

[64] X. Zhu, Assessing Drying Shrinkage Induced Deterioration of Concrete Stored at Distinct Exposure Conditions, Master of applied science, University of Ottawa, 2024.

[65] Y. Kawabata, R.-P. Martin, J.-F. Seignol, F. Toutlemonde, Modelling of evolution of transfer properties due to expansion of concrete induced by internal swelling reaction, in: H.M. Bernardes, N.P. Hasparyk (Eds.), 15th International Conference on Alkali-Aggregate Reaction in Concrete (ICAAR), São Paulo, Brazil, 2016: pp. 287–295. https://icaarconcrete.org/wp-content/uploads/2020/11/15ICAAR-KawabataY-2.pdf.

[66] P. Morenon, Modélisation des réactions de gonflement interne des bétons avec prise en compte des couplages poro- mécaniques et chimiques, PhD thesis, Université Toulouse III – Paul Sabatier, 2017.

Chapter 8: Paper III - Evaluation of the influence of reinforcement configurations on the diagnosis and prognosis of DEF-affected concrete under moisture gradients

Rennan Medeiros [1]; Leandro Sanchez [2]; Renaud-Pierre Martin[3]; François Toutlemonde [4]

[1]PhD Candidate – University of Ottawa, Department of Civil Engineering
[2]Full Professor – University of Ottawa, Department of Civil Engineering
[3]Univ Gustave Eiffel, MAST-EMGCU, F-77454 Marne - la- Vallée, France
[4] Univ Gustave Eiffel, MAST-EMGCU, F-77454 Marne - la- Vallée, France

ABSTRACT

This study investigates how reinforcement configuration influences the diagnosis and prognosis of delayed ettringite formation (DEF) in concrete beams exposed to moisture gradients. Three beams (non-, moderately, and heavily reinforced) cast with DEF-prone concrete, exposed to partial immersion and subsequently top-rewetted, were assessed using a multi-level protocol combining microscopic assessment (DRI and crack geometry), stiffness damage testing (SDT), residual expansion under 38 °C water immersion, and moisture-profile modelling. A Bayesian formulation of Larive's law, anchored to multi-level induced-expansion estimates, was used to project future swelling. Direction- and depth-dependent responses, including DRI number, crack openings, residual stiffness, and residual expansion, reflected the combined influence of reinforcement-induced restraint, moisture exposure history, and accommodation of additional DEF-induced swelling during residual expansion testing within the pre-existing crack network.

Keywords: Delayed ettringite formation (DEF); Reinforced concrete beams; Diagnosis; Prognosis; Moisture gradients; Multi-level diagnostics (DRI, SDT); Residual expansion.

8.1 Introduction

Delayed ettringite formation (DEF) is a chemical reaction involving the recrystallization of late ettringite after the decomposition of primary ettringite during exposure to elevated temperature at early ages, typically exceeding 65 °C, under sufficient moisture [1,2]. DEF induces internal pressures within the micropores of the cement paste, leading to expansion and progressive

deterioration, and constitutes one of the most damaging mechanisms compromising the durability and structural performance of critical concrete infrastructure worldwide [3–5].

DEF-induced development has been extensively investigated under unrestrained and continuous-moisture conditions. Under these conditions, cracking initiates and propagates throughout the cement paste and the interfacial transition zone (ITZ), and mechanical properties decrease as expansion increases, with damage and expansion frequently reported as broadly isotropic [6–13]. Structural members, however, develop DEF under boundary conditions that include restraint imposed by reinforcement and non-uniform water supply. Restraint reduces expansion in the restrained directions, and the expansion is consequently redistributed towards the less restrained directions. This redistribution generates anisotropic expansion, leading to direction dependent microcracking patterns and distinct mechanical responses. [9,14,15]. Moreover, moisture gradients influence ionic transport and the dissolution–precipitation mechanisms associated with ettringite recrystallization, thereby affecting both the rate and extent of swelling [12,16–18]. These coupled effects complicate the definition of a representative "overall damage" state during condition assessment and constrain the direct transfer of laboratory relationships among expansion, microstructural deterioration, and mechanical response for the diagnosis and prognosis of DEF-affected members. This study addresses this gap by appraising the current condition and the remaining potential for induced expansion of DEF-affected beams with distinct reinforcement configurations (non-reinforced, moderately reinforced, and heavily reinforced) exposed to moisture gradients, using a multi-level protocol integrating microscopic analysis (i.e., Damage Rating Index - DRI), mechanical tests (i.e., Stiffness Damage Test - SDT), and residual expansion analysis.

8.2 Background

8.2.1 DEF-induced deterioration under unrestrained conditions

DEF-induced microcracking has been explained through two main theories: (i) localized crystallization and stress concentration within the interfacial transition zone (ITZ), in which ettringite precipitation promotes cracking and progressive debonding at the aggregate–paste interface (ii) distributed swelling of the cement paste, driven by ettringite formation in confined

micropores within the outer calcium silicate hydrate (C–S–H), particularly near the boundary with inner C–S–H, with the associated crystallization pressure leading to microcracking and expansion [1,19,20]. Both theories rely on crystallization pressure developing in confined spaces, yet experimental evidence has not established a unique basis for quantifying their respective contributions to the observed overall behaviour [1,21].

Under unrestrained, continuous moisture conditions, DEF-induced cracking is reported to initiate in the bulk cement paste and ITZ, outlining the aggregates and extending into the bulk paste. As expansion progresses, isolated paste cracks lengthen, and deterioration in the ITZ becomes more evident through the debonding of aggregate particles. At advanced expansion levels, the accumulated cracking forms an extensive network distributed throughout the affected concrete. This behavior has been broadly reported as reasonably isotropic in unrestrained specimens under uniform moisture exposure [6,8,15].

The mechanical response of DEF affected concrete under free expansion has been quantified through systematic studies linking predefined expansion levels to losses in compressive strength and modulus of elasticity [7,8]. These investigations show a progressive degradation as expansion increases, with significant reductions in strength and stiffness once microcracking coalesces into connected networks involving both the cement paste and the ITZ. The modulus of elasticity typically decreases more sharply than compressive strength because crack propagation and aggregate–paste debonding reduce the effective stiffness contribution of the coarse aggregates and promote strain localization before peak stress [8]. These reductions in mechanical properties have been shown to be essentially isotropic under unrestrained expansion conditions [7,8].

8.2.2 DEF-induced deterioration under restrained conditions: implications for current and future performance

DEF in restrained concrete differs from DEF under free expansion conditions because internal or external restraints limit the induced expansion in the restrained directions, even though the underlying chemical reaction and associated microcracking continue to progress [9,15,16]. Experimental studies on mortar and concrete mixtures show that free expansion conditions lead to essentially isotropic expansion, whereas the presence of restraint suppresses deformation along the restrained direction and produces anisotropic expansion; an effect commonly referred to as

expansion transfer [9,15,22]. Expansion in the restrained direction is typically severely reduced, often by 75–90%, depending on the level of restraint, while expansion in the less restrained directions remains similar to, or higher than, that measured under free expansion conditions [15]. For ASR-affected concrete, Zahedi [23,24] demonstrated that restraint primarily redistributes expansion among orthogonal directions, although the overall volumetric expansion remains essentially unchanged; in restrained conditions, the expansion simply reorients, with the imposed boundary conditions altering the directionality of strain rather than reducing its magnitude. In contrast, for DEF-affected concrete, Bouzabata et al. [15] reported a fundamentally different response: restrained specimens did not show a compensatory increase in the less restrained directions, leading instead to a net reduction in volumetric expansion compared with free expansion conditions. This divergence was attributed to differences in the mobility of reaction products—ASR gel can migrate through pores and cracks and therefore redistribute under restraint, whereas crystallized ettringite is far less mobile once formed, limiting its ability to reorient expansion.

Microstructural investigations have shown that DEF-induced cracking continues to develop under restraint; however, its characteristics differ from those observed under free-expansion conditions because restraint governs crack opening and orientation under the imposed stress states [9,14,15,22]. Thus, restrained specimens generally exhibit thinner cracks oriented parallel to the direction of restraint, reflecting the limited expansion in that direction. In contrast, the less restrained directions accumulate most of the induced expansion, leading to wider cracks aligned perpendicular to the dominant restraint [15]. At advanced deterioration levels, internal damage includes extensive discontinuities around aggregate particles and deterioration of the ITZ, which induces stiffness loss and increases plastic deformation during cyclic mechanical loading [14]. In reinforced concrete members, cracks may further develop radially around the reinforcement, leading to reduced restraint effectiveness due to deteriorated bond, which affects stress transfer at the steel–concrete interface [22]. Consequently, reduced expansion in restrained directions can coexist with advanced internal damage in the cement paste and ITZ, indicating that directional expansion alone can underestimate the current deterioration condition when restraint is significant [9,14,15,22]. These observations indicate that reinforcement-induced restraint modifies the magnitude, distribution, and progression of DEF-induced expansion while allowing microcracking

and ITZ deterioration to continue developing. This behaviour supports the importance of using microscopic analysis, mechanical testing, and residual expansion appraisal for diagnosing and prognosing DEF-affected members [9,14,15,22,23].

8.2.3 Advanced Appraisal of DEF-Induced Current Deterioration and potential for future development

8.2.3.1 Multi-level assessment protocol – diagnosis

The multi-level assessment protocol combines microscopic and mechanical techniques to evaluate the current damage condition of concrete affected by internal swelling reactions (ISR), including DEF. It integrates the Damage Rating Index (DRI) and the Stiffness Damage Test (SDT) to quantify internal cracking, mechanical degradation, and loss of material integrity.

The DRI is a semi-quantitative microscopy-based method developed to classify distress features on polished surfaces of ISR-affected concrete [24–27] Grattan-Bellew and Danay [28,29] for concrete damaged by alkali-silica reaction (ASR), it was later refined by Villeneuve and Fournier [30,31] to reduce variability and improve reproducibility. The analysis is performed on standardized 1 × 1 cm grids under 16× magnification, where each damage feature is assigned a weighting factor reflecting its diagnostic relevance. The resulting counts are normalized to 100 cm² to enable comparison across samples (Figure 8.1) [24].

To deepen insight into deterioration due to ASR and other mechanisms, including DEF, Sanchez et al. [24,32] proposed an extended version of the DRI. This approach includes unweighted counts and relative percentages of each feature type, allowing a more detailed appraisal of damage mechanisms and their contributions. Crack density (CD), calculated as the number of open cracks per unit area (counts/cm²), is also considered, along with the maximum crack width and length. These parameters provide a direct quantification of microcracking severity, thereby enhancing comparisons across specimens with varying degrees of deterioration. The extended DRI version has proven effective in correlating microstructural deterioration with reductions in mechanical performance across various ISR mechanisms, including DEF.

a)

Features of deterioration		Weighing factor
Aggregate	Closed crack (CCA)	0.25
	Opened crack (OCA)	2
	Opened crack with reaction product (OCA_RP)	2
Cement paste	Crack in the cement paste (CCP)	3
	Crack in the cement with reaction product (CCP_RP)	3
Disaggregate/corroded aggregate particle (DAP)		2
Coarse aggregate debonded (Debon)		3

$$DRI_{number} = \left[\frac{\sum_{i=1}^{i=n} 0.25(CCA)+2(OCA+OCA_{RP}+DAP)+3(CCP+CCP_{RP}+Debon)}{n\ of\ analyzed\ \ 1\ cm\ by\ 1\ cm\ squares}\right] \times 100\ cm^2$$

b)

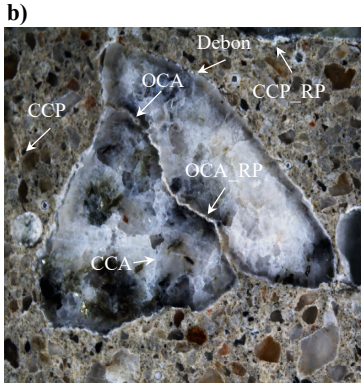


Figure 8.1 – Damage Rating Index, conventional method. a) Damage features classified in DRI analysis [30]. b) Micrograph section (1x1 cm) illustrates most of the damage features [33].

The Stiffness Damage Test (SDT) is a cyclic mechanical test used to quantify internal damage by analyzing the stress–strain response of the affected material. Originally developed by Walsh [34] for rock mechanics, the protocol was adapted by Crouch [35] and Crisp et al. [36,37] to evaluate concrete affected by ASR. Sanchez et al. [38–40] further developed the technique, proposing the use of maximum load relative to the compressive strength of sound concrete, introducing damage indices, and validating the SDT to assess concrete affected by various ISR, including DEF.

The test involves five loading–unloading cycles applied under uniaxial compression at 40% of the compressive strength of undamaged material. However, severely damaged concrete may not withstand the most diagnostic load (i.e., 40%); in this case, the test can be conducted under 30% of the corresponding compressive strength [27]. The SDT analysis yields four parameters: the Stiffness Damage Index (SDI), the Plastic Deformation Index (PDI), the Secant Modulus of Elasticity (E_SDT), and the Non-Linearity Index (NLI) (Figure 8.2). SDI quantifies the energy dissipated due to internal cracking. PDI represents the accumulated plastic deformation relative to total deformation. E_SDT, calculated as the average secant modulus from the second and third loading cycles, which reflects the remaining stiffness of the damaged material. NLI is calculated as the ratio between secant moduli at different stages of the first loading cycle, providing insight into crack orientation. Values above a unit indicate mainly transverse cracks, while values below one suggest cracks aligned with the loading direction.

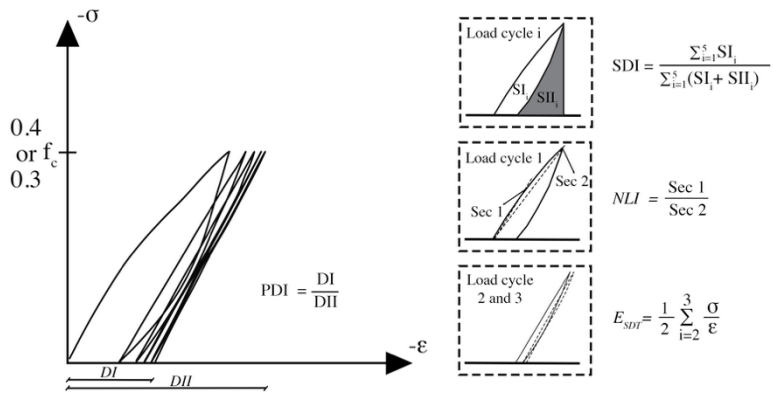


Figure 8.2 – SDT outcomes definition. Stiffness damage index (SDI). Plastic deformation index (PDI). Non-linear index (NLI). Modulus of elasticity (E_{SDT}).

Benchmark values derived from previous experimental studies enable the classification of DEF-induced deterioration severity and are synthesised in Table 8.1. For DEF-affected concrete, SDI values between 0.17 and 0.20 are typically associated with moderate damage, whereas values above 0.43 indicate very high or ultra-high deterioration. In parallel, DRI values commonly range from approximately 350 to more than 1000, depending on the number of cracks and the relative contribution of individual distress features. These mechanical and microstructural indices provide a consistent basis for quantifying the extent of DEF development and estimating the level of expansion already attained by comparing them with the calibrated ranges reported in Table 8.1.

In this context, the thresholds in Table 8.1 provide a structured framework for interpreting mechanical and microstructural results and for inferring the corresponding reference expansion levels from damage measurements. The damage class is assigned by comparing the measured SDI, DRI, and strength- and stiffness-loss values with the diagnostic ranges associated with each severity level, and the corresponding expansion is then estimated from the benchmark intervals. When the measured SDI, DRI, strength- or stiffness-loss values fall outside the tabulated ranges, damage classification and expansion estimates should not rely on simple mathematical extrapolation of the limits given in Table 8.1 [7]. In such cases, it is recommended to return to the original experimental dataset on which Table 8.1 is based, examine the relationships between expansion and the various damage indicators, and position the measured values with respect to the neighbouring data clusters for DEF and DEF + ASR, accounting for characteristics of the concrete under evaluation. This procedure ensures that interpolation remains anchored to the underlying

experimental evidence supporting the benchmark table [7]. Although these diagnostic tools and benchmark relationships have been validated for the appraisal of ISR-affected concrete in different structural contexts [41–43], their application to existing structures requires careful consideration of limiting factors such as stress release during core extraction, changes in in situ moisture conditions, and differences in thermal and restraint histories.

Table 8.1 – Benchmark table of ISR-induced development on affected concrete [7].

Distress Mechanism	Classification of damage degree	Reference level of expansion (%) [a]	Damage results				
			Stiffness loss (%)	Compressive strength loss (%)	Tensile strength loss (%)	SDI	DRI
DEF and DEF + ASR	Negligible	0.00–0.03	–	–	–	0.11	110–147
	Marginal	0.04 ± 0.01	–	–	–	–	–
	Moderate	0.11 ± 0.01	35–56	9–34	–	0.17–0.20	355–599
	High	0.20 ± 0.01	–	–	–	–	–
	Very high	0.30 to 0.50 ± 0.01	55–62	29–43	–	0.19–0.28	623–710
	Ultra-high	0.50 to 1.00 ± 0.01	56–77	40–47	–	0.27–0.43	828–1022
	–	≥1.00 ± 0.01	60–86	40–50	–	0.30–0.54	841–1363

[a] These levels of expansion should not be considered as strict limits among the various damage degrees, but rather indicators/reference levels.

8.2.3.2 Potential for future deterioration – prognosis

Residual expansion testing is used to assess the remaining swelling potential of DEF-affected concrete by accelerating ettringite reformation under controlled, prone conditions. Core specimens are extracted from affected members, re-saturated, and immersed in water at temperatures to stimulate delayed expansion (i.e., 20-38°C). Two main protocols are commonly applied. In one method, cores are immersed in water at 20 ± 2 °C. Length measurements begin after 24-hour moisture and temperature homogenization and continue at the same temperature until expansion stabilizes, revealing the residual swelling potential due to DEF [3,44]. An alternative method recommends maintaining cores in lime-saturated water at 23 °C to ensure the chemical stability of calcium and sulfate, while also encouraging alkali leaching. This environment promotes DEF-related expansion, especially when aggregates reactive to ASR were used in the concrete [45–47]. Despite their operational simplicity, test results are influenced by several factors, including stress release during coring, initial hygric swelling in partially desaturated specimens, leaching of ionic species, and variability in pre-existing damage [3,44].

Semi-empirical modeling of DEF-induced expansion has been used to analyze the residual expansion potential of DEF-affected concrete. The measured residual expansion curves are

represented by fitted functions that capture the main stages of reaction development. Larive's equation [48] describes the expansion of concrete affected by alkali-silica reaction through a sigmoidal law expressed in terms of three empirical parameters: the ultimate expansion (ε_∞), a latency time (τ_L) associated with the dormant or acceleration period, and a characteristic time (τ_C) inversely related to the swelling rate at the inflexion point of the S-shaped curve described by the equation. This law was later extended to analyze DFE-affected concrete [20,49,50]. Multon et al. [51] proposed, in the ASR context, a reconstruction approach in which residual expansion measured on drilled cores is interpreted relative to a pre-calibrated Larive-type free-expansion law representing the full ASR-induced expansion under 100% relative humidity. In their programme, expansion was measured on cylinders and prisms before coring and on extracted cores thereafter, so that the residual expansion curve could be treated as the continuation of the same free-expansion trajectory from an advanced reaction age, with a non-zero expansion at the time of coring; under these controlled conditions, the full "pre-coring + residual" history was reconstructed by summing the measured expansions before and after coring and comparing the result with the 100% relative-humidity reference curve [51]. Martin [20] extended this framework to DEF and DEF+ASR by introducing explicit time and expansion offsets, fitted together with the free-expansion parameters, to align residual expansion curves from cores with laboratory free-swelling references. This DEF adaptation retains the same core assumptions: (i) the affected material follows a parametric free-expansion law calibrated on laboratory free-swelling specimens under well-defined high-humidity conditions; (ii) residual expansion tests represent continuation of that law from an advanced reaction state; (iii) the sum of pre-coring and residual expansion converges toward a common ultimate swelling under favourable moisture; and (iv) restraint effects at the core scale are negligible or secondary.

Residual expansion testing is performed under standard conditions to obtain material characteristics that can later be implemented in different approaches to translate these results into in situ expansion developments. The interpretation of residual expansion outcomes in conjunction with diagnostic indicators such as microscopic damage evaluation and stiffness degradation enhances the assessment of DEF development under non-uniform boundary conditions.

Although the integration of diagnostic and prognostic tools provides a more comprehensive appraisal of DEF-induced deterioration in reinforced concrete under restraint, their combined

application to quantify how reinforcement configuration and moisture gradients influence current condition and future deterioration potential remains limited.

8.3 Scope of the work

As discussed in the previous sections, the combined influence of reinforcement and moisture gradients on DEF-induced deterioration remains insufficiently characterised at the materials scale in structural concrete members. To address this gap, three large-scale concrete beams were fabricated using a DEF-prone concrete mixture and distinct reinforcement configurations: non-reinforced, moderately reinforced, and heavily reinforced. Throughout conditioning, the lateral faces were sealed to limit transverse water transport. During the first 14 months, the bottom face was immersed to a depth of 7 cm, while the top face was maintained at 30% relative humidity. During the subsequent 14 months, water was also supplied to the top face to evaluate the effect of delayed wetting. After 28 months, the beams were tested to assess their residual load-bearing capacity and were subsequently stored under laboratory conditions (22 ± 4 °C; 50–70% relative humidity) for further assessment.

To evaluate the damage accumulated to date in the affected members, core samples were extracted in the transverse, vertical, and longitudinal directions and tested using a multi-level protocol combining the Damage Rating Index (DRI) and the Stiffness Damage Test (SDT). This protocol enabled the quantification of microstructural deterioration, mechanical degradation, and estimated induced expansion as functions of orientation (transverse, longitudinal, and vertical) and depth (upper and lower parts). Selected cores were further subjected to residual expansion (RE) testing to characterise the remaining free swelling capacity under favourable moisture conditions. RE curves were modelled using a Larive-type sigmoidal law [48], and the apparent empirical parameters were estimated within a probabilistic framework. The resulting RE projections were integrated with the corresponding expansion levels obtained from the multi-level protocol to provide a comprehensive picture of the induced expansion and deterioration experienced by the affected beams.

8.4 Materials and methods

8.4.1 Description of the specimens

Three concrete beams with distinct reinforcement configurations (i.e., non-reinforced, moderately reinforced, and heavily reinforced) were manufactured at the former *Laboratoire central des ponts et chaussées* (LCPC), currently the *Laboratoire Expérimentation et Modélisation pour le Génie Civil et Urbain* (EMGCU) of the *Département Matériaux et Structures* at *Université Gustave Eiffel* in Paris, France, as part of the research program developed by Martin [20]. The beams, with nominal dimensions of 0.25 m (height), 0.50 m (width), and 3.00 m (length) and simply supported over a span of 2.80 m (Figure 8.3), were cast with concretes designed to develop severe DEF. The severity of DEF was obtained using (i) Portland cement containing 4.97% C_3A, 3.46% SO_3, and 0.83% Na_2O_{eq}, and (ii) 1.1% raising the alkali content (Na_2O_{eq}) by adding 1.745 kg KOH per cubic meter to enhance primary ettringite decomposition.

The mixture yielded a 28-day compressive strength of 38.7 MPa and modulus of elasticity of 30.8 GPa, using a water-to-cement ratio of 0.46. The non-reinforced beam contained no structural reinforcement. The moderately reinforced beam was detailed with two 16 mm bars in the tensile (bottom) zone and two 10 mm bars in the compression (top) zone, together with 8 mm stirrups at 0.35 m spacing. The heavily reinforced beam used two 32 mm bars in the tensile zone and two 20 mm bars in the compression zone with 12 mm stirrups at 0.20 m spacing (Figure 8.3a). These layouts correspond to longitudinal reinforcement ratios of approximately 0.45% and 1.8% and transverse reinforcement ratios of 0.12% and 0.45% for the moderately and heavily reinforced beams, respectively.

To replicate cast-in-place massive-element curing conditions and trigger DEF, the beams were transferred 2 hours after casting to a temperature-controlled water bath with a programmed thermal cycle comprising an initial heating stage aligned with the adiabatic temperature rise of the mix, a constant plateau at 81 °C for 72 h, and a controlled cooling at about 1 °C h^{-1}, for a total duration of approximately 6 days [20,52]. Afterwards, the beams were subjected to vertical moisture gradients in two phases: (a) partial immersion of the bottom 7 cm for 14 months, with the top surface exposed to drying (≈30% RH), and (b) additional water supply at the top surface for another 14 months to evaluate the effect of late water supply. During this period, the beams were

stored at 38 ± 1 °C and 30% RH, with lateral faces sealed to prevent transverse water exchange (Figure 8.3). The reinforced beam experienced both phases, followed by a four-point bending test to evaluate its residual load-bearing capacity, whereas the non-reinforced beams failed prematurely during phase (a) due to self-weight and advanced deterioration (i.e., 330) [20]. The premature failure is examined in greater detail in Section 8.6. Following this event, the remaining structural members were maintained under controlled laboratory conditions (22 ± 4 °C; 50–70% RH) to enable subsequent analysis.

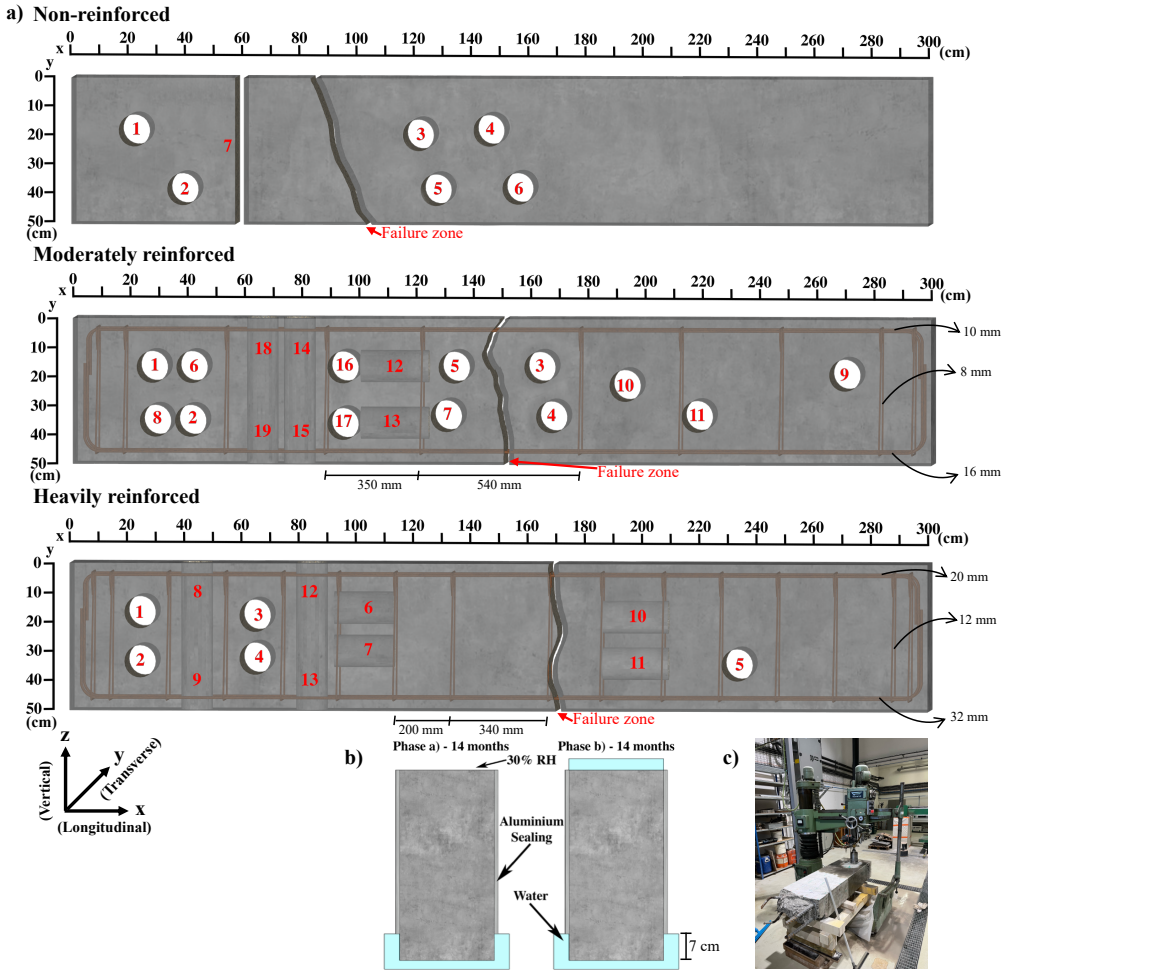


Figure 8.3 – Schematic illustration of a) the dimensions of the beams, the reinforcement configuration, and the locations where the slices and cylindrical cores were extracted. b) the water exposure setup. c) coring process.

A cross-section perpendicular to the longitudinal axis of the non-reinforced beam was cut to obtain one slice (50 × 25 × 5 cm) for microscopic analysis (Figure 8.3a). All three beams were then cored

to obtain cylinders for mechanical, microscopic, and RE tests, avoiding locations with major cracks and rebars during the sampling process. Because only a few intact cores could be taken from the severely damaged beams, microscopic analysis was limited to the transverse direction, and replication for the other tests was reduced.

Figure 8.3a illustrates the saw-cutting and coring locations in the non-reinforced, moderately reinforced, and heavily reinforced beams. Table 8.2 summarizes the specimens extracted from all three beams, categorized by depth, coring direction (see figure 8.3a for the definition of the directions), and testing method.

Table 8.2 – Location and identification of cores and slices extracted from non-, moderately, and heavily reinforced beams affected by severe DEF, including nominal coring depth, spatial coordinates, and associated testing program (DRI, SDT, and RE).

Beam	Sketch_ID (Figure 8.3a)	Sample_ID	Direction T – transverse L – longitudinal V - vertical	Location of coring			Testing 1			Testing 2
				Nominal location	Coordinate [cm] (x)	Coordinate [cm] (z)	DRI	SDT	RE	RE
Non-reinforced	1	P2_0,17 (2)	T	Upper	22.0	18.1			✓	
	2	P2_0,37 (2)	T	Lower	39.0	38.0			✓	
	3	P2_0.17_1	T	Upper	121.0	17.8		✓		
	4	P2_0,17_2	T	Upper	148.0	18.0		✓		
	5	P2_0,37_1	T	Lower	128.0	37.3		✓		
	6	P2_0,37_2	T	Lower	157.0	37.4		✓		
	7	P2_S1	T	Cross-section	59.75	-	✓			
Moderately reinforced	1	P3a_0,17 (1)	T	Upper	27.8	16.7	✓			
	2	P3a_0,34 (1)	T	Lower	28.9	35.2	✓			
	3	P3b_0,17 (1)	T	Upper	162.7	14.3	✓			
	4	P3b_0,34 (1)	T	Lower	166.9	36.9	✓			
	5	P3a_0,17 (2)	T	Upper	133.3	16.7		✓		✓
	6	P3a_0,17 (4)	T	Upper	41.7	16.7		✓		✓
	7	P3a_0,34 (2)	T	Lower	130.6	33.3		✓		✓
	8	P3a_0,34 (4)	T	Lower	41.2	35.2		✓		✓
	9	P3b_0,17 (2)	T	Upper	269.9	19.1		✓		✓
	10	P3b_0,24	T	Upper	193.1	22.8		✓		✓
	11	P3b_0,32	T	Lower	218.3	33.3		✓		✓
	12	P3a_0,17 (3a)	L	Upper	114.2	16.7		✓		✓
	13	P3a_0,34 (3a)	L	Lower	114.2	36.1		✓		✓
	14	P3a_H (1)	V	Upper	65.5	12.5		✓		✓
	15	P3a_H (3)	V	Lower	65.5	37.5		✓		✓
	16	P3a_0,17 (3b)	T	Upper	94.4	16.7			✓	
	17	P3a_0,34 (3b)	T	Lower	94.4	36.1			✓	
	18	P3a_H (2)	V	Upper	78.5	12.5			✓	
	19	P3a_H (4)	V	Lower	78.5	37.5			✓	

Table 8.2 – Continuation.

Beam	Sketch_ID (Figure 8.3a)	Sample_ID	Direction T – transverse L – longitudinal V - vertical	Location of coring			Testing 1			Testing 2
				Nominal location	Coordinate [cm] (x)	Coordinate [cm] (z)	DRI	SDT	RE	RE
Heavily reinforced	1	P4a_0,17 (1)	T	Lower	27.7	33.3	✓			
	2	P4a_0,34 (1)	T	Upper	27.7	16.7	✓			
	3	P4a_0,17 (2)	T	Lower	67.9	32.2		✓		✓
	4	P4a_0,34 (2)	T	Upper	67.9	17.7		✓		✓
	5	P4b_0,34 (2)	T	Upper	233.4	15.8		✓		✓
	6	P4a_0,17 (3)	L	Upper	137.5	15.4		✓		✓
	7	P4a_0,34 (3)	L	Lower	137.5	30.1		✓		✓
	8	P4a_H (1)	V	Lower	47.6	37.5		✓		✓
	9	P4a_H (2)	V	Upper	47.6	12.5		✓		✓
	10	P4b_0,17 (1)	L	Upper	198.9	18.4			✓	
	11	P4b_0,34 (1)	L	Lower	198.9	34.2			✓	
	12	P4a_H (3)	V	Lower	87.1	37.5			✓	
	13	P4a_H (4)	V	Upper	87.1	12.5			✓	

Obs.: SDT tests on the cores extracted from the non-reinforced beam were performed in 2015. Testing method 2 was applied after testing method 1 for a given core, considering the non-destructive aspect of the SDT [38–40].

8.4.2 Experimental procedures

8.4.2.1 Damage rating index (DRI)

The conventional and extended DRI versions were conducted on a slice of the cross-section of the non-reinforced beam and cylindrical cores from moderately and heavily reinforced beams that underwent different moisture gradients. After cutting (Figure 8.3), the specimens were polished using a handheld polishing device with diamond-impregnated pads applied in a sequential grit order: no. 50 (coarse), 120, 200, 400, 800, 1500, and 3000 (very fine) [24]. DRI analysis was performed on polished specimens with a surface area of 250 cm² of both the slice (non-reinforced beam) and cylinders (reinforced beams), and the results were normalized to 100 squares. The distress features were then evaluated as per Villeneuve and Fournier (i.e., conventional method – Figure 8.1) [30,31] and Sanchez et al. (i.e., extended version) [24,32].

The dimensions of the cracks (i.e., crack width and length) were initially screened using a transparent comparator card under a 15× magnification loupe. However, all crack width and length values reported in this study were obtained from calibrated digital images analyzed using ImageJ

(NIH) for the three beams, as the reinforced beams exhibited apertures below the 0.05 mm practical limit of the comparator. For each image, a physical scale was introduced into the field of view using a steel rule, and the image was captured in the same focal plane. The steel rule width was first checked with a digital caliper with 0.01 mm resolution to verify the reference dimension. The pixel-to-length conversion was obtained by counting the number of pixels corresponding to known physical distances (typically 1 mm), yielding conversion factors of 100 pixels per millimetre. Under these conditions, one pixel corresponds to approximately 0.01 mm on the specimen surface. Crack width was measured at the location of maximum apparent aperture, and crack length was traced along the visible crack path. Each measurement was repeated twice, and the average value was reported. Considering that manual point selection on the images is accurate to 1 pixel, the method's resolution is set to 0.01 mm, and crack widths and lengths are reported to 2 decimal places in millimetres.

The microscopic results were first analysed per specimen and then grouped by beam and sampling depth. For each beam (non-, moderately, and heavily reinforced), the data were organised into two layered zones along the height: an “upper” zone corresponding to cores extracted with centroids located within approximately 10–20 cm from the top surface and a “lower” zone corresponding to cores with centroids within approximately 30–40 cm from the top surface (Figure 8.3). The same layers were applied to the slice of the non-reinforced beam. Within each zone, DRI parameters were averaged over the available specimens to characterise the deterioration state at that depth, while the dispersion between cores was retained and discussed in the results. This layered grouping was adopted to capture the vertical variation of deterioration under the imposed moisture gradients and to compare the influence of reinforcement configuration, recognising that the non-reinforced beam was only exposed to phase (a), whereas the moderately and heavily reinforced beams experienced both exposure phases (a) and (b).

8.4.2.2 Stiffness damage test (SDT)

The SDT was conducted on cores from the upper and lower heights and in different directions: transverse, longitudinal, and vertical (Table 8.2), following the protocol proposed by Sanchez et al. [40]. The specimen cross-sections were finished with an automatic grinding machine to ensure uniformity. The specimens were then conditioned in a moist curing room at 20 ± 2°C for 48 hours

to restore moisture conditions and obtain more consistent results [37]. Given the advanced deterioration, the maximum load applied corresponds to 30% of the reference compressive strength (40 MPa), considering the damage level of the samples, at a rate of 0.10 MPa/s over five loading–unloading cycles. The test evaluation focuses on the stiffness damage index (SDI), plastic deformation index (PDI), non-linear index (NLI), and modulus of elasticity (E).

8.4.2.3 Residual expansion (RE)

Cylindrical concrete cores with nominal dimensions of 110 mm in diameter and 250 mm in height were used for RE testing in accordance with the experimental protocol previously described by Martin et al. [27]. To monitor longitudinal expansion, stainless-steel measurement pins were placed along the specimen vertical axis at 120° intervals, and a digital extensometer with a 100 mm gauge length was used for the readings. The specimens were then immersed in water at 38°C for 24 hours after pin installation, which restored moisture conditions and ensured temperature equilibrium before the zero reading. Length readings were taken to define the zero-measurement reference. By reducing the influence of hygric swelling on measured expansion, this procedure improves the appraisal of swelling primarily caused by DEF. After this initial measurement, the specimens remained stored in water at 38°C for approximately 406 days, during which axial expansion and mass gain were periodically monitored. The storage conditions of the samples were determined to represent the beams' storage conditions during the aging phases.

8.4.3 Interpretation framework for multi-level assessment and RE tests

The data interpretation within the proposed multi-level framework and the RE tests requires, first, that certain terminology be defined. In this study, induced expansion refers to expansion measured under reasonably unrestrained and favorable moisture conditions, whereas induced strain denotes the deformation that reflects both this induced expansion and the additional effects of structural factors such as reinforcement restraint and live or dead loads.

Within the present work, the multi-level assessment protocol is used to characterise the current deterioration state of DEF-affected concrete and to estimate the induced expansion at the time of coring, following the framework proposed by Sanchez et al. [7,53–55]. This damage extent, denoted $\varepsilon_{ML}(t_{coring})$, represents the induced expansion level inferred from the combined

microscopic and mechanical indicators measured on the extracted cores, and corresponds to the unrestrained expansion that would produce a comparable damage degree under the benchmark calibration of the multi-level database.

Conversely, RE testing quantifies the remaining free swelling capacity of extracted cores when placed under favourable conditions. “Potential chemical advancement” is defined as a normalised descriptor of reaction progress from 0 to 1, in which 1 corresponds to exhaustion of the free-expansion potential, representing the reaction advancement that would have been developed under favorable moisture and temperature and free swelling conditions. In the present framework, “potential chemical advancement” is inferred by comparing the residual expansion of a core to a reference full free-expansion potential measured on companion specimens. This interpretation remains conditional, since the measured residual expansion depends on both the remaining reaction potential and the accommodation capacity of the existing crack network, which can reduce the translation of additional product formation into expansion.

8.5 Results

8.5.1 Damage rating index (DRI)

The results of the microscopic assessment of DEF-affected beams with different reinforcement configurations are presented as averages over the cross-section and separately for the upper and lower parts, taking the top fibre as 0 cm and the bottom fibre as 50 cm (Figure 8.3). The non-reinforced beam exhibits an average DRI Number of 1,201, with a marked vertical gradient: 685 in the upper part and 1,717 in the lower part (Figure 8.4). This corresponds to approximately a 2.5-fold increase in microscopic damage from top to bottom, indicating that DEF-induced deterioration in the non-reinforced member is strongly concentrated in the wetter lower zone.

The moderately reinforced beam exhibits the highest average DRI Number among the three beams, at 1,350. The values remain elevated in both heights, with 1,256 in the upper part and 1,443 in the lower part. The vertical gradient is therefore less pronounced than in the non-reinforced beam (increase of about 15%), but the entire cross-section is characterised by advanced microscopic deterioration, reflecting the impact of the imposed moisture gradients.

The heavily reinforced beam presents the lowest average DRI Number, equal to 819, with 747 in the upper part and 890 in the lower part. Although a vertical gradient persists (increase of about 19% toward the bottom), the deterioration level is consistently lower than in the non-reinforced and moderately reinforced beams. The comparison of the three members indicates that the reinforcement configuration modifies both the magnitude and distribution of DEF-related microscopic damage, with a higher concentration observed in the lower part in all cases. It should also be noted that the non-reinforced beam was only exposed to the first moisture regime (phase a), whereas the moderately and heavily reinforced beams subsequently experienced a rewetting phase from the top surface (phase b), which influences the comparison of damage levels across reinforcement configurations.

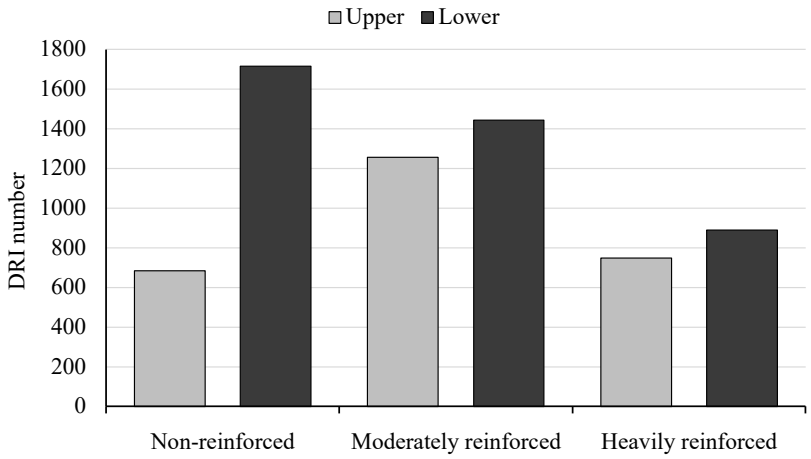


Figure 8.4 – DRI number of the non-, moderately, and heavily reinforced beams.

8.5.2 Stiffness damage test (SDT)

Figure 8.5 synthesises the SDT results for the three beams as a function of coring direction and height. In the transverse direction, the non-reinforced beam exhibits marked degradation, particularly in the lower part. SDI increases from 0.21 in the upper region to 0.50 in the lower part, while PDI rises from 0.13 to 0.32, and the modulus of elasticity decreases from 20.3 GPa to 6.6 GPa. This indicates an important number of cracks and loss of stiffness in the lower zone, consistent with the microscopic gradient identified through DRI analysis.

For the moderately reinforced beam, the transverse SDI remains within a narrower range (0.43 in the upper part and 0.39 in the lower part), with PDI between 0.25 and 0.23, and modulus of

elasticity between 8.7 GPa and 10.1 GPa, reflecting advanced deterioration across the full height, but with a less pronounced vertical contrast than in the non-reinforced member. The heavily reinforced beam exhibits lower transverse damage indices compared to the other beams, with SDI values of 0.29 (upper) and 0.35 (lower), PDI values between 0.19 and 0.22, and a modulus of elasticity ranging from 13.4 GPa to 11.4 GPa. These results indicate that the reinforcement configuration influences the magnitude of stiffness degradation, while the water supply (phase b) influences the vertical distribution of stiffness degradation. The non-reinforced beam shows the most severe transverse damage in the lower part; the moderately reinforced beam exhibits pronounced damage throughout the height, with a relatively small vertical gradient; and the heavily reinforced beam shows the greatest stiffness.

In the longitudinal direction, SDT outcomes are available only for the reinforced beams. The moderately reinforced beam shows SDI (0.19–0.20) and PDI (0.14–0.20), with modulus of elasticity of 20.4 GPa (upper) and 19.5 GPa (lower), indicating comparatively limited longitudinal stiffness damage. In contrast, the heavily reinforced beam presents a strong vertical gradient in the longitudinal direction: the upper region exhibits SDI = 0.34, PDI = 0.22, and a modulus of elasticity of 8.6 GPa, while the lower region shows SDI = 0.21, PDI = 0.21, and a modulus of elasticity of 20.0 GPa. This pattern suggests pronounced longitudinal deterioration in the upper part of the heavily reinforced beam, in contrast to the lower part.

Vertical SDT results are available for the reinforced beams. The moderately reinforced beam presents SDI values of 0.29 (upper) and 0.25 (lower), PDI between 0.20 and 0.16, and moduli of elasticity of 15.3 GPa and 17.5 GPa, respectively, indicating moderate vertical stiffness degradation with limited vertical contrast. For the heavily reinforced beam, only the lower vertical core could be tested because the upper core failed during extraction. This specimen shows SDI = 0.20, PDI = 0.14, and a modulus of elasticity of 16.8 GPa, which is rather similar to that of the moderately reinforced beam.

The SDT results indicate that the reinforcement configuration and position within the cross-section influence both the material's intensity and its anisotropic mechanical response. Specifically, the greatest transverse damage is observed in the non-reinforced beam, the moderately reinforced beam exhibits advanced damage throughout the height with a relatively small vertical gradient,

and the heavily reinforced beam shows more direction-dependent responses with higher residual stiffness.

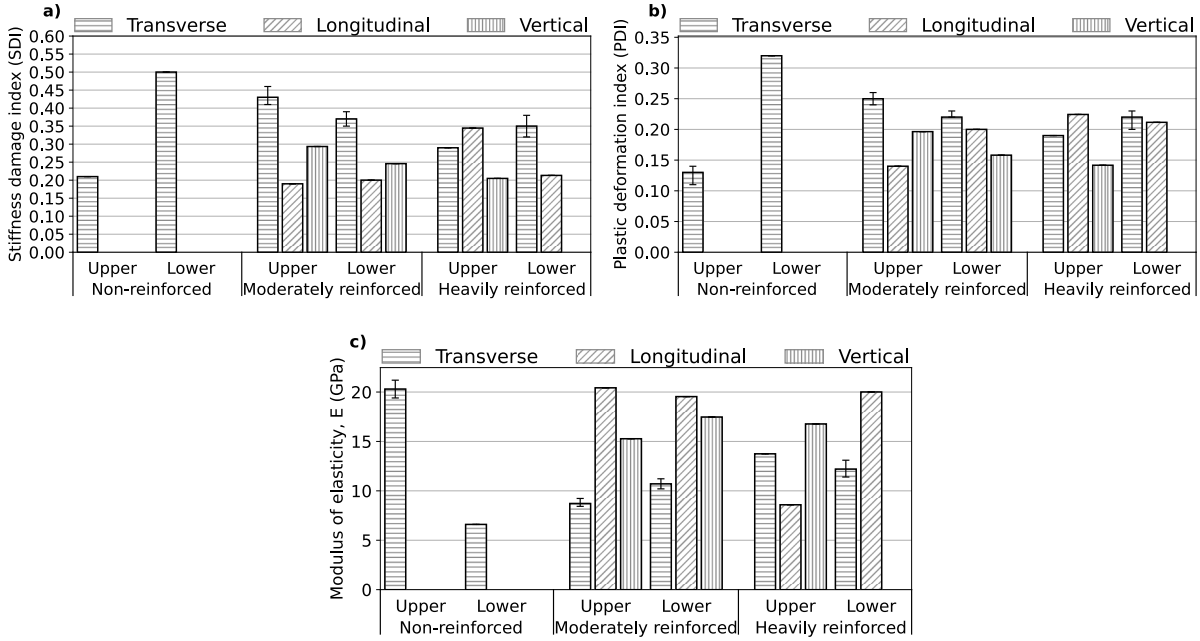


Figure 8.5 – SDT outcomes a) SDI, b) PDI, c) modulus of elasticity of non-, moderately, and heavily reinforced beams as a function of coring direction (transverse, longitudinal, vertical).

8.5.3 Residual expansion (RE)

Figure 8.6 presents the residual expansion measured during immersion at 38 °C, and Figure 8.7 shows the corresponding mass variation for the three beams. The averages are represented by the markers, and the error bars show the maximum and minimum values.

For the non-reinforced beam (Figures 8.6a and 8.7a), transverse cores show a rapid increase in residual expansion and mass gain during the first weeks, followed by a slower growth up to 83 days for the upper part and 406 days for the lower part. The upper part reaches an average residual expansion of approximately 0.52% and a mass gain of about 0.72%, whereas the lower part attains about 0.30% residual expansion and 0.72% mass gain. The upper part therefore exhibits greater residual expansion than the lower part, while the mass gain remains similar in both parts, indicating a vertical gradient in the remaining swelling potential. The upper part was monitored only up to 83 days because the corresponding sample was allocated to another stream of the project.

The moderately reinforced beam (Figures 8.6b and 8.7b) shows substantially lower residual expansion and mass gain than the non-reinforced member. Transverse residual expansions at 406 days reach approximately 0.21% (upper) and 0.15% (lower), with mass gains of about 0.49% and 0.36%, respectively. Longitudinal and vertical cores (up to 139 days) exhibit residual expansions of about 0.08–0.10% and mass gains of roughly 0.30–0.40% for both upper and lower parts. Vertical gradients remain limited in all directions, indicating a relatively more uniform distribution of remaining swelling potential and water uptake across the height.

The heavily reinforced beam (Figures 8.6c and 8.7c) presents an intermediate response. Transverse residual expansions at 406 days reach approximately 0.32% (upper) and 0.23% (lower), with mass gains of about 0.60% and 0.52%. In the longitudinal direction (up to 139 days), residual expansions of roughly 0.19% (upper) and 0.08% (lower) correspond to mass gains of about 0.54% and 0.44%. Vertical cores exhibit residual expansions of 0.12% (upper) and 0.10% (lower), with mass gains of 0.39% and 0.32%, respectively. The heavily reinforced beam depicts greater remaining swelling potential than the moderately reinforced beam, particularly in the upper transverse and both heights in the longitudinal direction, while still exhibiting lower values than the non-reinforced beam.

Across all beams and directions, higher residual expansions systematically coincide with higher mass gains, indicating that regions with greater moisture uptake during testing also exhibit greater remaining DEF-induced swelling potential. The comparison among beams shows that reinforcement configuration modifies both the magnitude and the spatial distribution of residual expansion and associated water uptake, with the non-reinforced beam characterised by the largest values and strongest vertical gradient, the moderately reinforced beam by lower and more homogeneous responses, and the heavily reinforced beam by intermediate magnitudes and more pronounced directional effects.

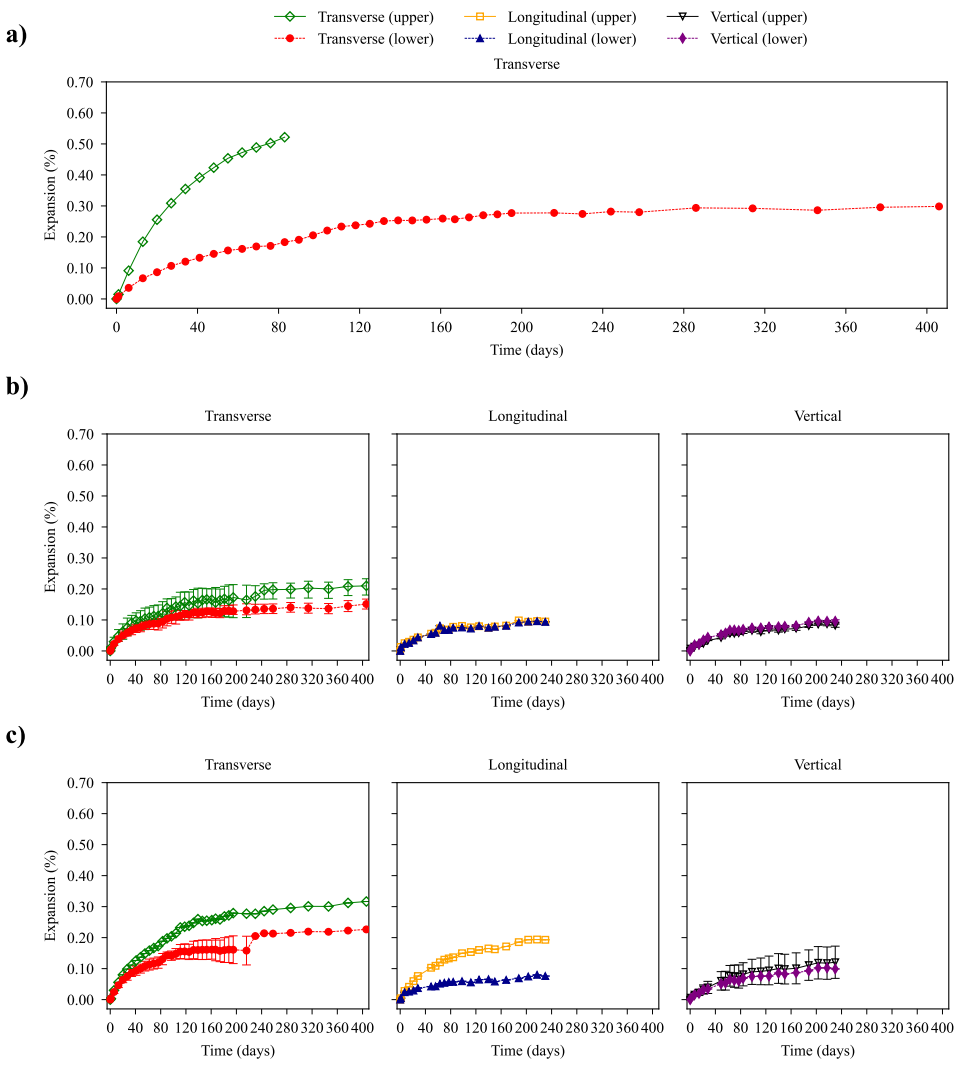


Figure 8.6 – Residual expansion: a) non-, b) moderately, and c) heavily reinforced beams.

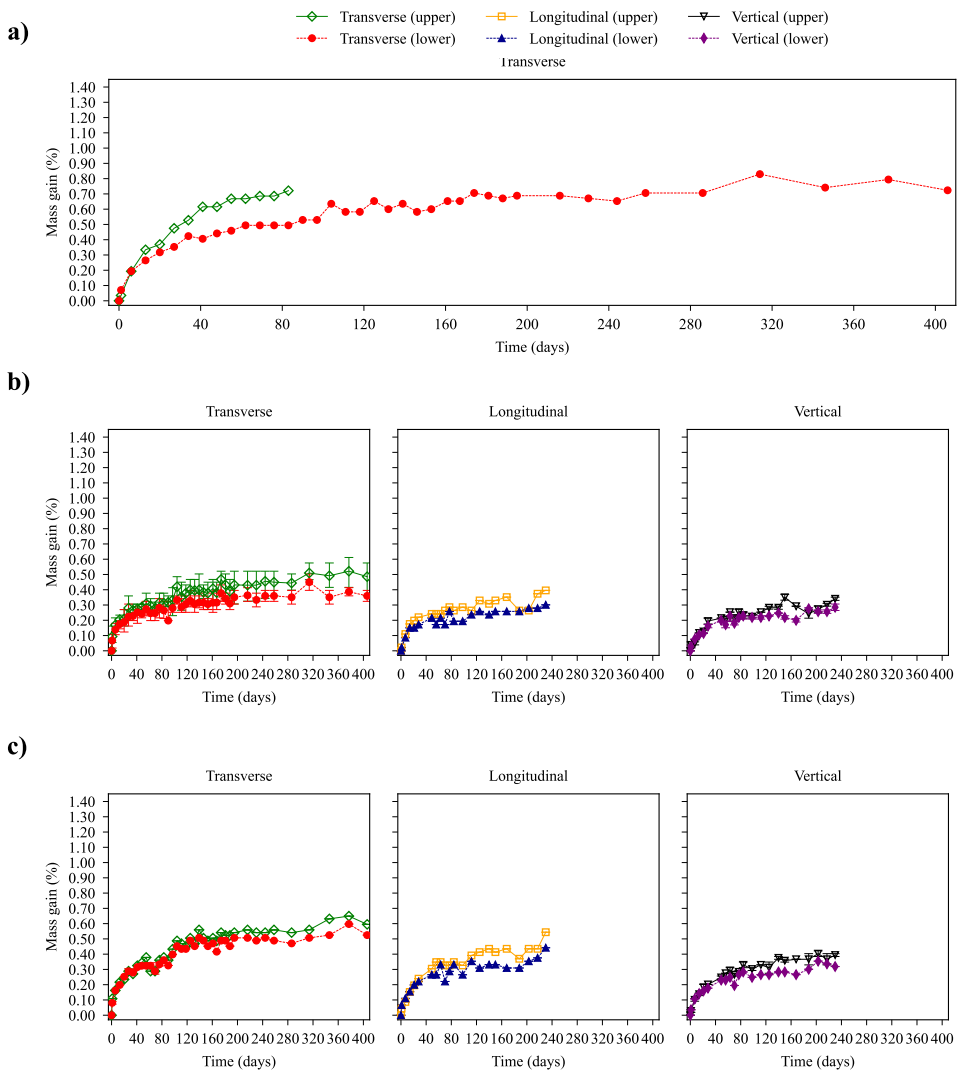


Figure 8.7 – Residual expansion: a) non-, b) moderately, and c) heavily reinforced beams.

8.6 Discussion

8.6.1 Evaluating the impact of reinforcement on the moisture gradients

The moisture transfer experienced by the beams was estimated following the framework illustrated in Figure 8.8, which combines beam weighing, automated γ-densimetry, and companion cylinders subjected to identical thermal and hydric histories, obtained by Martin [20], using a setup developed by Multon and Toutlemonde [56–58]. The approach represents water movement through three fronts that control moisture availability and swelling kinetics: a top-drying front, a bottom capillary imbibition front, and, once the top is rewetted, a top-rewetting front. During

"phase a", drying from the top and imbibition from the bottom act simultaneously, and the global mass variation is expressed as the sum of these two contributions (Equation 8.1-8.5 – Figure 8.8). During "phase b", bottom imbibition continues while the upper dry cap is progressively overtaken by a rewetting front, so that the total mass change results from ongoing imbibition and top rewetting (Equation 8.6-8.7 – Figure 8.8).

The drying front is defined as the depth where the local relative mass loss reaches an iso-loss threshold corresponding to a reduction in saturation from the post-curing value S_0 to the expansion-onset threshold S_{onset}. This threshold is obtained by linking relative mass loss to the saturation drop through a material balance that accounts for open porosity and concrete bulk density. The evolution of the drying front during phase (a) is derived from γ-densimetry profiles measured from the top surface of the moderate-DEF beam (Chapter 6), fitted with a depth-dependent kinetic function and then applied to both other beams, given their similar mixture and transport properties. To respect the γ-densimetry repeatability (±0.18 %) investigated in [20], an instrument floor of 0.20% was applied when $\delta m/m_{iso}\,(z,t) < -0.20\%$. At each time, the drying depth $h_{\text{dry}}\,(t)$ (t) is obtained by linear interpolation between instrumented depths where the computed relative mass loss reaches the iso-loss value (Equation 8.2 – Figure 8.8).

The ascent of the capillary imbibition front from the bottom is described by a square-root-in-time law with an absorption coefficient D_{imb}, as proposed by Multon and Toutlemonde [56–58]. The corresponding mass gain is evaluated by integrating the associated saturation increase over the wetted height, while the contribution of DEF-related swelling to the measured mass variation is introduced through a sigmoidal correction calibrated on companion cylinders, as proposed by Martin [20] for DEF-affected members. The coefficient D_{imb} is identified by minimising the difference between modelled and measured beam masses with a least square method (Equation 8.5 – Figure 8.8).

In this work, a complementary approach inspired by [56–58] was developed to evaluate the penetration of water during the rewetting of DEF-affected beams. During phase (b), the drying front is held fixed at the transition time t_b, as drying is not active in phase b, and the global mass variation is written as the sum of three terms: an instantaneous rewetting contribution associated with a rewetting height H_{inst} on the top surface that captures the initial capillary surge at the top

surface, a diffusion-controlled rewetting term described by a rewetting coefficient D_{rwt} and a characteristic time constant, and the continuing bottom imbibition governed by the previously identified D_{rwt} . The parameters H_{inst} and D_{rwt} are obtained by fitting the mass–time curves during "phase b" with least square method, providing a consistent description of the rewetting kinetics for subsequent analysis of reinforcement effects on DEF-induced deterioration.

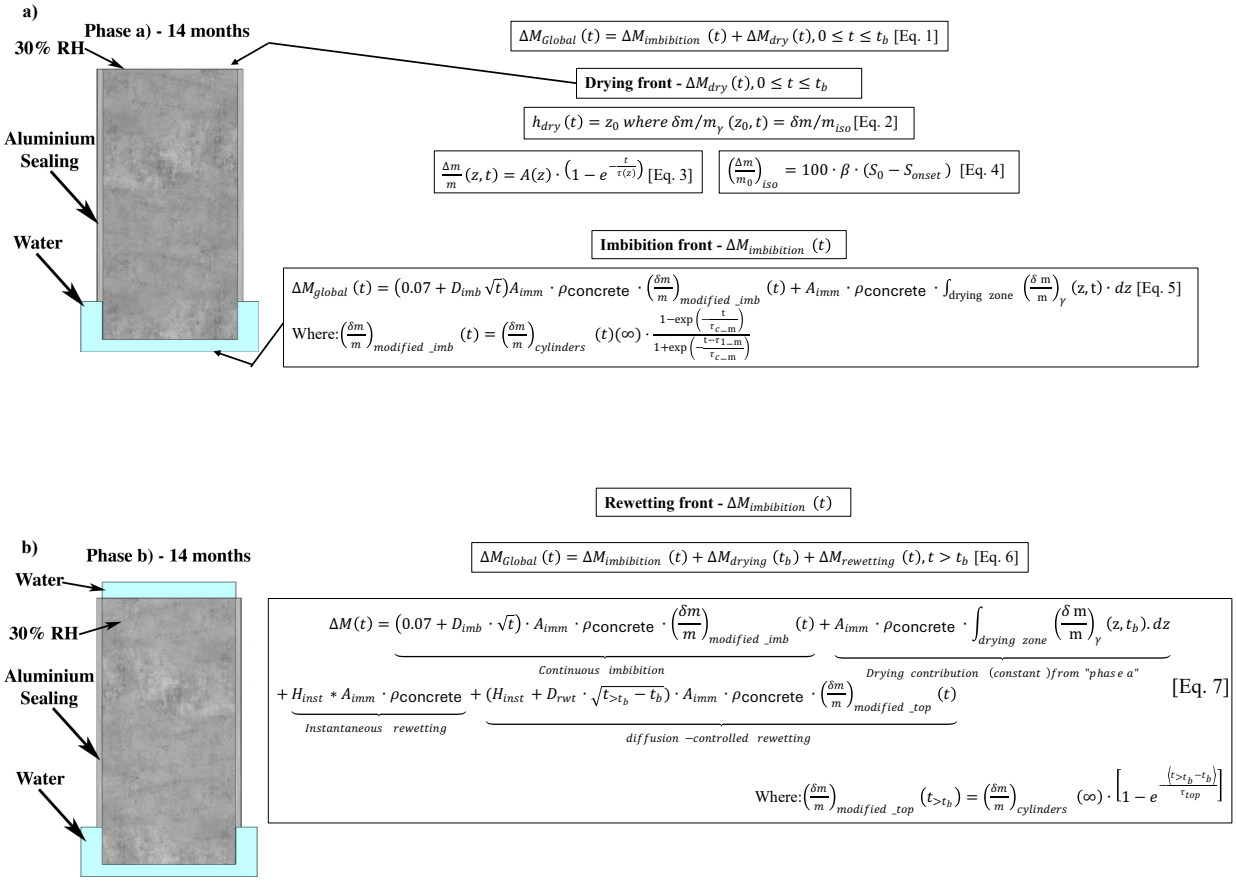


Figure 8.8 – Estimating moisture-transfer behavior. a) Phase a, b) Phase b.

Table 8.3 presents the parameters used to estimate the water-transfer behavior, and Figure 8.9 illustrates the global mass variation of non-, moderately, and heavily reinforced concrete beams affected by DEF.

Table 8.3 – Parameters used to estimate the water-transfer behavior of non-, moderately, and heavily reinforced DEF-affected concrete beams.

		Non-reinforced	Moderately reinforced	Heavily reinforced
Drying	$\rho_{concrete}$(kg/m³) [20]	2320	2320	2320
	p (%) [20]	14.6	14.6	14.6
	S_0 [20]	0.93	0.93	0.93
	β	0.06293	0.06293	0.06293
	ΔS	-0.030	-0.030	-0.030
	Iso-loss (raw) %	-0.189	-0.189	-0.189
	Iso-loss used %	-0.200	-0.200	-0.200
Imbibition	$(\delta m/m)\ \infty$	0.0241	0.0241	0.0241
	$\tau_{c\,m}\ (days)$ [20]	50	60	90
	$\tau_{l\,m}\ (days)$ [20]	290	230	280
	$D_{imb}\ (m \cdot \sqrt{t})$ [20]	2.12×10^{-2}	1.210×10^{-2}	2.410×10^{-2}
	RMSE (kg)	0.1588	0.3262	0.4813
Rewetting	H_{inst} (m)	-	1.27×10^{-3}	7.130×10^{-4}
	$D_{rwt}(m \cdot \sqrt{t})$	-	2.159×10^{-3}	2.450×10^{-3}
	τ_{top} (days)	-	0.15	0.09
	RMSE (kg)	-	0.8860	0.9149

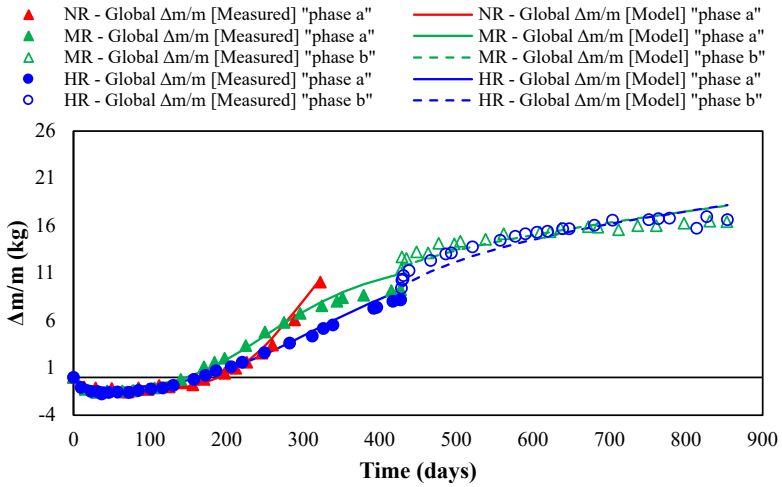


Figure 8.9 – Global mass variation of non- (NR), moderately (MR), and heavily (HR) reinforced beams

Figure 8.10 shows the time evolution of the drying, imbibition, and rewetting fronts for the three beams. Front depths are expressed with respect to the 50 cm beam height, with the drying and rewetting fronts measured from the top surface and the imbibition front measured from the bottom surface.

For the non-reinforced beam (Figure 8.10a), only the drying and imbibition fronts are present, since this beam did not experience the rewetting phase "phase b". During "phase a", the drying

front advances from the top to 9 cm at 322 days, while the imbibition front advances 45 cm from the bottom, reaching 5 cm from the top. The estimated fronts, therefore, indicate a thin, persistently dry cap near the top and a wet zone that, over time, sweeps across almost the full height of the section. Moisture availability is thus limited in time rather than in space: at a given instant, a vertical moisture gradient is present, but over the duration of phase (a), nearly all depths experience conditions favourable to DEF development at some stage with different time extent.

The moderately reinforced beam (Figure 8.10b) exhibits a drying front that advances from zero to 9 cm over 0 to 427 days, while the imbibition front moves from 50 cm to 18 cm. At the end of "phase a", the bottom wet zone therefore extends to about 32 cm long, shorter than in the non-reinforced beam at failure. During "phase b", a rewetting front develops from the top, increasing from 0.9 cm at 427 days to 4.6 cm at 854 days, reducing the remaining drying layer from 0-9 cm to 4.6-9 cm (4.4 cm), and the imbibition front recedes from 18 cm to 7.7 cm (total of 42.3 cm height from the bottom). The hydric profile at 854 days is thus characterised by a rewetted layer of about 4–5 cm at the top, a wet zone of about 42 cm from the bottom, and a central region with reduced saturation between these two fronts.

The heavily reinforced beam (Figure 8.10c) shows front evolutions similar to those of the moderately reinforced beam. In "phase a", the drying front again progresses from zero to 9 cm, while the imbibition front advances from 50 cm to 17.8 m (32.cm) over 427 days. In "phase b", the rewetting front advances from 1.0 cm to 5.2 m between 427 and 854 days. Concurrently, the remaining drying front is 3.8 cm thick from the rewetting downwards, and the imbibition front advances from 17.8 cm to 7.3 cm (total of 42.7 cm height from the bottom). The final hydric state is therefore very similar to that of the moderately reinforced beam, with a slightly deeper rewetted zone at the top and a slightly thinner wet zone at the bottom.

The hydric behavior illustrated in Figure 8.10 is consistent with the modelling results obtained by Morenon [18] for the same beams from Martin [20]. In that work, the hydric state results from desorption near the top surface and capillary uptake from the bottom surface, producing a dried upper zone and a saturated lower zone separated by a transition region of intermediate saturation [18]. This configuration matches the present front-based interpretation, in which the drying front stabilises within the first approximately 9 centimetres from the top, while the imbibition-controlled

wet zone remains anchored at the bottom and progressively encroaches upward, leaving a central region of lower saturation.

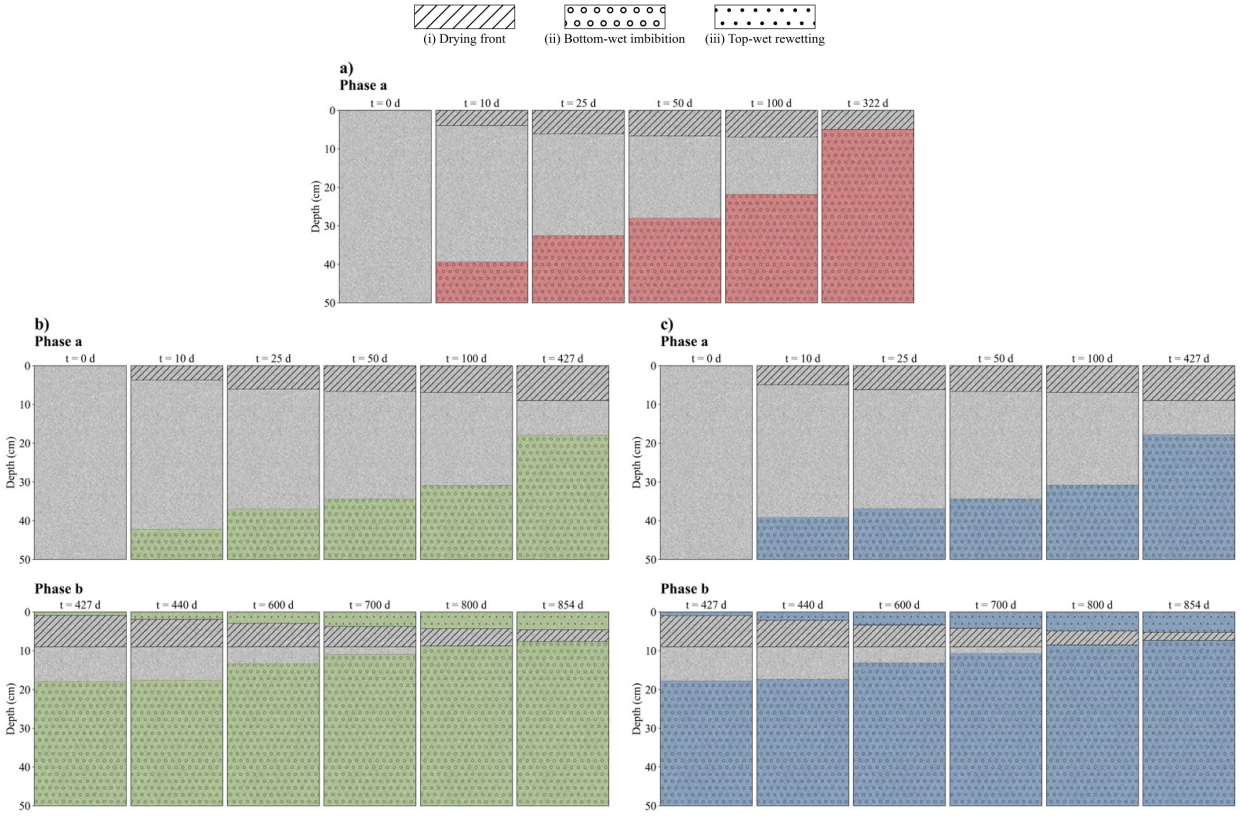


Figure 8.10 – Water transfer behavior as a function of time of a) non-, b) moderately, and c) heavily reinforced beams affected by DEF.

For the reinforced beams, the top-surface-imposed rewetting phase introduces an additional near-surface wetting process that Morenon treated as a regime change after 428 days and analysed through a parametric assessment of the post-rewetting saturated-zone height, including a highly localised case limited to the first 3 centimetres below the top surface [18]. The rewetting fronts obtained here at 854 days (approximately 4.6 centimetres for the moderately reinforced beam and 5.2 centimetres for the heavily reinforced beam) are of the same order of magnitude. Under these conditions, ‘phase b’ primarily restores moisture within a limited top layer while the bottom zone remains governed by capillary supply [18].

8.6.2 Understanding the role of the reinforcement on DEF-induced development

To elucidate the role of reinforcement in DEF-induced development, this section analyses the multi-level diagnostic results for the non-, moderately, and heavily reinforced beams, focusing on microscopic damage features, mechanical response, and residual swelling potential.

- Microscopic assessment

Figure 8.11 presents the microscopic features as absolute counts and percentages, normalized to 100 squares, for the three beams, and Figure 8.12 presents the crack density and crack geometry, which corroborate the analysis of the DRI number (Figure 8.4).

For the non-reinforced beam, Group III counts an average of 368 per 100 cm², increasing from 202 in the upper part to 533 in the lower part (Figure 8.11a). Group IV counts also show a vertical gradient, from 26 to 32 per 100 cm². When expressed as percentages (Figure 8.11b), paste-related deterioration features represent 91% of all counts, while debonding contributes 5–11%. Crack density also shows markedly non-uniformity, averaging 4.05 cracks cm^{-2} and increasing from 2.29 cracks cm^{-2} in the upper part to 5.81 cracks cm^{-2} in the lower part (Figure 8.12a). Maximum crack widths and lengths also reach high values, averaging 0.27 mm and 25.15 mm, with lower-part cracks extending up to 31.40 mm (Figure 8.12b-c). These results, combined with the high DRI Number in the lower part, confirm a highly advanced DEF state, with a pronounced deterioration intensity, particularly near the bottom, where moisture exposure has been more favourable to DEF development (Figure 8.10a).

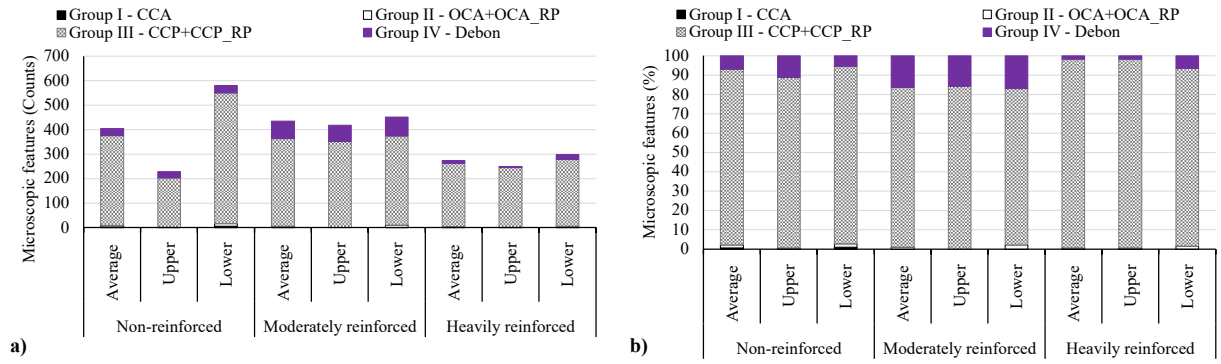


Figure 8.11 – Microscopic features of deterioration: a) Counts normalized to 100 cm². b) Percentage without applying the weighting factors.

For the moderately reinforced beam, the microscopic features indicate an advanced deterioration level with limited vertical contrast. Group III counts average 358 per 100 cm² (352 in the upper

part and 364 in the lower part), while Group IV ranges between 67 and 77 per 100 cm² (Figure 8.11a). In percentage terms, paste-related deterioration features represent approximately 82% of all counts and debonding contributes about 16% (Figure 8.11b). Crack density corroborates this distribution, averaging 4.35 cracks cm^{-2} and varying from 4.19 cracks cm^{-2} in the upper part to 4.51 cracks cm^{-2} in the lower part (Figure 8.12a), while maximum crack widths and lengths remain moderate (0.13 mm and 8.70 mm on average; Figure 8.12b–c). This combination, together with the comparatively reduced vertical contrast in the DRI Number, supports a damage state in which moderate internal restraint limited crack growth and coalescence in the region with longer exposure to water, while maintaining a substantial contribution of aggregate–paste bond deterioration (Figure 8.10b). Such refinement of crack geometry under moderate restraint is coherent with microstructural observations in restrained DEF mortars and prisms, where crack widths decrease and crack networks become less localised as restraint increases [9,15,22].

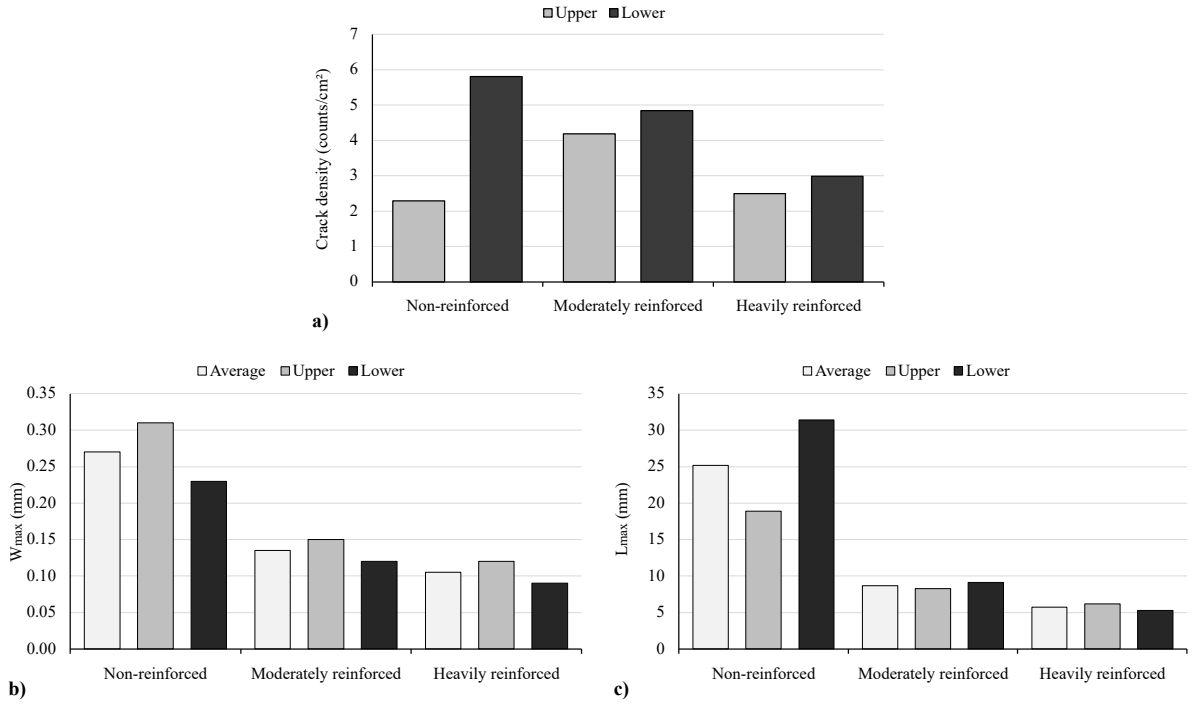


Figure 8.12 – Crack characteristics of DEF-affected beams with distinct reinforcement configurations: a) crack density; b) maximum crack width; and c) maximum crack length for the upper and lower halves of the non-, moderately, and heavily reinforced beams.

For the heavily reinforced beam, the deterioration expression differs from that of the moderately reinforced beam through the predominance of cement paste cracking and the suppression of

debonding features, especially in the upper part. Group III counts average 259 per 100 cm² (244 in the upper part and 273 in the lower part), whereas Group IV remains limited (Figure 8.11a). When expressed as percentages, paste-related deterioration features represent about 98% of all counts in the upper part and more than 90% in the lower part, while debonding contributes 2–7% (Figure 8.11b). Crack density is lower than in the moderately reinforced beam, averaging 2.74 cracks cm^{-2} (2.50 in the upper part and 2.98 in the lower part; Figure 8.12a), and maximum crack widths and lengths reach the smallest values (0.11 mm and 5.73 mm on average; Figure 8.12b–c). These results, combined with the lower DRI Number, indicate an advanced DEF state in which deterioration develops through numerous fine cracks rather than through wide, long cracks and associated debonding features, consistent with stronger internal restraint. It is important to note that Martin [20] reported a two-stage evolution of deflection, characterized by an initial downward deflection followed by a progressive inversion leading to an upward deflection, which was associated with sufficient engagement of the lower longitudinal reinforcement. An upward-bending state modifies the section stress field and can redistribute tensile and compressive strain across the height, potentially promoting a response dominated by distributed cement paste cracking while limiting debonding features in the upper part.

- Mechanical assessment

Figure 8.13 presents the residual modulus of elasticity and the non-linearity index (NLI) obtained from SDT, complementing the SDI and PDI results in Figure 8.5. In the transverse direction, the non-reinforced beam shows severe stiffness degradation, with the modulus decreasing from 20.3 GPa in the upper part (E/E_0 = 66.0%) to 6.6 GPa in the lower part (E/E_0 = 21.6%). This response is consistent with advanced paste deterioration and extensive coarse aggregate debonding (Group IV), with the latter importantly affecting the aggregate interlock. The associated NLI values remain below unity (0.79 in the upper part and 0.59 in the lower part), indicating preferential cracking parallel to the loading axis of the transverse cores and, therefore, preferential alignment of the cracking network with the transverse axis.

In the moderately reinforced beam, a pronounced stiffness reduction was observed in all directions, with a clear hierarchy among transverse, vertical, and longitudinal responses. Transverse residual moduli are 8.7 GPa in the upper part (E/E_0 = 28.3%) and 10.7 GPa in the lower part (E/E_0 = 34.8%), with SDI equal to 0.43 and 0.37 and PDI equal to 0.25 and 0.22 (Figure 8.5), respectively. Vertical

residual moduli increase to 15.3 GPa in the upper part (E/E_0 = 49.6%) and 17.5 GPa in the lower part (E/E_0 = 56.7%), with SDI equal to 0.29 and 0.25 and PDI equal to 0.20 and 0.16. Longitudinal residual moduli are 20.4 GPa in the upper part (E/E_0 = 66.3%) and 19.5 GPa in the lower part (E/E_0 = 63.4%), with SDI equal to 0.19 and 0.20 and PDI equal to 0.14 and 0.20. The microscopic assessment in the transverse direction indicates an advanced level of deterioration, with high DRI Numbers and crack density, and Group IV frequencies that reduce aggregate interlock, supporting the magnitude of the transverse modulus reduction. NLI values align with this directional hierarchy. In transverse cores, NLI exceeds unity (1.65 in the upper part and 1.44 in the lower part), and in vertical cores, it remains above unity (1.30 and 1.27), indicating preferential cracking orthogonal to the transverse and vertical axes. In contrast, longitudinal cores show NLI close to unity in the upper part (1.16) and below unity in the lower part (0.87), indicating cracking more frequently aligned with the longitudinal axis, particularly in the lower part. When these three directions are interpreted together, the cracking network is preferentially aligned with the beam longitudinal axis, parallel to the longitudinal reinforcement, while transverse and vertical loading directions intersect the cracking more frequently, resulting in lower residual moduli measured in those directions.

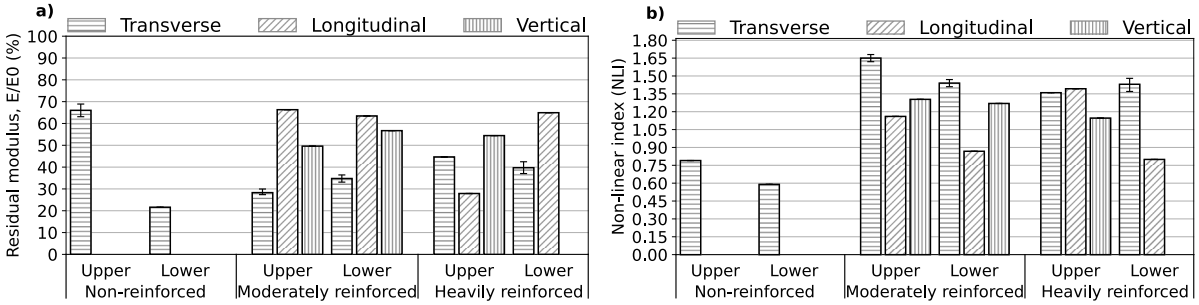


Figure 8.13 – Mechanical response from SDT for DEF-affected beams with distinct reinforcement configurations: a) residual modulus of elasticity and b) non-linear index (NLI) for the upper and lower parts of the non-, moderately, and heavily reinforced beams.

In the heavily reinforced beam, transverse stiffness degradation is less pronounced than in the moderately reinforced beam, with residual moduli of 13.8 GPa in the upper part (E/E_0 = 44.6%) and 12.2 GPa in the lower part (E/E_0 = 39.7%), associated with SDI equal to 0.29 and 0.35 and PDI equal to 0.19 and 0.22 (Figure 8.5). The longitudinal response shows a contrast, with a residual modulus of 8.6 GPa in the upper part (E/E_0 = 27.9%) and 20.0 GPa in the lower part (E/E_0 =

65.0%), while the vertical core shows a residual modulus of 16.8 GPa (E/E_0 = 54.5%) in the lower part. NLI values further constrain preferential cracking orientation. Transverse NLI remains above unity (1.36 in the upper part and 1.43 in the lower part), vertical NLI is 1.15, and longitudinal NLI shifts from above unity in the upper part (1.39) to below unity in the lower part (0.80). When these directions are interpreted together, the transverse and vertical responses remain consistent with crack systems that include a longitudinal component, while the longitudinal cores indicate a regional change in preferential alignment that reflects the contrast in longitudinal residual modulus between the upper and lower parts. These differences can also be interpreted in light of the upward-bending behaviour reported by Martin [20] for the heavily reinforced beam, as previously discussed.

It is important to note that reinforcement ratios of the moderately and heavily reinforced beams differ by approximately a factor of four in both longitudinal (0.45% versus 1.80%) and transverse (0.12% versus 0.45%), with the heavily reinforced beam also exhibiting a substantially tighter stirrup spacing. This increase in internal restraint has been observed to limit crack opening and extension [9,15,22,23], likely reducing the frequency of coarse aggregate debonding and decreasing the severity of stiffness degradation observed in this study, assuming a similar moisture exposure history (Figure 10b-c).

- Potential for further expansion

Figure 8.14 presents the maximum residual expansions measured on cores extracted from the non-, moderately, and heavily reinforced beams. The bars represent the average, and the error bars represent the maximum and minimum values. These values quantify the remaining DEF-induced swelling potential under free conditions during water immersion at 38 °C. The residual expansions are interpreted relative to the full free-expansion potential reported by Martin for companion cylinders (1.79 ± 0.06%) [20], using the chemical-advancement rationale defined in Section 4.4. It is important to note that the beams had different maturity: the non-reinforced beam was exposed to “phase a” for 330 days, while the moderately and heavily reinforced beams were exposed to “phase a” and “b” for 854 days.

The non-reinforced beam shows an average residual expansion potential of 0.41%, with a vertical gradient in the transverse direction from 0.52% in the upper part to 0.30% in the lower part. The lower part combines the highest microscopic and mechanical damage indicators, while the upper

part preserves a larger residual expansion due to moisture-limited DEF development because this beam experienced only 330 days of aging period.

The moderately reinforced beam shows an average of 0.12% (0.08%–0.23%) and a clearer directional hierarchy than a depth effect. The reduced depth difference is expected considering the moisture supply of both phases. In the upper part, residual expansion averaged 0.21% in the transverse direction (0.18%–0.23%), 0.09% in the longitudinal direction, and 0.08% in the vertical direction (0.08%–0.09%). While in the lower part, an average of 0.15% was observed in the transverse direction (0.14%–0.17%), 0.09% in the longitudinal direction, and 0.10% in the vertical direction (0.09%–0.10%). The directional dependency reflects the impact of the reinforcement, indicating a limited remaining swelling potential.

The heavily reinforced beam shows an intermediate residual expansion level, averaging 0.17% (0.07%–0.32%), and a combined depth- and direction-dependent effect. In the upper part, residual expansions reach 0.32% in the transverse direction, 0.19% in the longitudinal direction, and 0.12% in the vertical direction (0.07%–0.17%). In the lower part, residual expansions decrease to 0.23% in the transverse direction, 0.08% in the longitudinal direction, and 0.10% in the vertical direction.

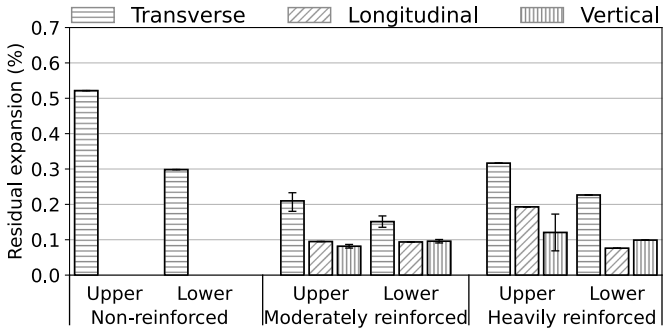


Figure 8.14 – Maximum residual expansion measured of non-, moderately, and heavily reinforced beams.

8.6.3 Current damage condition

The current expansion state was quantified using two approaches: (i) the multi-level (ML) estimate derived from microscopic and mechanical indicators, denoted ε_{ML} [7] and (ii) the reconstruction approach proposed by Martin [20], in which time and expansion offsets are fitted simultaneously with the parameters of Larive's law [48] to reconstruct the residual-expansion response and obtain

an equivalent free-expansion offset, denoted ε_{rec}. These two estimates refer to different physical quantities and are therefore compared to support interpretation.

The multi-level estimate ε_{ML} provides comparatively lower induced expansion, particularly for the reinforced beams (Figure 8.15a). The non-reinforced beam presents an average ε_{ML} of 1.00%, ranging from 0.40% in the upper part to 1.60% in the lower part, reflecting the concentration of damage at the bottom part. In contrast, the moderately and heavily reinforced beams exhibit lower ε_{ML} values of 0.65% and 0.60%, respectively. In these beams, the transverse components remain high, ranging from 1.45% to 1.51%, whereas the longitudinal and vertical components remain substantially lower. In the moderately reinforced beam, the longitudinal and vertical induced expansion do not exceed 0.39%. In the heavily reinforced beam, the longitudinal induced expansion does not exceed 0.74%, while the vertical damage extent remains limited to 0.15%.

The reconstruction approach ε_{rec} yielded average free-expansion offsets of 1.38%, 1.68%, and 1.67% for the non-reinforced, moderately reinforced, and heavily reinforced beams, respectively (Figure 8.15b). Using the full free-expansion potential of 1.79% as the reference, these offsets correspond to average the "potential chemical advancements" of 0.77, 0.94, and 0.93. In the non-reinforced beam, ε_{rec} indicates a height dependence, with 1.27% in the upper part and 1.49% in the lower part, which corresponds to "potential chemical advancements" of 0.71 and 0.83, respectively, and indicates a more advanced free-expansion position in the lower part. For the reinforced beams, ε_{rec} remains high and comparatively uniform across sampling directions and locations, with the moderately reinforced beam ranging from 1.65% to 1.70% ("potential chemical advancement" 0.92–0.95) and the heavily reinforced beam showing comparable magnitudes (longitudinal 1.60–1.71%, "potential chemical advancement" 0.89–0.96; vertical 1.67–1.69%, "potential chemical advancement" 0.93–0.94).

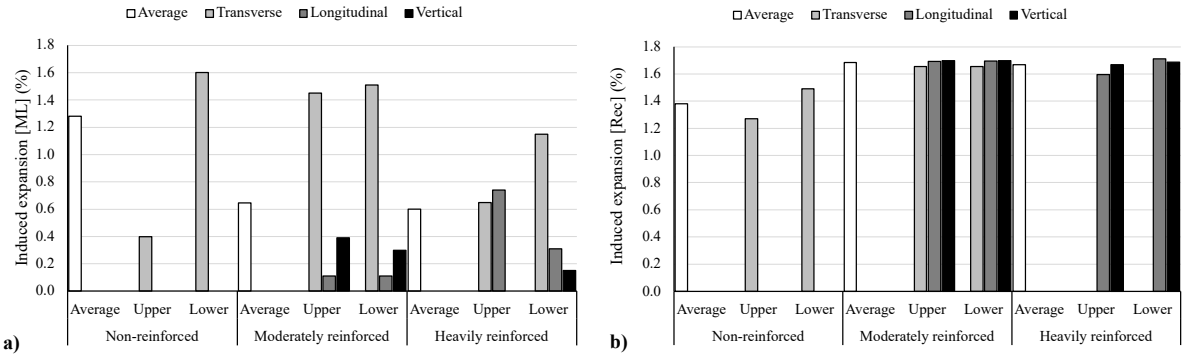


Figure 8.15 – Estimated current condition through a) multi-level induced expansion estimates (ε_{ML}) and b) reconstruction-based equivalent free-expansion offsets (ε_{rec})

The multi-level estimate, $\varepsilon_{ML}(t_{coring})$, is adopted as the diagnostic offset in the integrated diagnosis-to-prognostic approach because it expresses the current deterioration level as an induced unrestrained expansion estimate derived from the combined microscopic and mechanical indicators, interpreted through the calibrated benchmark ranges of the multi-level database [7]. In contrast, the reconstruction approach proposed by Martin [20] is formulated to provide an equivalent position on a free-expansion reference curve obtained under idealised conditions of continuous saturation and negligible restraint. This position is inferred by simultaneously fitting time and expansion offsets together with the Larive-type parameters. The approach assumes that the residual expansion measured on extracted cores represents the continuation of the same free-expansion kinetics from an advanced reaction state, and that the resulting reconstructed position reflects the advancement of the chemical swelling potential under favourable moisture conditions. This distinction is central for the present beams. The reconstruction approach and "potential chemical advancement" results show that reinforced beams can reach a high "potential chemical advancement" while exhibiting lower deterioration levels, represented by a low DRI number, reduced coarse aggregate debonding, and smaller crack widths and lengths than the non-reinforced member. Under these conditions, an offset defined by reconstruction would position the DEF-affected material on a free-expansion trajectory that does not represent the induced expansion differences throughout the affected members, whereas the ML estimate provides a prognosis starting point that remains consistent with the measured deterioration level and its associated uncertainty.

8.6.4 Integrated diagnostic-to-prognostic approach

The diagnostic-to-prognostic framework combines, for each beam part and coring direction, the multi-level estimate of the current induced expansion with a Bayesian modelling of the residual expansion capacity measured under free, favourable moisture conditions. The residual expansion test provides time-series measured expansion $\varepsilon_{meas}(t_i)$ recorded since test initiation. To ensure that the Bayesian calibration captures only the additional swelling occurring during the residual expansion test, the measured series is expressed as an increment relative to the first finite reading t_0, defined as the observed residual increment (Equation 8.8). The residual response is represented using a Larive-type sigmoidal law written in residual form (Equation 8.9), where $\varepsilon_{\infty,res}$ is the asymptotic residual expansion and $\tau_{L,res}$ and $\tau_{C,res}$ are apparent residual time parameters defined with respect to the residual test time origin. These parameters describe the residual response of the core under the residual expansion test conditions and are not interpreted as free-expansion parameters. The observed residual increments are modelled as Gaussian random variables with mean $\mu_{res,i}$ defined by the residual Larive law (Equation 8.10), with within-test scatter represented by σ_{res}. Weakly informative priors are adopted for the apparent residual parameters (Equation 8.11). The posterior distribution is obtained through Bayes' theorem (Equation 8.12) using a Gaussian likelihood written as a product over the observations (Equation 8.13). Posterior sampling is performed by Markov chain Monte Carlo. For each posterior draw, the residual Larive law is evaluated on a uniform time grid to generate the predicted residual expansion increment $\varepsilon_{res}^{pred}(t)$. At each time t, the uncertainty of $\varepsilon_{res}^{pred}(t)$ is summarised by a 95% highest-density interval (Equation 8.14).

In the integrated framework, the residual expansion increment predicted by the Bayesian model is combined with the current induced expansion inferred from the multi-level protocol. For each region and direction, the diagnostic-to-prognostic induced expansion trajectory is written as $\varepsilon_{tot}(t) = \varepsilon_{ML}(t_{coring}) + \varepsilon_{res}^{pred}(t)$ (Equation 8.15). The corresponding uncertainty envelope is obtained by shifting the residual highest-density interval by the deterministic offset $\varepsilon_{ML}(t_{coring})$, yielding $HDI_{0.95}^{tot}(t)$ (Equation 8.16).

$$\varepsilon_{res,i}^{obs} = \varepsilon_{meas}(t_i) - \varepsilon_{meas}(t_0) \tag{8.8}$$

$$\varepsilon_{res}(t \mid \varepsilon_{\infty,res}, \tau_{L,res}, \tau_{C,res}) = \varepsilon_{\infty,res} \frac{1 - exp\left(-\frac{t}{\tau_{C,res}}\right)}{1 + exp\left(-\frac{t - \tau_{L,res}}{\tau_{C,res}}\right)} \tag{8.9}$$

$$\varepsilon_{res,i}^{obs} \backsim N\left(\mu_{res,i}, \sigma_{res}^2\right), \quad \mu_{res,i} = \varepsilon_{res}\left(t_i \mid \varepsilon_{\infty,res}, \tau_{L,res}, \tau_{C,res}\right), \tag{8.10}$$

$$\varepsilon_{\infty,res} \backsim Uniform\left(0, 2.0 \max \varepsilon_{res,i}^{obs}\right), \tau_{C,res} \backsim Uniform(1, 200), \tau_{L,res} \backsim Uniform(0, 200), \quad \sigma_{res} \backsim HalfUniform(0.01), \tag{8.11}$$

$$p\left(\varepsilon_{\infty,res}, \tau_{L,res}, \tau_{C,res}, \sigma_{res} \mid \varepsilon_{res}^{obs}\right) \propto p\left(\varepsilon_{res}^{obs} \mid \varepsilon_{\infty,res}, \tau_{L,res}, \tau_{C,res}, \sigma_{res}\right) \; p(\varepsilon_{\infty,res})\, p\left(\tau_{L,res}\right) p\left(\tau_{C,res}\right) p(\sigma_{} \tag{8.12}$$

$$p\left(\varepsilon_{res}^{obs} \mid \varepsilon_{\infty,res}, \tau_{L,res}, \tau_{C,res}, \sigma_{res}\right) = \prod_i N\left(\varepsilon_{res,i}^{obs} \mid \varepsilon_{res}\left(t_i \mid \varepsilon_{\infty,res}, \tau_{L,res}, \tau_{C,res}\right), \sigma_{res}^2\right), \tag{8.13}$$

$$HDI_{0.95}(t) = \left[\varepsilon_{low,res}(t), \varepsilon_{high,res}(t)\right] \tag{8.14}$$

$$\varepsilon_{tot}(t) = \varepsilon_{ML}(t_{coring}) + \varepsilon_{res}^{pred}(t) \tag{8.15}$$

$$HDI_{0.95}^{tot}(t) = \left[\varepsilon_{ML}\left(t_{coring}\right) + \varepsilon_{low,res}(t), \varepsilon_{ML}\left(t_{coring}\right) + \varepsilon_{high,res}(t)\right] \tag{8.16}$$

Figure 8.16 presents the diagnostic-to-prognostic induced-expansion trajectories obtained by adding the Bayesian residual-expansion increment to the current induced expansion estimated by the multi-level assessment protocol. In all beams, the projections rise rapidly at early times and then evolve more gradually, while the uncertainty bands remain narrow, indicating a stable calibration of the residual response.

In the non-reinforced beam (Figure 8.16a), only transverse results are available. The lower part exhibits a higher estimated induced expansion at the start of the residual expansion test than the upper part. The upper part shows a steeper initial increase in residual expansion and a wider HDI, whereas the lower part shows a more progressive increase over time with a narrower HDI. This behaviour is explained by the moisture exposure behaviour discussed in the previous sections. The lower part experienced longer favorable hydric conditions (i.e., 295 days), and the DEF expansion developed more, leading to less induced development in the residual expansion, compared to the upper part, providing a quite narrow probabilistic interval (i.e., 0.02%). Furthermore, modest further deterioration is expected from the future expansion potential. The upper part, on the other

hand, experienced relatively shorter, favorable hydric conditions (i.e., 87 days), resulting in more limited DEF development and more induced residual expansion potential. The steeper initial development, until around 50 days of the measurements, resulted in a wider HDI (i.e., 0.06%) compared to the upper part, increasing the uncertainty of the projection. An important advancement of the deterioration is also expected, taking into account the other results observed of the same concrete and the HDI projection; for instance, the modulus may reduce to approximately 30-40% of the current value (20.3 GPa).

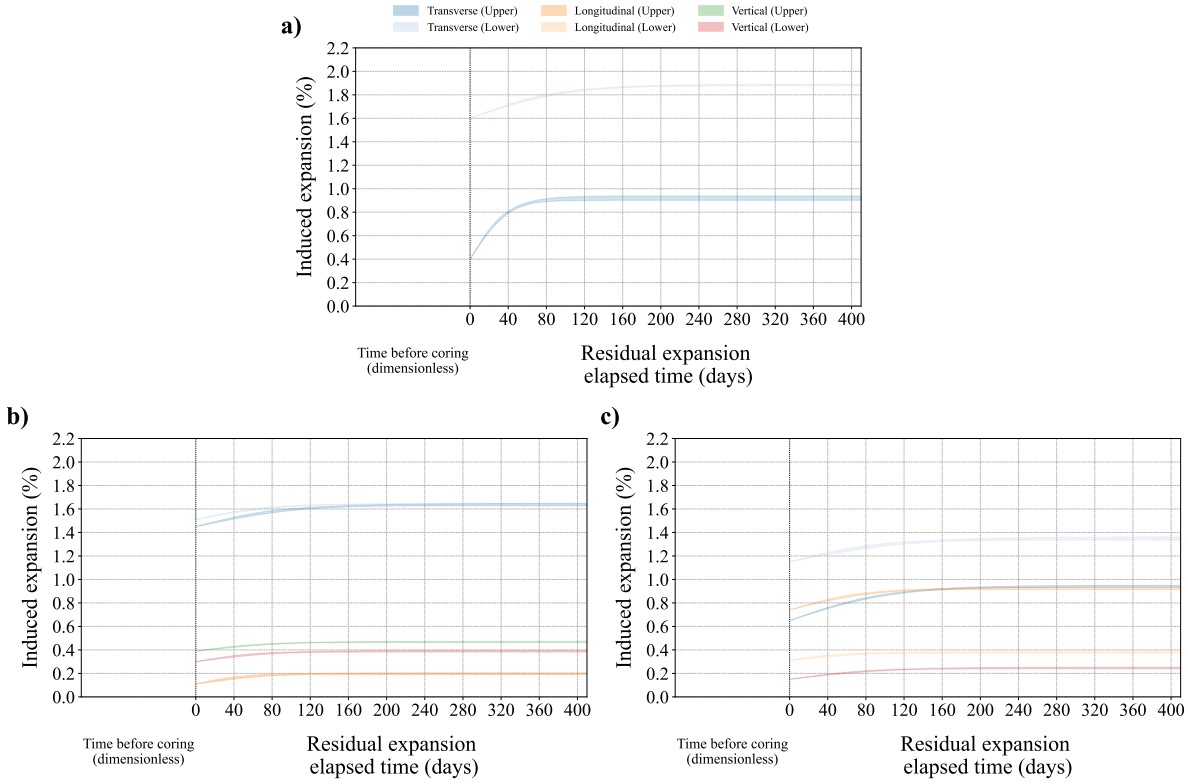


Figure 8.16 – Diagnostic-to-prognostic representation of a) non-, b) moderately, and c) heavily reinforced beams, obtained by combining the current induced-expansion estimated through the multi-level assessment protocol with the Bayesian modeling of residual expansion.

In the moderately reinforced beam (Figure 8.16b), the Bayesian projection indicates that the reaction induced greater damage in the longitudinal direction, since cracking preferentially developed parallel to the longitudinal reinforcement, leading to the largest mechanical consequence in transverse and vertical directions. The residual expansion trajectories indicate that future development remains more pronounced in the transverse and vertical directions, which show

a steeper early increase and a wider HDI than the longitudinal direction, indicating an important expansion potential.

In the heavily reinforced beam (Figure 8.16c), the reaction induced greater damage in the longitudinal direction in the upper part, while the lower part remains more constrained, which can be related to upwards bending reported by Martin [20]. The residual expansion trajectories indicate that future development remains more pronounced in the transverse and vertical directions, while the longitudinal direction remains the most constrained and shows the lowest potential, with narrower HDIs.

8.7 Conclusions

The present study evaluated how reinforcement configuration influences the diagnosis and prognosis of DEF-affected concrete beams subjected to moisture gradients by combining microscopic assessment (DRI and crack geometry), mechanical testing (SDT), residual expansion measurements, moisture-transfer semi-empirical modeling, and Bayesian modeling of residual expansion.

- DEF-induced damage exhibited a clear dependence on beams' height due to different moisture histories prior to coring. Reinforcement effects are therefore interpreted mainly through within-history comparisons between reinforced beams, where increased reinforcement reduced DEF-induced damage evaluated via microscopic (i.e., DRI) and mechanical (i.e., SDT).
- Mechanical results confirmed that stiffness reduction was direction- and depth-dependent, and that the observed anisotropy was consistent with the combined influence of moisture gradients, direction-dependent restraint imposed by the reinforcement layout, and resulting crack network orientation.
- The magnitude and directional distribution of residual expansion results of reinforced beams reflected the coupled effects of residual capacity for DEF-induced development, accommodation within the existing crack network, and restraint and moisture history, rather than a restraint-only influence.
- The diagnostic-to-prognostic framework provided probabilistic projections of future DEF-induced development at the region and direction levels, clear demonstrating the direction

dependency of the induced damage and future expansion potential. This approach showed suitable for complementing condition assessment of DEF-affected concrete under non-uniform hydric exposure and different reinforcement ratios.

8.8 References

[1] K.L. Scrivener, J.P. Skalny, Conclusions of the International RILEM TC 186-ISA workshop on Internal Sulfate Attack and Delayed Ettringite Formation (4–6 September 2002, Villars, Switzerland), Materials and Structures/Materiaux et Constructions 38 (2005) 659–663. https://doi.org/10.1617/14111.

[2] H.F.W. Taylor, C. Famy, K.L. Scrivener, Delayed ettringite formation, Cem Concr Res 31 (2001) 683–693. https://doi.org/10.1016/S0008-8846(01)00466-5.

[3] P. Fasseu, B. Mahut, Aide à la gestion des ouvrages atteints de réactions de gonflement interne : Guide méthodologique, GUIDES TECHNIQUES, Laboratoire Central des Ponts et Chaussées (LCPC), Paris, 2003.

[4] F. Toutlemonde, Structural implications and management of infrastructure assets affected by ISR: example of French experience on road bridges, Canadian Journal of Civil Engineering 52 (2025) 1843–1851. https://doi.org/10.1139/cjce-2025-0120.

[5] B. Godart, O. Omikrine-Metalssi, B. Kchakech, S. Lavaud, The effects of delayed ettringite formation on the expansion of a massive bridge pier and a precast prestressed concrete beam of a bridge, in: International Conference on Alkali Aggregate Reaction (ICAAR), São Paulo (Brazil), 2016.

[6] L.F.M. Sanchez, T. Drimalas, B. Fournier, Assessing condition of concrete affected by internal swelling reactions (ISR) through the Damage Rating Index (DRI), Cement 1–2 (2020) 100001. https://doi.org/10.1016/j.cement.2020.100001.

[7] L.F.M. Sanchez, T. Drimalas, B. Fournier, D. Mitchell, J. Bastien, Comprehensive damage assessment in concrete affected by different internal swelling reaction (ISR) mechanisms, Cem Concr Res 107 (2018) 284–303. https://doi.org/10.1016/j.cemconres.2018.02.017.

[8] N.R. Joshi, A. Matsumoto, S. Asamoto, T. Miura, Y. Kawabata, Investigation of the mechanical behaviour of concrete with severe delayed ettringite formation expansion focusing on internal damage propagation under various compressive loading patterns, Cem Concr Compos 128 (2022) 104433. https://doi.org/10.1016/j.cemconcomp.2022.104433.

[9] Y. Thiebaut, S. Multon, A. Sellier, L. Lacarrière, L. Boutillon, D. Belili, L. Linger, F. Cussigh, S. Hadji, Effects of stress on concrete expansion due to delayed ettringite formation, Constr Build Mater 183 (2018) 626–641. https://doi.org/10.1016/j.conbuildmat.2018.06.172.

[10] G. Escadeillas, J.-E. Aubert, M. Segerer, W. Prince, Some factors affecting delayed ettringite formation in heat-cured mortars, Cem Concr Res 37 (2007) 1445–1452. https://doi.org/10.1016/j.cemconres.2007.07.004.

[11] M. Al Shamaa, S. Lavaud, L. Divet, G. Nahas, J.M. Torrenti, Influence of relative humidity on delayed ettringite formation, Cem Concr Compos 58 (2015) 14–22. https://doi.org/10.1016/j.cemconcomp.2014.12.013.

[12] R.-P. Martin, F. Toutlemonde, C. Sauvaget, Effects of Alternative Wetting and Drying on the Development of Delayed Ettringite Formation, in: L.F.M. Sanchez, C. Trottier (Eds.), 17th International Conference on Alkali-Aggregate Reaction in Concrete (ICAAR), RILEM Bookseries, Volume 49, Springer, Ottawa, 2024: pp. 176–183. https://doi.org/10.1007/978-3-031-59419-9_21.

[13] L. Divet, A. Pavoine, Delayed Ettringite Formation in massive concrete structures: an account of some studies of degraded bridges, in: K. and S.J.P. Scrivener (Ed.), International RILEM TC 186-ISA Workshop on Internal Sulfate Attack and Delayed Ettringite Formation, Villars, Switzerland, 2002: pp. 98–126.

[14] N.R. Joshi, A. Matsumoto, S. Asamoto, T. Miura, Y. Kawabata, Investigation of the mechanical behaviour of concrete with severe delayed ettringite formation expansion focusing on internal damage propagation under various compressive loading patterns, Cem Concr Compos 128 (2022) 104433. https://doi.org/10.1016/j.cemconcomp.2022.104433.

[15] H. Bouzabata, S. Multon, A. Sellier, H. Houari, Effects of restraint on expansion due to delayed ettringite formation, Cem Concr Res 42 (2012) 1024–1031. https://doi.org/10.1016/j.cemconres.2012.04.001.

[16] M. Collepardi, A state-of-the-art review on delayed ettringite attack on concrete, Cem Concr Compos 25 (2003) 401–407. https://doi.org/10.1016/S0958-9465(02)00080-X.

[17] M. Malbois, B. Nedjar, S. Lavaud, C. Rospars, L. Divet, J.-M. Torrenti, On DEF expansion modelling in concrete structures under variable hydric conditions, Constr Build Mater 207 (2019) 396–402. https://doi.org/10.1016/j.conbuildmat.2019.02.142.

[18] P. Morenon, Modélisation des réactions de gonflement interne des bétons avec prise en compte des couplages poro- mécaniques et chimiques, PhD thesis, Université Toulouse III – Paul Sabatier, 2017.

[19] B. Godart, L. Divet, Recommendations for preventing disorders due to delayed ettringite formation: technical guide, Ifsttar, Techniques et Méthodes - Guide Technique - GTI5 (2018).

[20] R.P. Martin, Analyse sur structures modèles des effets mécaniques de la réaction sulfatique interne du béton, PhD thesis, Université Paris Est., 2010. https://theses.hal.science/tel-00558200.

[21] H.F.W. Taylor, C. Famy, K.L. Scrivener, Delayed ettringite formation, 31 (2001) 683–693. https://doi.org/10.1016/S0008-8846(01)00466-5.

[22] Y. Kawabata, T. Miura, M. Fujishima, N. Ueda, Y. Takahashi, S. Asamoto, S. Multon, R.-P. Martin, J.-F. Seignol, Influence of Reinforcing Rebar on Expansion due to Delayed Ettringite Formation along the Bonding Length – Part I: The Role of Bond on Expansive Behavior of Concrete, Journal of Advanced Concrete Technology 21 (2023) 851–868. https://doi.org/10.3151/jact.21.851.

[23] T. Miura, M. Fujishima, Y. Kawabata, S. Multon, R.-P. Martin, N. Ueda, Y. Takahashi, S. Asamoto, J.-F. Seignol, Influence of Reinforcing Rebar on Expansion due to Delayed Ettringite Formation along the Bonding Length – Part II: Bond Performance of Reinforced Concrete Affected by DEF Expansion, Journal of Advanced Concrete Technology 21 (2023) 869–888. https://doi.org/10.3151/jact.21.869.

[24] L.F.M. Sanchez, B. Fournier, M. Jolin, J. Duchesne, Reliable quantification of AAR damage through assessment of the Damage Rating Index (DRI), Cem Concr Res 67 (2015) 74–92. https://doi.org/10.1016/j.cemconres.2014.08.002.

[25] L.F.M. Sanchez, B. Fournier, M. Jolin, D. Mitchell, J. Bastien, Overall assessment of Alkali-Aggregate Reaction (AAR) in concretes presenting different strengths and incorporating a wide range of reactive aggregate types and natures, Cem Concr Res 93 (2017) 17–31. https://doi.org/10.1016/j.cemconres.2016.12.001.

[26] A. Zahedi, C. Trottier, L.F.M. Sanchez, M. Noël, Microscopic assessment of ASR-affected concrete under confinement conditions, Cem Concr Res 145 (2021) 106456. https://doi.org/10.1016/j.cemconres.2021.106456.

[27] R.-P. Martin, L. Sanchez, B. Fournier, F. Toutlemonde, Evaluation of different techniques for the diagnosis & prognosis of Internal Swelling Reaction (ISR) mechanisms in concrete, Constr Build Mater 156 (2017) 956–964. https://doi.org/10.1016/j.conbuildmat.2017.09.047.

[28] P.A. Dunbar, P.E. Grattan-Bellew, Results of damage rating evaluation of condition of concrete from a number of structures affected by AAR, in: B. Fournier (Ed.), Proceedings of the CANMET/ACI International Workshop on Alkali-Aggregate Reactions in Concrete, CANMET/ACI, Dartmouth (Nova Scotia), 1995: pp. 257–265.

[29] P.E. Grattan-Bellew, A. Danay, Comparison of laboratory and field evaluation of alkali-silica reaction in large dams, in: Proceedings of the International Conference on Concrete Alkali–Aggregate Reactions in Hydroelectric Plants and Dams, Canadian Electrical Association; Canadian National Committee of the International Commission on Large Dams, Fredericton, New Brunswick, Canada , 1992: p. 23.

[30] V. Villeneuve, B. Fournier, J. Duchesne, Determination of the Damage in Concrete Affected by ASR—The Damage Rating Index (DRI), in: T. Drimalas, J. H. Ideker, B. Fournier (Eds.), 14th International Conference on Alkali-Aggregate Reaction (ICAAR), University of Texas at Austin, Austin, Texas, USA, 2012: p. 10. https://icaarconcrete.org/wp-content/uploads/2022/10/14ICAAR-VilleneuveV-1.pdf.

[31] V. Villeneuve, Détermination de l'endommagement du béton par méthode pétrographique quantitative, Master's thesis (Mémoire de maîtrise), Université Laval, 2011. https://www.collectionscanada.gc.ca/obj/thesescanada/vol2/QQLA/TC-QQLA-27962.pdf.

[32] L. Sanchez, B. Fournier, M. Jolin, M.A.B. Bedoya, J. Bastien, J. Duchesne, Use of Damage Rating Index to Quantify Alkali-Silica Reaction Damage in Concrete: Fine versus Coarse Aggregate, ACI Mater J 113 (2016) 395–407. https://doi.org/10.14359/51688983.

[33] R. Medeiros, L. Sanchez, A.C. dos Santos, Assessing Alkali-Carbonate Reaction-Induced Damage in Critical Concrete Infrastructure: The First ACR-Affected Field Structure Reported in

Brazil, in: L.F. Sanchez, C. Trottier (Eds.), Proceedings of the 17th International Conference on Alkali-Aggregate Reaction in Concrete. ICAAR 2024.RILEM Bookseries, Springer, 2024: pp. 445–452. https://doi.org/10.1007/978-3-031-59349-9_51.

[34] J.B. Walsh, The effect of cracks on the compressibility of rock, J Geophys Res 70 (1965) 381–389.

[35] R.S. Crouch, Specification for the Determination of Stiffness Damage Parameters from the Low Cyclic Uniaxial Compression of Plain Concrete Cores, Revision A, Mott, Hay & Anderson, Special Services Division, Internal Technical Note. (1987).

[36] T.M. Crisp, J.G.M. Wood, P. Norris, Towards Quantification of Microstructural Damage in AAR Deteriorated Concrete, in: International Conference on Recent Developments on the Fracture of Concrete and Rock, 1993.

[37] T.M. Crisp, P. Waldron, J.G.M. Wood, Development of a non destructive test to quantity damage in deteriorated concrete, Magazine of Concrete Research 45 (1989).

[38] L.F.M. Sanchez, B. Fournier, M. Jolin, J. Bastien, Evaluation of the Stiffness Damage Test (SDT) as a tool for assessing damage in concrete due to alkali-silica reaction (ASR): Input parameters and variability of the test responses, Constr Build Mater 77 (2015) 20–32. https://doi.org/10.1016/j.conbuildmat.2014.11.071.

[39] L.F.M. Sanchez, B. Fournier, M. Jolin, J. Bastien, Evaluation of the stiffness damage test (SDT) as a tool for assessing damage in concrete due to ASR: Test loading and output responses for concretes incorporating fine or coarse reactive aggregates, Cem Concr Res 56 (2014) 213–229. https://doi.org/10.1016/j.cemconres.2013.11.003.

[40] L.F.M. Sanchez, B. Fournier, M. Jolin, J. Bastien, D. Mitchell, Practical use of the Stiffness Damage Test (SDT) for assessing damage in concrete infrastructure affected by alkali-silica reaction, Constr Build Mater 125 (2016) 1178–1188. https://doi.org/10.1016/j.conbuildmat.2016.08.101.

[41] L.F.M. Sanchez, B. Fournier, D. Mitchell, J. Bastien, Condition assessment of an ASR-affected overpass after nearly 50 years in service, Constr Build Mater 236 (2020) 117554. https://doi.org/10.1016/j.conbuildmat.2019.117554.

[42] R. Medeiros, L. Sanchez, A.C. dos Santos, Exploring microscopic and mechanical tools to uncover the anisotropic damage evolution of prestressed concrete sleepers affected by internal swelling reactions, Magazine of Concrete Research 77 (2025) 891–902. https://doi.org/10.1680/jmacr.25.00060.

[43] R. Medeiros, D.J. De Souza, L.F.M. Sanchez, A.C. Santos, Condition assessment of pre-tensioning prestressed concrete sleepers distressed by internal swelling reactions (ISR), CEMENT 21 (2025) 100154. https://doi.org/10.1016/j.cement.2025.100154.

[44] A. Pavoine, L. Divet, Réaction sulfatique interne au béton : Essai d'expansion résiduelle sur carotte de béton extraite de l'ouvrage : Méthode d'essai n° 67, Techniques et méthodes des laboratoires des ponts et chaussées., Paris, 2009. https://doi.org/https://doi.org/10.3829/me67-fr.

[45] T. Ramlochan, P. Zacarias, M.D.A. Thomas, R.D. Hooton, The effect of pozzolans and slag on the expansion of mortars cured at elevated temperature, Cem Concr Res 33 (2003) 807–814. https://doi.org/10.1016/S0008-8846(02)01066-9.

[46] K.J. Folliard, M.D.A. Thomas, B. Fournier, Protocol for the Diagnosis and Prognosis of Concrete Structures Affected by Alkali-Silica Reaction and/or Delayed Ettringite Formation, Concrete Durability Center, The University of Texas at Austin, Austin, Texas, USA, 2007.

[47] E. Giannini, K. Folliard, J. Zhu, O. Bayrak, K. Kreitman, B. Hanson, Non-Destructive Evaluation of In-Service Concrete Structures Affected by Alkali-Silica Reaction (ASR) or Delayed Ettringite Formation (DEF)—Final Report, Part I, 2013.

[48] C. Larive, Apports combinés de l'expérimentation et de la modélisation à la compréhension de l'alcali-réaction et de ses effets mécaniques, PhD, Ecole Nationale des Ponts et Chaussées, 1997. https://theses.hal.science/tel-00520676.

[49] X. Brunetaud, Étude de l'influence de différents paramètres et de leurs interactions sur la cinétique de l'amplitude de la réaction sulfatique interne au béton, Ph.D. thesis, Châtenay-Malabry, Ecole centrale de Paris, 2005. https://theses.fr/2005ECAP1025.

[50] A. Pavoine, X. Brunetaud, Développement et validation d'une méthode d'essai vis-à-vis de la formation différée de l'ettringite Application à l'étude d'impact de différents paramètres sur la cinétique et l'amplitude de gonflement, (2010). https://doi.org/10.3829/erlpc.oa65-fr.

[51] S. Multon, F.-X. Barin, B. Godart, F. Toutlemonde, Estimation of the Residual Expansion of Concrete Affected by Alkali Silica Reaction, Journal of Materials in Civil Engineering 20 (2008) 54–62. https://doi.org/10.1061/(asce)0899-1561(2008)20:1(54).

[52] R.-P. Martin, F. Toutlemonde, Theoretical and experimental validation of a simple method to reproduce representative DEF-prone conditions in laboratory, Mater Struct 46 (2013) 1245–1255. https://doi.org/10.1617/s11527-012-9967-2.

[53] L.F.M. Sanchez, B. Fournier, M. Jolin, D. Mitchell, J. Bastien, Overall assessment of Alkali-Aggregate Reaction (AAR) in concretes presenting different strengths and incorporating a wide range of reactive aggregate types and natures, Cem Concr Res 93 (2017) 17–31. https://doi.org/10.1016/j.cemconres.2016.12.001.

[54] L.F.M. Sanchez, Contribution to the assessment of damage in aging concrete infrastructures affected by alkali-aggregate reaction, PhD thesis, Université Laval, 2014. https://www.collectionscanada.ca/obj/thesescanada/vol2/QQLA/TC-QQLA-30764.pdf.

[55] L.F.M. Sanchez, Internal Swelling Reactions in Concrete: Mechanisms and Condition Assessment, 1st ed., CRC Press, Boca Raton, 2024. https://doi.org/10.1201/9781003188155.

[56] S. Multon, F. Toutlemonde, Water distribution in concrete beams, Mater Struct 37 (2004) 378–386. https://doi.org/10.1007/BF02479634.

[57] S. Multon, F. Toutlemonde, Effect of moisture conditions and transfers on alkali silica reaction damaged structures, Cem Concr Res 40 (2010) 924–934. https://doi.org/10.1016/j.cemconres.2010.01.011.

[58] S. Multon, Évaluation expérimentale et théorique des effets mécaniques de l'alcali-réaction sur des structures modèles (Études et recherches des Laboratoires des Ponts et Chaussées, Série Ouvrages d'art, OA 46), Laboratoire Central des Ponts et Chaussées - LCPC., Paris, France, 2004.

Chapter 9: Paper IV - Understand the impact of distinct reinforcement configurations (i.e., none and heavily reinforced) and different moisture gradients on the current and future deterioration of DEF+ASR-affected concrete

Rennan Medeiros [1]; Leandro Sanchez [2]; Renaud-Pierre Martin[3]; François Toutlemonde [4]

[1]PhD Candidate – University of Ottawa, Department of Civil Engineering
[2]Full Professor – University of Ottawa, Department of Civil Engineering
[3]Univ Gustave Eiffel, MAST-EMGCU, F-77454 Marne - la- Vallée, France
[4] Univ Gustave Eiffel, MAST-EMGCU, F-77454 Marne - la- Vallée, France

ABSTRACT

Concrete affected by delayed ettringite formation (DEF) and coupled DEF and alkali–silica reaction (DEF+ASR) develops heterogeneous deterioration under moisture gradients and reinforcement-induced restraint. This study evaluates four beams (non-reinforced and heavily reinforced; DEF and DEF+ASR) exposed to moisture gradients. Current damage was assessed using a multi-level protocol that combined microscopic (damage rating index - DRI) and mechanical (stiffness damage test - SDT) analyses. The potential for future expansion was appraised through residual expansion testing. A semi-empirical moisture-front reconstruction was used to support the condition assessment results. Two current-expansion estimates were compared: deterioration-based induced expansion and reconstruction-based "potential chemical advancement". A diagnosis-to-prognosis framework combined induced expansion at coring with Bayesian modelling of residual expansion to provide probabilistic projection intervals. Results show height-dependent deterioration governed by moisture history, direction-dependent restraint effects on damage expression, and moisture-controlled contribution of DEF and ASR damage features to the overall damage.

Keywords: Delayed ettringite formation (DEF); Alkali–silica reaction (ASR); ASR+DEF; Reinforcement-induced restraint; Moisture gradients; Current induced deterioration; Future expansion potential.

9.1 Introduction

Delayed ettringite formation (DEF) and alkali–silica reaction (ASR) are major internal swelling reaction (ISR) mechanisms that compromise the durability and serviceability of concrete infrastructure worldwide [1–4]. These reactions may develop independently or concurrently, and their combined occurrence has been widely reported in field structures [5–12]. Their coexistence is promoted by physicochemical interactions. ASR products alter pore-solution chemistry by reducing free-alkali concentrations and modifying sulfate-ion availability, promoting favourable thermodynamic conditions for delayed ettringite recrystallisation. This chemical shift is complemented by a transport effect in which cracking associated with ISR or other damage mechanisms (e.g., dynamic loading, shrinkage, and freezing and thawing, etc.) increases pore-network connectivity and permeability, thereby enhancing moisture and ion transport, which supports further swelling-product development [13–16].

DEF+ASR-induced expansion and deterioration have been reported as broadly isotropic under unrestrained conditions and continuous moisture supply [17–19]. However, boundary conditions, including reinforcement-induced restraint and nonuniform moisture exposure, are imposed on structural members. Restraint reduces induced expansion in restrained directions and redirects damage development toward less restrained directions through increased microcracking and associated reductions in mechanical properties [9,20–23], while moisture gradients affect ion transport and dissolution–precipitation processes governing reaction-product formation [9,15,16,20–23]. These coupled effects influence the interplay between DEF and ASR and generate heterogeneous deterioration, complicating the definition of a representative overall current deterioration condition and the estimation of remaining potential for future deterioration [24,25].

This study appraises four non-reinforced and heavily reinforced beams affected by DEF and DEF+ASR, which had been previously exposed to imposed moisture gradients. The current extent of deterioration is estimated using a multi-level assessment protocol that combines semi-quantitative petrographic analysis (Damage Rating Index - DRI) and mechanical testing (Stiffness Damage Test - SDT), while the potential for further expansion is assessed through residual expansion testing.

9.2 Background

9.2.1 DEF- and DEF+ASR-induced damage development under unrestrained conditions

The development of DEF-, ASR-, and combined DEF + ASR-induced expansion and damage has been primarily investigated under unrestrained conditions with uniform moisture exposure [18,19,26,27]. Under these boundary conditions, induced expansion measurements provide a common basis for describing reaction progress. Expansion and deterioration are essentially isotropic, with microcracking and reductions in mechanical properties showing no preferential direction [17–19].

Under unrestrained and uniformly moist exposure, DEF-induced deterioration initiates through microcracking in the cement paste and at the interfacial transition zone (ITZ), and the progressive increase in crack density and connectivity leads to a distributed crack network as expansion advances [15,23,28,29]. Whereas ASR-induced damage develops within the aggregate particles, extending into the surrounding cement paste and progressively connecting at higher expansion levels [30,31]. In both mechanisms, the transition from isolated microcracks to a connected crack network progressively degrades the mechanical response, with stiffness reduction and modulus of elasticity loss typically preceding substantial compressive-strength reductions, while compressive-strength losses become more pronounced at moderate to high expansion levels (i.e., 0.20%) in ASR-affected concrete [17–19,32].

Combined DEF+ASR-induced development has been described as promoted by chemical and physical synergies [5,13,14,16,23]. From a chemical standpoint, alkali uptake by ASR products can alter pore-solution composition and the balance between free and bound alkalis, thereby modifying sulfate availability and favouring thermodynamic conditions conducive to delayed ettringite precipitation [15,16,33]. From a physical standpoint, cracking induced by ASR or other damage processes increases pore-network connectivity, thereby accelerating moisture and ion transport, facilitating ettringite recrystallisation, and subsequently promoting crack propagation [13,14]. Early thermal exposure can further influence the coupled response by increasing ASR reaction rates at early ages [34]. In addition, the partitioning of alkalis between the pore solution and cement hydrates, which is controlled by hydrate chemistry (including aluminium-bearing

calcium–silicate–hydrate, C–S–H), modifies pore-solution alkalinity and can therefore affect the chemical conditions associated with subsequent reaction development [33].

Under unrestrained and continuously moist conditions, experimental observations have reported broadly isotropic induced expansion, deterioration, and reductions in mechanical properties in concrete affected by DEF, ASR, and DEF+ASR [17–19].

9.2.2 Influence of restraint and moisture gradients on DEF- and DEF+ASR-induced development

Restraint affects DEF-, ASR-, and combined DEF+ASR-induced development by limiting induced expansion in restrained directions and redirecting it towards less restrained directions; an effect commonly described as expansion transfer [15,17–19]. The available literature reports divergences on the magnitude of restraint effects; on the one hand, a few investigations indicate limited differences between restrained and unrestrained directions [35,36], whereas most studies reported substantial reductions of expansion along restrained directions, with more pronounced anisotropy at higher expansion levels and under higher confinement or restraint ratios [37–41]. Studies on mortar and concrete have reported decreases in induced expansion of 15-70% and 75-90% in the restrained direction for ASR- and DEF-affected concrete, respectively [19,37,42–47]. These differences have been attributed to specimen size, restraint configuration, and confinement level [48].

Microstructural evidence indicates that ASR- and DEF-induced cracking continues to develop under restraint, while its characteristics differ from those observed under free-expansion conditions because restraint influences crack opening and crack orientation under the imposed stress state, leading to thinner and wider cracks oriented parallel and perpendicular to the restraint directions, respectively [47,49–51]. Semi-quantitative petrographic investigations using the damage rating index (DRI) further indicate a restraint effect on ASR-induced damage, reporting sharper and more localised cracks for coarse reactive aggregate particles and more diffuse cracking for fine reactive aggregate particles [52]. While studies addressing DEF-induced cracking under restrained conditions reported deterioration localized in the ITZ and in the steel–concrete bond interface in reinforced configurations [47,49–51].

The anisotropic development of ASR-induced deterioration affects mechanical performance under restraint. Compressive strength comparisons between cores extracted parallel and perpendicular to reinforcement show variable outcomes, with reports ranging from minimal differences to 7%–35% reductions for perpendicular extraction [35,42,53–55]. In contrast, modulus of elasticity losses show higher sensitivity to restraint and crack orientation, with greater stiffness reduction measured perpendicular to reinforcement than parallel to it [56]. Zahedi et al. quantified this behaviour under distinct confinement configurations, showing that at 0.15% expansion, compressive strength decreased by 10%–30% while modulus of elasticity decreased by 28%–48%, with the least reduction measured parallel to the principal restraint direction [57]. This direction dependence intensified with increasing restraint, reaching compressive-strength reductions of 25%–26% and modulus losses of 38%–40% under one-dimensional restraint, and modulus losses up to 48% under two-dimensional restraint [57]. Triaxial confinement further reduced stiffness degradation compared with uniaxial or biaxial confinement, consistent with crack-opening constraints at higher confinement levels [56].

Moisture gradients introduce a location-dependent boundary condition because local water availability influences ionic transport and swelling product development along the height or depth [14,58–60]. DEF has been reported to require high moisture availability to induce pronounced expansion (i.e., >92% [61]), whereas ASR can progress under lower moisture availability, with damage development commonly occurring within a relative humidity (RH) range of 70-85% [62–64]. Under combined DEF+ASR-induced damage, moisture gradients can concentrate DEF advancement in the most saturated locations, while ASR-related development persists in moderately humid regions, increasing damage heterogeneity across the affected members (Paper I – Chapter 6).

9.2.3 Diagnostic and prognostic tools

9.2.3.1 Diagnosis: microscopic and mechanical tools

The Damage Rating Index (DRI) is a semi-quantitative microscopy-based method used to characterise distress features in concrete affected by internal swelling reactions [17,65–69]. In the conventional procedure, polished sections are subdivided into 1 × 1 cm grids and examined under

stereomicroscopy (typically 15–16×); predefined distress features are counted per grid cell, multiplied by weighting factors that reflect diagnostic relevance, summed, and normalised to 100 cm² to support comparisons across specimens and sampling locations [67,69,70]. The feature set commonly includes aggregate cracking (closed and open, with or without reaction products), cement-paste cracking (with or without reaction products), aggregate debonding, and disaggregated aggregate particles, with higher weightings generally assigned to paste cracking and debonding associated with advanced swelling-related damage (Figure 9.1) [67,71]. Although initially developed for alkali–silica reaction (ASR), the DRI has been extended to delayed ettringite formation (DEF) and combined DEF+ASR to support comparative diagnosis across mechanisms [17,24].

a)

Features of deterioration		Weighing factor
Aggregate	Closed crack (CCA)	0.25
	Opened crack (OCA)	2
	Opened crack with reaction product (OCA_RP)	2
Cement paste	Crack in the cement paste (CCP)	3
	Crack in the cement with reaction product (CCP_RP)	3
Disaggregate/corroded aggregate particle (DAP)		2
Coarse aggregate debonded (Debon)		3

$$DRI_{number} = \left[\frac{\sum_{i=1}^{i=n} 0.25(CCA)+2(OCA+OCA_{RP}+DAP)+3(CCP+CCP_{RP}+Debon)}{n\ of\ analyzed\quad 1\ cm\ by\ 1\ cm\ squares}\right] \times 100\ cm^2$$

b)

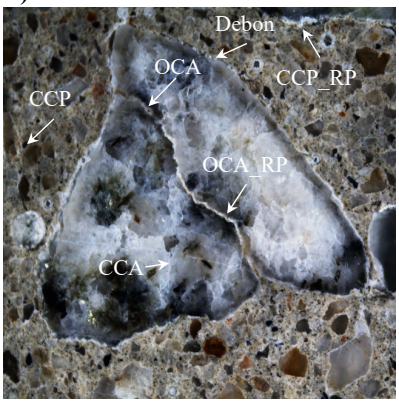


Figure 9.1 – Damage Rating Index, conventional method. a) Damage features classified in DRI analysis [67]. b) Micrograph section (1x1 cm) illustrates most of the damage features [72].

An extended DRI approach has been proposed to strengthen mechanistic interpretation by complementing the weighted index with unweighted counts and relative proportions for each feature of deterioration category, and by introducing crack density (CD), defined as the number of open cracks per unit area, as a quantitative descriptor of microcracking extent [69,73]. The extended DRI enables more detailed comparisons between samples and has proven effective in explaining mechanical performance loss due to microstructural damage [52,74].

The Stiffness Damage Test (SDT) is a cyclic mechanical test that quantifies internal damage by analysing the stress–strain response of the affected material. Initially proposed by Walsh [75] for rock mechanics, it was adapted to ASR-affected concrete by Crouch [76] and Crisp et al. [77,78]

and further refined by Sanchez et al. [79–81] through the use of a maximum load normalised to the compressive strength of sound concrete and the definition of damage indices for application across internal swelling reaction (ISR) mechanisms.

The SDT applies five uniaxial loading–unloading cycles to a maximum stress typically set at 40% of the compressive strength of undamaged material; for severely damaged concrete, the maximum stress can be reduced to 30% to maintain test feasibility [24]. Four parameters are derived from the SDT analysis: the Stiffness Damage Index (SDI), the Plastic Deformation Index (PDI), the secant modulus of elasticity (E_{SDT}), and the Non-Linearity Index (NLI) (Figure 9.2). SDI represents the fraction of dissipated energy associated with internal cracking, PDI quantifies accumulated plastic deformation relative to total deformation, E_{SDT} is taken as the average secant modulus from the second and third cycles to represent residual stiffness, and NLI is computed from the ratio of secant moduli at different stages of the first loading cycle to indicate crack orientation (NLI > 1 primarily perpendicular; NLI < 1 primarily parallel to the loading direction).

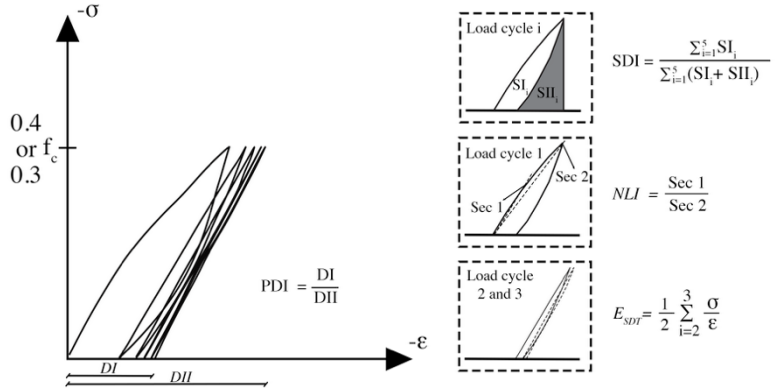


Figure 9.2 – SDT outcomes definition. Stiffness damage index (SDI). Plastic deformation index (PDI). Non-linear index (NLI). Modulus of elasticity (E_{SDT}).

The combined use of semi-quantitative petrography (DRI) and cyclic mechanical testing (SDT) constitutes the cornerstone of the multi-level assessment protocol for ISR-affected concrete. In this framework, microscopic and mechanical indicators (DRI, SDI, and stiffness and strength loss) are interpreted against calibrated severity intervals that link damage indicators to reference expansion levels (Table 9.1) [18].

The benchmark database was generated using laboratory-made concrete mixtures in which DEF and combined DEF+ASR were promoted under controlled boundary conditions. DEF was induced

through a prescribed early-age thermal treatment followed by continuous saturated storage. Heating started 4 hours after casting, and the temperature was increased to 95 °C at 18 °C h–1, maintained at 95 °C for 12 hours, and subsequently reduced to 23 °C at 6 °C h–1. After cooling, specimens were stored in water at 23 °C throughout the monitoring period. The concrete mixtures were non-air-entrained and incorporated a CSA Type GU/ASTM Type I Portland cement with an equivalent alkali content (Na_2O_{eq}) of 0.90%, while the total alkali content was adjusted to 1.25% by cement mass. The DEF concrete mixtures incorporated a limestone coarse aggregate from San Antonio, Texas (USA), non-reactive to ASR. The DEF+ASR concrete mixtures incorporated a highly reactive polymictic gravel coarse aggregate from New Mexico (USA) [18]. Within this extensive experimental program, expansion was monitored concurrently with stiffness loss, strength reductions, and DRI/SDT outputs, enabling calibration of benchmark intervals presented in Table 9.1 [18].

In practice, the damage degree is estimated by analyzing the DRI, SDI, stiffness reduction, and mechanical-property losses in the bands shown in Table 9.1 [18]. When indicators fall outside tabulated ranges, interpretation should avoid direct extrapolation and instead return to the underlying dataset to position the measurements relative to neighbouring DEF and DEF+ASR clusters while considering concrete-specific characteristics [18]. Although these benchmark relationships have been applied in different ISR-affected concrete infrastructures [82–84], interpretation for existing members remains sensitive to stress release during coring, in situ moisture state, and differences in thermal and restraint histories.

Table 9.1 – Benchmark table of ISR-induced development on affected concrete [18].

Distress Mechanism	Classification of damage degree	Reference level of expansion (%) [a]	Damage results				
			Stiffness loss (%)	Compressive strength loss (%)	Tensile strength loss (%)	SDI	DRI
DEF and DEF + ASR	Negligible	0.00–0.03	–	–	–	0.11	110–147
	Marginal	0.04 ± 0.01	–	–	–	–	–
	Moderate	0.11 ± 0.01	35–56	9–34	–	0.17–0.20	355–599
	High	0.20 ± 0.01	–	–	–	–	–
	Very high	0.30 to 0.50 ± 0.01	55–62	29–43	–	0.19–0.28	623–710
	Ultra-high	0.50 to 1.00 ± 0.01	56–77	40–47	–	0.27–0.43	828–1022
	–	≥1.00 ± 0.01	60–86	40–50	–	0.30–0.54	841–1363

[a] These levels of expansion should not be considered as strict limits among the various damage degrees, but rather indicators/reference levels.

9.2.3.2 Prognosis: Residual expansion testing and modeling

Residual expansion testing is used to appraise the remaining swelling potential of concrete affected by DEF and coupled DEF + ASR by conditioning extracted cores under moisture and temperature conditions that promote further reaction development. In DEF-oriented protocols, cores are commonly re-saturated and stored in water at 20 ± 2 °C, with length measurements initiated after a short conditioning period to stabilise temperature and moisture and continued until expansion approaches a plateau [2,85]. In parallel, protocols using lime-saturated water at approximately 23 °C are applied to maintain calcium availability while promoting ionic exchange, including alkali leaching; this testing condition is particularly relevant for fostering DEF development when the original concrete contains ASR-reactive aggregates, as expected in coupled DEF+ASR-affected concrete [25,86,87]. The analysis of residual expansion outputs must account for (i) early hygric swelling during re-saturation of partially desaturated cores, (ii) stress release and crack induced by coring, (iii) leaching-driven changes in pore-solution chemistry, and (iv) variability in pre-existing damage and saturation state across coring locations [2,85].

Residual expansion curves are commonly analysed using sigmoidal formulations originally developed for ASR, in which the experimental measurements are represented by latency, and characteristic times that describe, respectively, the dormant period and the reaction-rate development around the inflection point, and an ultimate expansion parameter [88]. This representation has been adopted in DEF to facilitate consistent parameterization of time-dependent expansion kinetics under controlled exposure [23,89,90]. In the ASR context, a reconstruction approach interprets residual expansion measured on cores as the continuation of a pre-calibrated free-expansion trajectory established on laboratory specimens under high-humidity conditions, thereby linking core measurements to an ultimate swelling potential under favourable moisture [88]. Extensions to DEF and DEF+ASR follow the same principle but introduce explicit time and expansion offsets fitted alongside the sigmoidal parameters to optimize residual expansion curves to be aligned with laboratory free-swelling references, assuming the premise that extracted cores represent an advanced reaction state rather than the full initiation-to-stabilisation history [23].

Optimized diagnostic and prognostic tools have advanced condition assessment of DEF- and DEF+ASR-affected concrete. However, evidence remains limited on how reinforcement

configuration and moisture gradients influence current damage and remaining swelling potential at the material scale in structural members.

9.3 Research significance

To investigate the effects of reinforcement-induced restraint and moisture gradients on ISR-induced expansion and deterioration, an experimental investigation was conducted on four concrete beams, displaying two reinforcement configurations (i.e., non- and heavily reinforced), affected by DEF and DEF+ASR. All beams were subjected to a thermal-curing protocol representative of massive cast-in-place structures and then exposed to vertical moisture gradients. The lateral faces were sealed to prevent transverse water transfer. These gradients were created by partially immersing the lower faces of the beams in water while exposing the upper faces to drying conditions. Water was later added to assess the effect of delayed water supply [23]. Cylindrical cores were extracted from the upper and lower parts of the beams in three directions (i.e., transverse, longitudinal, and vertical), as well as cross-sectional slices were prepared for further analysis.

The current damage extent was evaluated using the multi-level protocol based on induced deterioration indicators obtained through the combination of the damage rating index (DRI) and the stiffness damage test (SDT) analysis. The future induced swelling potential was assessed by subjecting cores to residual expansion testing under favourable moisture conditions. The current-induced expansion was compared with the "potential chemical advancement" estimated using the reconstruction approach proposed by *Université Gustave Eiffel* [23,88], which analyzes the residual expansion curve relative to the free expansion of companion specimens. Finally, the current-induced expansion was combined with the high-density interval (HDI) of the residual expansion obtained via a probabilistic time-series Bayesian approach, providing a diagnosis-to-prognosis representation of future DEF- and DEF+ASR-induced development.

9.4 Materials and methods

9.4.1 Description of the specimens

Four concrete beams were considered in this study, comprising two deterioration mechanisms, delayed ettringite formation (DEF) and combined delayed ettringite formation plus alkali–silica

reaction (DEF+ASR), and two reinforcement configurations, non-reinforced and heavily reinforced. The beams were manufactured at the former *Laboratoire central des ponts et chaussées* (LCPC), currently the *Laboratoire Expérimentation et Modélisation pour le Génie Civil et Urbain* (EMGCU) of the *Département Matériaux et Structures* at *Université Gustave Eiffel* (Paris, France), within the research programme developed by Martin [23]. All beams had nominal dimensions of 0.25 m × 0.50 m × 3.00 m and were simply supported with a span of 2.80 m (Figure 9.3a). Concrete mixtures were proportioned at a water-to-cement ratio of 0.46. The DEF and DEF+ASR mixtures exhibited 28-day compressive strengths of 38.7±5.5 MPa and 41.4±2.5 MPa, respectively, with corresponding moduli of elasticity of 30.8±3.2 GPa and 31.5±0.8 GPa. The heavily reinforced beams were detailed with two 32 mm longitudinal bars in the tensile zone and two 20 mm longitudinal bars in the compression zone, together with 12 mm stirrups at 0.20 m spacing (Figure 9.3a), corresponding to longitudinal and transverse reinforcement ratios of approximately 1.79% and 0.45%, respectively.

To replicate massive-element curing conditions and trigger DEF, the beams were transferred 2 hours after casting to a temperature-controlled water bath and subjected to a programmed thermal cycle comprising an initial heating stage aligned with the adiabatic temperature rise of the concrete mixture, a constant plateau at 81 °C for 72 hours, and a controlled cooling stage at 1 °C h^{-1}, for a total thermal-treatment duration of about 6 days [23,91]. After heat treatment, the beams were exposed to moisture gradients under two successive phases: (a) partial immersion of the bottom 7 cm for 14 months while the top surface remained exposed to drying conditions (approximately 30% relative humidity), and (b) additional water supply applied at the top surface for a further 14 months to evaluate the effect of later water supply. During both phases, the beams were stored in a controlled environment at 38 ± 1 °C and approximately 30% relative humidity, with lateral faces sealed to limit transverse moisture exchange (Figure 9.3b) [23]. The heavily reinforced beams experienced both phases, and subsequent evaluation of the residual load-bearing capacity (i.e., four-point bending test), whereas the non-reinforced beams failed prematurely during phase (a) due to self-weight and advanced deterioration [23]. Following completion of the original programme, the remaining members and fragments were stored under laboratory conditions (22 ± 4 °C and 50–70% relative humidity) without imposed wetting until coring and specimen preparation for the present experimental campaign.

Both the DEF and DEF+ASR mixtures were manufactured using a Portland cement containing 4.97% C_3A, 3.46% SO_3, and 0.83% Na_2O_{eq}. The total alkali content was increased to 1.1% Na_2O_{eq} by adding 1.745 kg KOH per cubic metre in mixing water, with the objectives of enhancing primary ettringite decomposition and promoting ASR development when reactive aggregates were present [23]. The DEF mixture incorporated a non-reactive siliceous limestone as coarse aggregate, whereas the DEF+ASR mixture incorporated a highly reactive siliceous limestone aggregate with an expansion potential of 0.16% (soaked in water); classified according to ASTM C1778 (Table 1) [92].

Each non-reinforced beam was saw-cut perpendicular to its longitudinal axis to obtain one slice (50 cm × 25 cm × 5 cm) for microscopic analysis. All four beams were then cored to obtain cylinders for mechanical, microscopic, and residual expansion testing, while avoiding major cracks and, where applicable, reinforcement during sampling (Figure 9.3c). Table 9.2 summarises the specimens extracted from all four beams, categorised by depth, coring direction (Figure 9.3a), and testing method. The replication of the tests was constrained by the limited number of intact cores obtained due to the severely damaged condition of the beams. Additionally, the microscopic assessment was restricted to the transverse direction due to the number of cores retrieved.

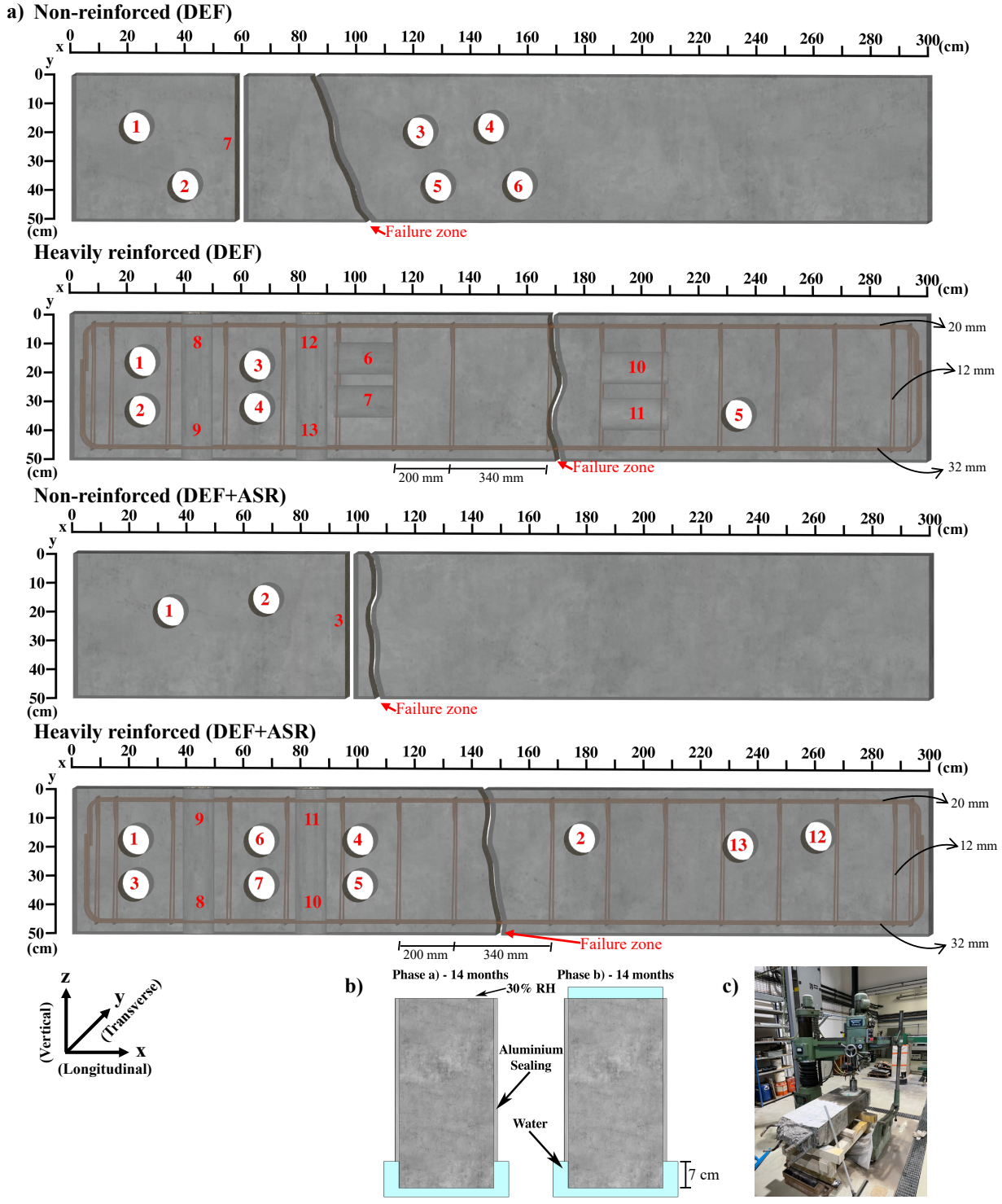


Figure 9.3 – Schematic illustration of a) the dimensions of the beams (cm), and the locations where the slices and cylindrical cores were extracted. b) the water exposure setup. c) coring process.

Table 9.2 – Location and identification of cores and slices extracted from non- and heavily reinforced beams affected by DEF and DEF+ASR, including nominal coring depth, spatial coordinates, and associated testing program (DRI, SDT, and RE).

Beam	Sketch_ID (Figure 9.3a)	Sample_ID	Direction T – transverse L – longitudinal V - vertical	Location of coring			Testing 1			Testing 2
				Nominal location	Coordinate [cm] (x)	Coordinate [cm] (z)	DRI	SDT	RE	RE
Non-reinforced (DEF)	1	P2_0,17 (2)	T	Upper	22.0	18.1			✓	
	2	P2_0,37 (2)	T	Lower	39.0	38.0			✓	
	3	P2_0.17_1	T	Upper	121.0	17.8		✓		
	4	P2_0,17_2	T	Upper	148.0	18.0		✓		
	5	P2_0,37_1	T	Lower	128.0	37.3		✓		
	6	P2_0,37_2	T	Lower	157.0	37.4		✓		
	7	P2_S1	T	Cross-section	59.75	-	✓			
Heavily reinforced (DEF)	1	P4a_0,17 (1)	T	Lower	27.7	33.3	✓			
	2	P4a_0,34 (1)	T	Upper	27.7	16.7	✓			
	3	P4a_0,17 (2)	T	Lower	67.9	32.2		✓		✓
	4	P4a_0,34 (2)	T	Upper	67.9	17.7		✓		✓
	5	P4b_0,34 (2)	T	Upper	233.4	15.8		✓		✓
	6	P4a_0,17 (3)	L	Upper	137.5	15.4		✓		✓
	7	P4a_0,34 (3)	L	Lower	137.5	30.1		✓		✓
	8	P4a_H (1)	V	Lower	47.6	37.5		✓		✓
	9	P4a_H (2)	V	Upper	47.6	12.5		✓		✓
	10	P4b_0,17 (1)	L	Upper	198.9	18.4			✓	
	11	P4b_0,34 (1)	L	Lower	198.9	34.2			✓	
	12	P4a_H (3)	V	Lower	87.1	37.5			✓	
	13	P4a_H (4)	V	Upper	87.1	12.5			✓	
Non-reinforced (DEF+ASR)	1	P5_0,17 (2)	T	Upper	33.3	20.4			✓	
	2	P5_0,17 (3)	T	Upper	66.8	16.2		✓		
	3	P5_S1	T	Cross-section	98.0	-	✓			
Heavily reinforced (DEF+ASR)	1	P6a_0,17 (1)	T	Upper	21.4	18.0	✓			
	2	P6b_0,17 (1)	T	Upper	177.7	17.0	✓			
	3	P6a_0,34 (1)	T	Lower	21.4	33.3	✓			
	4	P6a_0,17 (3b)	T	Upper	100.0	18.0		✓		✓
	5	P6a_0,34 (3b)	T	Lower	100.0	33.3		✓		✓
	6	P6a_0,17 (2)	T	Upper	65.5	180		✓		✓
	7	P6_ 0,34 (2)	T	Lower	65.5	33.3		✓		✓
	8	P6a_H (1)	V	Lower	43.4	37.5		✓		✓
	9	P6a_H (2)	V	Upper	43.4	12.5		✓		✓
	10	P6a_H (3)	V	Lower	82.7	37.5			✓	
	11	P6a_H (4)	V	Upper	82.7	12.5			✓	
	12	P6b_0,16	T	Upper	260.6	16.2			✓	
	13	P6b_0,18	T	Upper	233.2	19.3			✓	

Obs.: The specimens from the non-reinforced beam affected by DEF tested for SDT were extracted and tested in 2015. Testing method 2 was applied after testing method 1 for a given core, considering the non-destructive aspect of the SDT [79–81].

9.4.2 Experimental procedures

For each beam, results were grouped by depth along the member height into two parts. The “upper” part comprised cores whose centroids were located approximately 10 to 20 cm below the top surface, whereas the “lower” part comprised cores with centroids approximately 30 to 40 cm below the top surface (Figure 9.3a). This depth-based grouping was adopted to evaluate the imposed moisture gradients and to compare the influence of reinforcement, recognizing that the non-reinforced beams experienced moisture exposure phase (a), whereas the heavily reinforced beams experienced moisture exposure phases (a) and (b).

9.4.2.1 Damage rating index (DRI)

The conventional and extended DRI versions, as per Sanchez et al. [69,73], were performed on a cross-sectional slice from the non-reinforced beam and on cylindrical cores extracted from heavily reinforced beams subjected to different moisture gradients. Following cutting (Figure 9.3), specimens were polished using a handheld polishing device with diamond-impregnated pads applied in sequential grit order: no. 50 (coarse), 120, 200, 400, 800, 1500, and 3000 (very fine) [69]. DRI analysis was conducted on polished surfaces with an area of 250 cm² for both the slice (non-reinforced beam) and the cylinders (reinforced beams), and results were normalized to 100 squares. Distress features were assessed according to Villeneuve and Fournier (i.e., conventional method – Figure 9.1) [67,71] and Sanchez et al. (i.e., extended version) [69,73].

A transparent comparator card used under a 15× magnification loupe provided an initial screening of crack dimensions (crack width and length). The crack width and length values reported for the three beams were subsequently determined from calibrated digital images analyzed using ImageJ (NIH), since the reinforced beams exhibited apertures below the 0.05 mm practical limit of the comparator. Each image included a steel rule placed within the field of view, and image acquisition was performed in the same focal plane. The reference dimension was validated by checking the steel rule width using a digital caliper with 0.01 mm resolution. Calibration was then established through pixel-to-length conversion by counting the number of pixels spanning known physical distances, typically 1 mm, which yielded conversion factors of 100 pixels per millimetre; under these conditions, one pixel corresponds to approximately 0.01 mm on the specimen surface. Crack width was taken at the location of maximum apparent aperture, whereas crack length was traced

along the visible crack path. Each measurement was repeated twice, and the reported value corresponds to the average. Given that manual point selection on the images is accurate to 1 pixel, the method resolution was defined as 0.01 mm, and crack widths and lengths are reported to 2 decimal places in millimetres.

9.4.2.2 Stiffness damage test (SDT)

The SDT was performed on cores extracted at the upper and lower heights and oriented in transverse, longitudinal, and vertical directions (Table 9.2), in accordance with the protocol proposed by Sanchez et al. [81]. Specimen cross-sections were ground using an automatic grinding machine to ensure uniformity. Specimens were subsequently conditioned in a moist curing room at 20 ± 2°C for 48 hours to restore moisture conditions and improve result consistency [81]. Due to advanced deterioration, the maximum load was limited to 30% of the reference compressive strength and applied at 0.10 MPa/s over five loading–unloading cycles, as validated by Martin et al. [24]. The resulting stress-strain curves were analyzed to obtain the stiffness damage index (SDI), plastic deformation index (PDI), non-linear index (NLI), and modulus of elasticity (E).

9.4.2.3 Residual expansion

Residual expansion (RE) testing was performed on cylindrical concrete cores with nominal dimensions of 110 mm in diameter and 250 mm in height, in accordance with the experimental protocol previously described by Martin et al. [24]. Longitudinal expansion was monitored using stainless-steel measurement pins installed along the specimen's vertical axis at 120° intervals, with readings collected using a digital extensometer with a 100 mm gauge length. Following pin installation, specimens were immersed in water at 38°C for 24 hours to restore moisture conditions and to ensure temperature equilibrium prior to establishing the zero reading. Length readings were then taken to define the zero-measurement reference. Inspired by [85], this preconditioning step reduces the influence of hygric swelling on measured expansion, thereby improving the appraisal of swelling primarily caused by DEF and DEF+ASR. After the initial measurement, specimens were stored in water at 38°C for approximately 406 days, during which axial expansion and mass gain were monitored at regular intervals. The selected storage conditions were established to represent the beams' storage conditions during the aging phases.

9.4.3 Interpretation of the multi-level assessment and residual expansion

The interpretation of the multi-level assessment results and residual expansion (RE) tests requires consistent terminology. In the present work, induced expansion refers to the expansion measured under reasonably unrestrained conditions with favourable moisture availability, whereas induced strain refers to the deformation observed in structural members in which the induced expansion is combined with structural influences, including internal restraint and sustained or applied loading. In this study, the multi-level assessment protocol is used to characterise the current deterioration condition of ISR-affected concrete and to estimate the equivalent induced expansion at the time of coring, following the approach proposed by Sanchez et al. [3,18,93,94]. This damage extent, denoted $\varepsilon_{ML}(t_{coring})$, corresponds to the unrestrained expansion level that would generate a comparable degree of damage under the benchmark calibration provided by the multi-level database, based on the combined microscopic and mechanical indicators measured on extracted cores.

Residual expansion testing, in turn, quantifies the remaining free swelling capacity of the extracted cores when exposed to favourable conditions. The "potential chemical advancement" is defined as a normalised indicator of reaction progress ranging from 0 to 1, where 1 represents exhaustion of the free-expansion potential. This is inferred by comparing the core residual expansion to a reference full free-expansion potential measured on companion specimens. This inference remains conditional because the measured residual expansion reflects both the remaining reaction potential and the accommodation capacity of the existing crack network, which can reduce the conversion of additional swelling-product formation into measurable expansion., corresponds to the unrestrained expansion level that would generate a comparable degree of damage under the benchmark calibration provided by the multi-level database, based on the combined microscopic and mechanical indicators measured on extracted cores.

9.5 Results

9.5.1 Damage rating index (DRI)

The DRI results were first examined at the specimen level and then consolidated by beam and by depth, separating the upper and lower parts. Each "layer" has a surface area of at least 250 cm² for

each part (i.e., upper and lower), in accordance with the minimum representative area of 200 cm² recommended for damage assessment through the DRI [66,68,69]. Figure 9.4 displays the DRI number for non-reinforced (NR) and heavily reinforced (HR) beams affected by delayed ettringite formation (DEF) and combined delayed ettringite formation and alkali–silica reaction (DEF+ASR).

The DRI values were higher in the lower part of all beams than in the upper part. For the NR beams, the DRI numbers equal 685 in the upper part and 1,717 in the lower part for NR (DEF), and 1,384 in the upper part and 2,082 in the lower part for NR (DEF+ASR). For the HR beams, the DRI numbers equal 747 in the upper part and 890 in the lower part for HR (DEF), and 640 in the upper part and 1,092 in the lower part for HR (DEF+ASR).

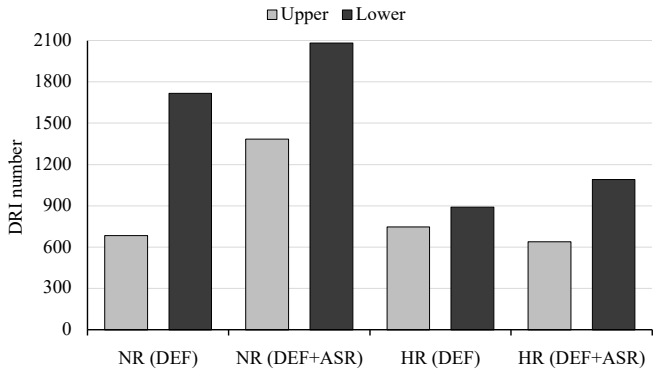


Figure 9.4 – DRI numbers of non-reinforced (NR) and heavily reinforced (HR) beams affected by delayed ettringite formation (DEF) and combined delayed ettringite formation and alkali–silica reaction (DEF+ASR).

9.5.2 Stiffness damage test (SDT)

Figure 9.5 presents the Stiffness Damage Test (SDT) outcomes for non-reinforced (NR) and heavily reinforced (HR) beams affected by delayed ettringite formation (DEF) and combined delayed ettringite formation and alkali–silica reaction (DEF+ASR). The results are organised by height (upper and lower parts) and coring direction (transverse, longitudinal, and vertical). Bars represent average values, while error bars correspond to the minimum and maximum values obtained from the available specimens (Table 9.2).

In the NR beams, the transverse SDI was higher in the lower part than in the upper part for NR (DEF) (0.50 versus 0.21). The NR (DEF+ASR) beam showed an upper-part transverse SDI of 0.34, which is higher than the NR (DEF) upper-part value. No specimens were possible to extract

in the lower part of NR (DEF+ASR) due to the damage level of the beam. In the HR (DEF) beam, the upper-part SDI showed direction-dependent differences, with the highest value in the longitudinal direction (0.34), followed by the transverse direction (0.29), and the lowest value in the vertical direction (0.20). In the lower part of HR (DEF), transverse SDI (0.35) was higher than longitudinal SDI (0.21), whereas no specimen was available in the vertical direction. For HR (DEF+ASR), transverse SDI was higher than vertical SDI in both parts (upper: 0.16 versus 0.12; lower: 0.21 versus 0.10), while the lower part presented a higher transverse SDI than the upper part (0.21 versus 0.16). No specimen was available in the longitudinal direction.

For NR (DEF), transverse PDI was higher in the lower part (0.32) than in the upper part (0.13). The NR (DEF+ASR) upper part presented a transverse PDI of 0.22, which was higher than the NR (DEF) upper-part value. In the HR (DEF) beam, the upper part showed PDI values of 0.22, 0.19, and 0.14 in the longitudinal, transverse, and vertical directions, whereas similar PDI values were observed in the transverse (0.22) and longitudinal (0.21) directions in the lower part. For HR (DEF+ASR), transverse PDI was higher than vertical PDI in both parts (upper: 0.10 versus 0.07; lower: 0.13 versus 0.07), and the lower part presented higher transverse PDI than the upper part (0.13 versus 0.10).

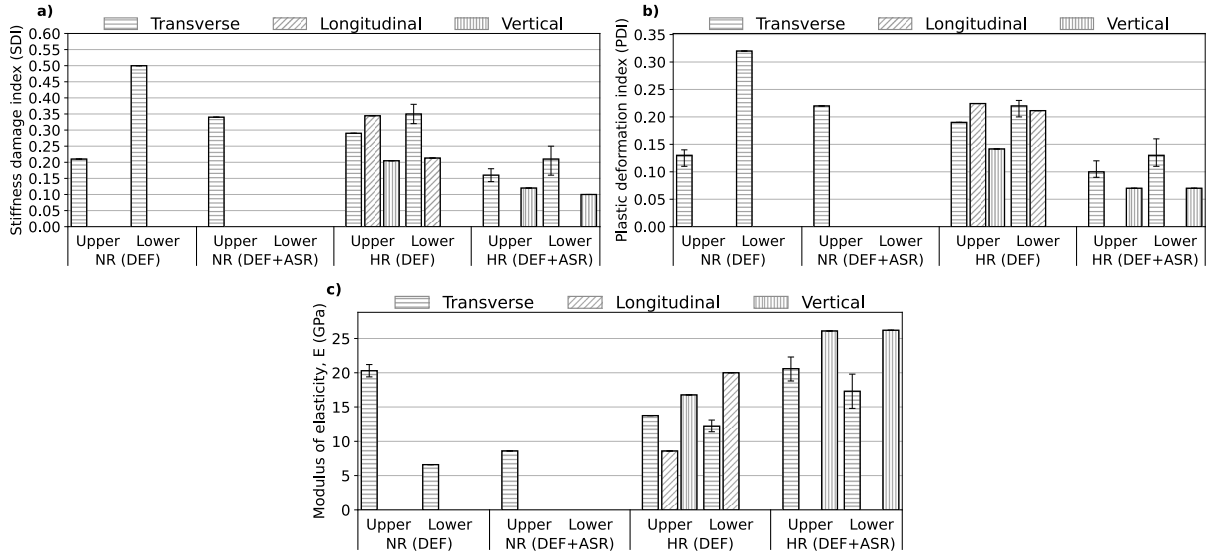


Figure 9.5 – SDT outcomes a) SDI, b) PDI, c) modulus of elasticity of non-reinforced (NR) and heavily reinforced (HR) beams affected by delayed ettringite formation (DEF) and combined delayed ettringite formation and alkali–silica reaction (DEF+ASR).

In the NR (DEF) beam, the modulus of elasticity in the transverse direction was higher in the upper part (20.3 GPa) than in the lower part (6.6 GPa). The upper-part transverse modulus of elasticity of NR (DEF+ASR) was markedly lower (8.6 GPa) than the same part and direction of NR (DEF). In the HR (DEF) beam, the upper part showed the highest modulus of elasticity in the vertical direction (16.8 GPa), followed by the transverse direction (13.7 GPa), and the lowest value in the longitudinal direction (8.6 GPa). In the lower part, the modulus of elasticity in the longitudinal direction (20.0 GPa) was higher than in the transverse direction (12.2 GPa). For HR (DEF+ASR), the modulus of elasticity in the vertical direction presented similar values in the upper (26.1 GPa) and lower (26.2 GPa) parts, while in the transverse direction, lower values than in the vertical direction were observed in both upper (20.60 GPa) and lower parts (17.30 GPa). In the transverse direction, HR (DEF+ASR) presented lower SDI and PDI values and higher modulus of elasticity values than HR (DEF) at both heights (upper: SDI 0.16 versus 0.29, PDI 0.10 versus 0.19, modulus of elasticity 20.60 GPa versus 13.75 GPa; lower: SDI 0.21 versus 0.35, PDI 0.13 versus 0.22, modulus of elasticity 17.30 GPa versus 12.20 GPa).

9.5.3 Residual expansion

Figure 9.6 presents the residual expansion measured during immersion in water at 38 °C, and Figure 9.7 presents the corresponding mass variation for the non-reinforced (NR) and heavily reinforced (HR) beams. Average values are represented by the markers, whereas error bars delimit the maximum and minimum values obtained from the available specimens.

For the NR (DEF) beam (Figures 9.6b and 9.7b), transverse cores showed a pronounced early development of residual expansion and mass variation, followed by a slower evolution over the remainder of monitoring. The upper part reached an average residual expansion of 0.52% and mass variation of 0.72% at 83 days. The lower part reached an average residual expansion of 0.30% at 406 days, with a mass variation of 0.72%. The upper part was monitored for only up to 83 days because the related sample was assigned to a different stream project.

The NR (DEF) beam (Figures 9.6b and 9.7b) presented higher residual expansion in the upper part than in the lower part, whereas similar mass variation values were measured in both parts at the last available time in each series. For the NR (DEF+ASR) beam (Figures 9.6b and 9.7b), results were available for the upper transverse cores, with an average residual expansion of 0.26% and a

mass variation of 0.71% at 406 days. No specimens could be extracted from the lower part due to the damage level of the beam.

For the HR (DEF) beam (Figures 9.6c and 9.7c), residual expansion and mass gain were compared across transverse, longitudinal, and vertical directions at 230 days, which corresponds to the latest common time-point available for the three directions. At 230 days, the upper part presented residual expansion values of 0.28% (transverse), 0.19% (longitudinal), and 0.12% (vertical), associated with mass gains of 0.54% (transverse), 0.54% (longitudinal), and 0.39% (vertical). In the lower part at 230 days, residual expansion values of 0.21% (transverse), 0.08% (longitudinal), and 0.10% (vertical), with corresponding mass gains of 0.49% (transverse), 0.44% (longitudinal), and 0.32% (vertical). Vertical residual expansion values obtained were similar between the upper and lower parts at 230 days (0.12% and 0.10%), with overlapping minimum–maximum ranges. Transverse monitoring extended to 406 days, for which residual expansion reached 0.32% (upper) and 0.23% (lower), and mass gain reached 0.60% (upper) and 0.52% (lower). The specimens remain under monitoring to confirm stabilisation of the measured residual expansions.

For the HR (DEF+ASR) beam (Figures 9.6d and 9.7d), residual expansion and mass gain were lower than in HR (DEF) over the monitored period. At 230 days, the upper part presented a transverse residual expansion of 0.11% and a vertical residual expansion of 0.06%, with corresponding mass variations of 0.35% and 0.30%. In the lower part at 230 days, residual expansion values were similar in the transverse and vertical directions (0.09% and 0.09%), and the associated mass variation was also similar (0.29% and 0.29%). Direction-dependent differences were more pronounced in the upper part, where transverse values were higher than vertical values for both residual expansion and mass variation, while the lower part showed similar transverse and vertical values for both quantities at 230 days.

The residual expansion results indicate that higher residual expansion values were generally associated with greater mass variation, consistent with the moisture uptake behavior expected during immersion in water at 38 °C. This relationship was more apparent in the HR beams, for which transverse values were higher than vertical values at comparable ages for both residual expansion and mass variation. In contrast, the NR (DEF) beam showed similar mass variations in both the upper and lower parts in the transverse direction, with higher residual expansion in the upper part, indicating that water uptake during testing did not translate into the same residual

expansion magnitude at both heights for this member. Comparisons between NR and HR beams should be interpreted with caution because the NR beams did not experience the moisture exposure phase (b), whereas the HR beams experienced moisture exposure phases (a) and (b), which can influence the deterioration state at coring and the residual expansion testing results.

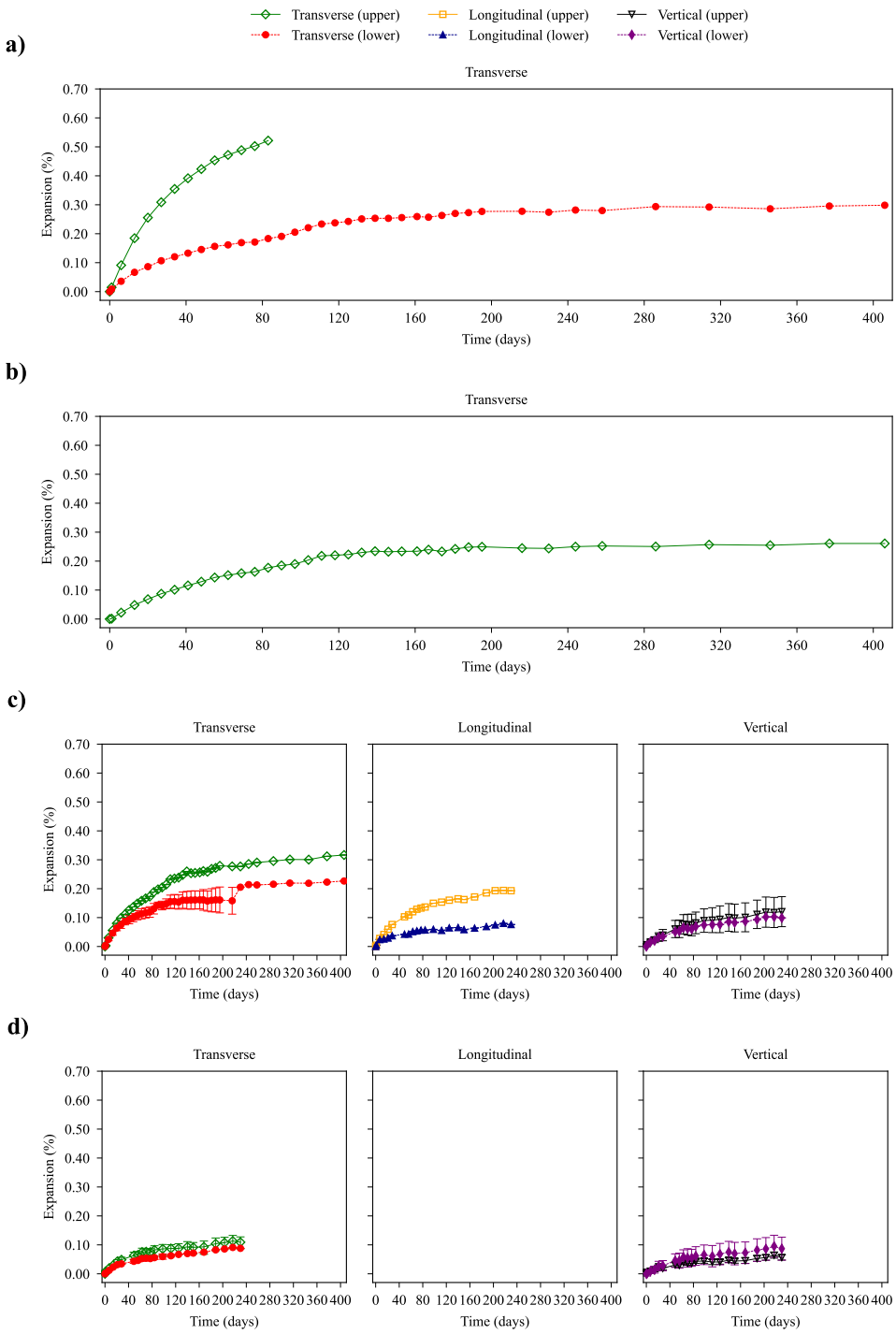


Figure 9.6 – Residual expansion: a) non-reinforced (DEF), b) non-reinforced (DEF+ASR), and c) heavily reinforced (DEF), and d) heavily reinforced (DEF+ASR) beams.

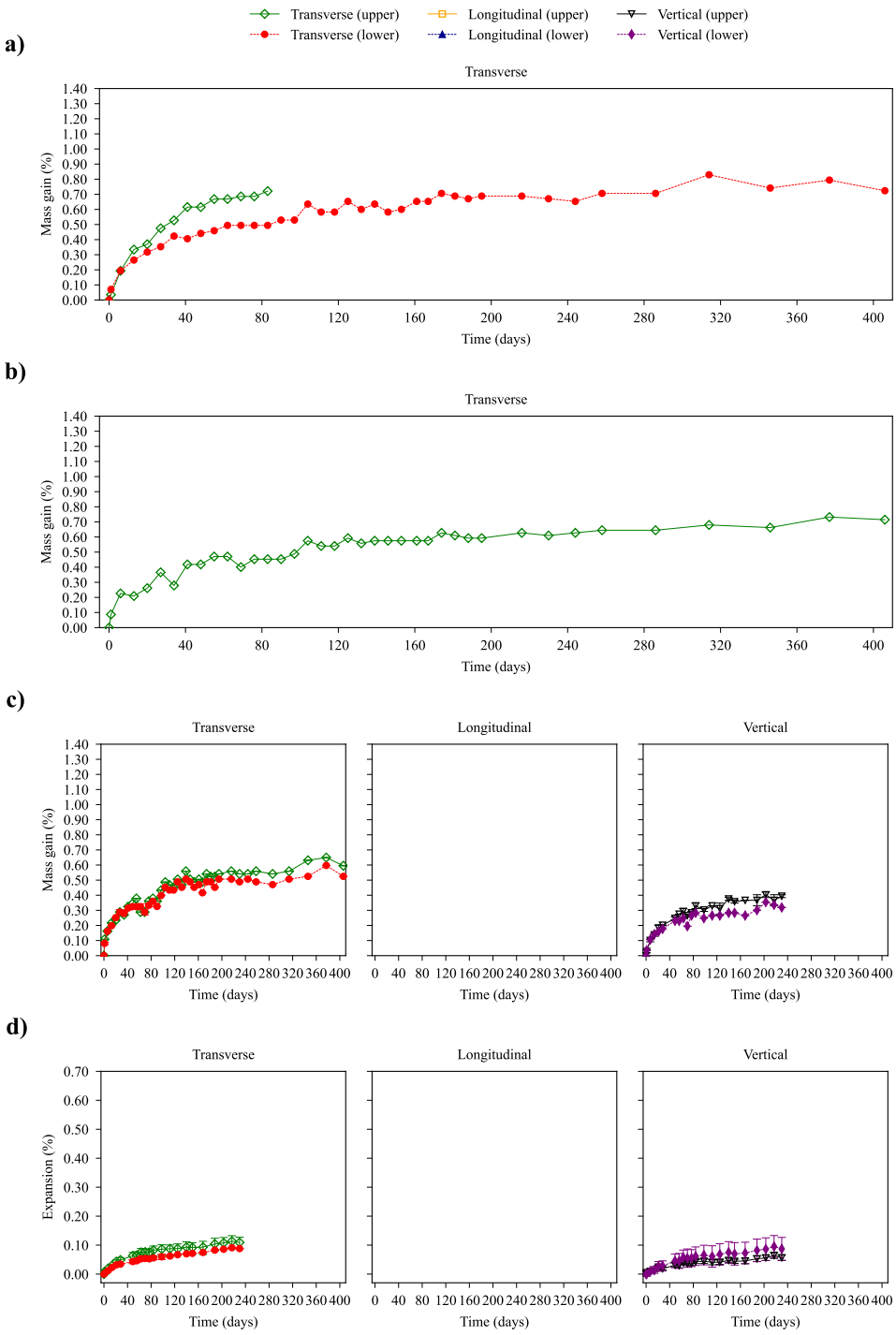


Figure 9.7 – Mass gain during residual expansion testing: a) non-reinforced (DEF), b) non-reinforced (DEF+ASR), and c) heavily reinforced (DEF), and d) heavily reinforced (DEF+ASR) beams.

9.6 Discussion

9.6.1 Water-transfer boundary conditions during aging exposure

The condition assessment performed in this study, including microscopic (DRI number; Figure 9.4), mechanical (SDT outcomes; Figure 9.5), and residual expansion testing (residual expansion; Figure 9.6 and mass variation; Figure 9.7), supports an interpretation of DEF- and DEF+ASR-induced deterioration in non- and heavily reinforced beams governed by the combined action of water-transfer gradients and reinforcement-induced restraint. This section uses semi-empirical moisture-transfer modelling to interpret the measured height- and direction-dependent deterioration patterns and to connect current damage state with the remaining free swelling capacity.

9.6.1.1 Semi-empirical moisture-transfer modelling and moisture-front interpretation

Moisture transfer during aging exposure was interpreted within a one-dimensional vertical domain of height $H = 0.50m$, with depth $z \in [0, H]$ measured from the top surface downwards. The reconstruction used the framework developed by Martin based on beam-scale weighing and automated γ-densimetry, supported by companion-cylinder characterisation subjected to identical thermal and hydric histories, following the experimental approach originally introduced by Multon and Toutlemonde [95–97] and extended to DEF and DEF+ASR conditions by Martin [23]. In the present work, this modelling was complemented to estimate the water-distribution during phase b. The objective of the present semi-empirical modelling was to reconstruct moisture availability in the beams through physically grounded descriptors suitable for interpreting deterioration gradients, rather than to solve a fully predictive coupled transport problem.

The global mass variation of a beam, $\Delta M_{Global}(t)$, was decomposed into contributions associated with the governing transfer fronts active during each exposure phase. During moisture exposure phase (a), drying from the top and capillary imbibition from the bottom were assumed to act simultaneously, such that the global mass variation was expressed as the sum of the imbibition and drying contributions (Equation 1) [23]. During phase (b), bottom imbibition was assumed to continue while the upper dry cap formed in phase (a) was progressively overtaken by rewetting

from the top, and the global mass variation was written as the sum of ongoing imbibition, the drying contribution frozen at the transition time t_b, and the rewetting contribution (Equation 2).

The top-drying front, $h_{dry}(t)$, was defined as the depth where the local relative mass loss reconstructed from γ-densimetry reached an iso-loss threshold $\left(\delta \mathrm{m}/m_0\right)_{iso}$ (Equation 3). The local drying kinetics during phase (a) were represented using a depth-dependent asymptotic magnitude $A(z)$ and characteristic time $\tau(z)$ fitted to γ-densimetry measurements, giving the local relative mass-variation profile $\left(\delta \mathrm{m}/m_\gamma\right), (\mathrm{z}, \mathrm{t})$ (Equation 4) [23]. The iso-loss threshold was defined through a material balance that links a saturation decrease to relative mass loss using $\beta = \frac{\rho_{\mathrm{water}} \cdot p}{\rho_{\mathrm{concrete}}}$, where p is the open porosity and ρ_{concrete} is the concrete bulk density, with $\Delta \mathrm{S} = (S_{onset} - S_0)$ defined from the post-curing saturation S_0 to the expansion-onset threshold S_{onset} (Equation 5). At each time, $h_{dry}(t)$ was obtained as the first depth where $\left(\delta \mathrm{m}/m_\gamma\right), (\mathrm{z}, \mathrm{t})$ matched $\left(\delta \mathrm{m}/m_0\right)_{iso}$, using linear interpolation between instrumented depths [23]. To respect γ-densimetry repeatability reported by Martin (±0.18%) [23], an instrument floor of 0.20% was applied when the computed iso-loss magnitude was smaller in absolute value.

The bottom imbibition front was described using a square-root-in-time formulation with an absorption coefficient D_{imb}, $\zeta = D_{imb}\sqrt{t}$, and an absolute imbibition height $h_{imb}(t) = h_{imm} + \zeta(\mathrm{t})$, with $h_{imm} = 0.07m$ representing the immersed zone (Equation 6) [23,95–97]. The corresponding beam-scale mass gain during phase (a) was written using the wetted height, the immersed cross-section A_{imm}, and ρ_{concrete}, combined with a modified sigmoidal kinetics function $(\delta \mathrm{m}/m)_{modified\_imb}$ calibrated from companion-cylinder mass-variation kinetics to transfer the material-scale uptake response to the structural scale (Equations 7 and 8) [23]. In Equation (7), the drying contribution was introduced through integration of the γ-densimetry-based local mass variation over the drying zone [23]. The absorption coefficient D_{imb} was identified by minimising the difference between the modelled and measured beam-scale mass variation during phase (a), using a least-squares procedure [23]. Equation 7 is the detailed version of equation 1.

During phase (b), the rewetting contribution was formulated to represent (i) an instantaneous uptake component associated with a rewetting thickness H_{inst} at the top surface and (ii) a diffusion-controlled advance governed by a rewetting coefficient D_{rwt}, while bottom imbibition continued

with the coefficient D_{imb} identified in phase (a). Under this approach, the global mass variation during phase (b) was expressed as the sum of continuous imbibition, a drying term held constant at t_b, an instantaneous rewetting contribution, and a diffusion-controlled rewetting term coupled with a simplified top-uptake kinetics $(\delta \mathrm{m}/m)_{modified\_top}$ (Equation 9), with $(\delta \mathrm{m}/m)_{modified\_imb}$ defined by Equation (10). Equation 9 is the detailed version of equation 2. The rewetting-front position from the top surface was expressed as $h_{rwt} = H_{inst} + D_{rwt} \cdot \sqrt{t_{>t_b} - t_b}$ (Equation 11). The parameters H_{inst}, D_{rwt}, and τ_{top} were obtained by fitting the phase (b) mass–time curve, while keeping D_{imb} fixed to its phase (a) estimate [23].

$$\Delta M_{Global}(t) = \Delta M_{imbibition}(t) + \Delta M_{dry}(t), 0 \le t \le t_b, phase\ a \tag{9.1}$$

$$\Delta M_{Global}(t) = \Delta M_{imbibition}(t) + \Delta M_{drying}(t_b) + \Delta M_{rewetting}(t), t > t_b, phase\ b \tag{9.2}$$

$$h_{dry}(t) = z_0\ where\ \delta m/m_\gamma\,(z_0, t) = \delta m/m_{iso} \tag{9.3}$$

$$\left(\frac{\delta\,\mathrm{m}}{\mathrm{m}}\right)_\gamma (\mathrm{z,t}) = A(z) \cdot \left(1 - e^{-\frac{t}{\tau(z)}}\right) \tag{9.4}$$

$$\left(\frac{\delta m}{m_0}\right)_{iso} = \beta \cdot \Delta \mathrm{S}, \quad \beta = \frac{\rho_{\mathrm{water}} \cdot p}{\rho_{\mathrm{concrete}}}, \quad \Delta \mathrm{S} = (S_{onset} - S_0) \tag{9.5}$$

$$\zeta = D_{imb}\sqrt{t}, \quad h_{imb}(t) = h_{imm} + \zeta(\mathrm{t}), \quad h_{imm} = 0.07m \tag{9.6}$$

$$\Delta M_{global}(t) = \left(0.07 + D_{imb}\sqrt{t}\right) A_{imm} \cdot \rho_{\mathrm{concrete}} \cdot \left(\frac{\delta m}{m}\right)_{modified\_imb}(t) + A_{imm} \cdot \rho_{\mathrm{concrete}} \cdot \int_{\mathrm{drying\ zone}} \left(\frac{\delta\,\mathrm{m}}{\mathrm{m}}\right)_\gamma (\mathrm{z,t}) \tag{9.7}$$

$$\left(\frac{\delta m}{m}\right)_{modified\_imb}(t) = \left(\frac{\delta m}{m}\right)_{cylinders}(\infty) \cdot \frac{1 - exp\left(-\frac{t}{\tau_{c_m}}\right)}{1 + \exp\left(-\frac{t - \tau_{l_m}}{\tau_{c_m}}\right)} \tag{9.8}$$

$$\Delta M(t) = \underbrace{\left(0.07 + D_{imb} \cdot \sqrt{t}\right) \cdot A_{imm} \cdot \rho_{\mathrm{concrete}} \cdot \left(\frac{\delta m}{m}\right)_{modified\_imb}(t)}_{Continuous\ imbibition} + \underbrace{A_{imm} \cdot \rho_{\mathrm{concrete}} \cdot \int_{drying\ zone} \left(\frac{\delta\,\mathrm{m}}{\mathrm{m}}\right)_\gamma (\mathrm{z}, t_b).}_{Drying\ contribution\ (constant)\ from\ "phase\ a"}$$

$$+ \underbrace{H_{inst} * A_{imm} \cdot \rho_{\mathrm{concrete}}}_{Instantaneous\ rewetting} + \underbrace{\left(H_{inst} + D_{rwt} \cdot \sqrt{t_{>t_b} - t_b}\right) \cdot A_{imm} \cdot \rho_{\mathrm{concrete}} \cdot \left(\frac{\delta m}{m}\right)_{modified\_top}(t)}_{diffusion-controlled\ rewetting} \tag{9.9}$$

$$\left(\frac{\delta m}{m}\right)_{modified\_top}\left(t_{>t_b}\right) = \left(\frac{\delta m}{m}\right)_{cylinders}(\infty) \cdot \left[1 - e^{-\frac{\left\langle t_{>t_b} - t_b \right\rangle}{\tau_{top}}}\right] \tag{9.10}$$

$$h_{rwt} = H_{inst} + D_{rwt} \cdot \sqrt{t_{>t_b} - t_b} \tag{9.11}$$

he fitted parameters adopted for the present beams are summarised in Table 9.3, and the measured mass-variation curves used for parameter identification and the corresponding reconstructed drying, imbibition, and rewetting fronts are presented in Figures 9.8 and 9.9.

Table 9.3 – Parameters used to estimate the water-transfer behavior of non-reinforced (NR) and heavily reinforced (HR) beams affected by delayed ettringite formation (DEF) and combined delayed ettringite formation and alkali–silica reaction (DEF+ASR).

		NR (DEF)	NR (ASR)	HR (DEF)	HR (DEF+ASR)
Drying	$\rho_{concrete}$(kg/m³) [23]	2320	2363	2320	2363
	p (%)[23]	14.6	14.6	14.6	14.6
	S_0 [23]	0.93	0.95	0.93	0.95
	β	0.06293	0.06179	0.06293	0.06179
	ΔS	-0.030	-0.050	-0.030	-0.050
	Iso-loss (raw) %	-0.189	-0.309	-0.189	-0.309
	Iso-loss used %	-0.200	-0.309	-0.200	-0.309
Imbibition	$(\delta m/m)\ \infty$	0.0241	0.0218	0.0241	0.0218
	$\tau_{c\,m}\ (days)$ [23]	50	22	90	60
	$\tau_{l\,m}\ (days)$ [23]	290	140	280	170
	$D_{imb}\ (m \cdot \sqrt{days}$ [23]	2.12×10^{-2}	4.66×10^{-2}	2.410×10^{-2}	7.42×10^{-3}
	RMSE (kg)	0.1588	0.6778	0.4813	0.3510
Rewetting	H_{inst} (m)	-	-	7.130×10^{-4}	2.748×10^{-3}
	$D_{rwt}(m \cdot \sqrt{days})$	-	-	2.450×10^{-3}	1.303×10^{-2}
	τ_{top} (days)	-	-	0.09	0.20
	RMSE (kg)	-	-	0.9149	1.1785

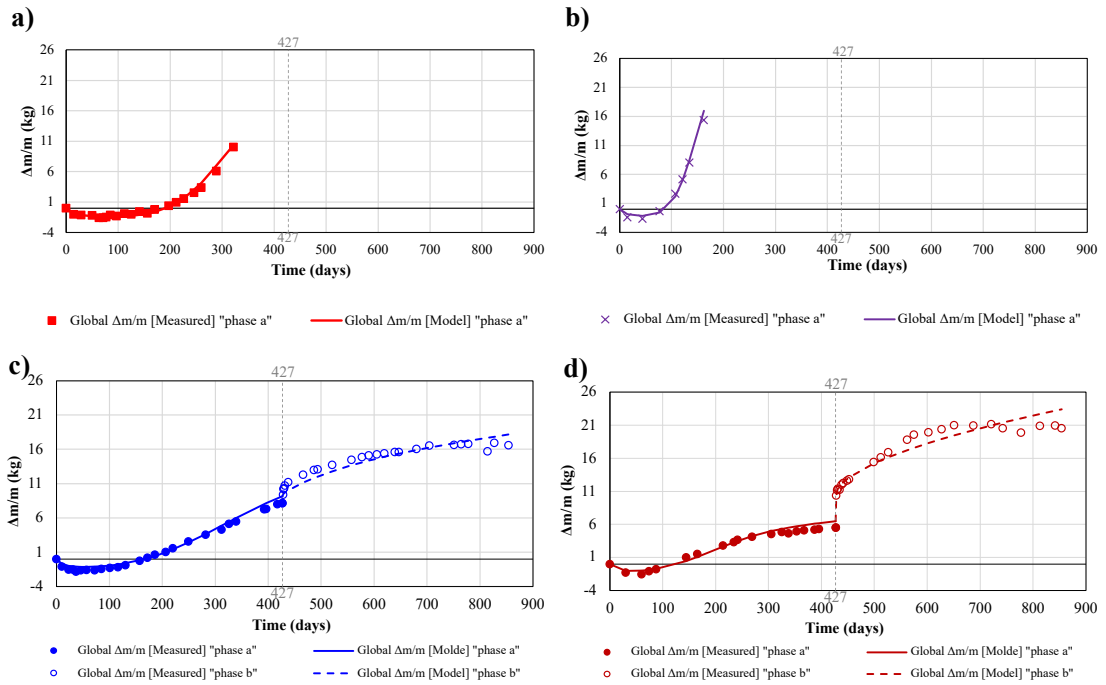


Figure 9.8 – Global mass variation: a) non-reinforced (DEF), b) non-reinforced (DEF+ASR), c) heavily reinforced (DEF), and d) heavily reinforced (DEF+ASR).

The time evolution of the drying, imbibition, and rewetting fronts is discussed for a beam height of 50 cm. The drying and rewetting fronts are measured from the top surface, while the imbibition front position is expressed as a depth coordinate along the member height, with 50 cm corresponding to the bottom surface and smaller values indicating a higher rise of the capillary front.

For the non-reinforced (DEF) beam (Figure 9.9a), only the drying and imbibition fronts were present because this member did not experience moisture exposure phase (b). During phase (a), the drying front stabilised within the upper 9 cm by 322 days, while the imbibition front reached 5 cm at 322 days. This evolution indicates a thin dry cap near the top surface, combined with a capillary supply that reached near the full beam height over the duration of exposure. At intermediate ages, the fronts defined a vertical gradient characterised by an upper dry zone and a lower wetted zone, while the long-term evolution indicates that most depths experienced periods of high water availability compatible with DEF development.

For the non-reinforced (DEF+ASR) beam (Figure 9.9b), the drying front stabilised within the upper 6 to 7 cm over 25 to 162 days, while the imbibition front reached approximately 3 cm at 75 days. These values indicate rapid establishment of water availability along the full height under the combined action of partial immersion and damage-enhanced transport associated with DEF+ASR. In this beam, the modelling suggests that the persistence of a thin top dry zone was primarily transient relative to the rapid upward progression of the imbibition front.

For the heavily reinforced (DEF) beam (Figure 9.9c), phase (a) exhibited a drying front stabilised at 9 cm by 427 days, while the imbibition front reached 17.8 cm at 427 days. This configuration corresponds to a top dry cap of about 9 cm and a bottom wetted zone extending to about 32.2 cm above the bottom surface, separated by a mid-height region of relatively reduced saturation, keeping the initial saturation of the concrete. During phase (b), the rewetting front advanced to 5.2 cm at 854 days, while the remaining drying layer thickness reduced from 9 cm at the start of phase (b) to 3.8 cm at 854 days, indicating partial restoration of moisture conditions within the near-surface top region. Over the same interval, the imbibition front reached 7.3 cm at 854 days, corresponding to capillary penetration of about 42.7 cm above the bottom surface. The resulting hydric state at the end of monitoring is characterised by a thin, rewetted cap near the top and a persistent wetted zone near the bottom.

For the heavily reinforced (DEF+ASR) beam (Figure 9.9d), phase (a) showed a drying front stabilised near 9 cm by 427 days, while the imbibition front reached 27.7 cm at 427 days, indicating a smaller wetted height from bottom supply than in the heavily reinforced (DEF) beam at the same age, which is likely influenced by the presence of ASR. During phase (b), the rewetting front progressed rapidly, reaching 17.4 cm at 600 days and 27.2 cm at 854 days, while the remaining drying layer thickness reduced to 0.0 cm by 440 days, indicating elimination of the dry cap within the modelling resolution. At 854 days, the rewetting front depth and the imbibition front depth approached convergence, which indicates widespread restoration of high water availability over the member height under combined top supply and bottom capillary ingress. Under these conditions, the distinction between top- and bottom-driven wetting becomes less meaningful, and the front-based reconstruction is interpreted as semi-quantitative for describing water availability rather than as a strict partition of water sources.

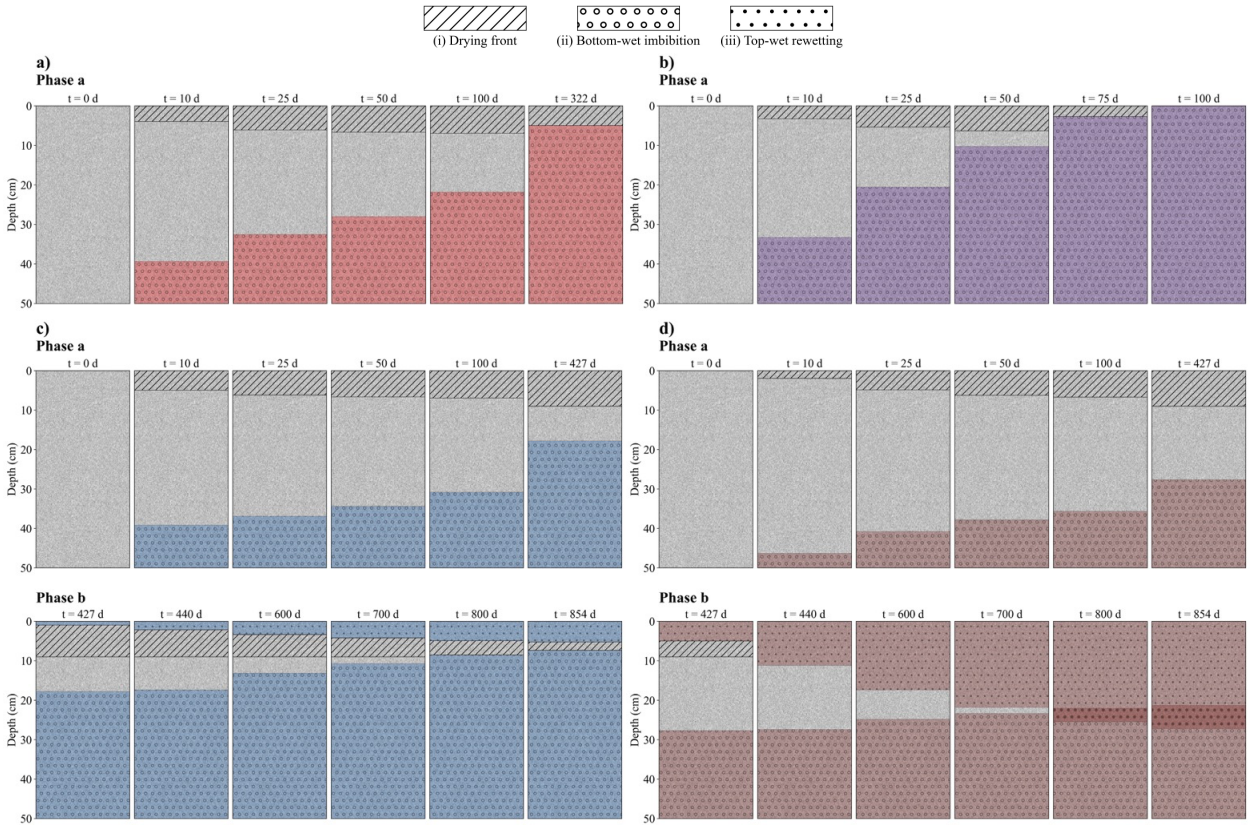


Figure 9.9 – Water transfer behavior as a function of time of a) non-reinforced (DEF), b) non-reinforced (DEF+ASR), c) heavily reinforced (DEF), and d) heavily reinforced (DEF+ASR).

The reconstructed front patterns are consistent with the hydric-state interpretation reported by Morenon [22] for Martin's beam dataset, in which desorption near the top boundary and capillary uptake from the bottom produce a dried upper zone, a saturated lower zone, and a transition region of intermediate saturation. The heavily reinforced (DEF) beam presents a rewetting depth of about 5 cm at 854 days, which aligns with the highly localised rewetting sensitivity case discussed by Morenon and remains well below the larger near-surface penetration depths inferred shortly after rewetting in experimental interpretations. In contrast, the heavily reinforced (DEF+ASR) beam presents substantially deeper rewetting penetration, indicating a stronger top-surface wetting contribution during phase (b), which is consistent with damage-enhanced transport effects expected under combined mechanisms. These reconstructed moisture-transfer conditions provide the boundary-condition basis for interpreting the height-dependent deterioration patterns discussed in the following subsections.

The reconstruction presented herein remains a front-based interpretation of water availability derived from global mass change and, in phase (a), from the γ-densimetry-based drying kinetics. This semi-empirical approach does not explicitly account for additional cracking induced by drying shrinkage under the imposed low relative humidity boundary at the upper surface. Drying shrinkage can generate a cracking network in the cement paste and increase near-surface transport connectivity, which may accelerate water penetration and reduce the persistence of the dry cap relative to an intact material. Zhu [98] showed that the DRI increases with decreasing relative humidity in concrete not affected by internal swelling reactions, following the evolution of shrinkage measurements, which supports the possibility that part of the upper-zone cracking record and part of the transport connectivity in this programme can originate from exposure-induced shrinkage. Under these conditions, the reconstructed fronts are interpreted as semi-quantitative indicators of water availability, and local deviations may arise from shrinkage-induced cracking not accounted for in the modelling assumptions.

9.6.1.2 Microscopic assessment

The distribution of microscopic damage features in absolute counts normalized per 100 cm² and the corresponding proportions (Figure 9.10), and the crack characteristics, including crack density, maximum crack width, and length (Figure 9.11), complement the quantitative damage analysis via

the DRI number (Figure 9.4). To further investigate the influence of moisture transfer and reinforcement on the proportions of damage induced by each mechanism, the contributions of DEF and ASR to overall deterioration were estimated by reclassifying DRI distress features into two groups and analysing their absolute counts and corresponding proportions (Figure 9.12). Group V includes ASR-related features (i.e., OCA, OCA_RP, CCP_ag, and CCP_RP_ag), whereas Group VI includes DEF-related features (i.e., Debon, CCP_paste, and CCP_RP_paste). Where 'ag" and "paste" stand for aggregate- and paste-related deterioration features.

In the non-reinforced (DEF) beam, higher absolute counts were observed in the lower part than in the upper part, predominantly of Group III, followed by Group IV. This difference indicates that DEF-induced damage in the lower part was at a more advanced stage of the mechanism, with a greater proportion of cracks in the bulk cement paste (Group III), while the upper part showed a relatively pronounced proportion of cracks in the ITZ (Group IV). The effect of moisture transfer is further evident in the crack density and maximum width and length, with the lower part showing longer, thinner cracks than the upper part.

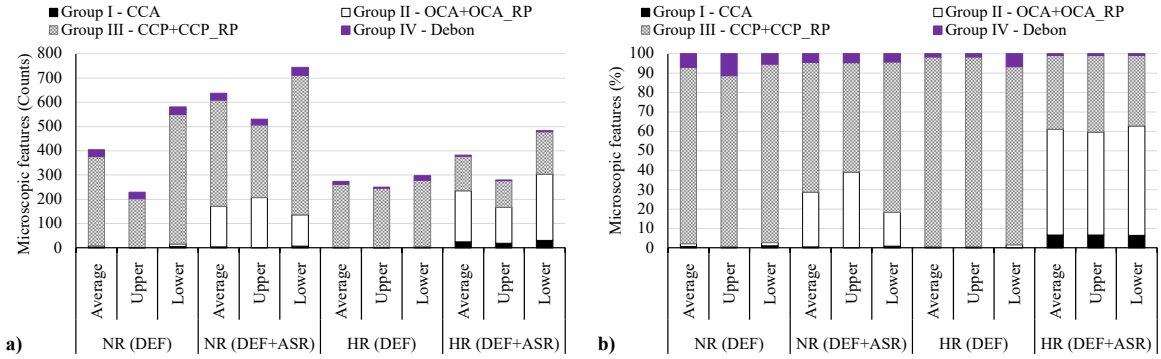


Figure 9.10 – Microscopic features of deterioration: a) Counts normalized to 100 cm². b) Percentage without applying the weighting factors.

In the non-reinforced (DEF+ASR) beam, higher absolute counts in Group II than in Group III indicate that ASR has progressed more in the upper part than in the lower part. This difference in the proportion of damage features can be attributed to moisture-transfer conditions: the lower part experienced greater water availability over time, which fostered the development of DEF-induced cracking. Since ASR requires less water than DEF to progress [59,62,99], a greater proportion of Group II was observed in the upper part, and some leaching may have occurred. The mechanism contribution estimate confirmed that DEF was more influential on the overall deterioration in the

lower part than in the upper part, whereas ASR was more influential in the upper part than in the lower part (Figure 9.12). Crack density and maximum crack dimensions provide an additional indication of the moisture-transfer effect, with higher crack density and wider, longer cracks in the lower part than in the upper part.

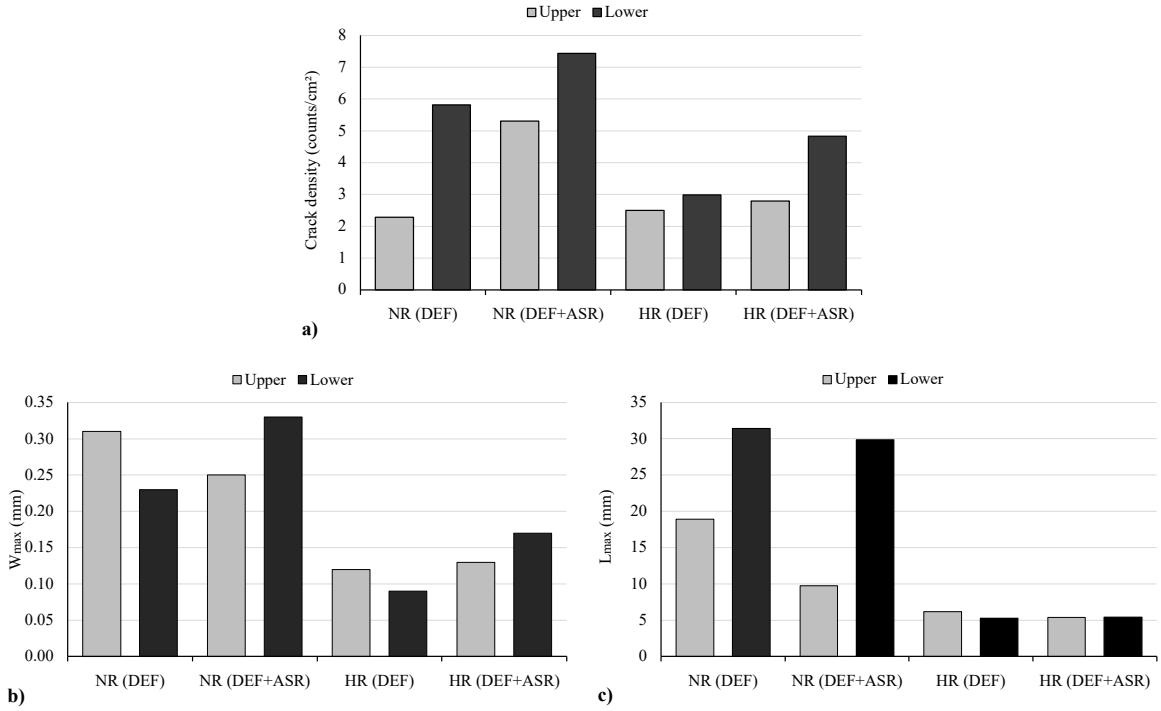


Figure 9.11 – Crack characteristics: a) crack density; b) maximum crack width; and c) maximum crack length.

In the heavily reinforced (DEF) beam, the difference in microscopic crack counts between the upper and lower parts was smaller than in the non-reinforced configuration, which can be attributed to the additional water supply during phase (b). Reinforcement further influenced the observed DEF-induced damage, as reflected in crack density and maximum crack dimensions, indicating a limited upper-to-lower contrast and comparatively small crack widths and lengths, suggesting that restraint restricted crack opening and limited the development of longer cracking networks even with a longer water supply from the lower part and additional water supply from the upper part. It is important to note that Martin [23] reported a two-stage evolution of deflection, characterized by an initial downward deflection followed by a progressive inversion leading to an upward deflection, which was associated with sufficient engagement of the lower longitudinal

reinforcement. An upward-bending state modifies the section stress field and can redistribute the localisation of tensile and compressive strains across the height, potentially promoting a response dominated by distributed cement paste cracking while limiting debonding features in the upper part.

In the heavily reinforced (DEF+ASR) beam, the proportion of Group II features in both the upper and lower parts indicates that ASR-induced damage features were an important component of the microscopic deterioration in both parts evaluated, rather than being more evident in the upper part as observed in the non-reinforced (DEF+ASR) beam. This distribution can be attributed to the moisture-transfer conditions during phase (b), in which the additional water supply from the top fostered the later development of DEF-induced cracks in the upper part and reduced the upper-to-lower contrast in moisture exposure, which favoured the presence of both Group II and Group III features in the upper and lower parts. The mechanism contribution estimate further indicates that ASR was more influential on the overall deterioration in both parts evaluated than in the non-reinforced (DEF+ASR) beam, with a limited upper-to-lower contrast in the relative contributions of ASR- and DEF-related features (Figure 9.12). Reinforcement further influenced the expression of DEF- and ASR-induced damage by restricting crack opening, as indicated by the maximum crack width, which was thinner than in the non-reinforced (DEF+ASR) beam but wider than in the heavily reinforced (DEF) beam. This crack opening indicates a different magnitude of reinforcement-induced restraint effect on deterioration features induced by combined DEF+ASR than on deterioration features induced by DEF.

9.6.1.3 Mechanical assessment

The residual modulus of elasticity, obtained by comparing the modulus of elasticity (Figure 9.5c) to the reference 28-day modulus of elasticity of the mixtures used for DEF (i.e., 30.8 GPa) and DEF+ASR (i.e., 31.5 GPa), and the non-linear index (NLI) provide further understanding of the impact of induced deterioration on the mechanical response of the affected material (Figure 9.13). The bars indicate average values, and the error bars span the maximum and minimum values among the tested specimens (Table 9.2).

In the non-reinforced (DEF) beam, the transverse response showed a marked stiffness loss with a pronounced upper-to-lower contrast, which follows the localisation of microscopic damage and

the moisture-transfer conditions discussed in Sections 9.6.1.1 and 9.6.1.2. The upper part showed 66.0% of the reference modulus, while the lower part showed 21.6%. The higher damage indices in the lower part (SDI = 0.50; PDI = 0.32 – Figure 9.5a-b) than in the upper part (SDI = 0.21; PDI = 0.13 – Figure 9.5a-b), together with the higher crack density and the higher proportion of cracking in the bulk cement paste and ITZ observed microscopically, explain the more pronounced stiffness loss in the lower part. The SDI and PDI indicate greater energy dissipation and irreversible deformation in the lower part, which is compatible with a more connected cracking network and reduced efficiency of load transfer through the aggregate–paste skeleton. The NLI values were below unity in both parts (0.79 in the upper part and 0.59 in the lower part), indicating preferential cracking parallel to the loading direction of the transverse cores.

In the non-reinforced (DEF+ASR) beam, the transverse core extracted from the upper part presented a low residual modulus (27.4% of the reference modulus) together with elevated damage indices (SDI = 0.34; PDI = 0.22 – Figure 9.5a-b), explained by the microscopic evidence of an important damage in the upper part, including a greater contribution of ASR-related features, (higher proportion of Group II features), in which cracking in the aggregate particles contributes to early stiffness loss even when moisture availability is lower than in the lower part. The NLI exceeded unity (1.39), indicating preferential cracking perpendicular to the loading direction. The lower-part transverse SDT results were not available for this beam; therefore, the expected further stiffness reduction associated with the higher crack density and larger crack dimensions measured in the lower part cannot be quantified mechanically within the present dataset.

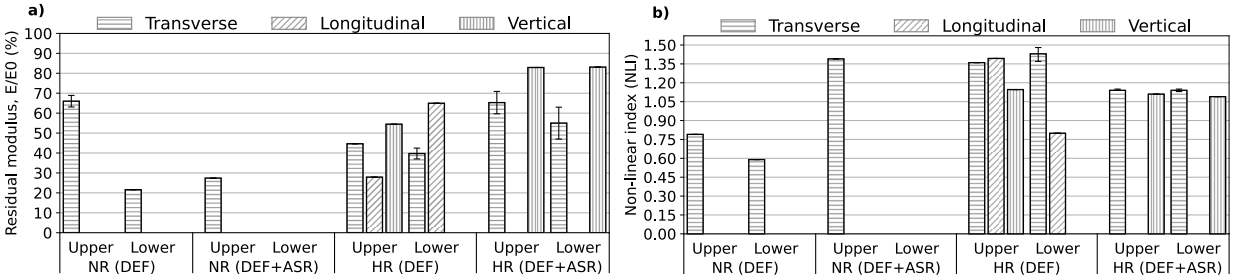


Figure 9.12 – Mechanical response from SDT for of non-reinforced (NR) and heavily reinforced (HR) beams affected by delayed ettringite formation (DEF) and combined delayed ettringite formation and alkali–silica reaction (DEF+ASR): a) residual modulus of elasticity and b) non-linear index (NLI).

In the heavily reinforced (DEF) beam, the transverse response presented a smaller upper-to-lower contrast than in the non-reinforced configuration, with residual moduli of 44.6% in the upper part and 39.7% in the lower part, and intermediate damage indices (upper: SDI = 0.29, PDI = 0.19; lower: SDI = 0.35, PDI = 0.22 – Figure 9.5a-b). This reduced difference indicates that the additional water supply during phase (b) increased damage development in the upper part. The NLI values were above unity in the transverse direction for both parts (upper: 1.36; lower: 1.43), indicating cracking preferentially perpendicular to the loading direction; the vertical direction shows the same trend in the upper part (NLI = 1.15). In the longitudinal direction, the NLI shifted from above unity in the upper part (1.39) to below unity in the lower part (0.80), indicating a change in preferential crack orientation with depth relative to longitudinal loading.

The directional NLI response can be related to the anisotropic restraint introduced by the reinforcement layout, in which the high longitudinal reinforcement ratio (approximately 1.8%) and the transverse confinement provided by stirrups (approximately 0.45%) promote a mechanically constrained crack development that favours cracks intersecting the loading direction in transverse and vertical cores (NLI > 1), while allowing a change in preferential cracking orientation along the member axis with depth in the longitudinal cores (upper: NLI > 1; lower: NLI < 1). A microscopic evaluation is required to complement this mechanical analysis of the cracking orientation. These differences can also be interpreted in light of the upward-bending behaviour reported by Martin [23] for the heavily reinforced beam, as previously discussed.

In the heavily reinforced (DEF+ASR) beam, the transverse response presented higher residual moduli than in the non-reinforced (DEF+ASR) beam, together with lower damage indices (upper: 65.3%, SDI = 0.16, PDI = 0.10; lower: 55.0%, SDI = 0.21, PDI = 0.13 – Figure 9.5a-b), indicating that restraint reduced energy dissipation and irreversible deformation under combined mechanisms. This response aligns with the microscopic record in which both Group II and Group III features were present in the upper and lower parts, together with a reduced crack-opening level relative to the non-reinforced (DEF+ASR) beam. The transverse NLI remained above unity in both parts (1.14 and 1.14), indicating cracking preferentially perpendicular to transverse loading; the vertical NLI was also above unity in both parts (upper: 1.11; lower: 1.09), consistent with the vertical SDT response remaining comparatively stiff (upper: 82.9%, SDI = 0.12, PDI – Figure 9.5a-b).

9.6.1.4 Potential for further expansion

Residual expansion measured on extracted cores immersed in water at 38 °C (Figure 9.6) indicates the free swelling capacity remaining at the time of coring once the concrete material is placed under favourable conditions. It is important to note that the non-reinforced beams were exposed to the aging process for 330 and 160 days, NR (DEF) and NR (DEF+ASR, respectively, whereas HR (DEF) and HR (DEF+ASR) experienced the entire process, 854 days. The results of the maximum exposure measured during the residual expansion testing is discussion hereafter (Figure 9.13).

In the non-reinforced (DEF) beam, residual expansion indicates a substantial remaining free swelling capacity at the time of coring and a marked upper-to-lower contrast in the transverse direction, from 0.52% in the upper part to 0.30% in the lower part. DRI and SDT results indicate more advanced deterioration in the lower part, with higher crack density and greater stiffness loss, reducing the remaining capacity during immersion. The moisture-front reconstruction indicates a thin dry cap near the top and a sustained upward capillary supply during phase (a), maintaining higher water availability in the lower part while delaying deterioration development in the upper part. The upper part was monitored for 83 days, while the lower part was monitored for 406 days. The trend in residual expansion results and damage analysis indicates the relationship between deterioration already developed (damage extent) and residual expansion potential.

In the non-reinforced (DEF+ASR) beam, the 230-day residual expansion indicates limited remaining free swelling capacity in the upper part (0.26%). The microscopic analysis and the available transverse SDT results indicate an important deterioration condition already developed before coring, leaving limited remaining free swelling capacity when the core is later exposed to favorable conditions for further development. The moisture reconstruction indicates rapid establishment of water availability along most of the height during phase (a), which supports exposure conditions favourable to early reaction development under combined mechanisms. Residual expansion results were not available for the lower part.

In the heavily reinforced (DEF) beam, the residual expansion indicates a combined depth- and direction-dependent response. In the upper part, residual expansions reached 0.32% in the transverse direction, 0.19% in the longitudinal direction, and 0.12% in the vertical direction, while in the lower part they decreased to 0.23% in the transverse direction, 0.08% in the longitudinal

direction, and 0.10% in the vertical direction. The transverse direction preserves the largest remaining capacity in both parts, whereas the longitudinal direction shows the smallest remaining capacity, particularly in the lower part. The moisture-front reconstruction indicates persistence of a dried upper zone during phase (a), partial restoration of near-surface water availability during phase (b), and a continuous wetted zone near the bottom, which supports a depth-dependent deterioration condition captured by DRI and SDT. The direction-dependent differences reflect the influence of the reinforcement-induced restraint.

In the heavily reinforced (DEF+ASR) beam, the residual expansion indicates low remaining free swelling capacity in the transverse and vertical directions, with direction-dependent contrasts between upper and lower parts (transverse upper: 0.13%; transverse lower: 0.09%; vertical upper: 0.07%; vertical lower: 0.13%). Comparison between the heavily reinforced beams indicates lower remaining free swelling capacity in the DEF+ASR beam than in the DEF beam in the transverse and vertical directions, while both beams preserve direction-dependent contrasts. The moisture-front reconstruction indicates elimination of the dry cap and deeper penetration of rewetting during phase (b), increasing water availability over a larger fraction of the height, while the microscopic and SDT results indicate anisotropic cracking and a direction-dependent mechanical response under combined mechanisms.

Residual expansion differences do not reflect remaining reaction potential alone. Residual expansion is also influenced by the capacity of the existing crack network to accommodate further product formation during the test, particularly in highly cracked material, where additional expansive products can partially fill available crack space and reduce the fraction of further reaction that translates into measurable expansion.

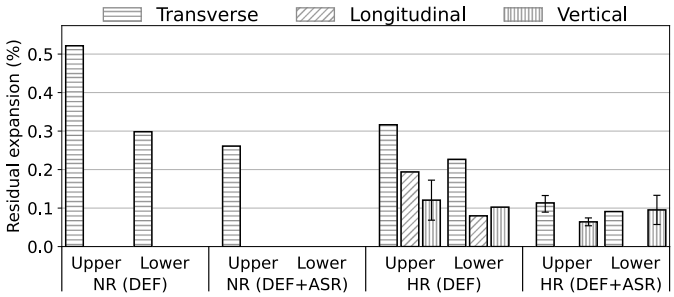


Figure 9.13 – Maximum residual expansion measured of non-reinforced (NR) and heavily reinforced (HR) beams affected by DEF and DEF+ASR.

9.6.2 Current damage extent condition

This section consolidates the current damage condition of the beams investigated, estimated through two approaches. First, the deterioration-based approach estimates the induced expansion ε_{ML} at coring time, using the multi-level assessment protocol that interprets microscopic and mechanical indicators of damage severity against a specific database. Second, the "potential chemical advancement"-based approach estimates the fraction of the free-expansion potential already mobilised at coring by comparing residual expansion to the reference free-expansion potential of companion specimens, and it converts this "potential chemical advancement" into an equivalent current expansion state that would have been developed under favorable conditions. The estimations obtained for all beams evaluated in this thesis (Papers II and III – Chapters 7 and 8) are discussed to identify where the induced response inferred from deterioration aligns with the expansion state inferred from reaction progress, and where discrepancies indicate the influence of moisture availability, restraint, directional cracking, and crack-network accommodation of reaction products.

9.6.2.1 Deterioration-based estimations of induced expansion

The deterioration-based estimations of induced expansion, ε_{ML}, were obtained using the benchmark database developed by Sanchez et al. [18]. Figure 8.14 summarises the resulting induced expansion estimates for the investigated beams at specific locations.

In the non-reinforced (DEF) beam, the induced expansion was high in both parts, with 0.40% in the upper part and 1.60% in the lower part. In the non-reinforced (DEF+ASR) beam, the induced expansion in the upper part reached 1.70%, while the lower part was not available. In the heavily reinforced (DEF) beam, the induced expansion showed a marked direction dependence, with transverse induced expansion of 0.35% in the upper part and 1.15% in the lower part, longitudinal induced expansion of 0.74% in the upper part and 0.31% in the lower part, and a vertical induced expansion of 0.15% in the lower part (upper vertical not available). In the heavily reinforced (DEF+ASR) beam, the induced expansion remained comparatively low in the measured directions, with transverse induced expansion of 0.18% in the upper part and 0.40% in the lower part, and vertical induced expansion of 0.11% and 0.12% in the upper and lower parts, respectively (longitudinal not available). These values indicate that, even in beams affected by combined

mechanisms (DEF+ASR), the induced microscopic and mechanical deterioration was reduced in the reinforcement-induced restraint directions, resulting in anisotropic induced expansion, while HR (DEF+ASR) showed a greater reduction than HR (DEF). Moreover, the estimated extent of damage reached or exceeded the theoretical threshold of steel yielding (i.e., 0.20%), specifically in the longitudinal and transverse of HR (DEF) and in the longitudinal of HR (DEF+ASR). This implies further structural implications and must be investigated in future analysis.

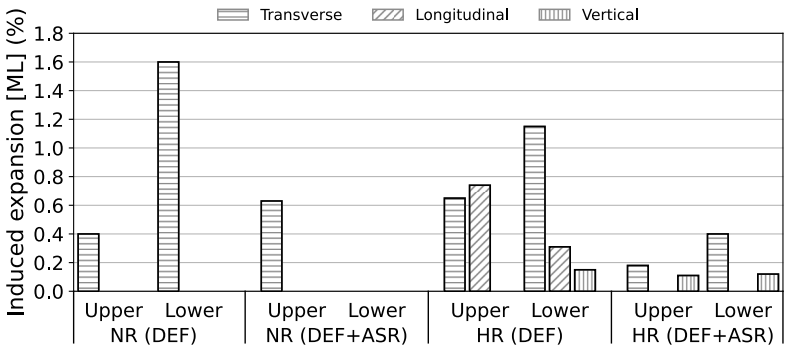


Figure 9.14 – Current damage extent condition estimated through the multi-level assessment protocol.

9.6.2.2 “Potential chemical advancement”-based estimations of current expansion

The “potential chemical advancement”-based estimation of current expansion follows the reconstruction approach originally proposed by Multon et al. [88] for ASR-affected concrete, in which a calibrated free-expansion law serves as a reference for interpreting residual expansion tests performed on extracted cores. Martin [23] extended this approach to DEF- and DEF+ASR-affected beams by defining reference free-expansion curves from companion specimens cast with the same concrete mixtures as the beams and stored under favourable, uniform moisture conditions, and by introducing a combined fitting of time and expansion offsets with the free-expansion law parameters. In the present study, the reconstruction adopts this approach: the reference free-expansion curves for DEF (τ_L 84.4 days, τ_C 12.1 days, ε_∞ 1.79%) and DEF+ASR (τ_L 62.8 days, τ_C 10.4 days, ε_∞ 1.77%) measured on companion specimens [23], together with the residual expansion results (Section 9.5.3), are used to estimate the equivalent current expansion state for each beam and part evaluated. The “potential chemical advancement” is defined on a 0 to 1 scale, where 1 corresponds to exhaustion of the free-expansion potential. This estimate remains

conditional because the measured residual expansion reflects both the remaining reaction potential and the influence of the existing crack network in the cores extracted from the beams.

Figure 15 summarises the reconstructed current expansion estimates. In the non-reinforced (DEF) beam, the estimated current expansion was 1.54% in the upper part and 1.67% in the lower part, indicating a high expansion state in both parts with a moderate upper-to-lower contrast ("potential chemical advancement": upper 0.71; lower 0.83). In the non-reinforced (DEF+ASR) beam, the upper part estimate reached 1.51%, while the lower part was not available ("potential chemical advancement" in the upper part: 0.86).

In the heavily reinforced (DEF) beam, the "potential chemical advancement"-based estimates were available in the longitudinal and vertical directions, with longitudinal current expansions of 1.60% in the upper part and 1.71% in the lower part, and vertical current expansions of 1.67% and 1.69% in the upper and lower parts, respectively (transverse not available) ("potential chemical advancement": longitudinal upper 0.89, longitudinal lower 0.96; vertical upper 0.93, vertical lower 0.94). In the heavily reinforced (DEF+ASR) beam, transverse current expansions reached 1.65% in the upper part and 1.67% in the lower part, while the vertical direction reached 1.67% and 1.69% in the upper and lower parts, respectively (longitudinal not available) ("potential chemical advancement": transverse upper 0.93, transverse lower 0.95; vertical upper 0.96, vertical lower 0.93).

These reconstructed values indicate that, at the time of coring, "potential chemical advancement" was high for both concretes and in all parts and directions for which reconstruction was available. The narrow ranges within each beam, and the clustering of estimates near the asymptotic free-expansion levels defined by the companion-specimen reference curves, indicate that the imposed moisture histories during aging exposure enabled extensive mobilisation of the free-expansion potential. The modest upper-to-lower contrasts further indicate that, once phase (b) introduced additional water supply from the top in the heavily reinforced beams, the "potential chemical advancement" state became more uniform along the height within the resolution of the reconstruction. Additionally, it may be influenced by the practical use of the approach, since only a short section of the full-expansion curve is available. In the combined-mechanism member, the similarly high reconstructed current expansions in both transverse and vertical directions indicate

that, under the applied exposure history, the DEF+ASR system also progressed to a late expansion state in the portions of the member captured by the residual expansion tests.

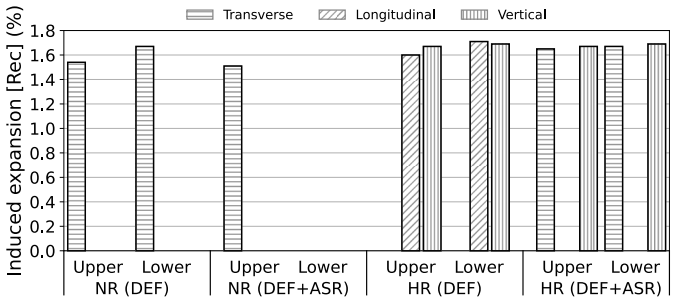


Figure 9.15 – Current expansion estimated through the reconstruction approach.

9.6.2.3 Comparison of estimating induced expansion approaches: Multi-level assessment protocol (deterioration-based) and reconstruction of residual expansion ("potential chemical advancement").

Figure 9.16 compares the current condition estimated through the deterioration-based induced expansion, ε_{ML}, and through the "potential chemical advancement"-based reconstruction. These two estimates refer to related, yet distinct, physical quantities. The "potential chemical advancement"-based estimate represents an equivalent free-expansion state under favourable moisture conditions and negligible restraint imposed locally on the structure by the reinforcement, inferred from the reference free-expansion curves and residual expansion testing [23,88]. The deterioration-based estimate represents an equivalent induced expansion that has developed in the member under the experienced boundary conditions, inferred from microscopic and mechanical indicators interpreted against the benchmark database of Sanchez et al. [18].

The equality line in Figure 9.16 provides a direct reference for interpreting the relationship between the two estimates. Data points close to the equality line indicate comparable magnitudes between the induced expansion inferred from deterioration and the equivalent expansion inferred from "potential chemical advancement". Data points below the equality line indicate that the "potential chemical advancement"-based estimate exceeds the deterioration-based induced expansion, suggesting that the reaction progress inferred under favourable free-expansion conditions was partially accommodated in the structural member through cracking and creep effects induced by stresses arising from restrained expansion, etc. Data points above the equality

line indicate an opposite trend: the induced expansion inferred from deterioration exceeds the reconstructed equivalent free-expansion state, suggesting that the response expressed by the damage indicators is comparatively high relative to the inferred reaction progress. This comparison takes into account all the beams investigated in this research program (Chapters 6, 7, and 8).

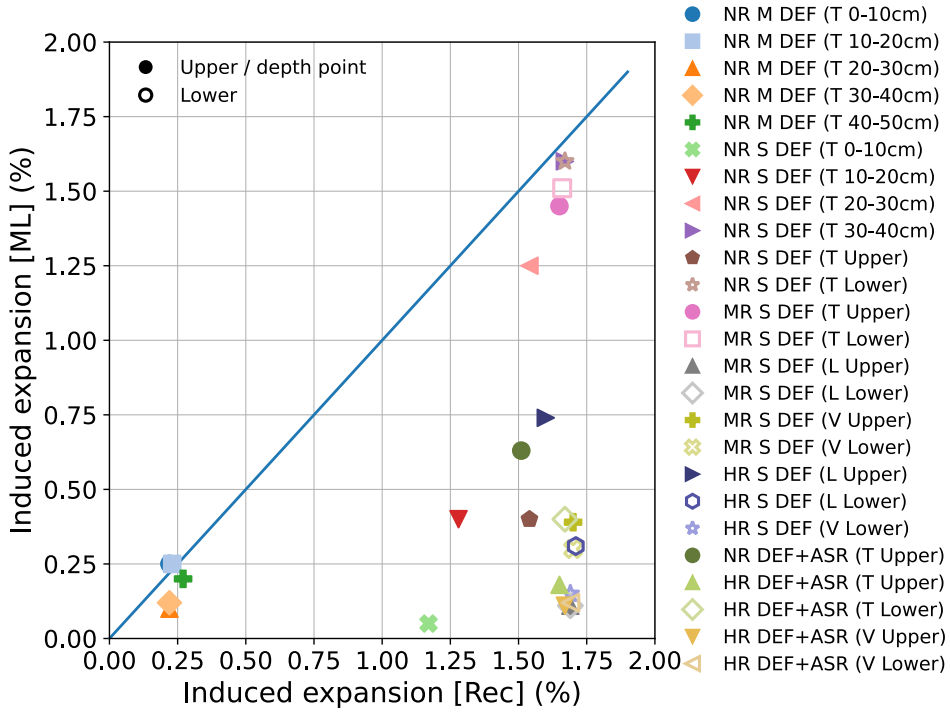
For the non-reinforced moderate DEF beam (NR M DEF), the "potential chemical advancement"-based estimates remain clustered at approximately 0.22–0.27%, whereas the deterioration-based induced expansion varies between 0.10% and 0.25% along the height. This pattern indicates that the reconstructed free-expansion state was relatively uniform, while the induced response inferred from deterioration was lower at intermediate depths. This separation follows the moisture-transfer conditions experienced, and the corresponding damage gradients, in which delayed wetting and a reduced damage expression at mid-height limited the translation of imposed chemical expansion into an induced expansion recorded by the multi-level indicators.

For the non-reinforced severe DEF beam (NR S DEF), Figure 9.16 shows a clearer separation between upper layers and mid-depth, with distinct degrees of alignment between both approaches. At 20–40 cm, the "potential chemical advancement"-based estimates (1.54–1.67%) and the deterioration-based induced expansion (1.25–1.60%) are of comparable magnitude, indicating that a large fraction of the imposed chemical expansion inferred from reaction progress was expressed as induced expansion in the member, which aligns with the advanced damage state identified by the microscopic and mechanical assessment. In contrast, at 0–20 cm, the "potential chemical advancement"-based estimates (1.17–1.28%) pronouncedly exceeded the deterioration-based induced expansion (0.05–0.40%), indicating that the equivalent free-expansion state inferred under favourable moisture conditions was not fully expressed as induced expansion in the upper part at coring time. This divergence follows the moisture-transfer behavior, in which the upper part experienced longer intervals of moisture limitation, thereby delaying DEF mobilisation and limiting the development of the cracking condition required for the imposed chemical expansion to translate into a comparable induced expansion.

The reinforced beams extend this comparison by showing that high "potential chemical advancement"-based expansion states can coexist with comparatively low deterioration-based induced expansions, and that this separation is direction dependent. For the moderately reinforced severe DEF beam (MR S DEF), the "potential chemical advancement"-based estimates remain

high and narrowly distributed (1.65–1.70%), whereas the deterioration-based induced expansion spans a wide range from 0.11% in the longitudinal direction to 1.45–1.51% in the transverse direction. For the heavily reinforced severe DEF beam (HR S DEF), the same trend persists, with "potential chemical advancement"-based estimates of 1.60–1.71% and induced expansion ranging from 0.15% to 1.15% depending on direction and part. For the heavily reinforced DEF+ASR beam (HR DEF+ASR), the "potential chemical advancement"-based estimates remain high (1.65–1.69%), whereas the induced expansions remain low (0.11–0.40%) in the evaluated directions. These patterns indicate that, under reinforcement-induced restraint, the reaction progress inferred through reconstruction can advance to a high equivalent free-expansion state without generating an equivalent induced expansion expressed by the deterioration indicators. This separation aligns with the anisotropic cracking condition discussed in Sections 9.6.1.2 and 9.6.1.3, in which reinforcement configuration influences crack orientation and crack opening, thereby affecting the efficiency with which imposed chemical expansion translates into an induced expansion recorded through stiffness loss and damage indices.

This comparison shows that the two approaches constrain complementary aspects of the current condition that must be carried forward into the prognosis discussion. The "potential chemical advancement"-based reconstruction constrains reaction progress relative to the free-expansion potential of the material, providing an estimate of the equivalent expansion state under favourable conditions. The deterioration-based induced expansion constrains the extent to which an equivalent induced expansion has developed in the affected structural members under their actual boundary conditions (i.e., moisture history and self-weight), integrating imposed expansion, time-dependent deformation, and prior cracking.



Legend: NR – non-reinforced. MR – moderately reinforced. HR – heavily reinforced. M – moderate (DEF potential). S- severe (DEF potential). T – transverse direction. L – longitudinal direction. V – vertical direction. The ranges (e.g., 0-10 cm), upper, and lower refer to specific height locations of the beams.

Figure 9.16 – Comparison between deterioration-based induced expansion and "potential chemical advancement"-based expansion estimates.

9.6.3 Projection of future expansion potential from the current condition

The projection approach combines, for each beam region and coring direction, the deterioration-based estimate of the induced expansion at coring time, $\varepsilon_{ML}(t_{coring})$, with a probabilistic representation of the residual expansion capacity measured under favourable immersion conditions. Residual expansion testing provides a time series of axial expansions, $\varepsilon_{meas}(t_i)$, and the analysis is formulated on the incremental swelling that develops during the test rather than on the absolute expansion level of the extracted core. For this reason, the measured series is expressed as a residual increment relative to the first finite reading t_0, defining the observed residual increment as stated in Equation (9.12).

The residual response is represented using a Larive-type sigmoidal function written in residual form, as given in Equation (9.13). In this formulation, $\varepsilon_{\infty,res}$ denotes the asymptotic residual expansion reached under the residual expansion test conditions, while $\tau_{L,res}$ and $\tau_{C,res}$ are apparent

residual time parameters referenced to the residual-test time origin. These parameters describe the kinetics of the residual test response and are not interpreted as material free-expansion parameters. The observed residual increments are then modelled as Gaussian random variables centred on the residual Larive prediction, with mean $\mu_{res,i}$ and within-test scatter σ_{res}, as defined in Equation (9.14).

Weakly informative priors are adopted to constrain the residual parameters to physically reasonable ranges while allowing the observed residual expansion data to govern the calibration. The prior definitions used for $\varepsilon_{\infty,res}$, $\tau_{L,res}$, $\tau_{C,res}$, and σ_{res} are provided in Equation (9.15). The posterior distribution of the residual parameters is obtained through Bayes' theorem (Equation 9.16), using a Gaussian likelihood expressed as a product over the observations (Equation 9.17). Posterior sampling is performed by Markov chain Monte Carlo, and each posterior draw is propagated through the residual Larive model to generate a predicted residual expansion increment trajectory, $\varepsilon_{res}^{pred}(t)$, evaluated on a uniform time grid. Uncertainty in the predicted residual increment is summarised at each time t using a 95% highest-density interval, as defined in Equation (9.18).

The diagnostic-to-prognostic projection is obtained by superimposing the predicted residual increment onto the current induced expansion inferred from the multi-level protocol. For each region and direction, the projected induced- expansion trajectory is therefore written as $\varepsilon_{tot}(t) = \varepsilon_{ML}(t_{coring}) + \varepsilon_{res}^{pred}(t)$, as stated in Equation (9.19). The corresponding uncertainty envelope is obtained by shifting the residual highest-density interval by the deterministic offset $\varepsilon_{ML}(t_{coring})$, yielding the total 95% highest-density interval defined in Equation (9.20).

$$\varepsilon_{res,i}^{obs} = \varepsilon_{meas}(t_i) - \varepsilon_{meas}(t_0) \tag{9.12}$$

$$\varepsilon_{res}(t \mid \varepsilon_{\infty,res}, \tau_{L,res}, \tau_{C,res}) = \varepsilon_{\infty,res} \frac{1 - exp\left(-\frac{t}{\tau_{C,res}}\right)}{1 + exp\left(-\frac{t - \tau_{L,res}}{\tau_{C,res}}\right)} \tag{9.13}$$

$$\varepsilon_{res,i}^{obs} \backsim N\left(\mu_{res,i}, \sigma_{res}^2\right), \quad \mu_{res,i} = \varepsilon_{res}\left(t_i \mid \varepsilon_{\infty,res}, \tau_{L,res}, \tau_{C,res}\right), \tag{9.14}$$

$$\varepsilon_{\infty,res} \backsim Uniform\left(0, 2.0 \max \varepsilon_{res,i}^{obs}\right), \tau_{C,res} \backsim Uniform(1, 200), \tau_{L,res} \backsim Uniform(0, 200), \quad \sigma_{res} \backsim HalfUniform(0.01), \tag{9.15}$$

$$p\left(\varepsilon_{\infty,res}, \tau_{L,res}, \tau_{C,res}, \sigma_{res} \mid \varepsilon_{res}^{obs}\right) \propto p\left(\varepsilon_{res}^{obs} \mid \varepsilon_{\infty,res}, \tau_{L,res}, \tau_{C,res}, \sigma_{res}\right)\ p(\varepsilon_{\infty,res})\, p\left(\tau_{L,res}\right) p\left(\tau_{C,res}\right) p(\sigma_r \quad (9.16)$$

$$p\left(\varepsilon_{res}^{obs} \mid \varepsilon_{\infty,res}, \tau_{L,res}, \tau_{C,res}, \sigma_{res}\right) = \prod_i N\left(\varepsilon_{res,i}^{obs} \mid \varepsilon_{res}\left(t_i \mid \varepsilon_{\infty,res}, \tau_{L,res}, \tau_{C,res}\right), \sigma_{res}^2\right), \quad (9.17)$$

$$HDI_{0.95}(t) = \left[\varepsilon_{low,res}(t), \varepsilon_{high,res}(t)\right] \quad (9.18)$$

$$\varepsilon_{tot}(t) = \varepsilon_{ML}(t_{coring}) + \varepsilon_{res}^{pred}(t) \quad (9.19)$$

$$HDI_{0.95}^{tot}(t) = \left[\varepsilon_{ML}\left(t_{coring}\right) + \varepsilon_{low,res}(t), \varepsilon_{ML}\left(t_{coring}\right) + \ \varepsilon_{high,res}(t)\right] \quad (9.20)$$

Figure 9.17 presents the diagnostic-to-prognostic induced- expansion trajectories obtained by adding the Bayesian residual-expansion increment to the current induced expansion estimated through the multi-level assessment protocol. For all beams, the projections rise rapidly at early times and then stabilise progressively, while the uncertainty envelopes remain narrow.

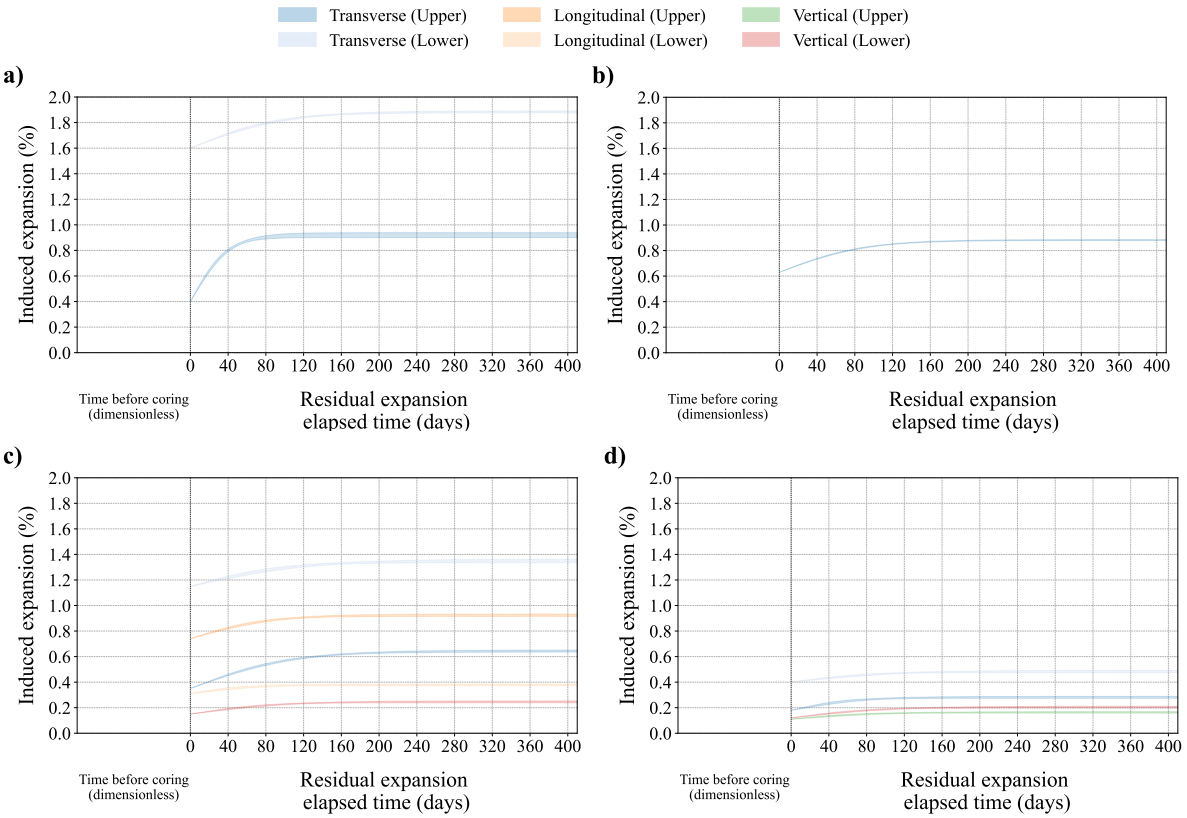


Figure 9.17 – Diagnostic-to-prognostic representation of a) non-reinforced (DEF), b) non-reinforced (DEF+ASR), c) heavily reinforced (DEF), and d) heavily reinforced (DEF+ASR) obtained by combining the current induced-expansion estimated through the multi-level assessment protocol with the Bayesian modeling of residual expansion.

The non-reinforced (DEF) (Figure 9.17a) shows a strong upper–lower contrast. The lower part shows a higher induced expansion at coring, indicating greater reaction advancement during ageing under higher moisture availability, and a smaller residual-expansion increment, which limits its additional swelling capacity under favourable moisture. The upper part shows a lower induced expansion at coring, indicating lower reaction advancement during aging, but it also shows a steeper early residual-expansion increment and reaches a similar plateau, indicating a larger remaining swelling capacity. The lower part concentrates the highest current damage extent, whereas the upper part concentrates the higher potential for additional induced damage development if moisture conditions become favourable.

The non-reinforced (DEF+ASR) (Figure 9.17b) shows extensive damage at coring, indicating a high degree of reaction advancement under aging exposure. The projected increment during residual expansion is modest, indicating limited remaining swelling capacity and the potential for further damage once favourable moisture is imposed.

The heavily reinforced (DEF) (Figure 9.17c) shows the clearest directional separation, indicating that reinforcement restraint redistributed the induced expansion among directions. The transverse trajectories reach the highest levels, while the longitudinal and vertical trajectories remain lower, indicating lower reaction advancement and lower induced damage in those directions at coring. The residual-expansion increments remain limited compared with the current induced-expansion. The direction-dependent induced expansion suggests that the transverse direction is likely to develop further induced cracking and stiffness loss than the other directions.

The heavily reinforced (DEF+ASR) (Figure 9.17d) remains at low induced-expansion levels and shows only a small residual-expansion increment in the measured directions, indicating limited reaction advancement at coring and limited remaining swelling capacity once favourable moisture is imposed. Upper–lower differences are small, and the trajectories stabilise early, which indicates a weak regional contrast under this configuration. Compared with the heavily reinforced (DEF) member (Figure 9.17c), the combined mechanism under heavy reinforcement leads to lower induced expansion at coring and a reduced potential for additional induced damage development, while the pronounced directional hierarchy observed in Figure 9.17c becomes much less expressed in Figure 9.17d.

9.7 Conclusions

This study evaluated how reinforcement-induced restraint and moisture gradients affect the diagnosis and prognosis of concrete beams affected by DEF- and DEF+ASR-. The analysis combined microscopic assessments (DRI and crack geometry), mechanical testing (SDT), measurements of residual expansion, semi-empirical moisture-transfer modeling, and Bayesian modeling of residual expansion. The following conclusion could be drawn.

- DEF- and DEF+ASR-induced damage exhibited a clear dependence on member height because upper and lower regions experienced distinct moisture histories prior to coring; this height dependence extended to prognosis, since regions with lower damage extent at coring exhibited higher residual-expansion increments and, consequently, a higher potential for additional induced deterioration under renewed favourable moisture.
- Reinforcement-induced restraint imposed direction-dependent constraints on damage development and on the potential for further deterioration, redistributing induced expansion among coring directions and limiting crack opening and stiffness loss in the most restrained directions, while preserving a higher susceptibility to additional induced damage in the less restrained direction(s), as evidenced by the directional hierarchy of the diagnostic-to-prognostic trajectories.
- Moisture availability governed the relative contribution of DEF- and ASR-type deterioration features to the overall damage: DEF-related features concentrated in the most water-available regions, whereas ASR-related features remained significant under less favourable moisture, leading to a height-dependent partitioning of mechanism contributions that became more uniform when top-surface wetting increased water availability over a larger fraction of the member.
- The comparison between the multi-level assessment protocol and the reconstruction-based "potential chemical advancement" estimation showed that reaction advancement can reach a late state while the induced damage expression inferred from microscopy and mechanics remains direction dependent under restraint; agreement between approaches occurred mainly where moisture exposure enabled sustained reaction development, whereas

divergence increased in restrained directions and in regions where crack-network accommodation reduced the measurable expansion and stiffness loss.

- The diagnosis-to-prognosis framework provided probabilistic uncertainty envelopes of future induced expansion, clearly expressing the influence of the boundary conditions on the diagnosis and prognosis of DEF- and DEF+ASR-affected concrete; the Bayesian formulation strengthened this representation by replacing a single deterministic residual-expansion increment with a bounded interval that captures measurement scatter and limited replication and supports conservative serviceability screening through the upper envelope.

9.8 References

[1] B. Fournier, M.-A. Bérubé, Alkali-aggregate reaction in concrete: a review of basic concepts and engineering implications, Canadian Journal of Civil Engineering 27 (2000) 167–191. https://doi.org/10.1139/l99-072.

[2] P. Fasseu, B. Mahut, Aide à la gestion des ouvrages atteints de réactions de gonflement interne : Guide méthodologique, GUIDES TECHNIQUES, Laboratoire Central des Ponts et Chaussées (LCPC), Paris, 2003.

[3] L.F.M. Sanchez, Internal Swelling Reactions in Concrete: Mechanisms and Condition Assessment, 1st ed., CRC Press, Boca Raton, 2024. https://doi.org/10.1201/9781003188155.

[4] F. Toutlemonde, Structural implications and management of infrastructure assets affected by ISR: example of French experience on road bridges, Canadian Journal of Civil Engineering 52 (2025) 1843–1851. https://doi.org/10.1139/cjce-2025-0120.

[5] B. Godart, J. Wood, Interaction of DEF and AAR, a review, Revista Portuguesa de Engenharia de Estruturas. Ed. LNEC. 3 (2021) 25–34.

[6] K. Scrivener, J.P. Skalny, eds., Internal sulfate attack and delayed ettringite formation: Proceedings of the International RILEM TC 186-ISA Workshop, Villars, Switzerland, 4–6 September 2002, RILEM Proceedings PRO 35, RILEM publications, in: 2004.

[7] A. Campos, C.M. López, A. Blanco, A. Aguado, Effects of an internal sulfate attack and an alkali-aggregate reaction in a concrete dam, Constr Build Mater 166 (2018) 668–683. https://doi.org/10.1016/j.conbuildmat.2018.01.180.

[8] V. Johansen, N. Thaulow, J. Skalny, Simultaneous presence of alkali — silica gel and ettringite in concrete, Advances in Cement Research 5 (1993) 23–29. https://doi.org/10.1680/adcr.1993.5.17.23.

[9] M.M. Karthik, J.B. Mander, S. Hurlebaus, Deterioration data of a large-scale reinforced concrete specimen with severe ASR/DEF deterioration, Constr Build Mater 124 (2016) 20–30. https://doi.org/10.1016/j.conbuildmat.2016.07.072.

[10] K. Ma, G. Long, Y. Xie, A real case of steam-cured concrete track slab premature deterioration due to ASR and DEF, Case Studies in Construction Materials 6 (2017) 63–71. https://doi.org/10.1016/j.cscm.2016.12.001.

[11] P. Tepponen, B.E. Eriksson, Damages in Concrete Railway Sleepers in Finland., Nordic Concrete Research (1987) 199–209.

[12] A.S. Silva, A.F. Gonçalves, M. Pipa, Diagnosis and prognosis of Portuguese concrete railway sleepers degradation – A combination of ASR and DEF, in: M.A.T.M. Broekmans, B.J. Wigum (Eds.), 13th International Conference on Alkali-Aggregate Reaction in Concrete (13th ICAAR), NGU/ICAAR, Trondheim, Norway, 2008.

[13] S.O. Ekolu, M.D.A. Thomas, R.D. Hooton, Implications of pre-formed microcracking in relation to the theories of DEF mechanism, Cem Concr Res 37 (2007) 161–165. https://doi.org/10.1016/j.cemconres.2006.10.014.

[14] M. Collepardi, A state-of-the-art review on delayed ettringite attack on concrete, Cem Concr Compos 25 (2003) 401–407. https://doi.org/10.1016/S0958-9465(02)00080-X.

[15] H.F.W. Taylor, C. Famy, K.L. Scrivener, Delayed ettringite formation, Cem Concr Res 31 (2001) 683–693. https://doi.org/10.1016/S0008-8846(01)00466-5.

[16] R.P. Martin, J.C. Renaud, F. Toutlemonde, Experimental investigations concerning combined delayed ettringite formation and alkali aggregate reaction, in: P. Castro-Borges, E.I. Moreno, K. Sakai, O.E. Gjørv, N. Banthia (Eds.), 6th International Conference on Concrete under Severe Conditions (CONSEC10), CRC Press, Mérida, Yucatán, Mexico, 2010: pp. 287–295. https://hal.science/hal-00904253.

[17] L.F.M. Sanchez, T. Drimalas, B. Fournier, Assessing condition of concrete affected by internal swelling reactions (ISR) through the Damage Rating Index (DRI), Cement 1–2 (2020) 100001. https://doi.org/10.1016/j.cement.2020.100001.

[18] L.F.M. Sanchez, T. Drimalas, B. Fournier, D. Mitchell, J. Bastien, Comprehensive damage assessment in concrete affected by different internal swelling reaction (ISR) mechanisms, Cem Concr Res 107 (2018) 284–303. https://doi.org/10.1016/j.cemconres.2018.02.017.

[19] H. Bouzabata, S. Multon, A. Sellier, H. Houari, Swellings due to alkali-silica reaction and delayed ettringite formation: Characterisation of expansion isotropy and effect of moisture conditions, Cem Concr Compos 34 (2012) 349–356. https://doi.org/10.1016/j.cemconcomp.2011.10.006.

[20] H.V.A.N. Sanjeewa, S. Asamoto, K. Nagai, J. Luo, Investigation of the compressive behaviour of restrained concrete with DEF and ASR-DEF deteriorations, Constr Build Mater 481 (2025) 141586. https://doi.org/10.1016/j.conbuildmat.2025.141586.

[21] J. Maalouf, H. Cagnon, J. Verdier, S. Multon, J. Jabbour, D. Bouhjiti, Impact of alkali-silica reaction and delayed ettringite formation-induced cracking on air permeability and water diffusivity in concrete, Case Studies in Construction Materials 22 (2025) e04183. https://doi.org/10.1016/j.cscm.2024.e04183.

[22] P. Morenon, Modélisation des réactions de gonflement interne des bétons avec prise en compte des couplages poro- mécaniques et chimiques, PhD thesis, Université Toulouse III – Paul Sabatier, 2017.

[23] R.P. Martin, Analyse sur structures modèles des effets mécaniques de la réaction sulfatique interne du béton, PhD thesis, Université Paris Est., 2010. https://theses.hal.science/tel-00558200.

[24] R.-P. Martin, L. Sanchez, B. Fournier, F. Toutlemonde, Evaluation of different techniques for the diagnosis & prognosis of Internal Swelling Reaction (ISR) mechanisms in concrete, Constr Build Mater 156 (2017) 956–964. https://doi.org/10.1016/j.conbuildmat.2017.09.047.

[25] K.J. Folliard, M.D.A. Thomas, B. Fournier, Protocol for the Diagnosis and Prognosis of Concrete Structures Affected by Alkali-Silica Reaction and/or Delayed Ettringite Formation, Concrete Durability Center, The University of Texas at Austin, Austin, Texas, USA, 2007.

[26] A. Shayan, I. Ivanusec, An experimental clarification of the association of delayed ettringite formation with alkali-aggregate reaction, Cem Concr Compos 18 (1996) 161–170. https://doi.org/10.1016/0958-9465(96)00012-1.

[27] Z. Owsiak, The effect of delayed ettringite formation and alkali-silica reaction on concrete microstructure, Ceramics – Silikáty 54 (2010) 277–283.

[28] P. Goltermann, Mechanical Predictions of Concrete Deterioration; Part 2: Classification of Crack Patterns, ACI Mater J 92 (1995) 58–63. https://doi.org/10.14359/1177.

[29] R.J. Detwiler, P.C. Taylor, Specifier's guide to durable concrete: Engineering Bulletin 221, Portland Cement Association, Skokie, IL, USA, 2005.

[30] J.M. Ponce, O.R. Batic, Different manifestations of the alkali-silica reaction in concrete according to the reaction kinetics of the reactive aggregate, Cem Concr Res 36 (2006) 1148–1156. https://doi.org/10.1016/j.cemconres.2005.12.022.

[31] F. Rajabipour, H. Maraghechi, G. Fischer, Investigating the Alkali-Silica Reaction of Recycled Glass Aggregates in Concrete Materials, Journal of Materials in Civil Engineering 22 (2010) 1201–1208. https://doi.org/10.1061/(ASCE)MT.1943-5533.0000126.

[32] N.R. Joshi, A. Matsumoto, S. Asamoto, T. Miura, Y. Kawabata, Investigation of the mechanical behaviour of concrete with severe delayed ettringite formation expansion focusing on internal damage propagation under various compressive loading patterns, Cem Concr Compos 128 (2022) 104433. https://doi.org/10.1016/j.cemconcomp.2022.104433.

[33] W. Chen, H.J.H. Brouwers, Alkali binding in hydrated Portland cement paste, Cem Concr Res 40 (2010) 716–722. https://doi.org/10.1016/j.cemconres.2009.12.007.

[34] Y. Kawabata, C. Dunant, K. Yamada, K. Scrivener, Impact of temperature on expansive behavior of concrete with a highly reactive andesite due to the alkali–silica reaction, Cem Concr Res 125 (2019) 105888. https://doi.org/10.1016/j.cemconres.2019.105888.

[35] A.E.K. Jones, L.A. Clark, The effects of restraint on ASR expansion of reinforced concrete, Magazine of Concrete Research 48 (1996) 1–13. https://doi.org/10.1680/macr.1996.48.174.1.

[36] C. Gravel, G. Ballivy, Expansion of AAR Concrete under Triaxial Stresses: Simulation with Instrumented Concrete Block, in: Proc. 11th Int. Conf. Alkali Aggreg. React., Quebec (Canada), 2000.

[37] S. Multon, F. Toutlemonde, Effect of applied stresses on alkali–silica reaction-induced expansions, Cem Concr Res 36 (2006) 912–920. https://doi.org/10.1016/j.cemconres.2005.11.012.

[38] M.-A. Bérubé, N. Smaoui, B. Fournier, B. Bissonnette, B. Durand, Evaluation of the expansion attained to date by concrete affected by alkali–silica reaction. Part III: Application to existing structures, Canadian Journal of Civil Engineering 32 (2005) 463–479. https://doi.org/10.1139/l04-104.

[39] J. Liaudat, I. Carol, C.M. López, V.E. Saouma, ASR expansions in concrete under triaxial confinement, Cem Concr Compos 86 (2018) 160–170. https://doi.org/10.1016/j.cemconcomp.2017.10.010.

[40] A. Zahedi, Evaluating ASR Physicochemical Process Under Distinct Restraint Conditions for a Better Assessment of Affected Concrete Infrastructure, PhD thesis, University of Ottawa, 2022.

[41] A. Allard, S. Bilodeau, F. Pissot, B. Fournier, J. Bastien, B. Bissonnette, Expansive behavior of thick concrete slabs affected by alkali-silica reaction (ASR), Constr Build Mater 171 (2018) 421–436. https://doi.org/10.1016/j.conbuildmat.2018.03.159.

[42] P. Morenon, S. Multon, A. Sellier, E. Grimal, F. Hamon, E. Bourdarot, Impact of stresses and restraints on ASR expansion, Constr Build Mater 140 (2017) 58–74. https://doi.org/10.1016/j.conbuildmat.2017.02.067.

[43] S. Multon, J.F. Seignol, F. Toutlemonde, Structural Behavior of Concrete Beams Affected by Alkali-Silica Reaction, ACI Mater J 102 (2005) 67–76. https://doi.org/10.14359/14299.

[44] D.M. Wald, M.T. Allford, O. Bayrak, T.D. Hrynyk, Development and multiaxial distribution of expansions in reinforced concrete elements affected by alkali–silica reaction, Structural Concrete 18 (2017) 914–928. https://doi.org/10.1002/suco.201600220.

[45] D. Wald, G.A. Martinez, O. Bayrak, Expansion behavior of a biaxially reinforced concrete member affected by alkali-silica reaction, Structural Concrete 18 (2017) 550–560. https://doi.org/10.1002/suco.201600143.

[46] W. Koyangi, K. Rokugo, Y. Uchida, Properties of Concrete Deteriorated by Alkali Aggregate Reaction under Various Reinforcement Ratios, in: Proc. 9th Int. Conf. Alkali-Aggregate React. Concr., London (UK), 1992: pp. 556–563.

[47] H. Bouzabata, S. Multon, A. Sellier, H. Houari, Effects of restraint on expansion due to delayed ettringite formation, Cem Concr Res 42 (2012) 1024–1031. https://doi.org/10.1016/j.cemconres.2012.04.001.

[48] N. Smaoui, Contribution à l'´evaluation du comportement structural des ouvrages d'arts affectés de réaction alcalis-silice, Québec, Canada, 2003.

[49] N.R. Joshi, A. Matsumoto, S. Asamoto, T. Miura, Y. Kawabata, Investigation of the mechanical behaviour of concrete with severe delayed ettringite formation expansion focusing on internal damage propagation under various compressive loading patterns, Cem Concr Compos 128 (2022) 104433. https://doi.org/10.1016/j.cemconcomp.2022.104433.

[50] Y. Thiebaut, S. Multon, A. Sellier, L. Lacarrière, L. Boutillon, D. Belili, L. Linger, F. Cussigh, S. Hadji, Effects of stress on concrete expansion due to delayed ettringite formation, Constr Build Mater 183 (2018) 626–641. https://doi.org/10.1016/j.conbuildmat.2018.06.172.

[51] Y. Kawabata, T. Miura, M. Fujishima, N. Ueda, Y. Takahashi, S. Asamoto, S. Multon, R.-P. Martin, J.-F. Seignol, Influence of Reinforcing Rebar on Expansion due to Delayed Ettringite Formation along the Bonding Length – Part I: The Role of Bond on Expansive Behavior of Concrete, Journal of Advanced Concrete Technology 21 (2023) 851–868. https://doi.org/10.3151/jact.21.851.

[52] A. Zahedi, C. Trottier, L.F.M. Sanchez, M. Noël, Microscopic assessment of ASR-affected concrete under confinement conditions, Cem Concr Res 145 (2021) 106456. https://doi.org/10.1016/j.cemconres.2021.106456.

[53] R.A. Barbosa, S.G. Hansen, K.K. Hansen, L.C. Hoang, B. Grelk, Influence of alkali-silica reaction and crack orientation on the uniaxial compressive strength of concrete cores from slab bridges, Constr Build Mater 176 (2018) 440–451. https://doi.org/10.1016/j.conbuildmat.2018.03.096.

[54] A. Allard, F. Bilodeau, F. Pissot, B. Founier, J. Bastien, B. Bissonnette, Performance evaluation of thick concrete slabs affected by alkali-silica reaction (ASR) – Part I: materials aspects, in: 15th ICAAR., São Paulo, Brazil, 2016.

[55] S.S. Kongshaug, O. Oseland, T. Kanstad, M.A.N. Hendriks, E. Rodum, G. Markeset, Experimental investigation of ASR-affected concrete – The influence of uniaxial loading on the evolution of mechanical properties, expansion and damage indices, Constr Build Mater 245 (2020) 118384. https://doi.org/10.1016/j.conbuildmat.2020.118384.

[56] B.P. Gautam, D.K. Panesar, S.A. Sheikh, F.J. Vecchio, Effect of Multiaxial Stresses on Alkali-Silica Reaction Damage of Concrete, ACI Mater J 114 (2017). https://doi.org/10.14359/51689617.

[57] A. Zahedi, C. Trottier, L. Sanchez, M. Noël, Evaluation of the induced mechanical deterioration of alkali-silica reaction affected concrete under distinct confinement conditions through the Stiffness Damage Test, Cem Concr Compos 126 (2022) 104343. https://doi.org/10.1016/j.cemconcomp.2021.104343.

[58] M. Al Shamaa, S. Lavaud, L. Divet, G. Nahas, J.M. Torrenti, Influence of relative humidity on delayed ettringite formation, Cem Concr Compos 58 (2015) 14–22. https://doi.org/10.1016/j.cemconcomp.2014.12.013.

[59] R.-P. Martin, F. Toutlemonde, C. Sauvaget, Effects of Alternative Wetting and Drying on the Development of Delayed Ettringite Formation, in: L.F.M. Sanchez, C. Trottier (Eds.), 17th International Conference on Alkali-Aggregate Reaction in Concrete (ICAAR), RILEM

Bookseries, Volume 49, Springer, Ottawa, 2024: pp. 176–183. https://doi.org/10.1007/978-3-031-59419-9_21.

[60] L. Divet, A. Pavoine, Delayed Ettringite Formation in massive concrete structures: an account of some studies of degraded bridges, in: K. and S.J.P. Scrivener (Ed.), International RILEM TC 186-ISA Workshop on Internal Sulfate Attack and Delayed Ettringite Formation, Villars, Switzerland, 2002: pp. 98–126.

[61] L. Graf, Effect of relative humidity on expansion and microstructure of heat- cured mortars, Skokie, Illinois, USA: RD139, 2007.

[62] O.D. Olajide, M.R. Nokken, L.F.M. Sanchez, Alkali–Silica Reactions: Literature Review on the Influence of Moisture and Temperature and the Knowledge Gap, Materials 17 (2023) 10. https://doi.org/10.3390/ma17010010.

[63] L.-O. Nilsson, O. Peterson, Alkali-silica reactions in Scania, Sweden: a moisture problem causing pop-outs in concrete floors, Lund, Sweden, 1983. https://portal.research.lu.se/files/4604450/1594285.pdf.

[64] H. Ólafsson, The Effect of Relative Humidity and Temperature on Alkali Expansion of Mortar Bars, in: P.E. Grattan-Bellew (Ed.), Concrete Alkali-Aggregate Reactions: Proceedings of the 7th International Conference, 1986, Ottawa, Canada, Noyes Publications, Ottawa, ON, Canada, 1987: pp. 461–465. https://icaarconcrete.org/wp-content/uploads/2024/04/7ICAAR-OlafssonH-1.pdf.

[65] P.A. Dunbar, P.E. Grattan-Bellew, Results of damage rating evaluation of condition of concrete from a number of structures affected by AAR, in: B. Fournier (Ed.), Proceedings of the CANMET/ACI International Workshop on Alkali-Aggregate Reactions in Concrete, CANMET/ACI, Dartmouth (Nova Scotia), 1995: pp. 257–265.

[66] P.E. Grattan-Bellew, A. Danay, Comparison of laboratory and field evaluation of alkali-silica reaction in large dams, in: Proceedings of the International Conference on Concrete Alkali–Aggregate Reactions in Hydroelectric Plants and Dams, Canadian Electrical Association; Canadian National Committee of the International Commission on Large Dams, Fredericton, New Brunswick, Canada , 1992: p. 23.

[67] V. Villeneuve, B. Fournier, J. Duchesne, Determination of the Damage in Concrete Affected by ASR—The Damage Rating Index (DRI), in: T. Drimalas, J. H. Ideker, B. Fournier (Eds.), 14th International Conference on Alkali-Aggregate Reaction (ICAAR), University of Texas at Austin, Austin, Texas, USA, 2012: p. 10. https://icaarconcrete.org/wp-content/uploads/2022/10/14ICAAR-VilleneuveV-1.pdf.

[68] P.E. Grattan-Bellew, L.D. Mitchell, Quantitative petrographic analysis of concrete –The Damage Rating Index (DRI) method, a review, in: Proc. Marc-André Bérubé Symposium on AAR in Concrete, CANMET/ACI Advances in Concrete Technology Seminar, CANMET/ACI, Montréal, Canada, 2006: pp. 321–334.

[69] L.F.M. Sanchez, B. Fournier, M. Jolin, J. Duchesne, Reliable quantification of AAR damage through assessment of the Damage Rating Index (DRI), Cem Concr Res 67 (2015) 74–92. https://doi.org/10.1016/j.cemconres.2014.08.002.

[70] B. Fournier, P.-L. Fecteau, V. Villeneuve, S. Tremblay, L. Sanchez, Description of petrographic features of damage in concrete used in the determination of the Damage Rating Index (DRI), Laval, Québec, Canada, 2015.

[71] V. Villeneuve, Détermination de l'endommagement du béton par méthode pétrographique quantitative, Master's thesis (Mémoire de maîtrise), Université Laval, 2011. https://www.collectionscanada.gc.ca/obj/thesescanada/vol2/QQLA/TC-QQLA-27962.pdf.

[72] R. Medeiros, L. Sanchez, A.C. dos Santos, Assessing Alkali-Carbonate Reaction-Induced Damage in Critical Concrete Infrastructure: The First ACR-Affected Field Structure Reported in Brazil, in: L.F. Sanchez, C. Trottier (Eds.), Proceedings of the 17th International Conference on Alkali-Aggregate Reaction in Concrete. ICAAR 2024.RILEM Bookseries, Springer, 2024: pp. 445–452. https://doi.org/10.1007/978-3-031-59349-9_51.

[73] L. Sanchez, B. Fournier, M. Jolin, M.A.B. Bedoya, J. Bastien, J. Duchesne, Use of Damage Rating Index to Quantify Alkali-Silica Reaction Damage in Concrete: Fine versus Coarse Aggregate, ACI Mater J 113 (2016) 395–407. https://doi.org/10.14359/51688983.

[74] O.D. Olajide, Multilevel Assessment of The Role of Moisture and Temperature in ASR-Induced Expansion and Deterioration, PhD, Concordia University, 2025.

[75] J.B. Walsh, The effect of cracks on the compressibility of rock, J Geophys Res 70 (1965) 381–389.

[76] R.S. Crouch, Specification for the Determination of Stiffness Damage Parameters from the Low Cyclic Uniaxial Compression of Plain Concrete Cores, Revision A, Mott, Hay & Anderson, Special Services Division, Internal Technical Note. (1987).

[77] T.M. Crisp, J.G.M. Wood, P. Norris, Towards Quantification of Microstructural Damage in AAR Deteriorated Concrete, in: International Conference on Recent Developments on the Fracture of Concrete and Rock, 1993.

[78] T.M. Crisp, P. Waldron, J.G.M. Wood, Development of a non destructive test to quantity damage in deteriorated concrete, Magazine of Concrete Research 45 (1989).

[79] L.F.M. Sanchez, B. Fournier, M. Jolin, J. Bastien, Evaluation of the Stiffness Damage Test (SDT) as a tool for assessing damage in concrete due to alkali-silica reaction (ASR): Input parameters and variability of the test responses, Constr Build Mater 77 (2015) 20–32. https://doi.org/10.1016/j.conbuildmat.2014.11.071.

[80] L.F.M. Sanchez, B. Fournier, M. Jolin, J. Bastien, Evaluation of the stiffness damage test (SDT) as a tool for assessing damage in concrete due to ASR: Test loading and output responses for concretes incorporating fine or coarse reactive aggregates, Cem Concr Res 56 (2014) 213–229. https://doi.org/10.1016/j.cemconres.2013.11.003.

[81] L.F.M. Sanchez, B. Fournier, M. Jolin, J. Bastien, D. Mitchell, Practical use of the Stiffness Damage Test (SDT) for assessing damage in concrete infrastructure affected by alkali-silica reaction, Constr Build Mater 125 (2016) 1178–1188. https://doi.org/10.1016/j.conbuildmat.2016.08.101.

[82] L.F.M. Sanchez, B. Fournier, D. Mitchell, J. Bastien, Condition assessment of an ASR-affected overpass after nearly 50 years in service, Constr Build Mater 236 (2020) 117554. https://doi.org/10.1016/j.conbuildmat.2019.117554.

[83] R. Medeiros, L. Sanchez, A.C. dos Santos, Exploring microscopic and mechanical tools to uncover the anisotropic damage evolution of prestressed concrete sleepers affected by internal swelling reactions, Magazine of Concrete Research 77 (2025) 891–902. https://doi.org/10.1680/jmacr.25.00060.

[84] R. Medeiros, D.J. De Souza, L.F.M. Sanchez, A.C. Santos, Condition assessment of pre-tensioning prestressed concrete sleepers distressed by internal swelling reactions (ISR), CEMENT 21 (2025) 100154. https://doi.org/10.1016/j.cement.2025.100154.

[85] A. Pavoine, L. Divet, Réaction sulfatique interne au béton : Essai d'expansion résiduelle sur carotte de béton extraite de l'ouvrage : Méthode d'essai n° 67, Techniques et méthodes des laboratoires des ponts et chaussées., Paris, 2009. https://doi.org/https://doi.org/10.3829/me67-fr.

[86] T. Ramlochan, P. Zacarias, M.D.A. Thomas, R.D. Hooton, The effect of pozzolans and slag on the expansion of mortars cured at elevated temperature, Cem Concr Res 33 (2003) 807–814. https://doi.org/10.1016/S0008-8846(02)01066-9.

[87] E. Giannini, K. Folliard, J. Zhu, O. Bayrak, K. Kreitman, B. Hanson, Non-Destructive Evaluation of In-Service Concrete Structures Affected by Alkali-Silica Reaction (ASR) or Delayed Ettringite Formation (DEF)—Final Report, Part I, 2013.

[88] S. Multon, F.-X. Barin, B. Godart, F. Toutlemonde, Estimation of the Residual Expansion of Concrete Affected by Alkali Silica Reaction, Journal of Materials in Civil Engineering 20 (2008) 54–62. https://doi.org/10.1061/(asce)0899-1561(2008)20:1(54).

[89] X. Brunetaud, Étude de l'influence de différents paramètres et de leurs interactions sur la cinétique de l'amplitude de la réaction sulfatique interne au béton, Ph.D. thesis, Châtenay-Malabry, Ecole centrale de Paris, 2005. https://theses.fr/2005ECAP1025.

[90] A. Pavoine, X. Brunetaud, Développement et validation d'une méthode d'essai vis-à-vis de la formation différée de l'ettringite Application à l'étude d'impact de différents paramètres sur la cinétique et l'amplitude de gonflement, (2010). https://doi.org/10.3829/erlpc.oa65-fr.

[91] R.-P. Martin, F. Toutlemonde, Theoretical and experimental validation of a simple method to reproduce representative DEF-prone conditions in laboratory, Mater Struct 46 (2013) 1245–1255. https://doi.org/10.1617/s11527-012-9967-2.

[92] ASTM International, ASTM C1778-22: Standard Guide for Reducing the Risk of Deleterious Alkali-Aggregate Reaction in Concrete, West Conshohocken, PA, 2022. https://doi.org/10.1520/C1778-22.

[93] L.F.M. Sanchez, B. Fournier, M. Jolin, D. Mitchell, J. Bastien, Overall assessment of Alkali-Aggregate Reaction (AAR) in concretes presenting different strengths and incorporating a wide range of reactive aggregate types and natures, Cem Concr Res 93 (2017) 17–31. https://doi.org/10.1016/j.cemconres.2016.12.001.

[94] L.F.M. Sanchez, Contribution to the assessment of damage in aging concrete infrastructures affected by alkali-aggregate reaction, PhD thesis, Université Laval, 2014. https://www.collectionscanada.ca/obj/thesescanada/vol2/QQLA/TC-QQLA-30764.pdf.

[95] S. Multon, F. Toutlemonde, Water distribution in concrete beams, Mater Struct 37 (2004) 378–386. https://doi.org/10.1007/BF02479634.

[96] S. Multon, F. Toutlemonde, Effect of moisture conditions and transfers on alkali silica reaction damaged structures, Cem Concr Res 40 (2010) 924–934. https://doi.org/10.1016/j.cemconres.2010.01.011.

[97] S. Multon, Évaluation expérimentale et théorique des effets mécaniques de l'alcali-réaction sur des structures modèles (Études et recherches des Laboratoires des Ponts et Chaussées, Série Ouvrages d'art, OA 46), Laboratoire Central des Ponts et Chaussées - LCPC., Paris, France, 2004.

[98] X. Zhu, Assessing Drying Shrinkage Induced Deterioration of Concrete Stored at Distinct Exposure Conditions, Master of applied science, University of Ottawa, 2024.

[99] R.-P. Martin, A. Bonnet, J.-C. Renaud, R. Chlela, F. Toutlemonde, C. Sauvaget, Influence of moisture on the development of delayed ettringite formation, Magazine of Concrete Research 75 (2023) 747–754. https://doi.org/10.1680/jmacr.22.00282.

Chapter 10: Scientific and Engineering contributions of the PhD thesis

As previously stated, this PhD study aims to have a better understanding of the effect of moisture gradients and reinforcement-induced restraint on the current induced damage condition and the potential for further deterioration of concrete affected by DEF and DEF+ASR. The specific findings of this research can be cited as being either scientific or engineering contributions, as presented hereafter:

Scientific contributions

- Understanding of the development of DEF- and ASR- (i.e., in single or combined mechanisms)-induced microscopic damage features, and the contribution of each mechanism to the "overall damage" in concrete members under distinct moisture gradients;
- Proposal of a qualitative microscopic damage model for concrete affected by DEF and DEF+ASR;
- Contributing the comprehension of the effect of reinforcement-induced restraint (≠ reinforcement configurations) on the DEF- and DEF+ASR-induced damage and future potential of expansion;
- Clarifying how microscopic damage features of DEF and DEF+ASR impact the mechanical behavior of restraint concrete specimens;
- Advancing the knowledge on the impact of the current damage condition on the future potential for further expansion of concrete affected by DEF and DEF+ASR.

Engineering contributions

- Demonstrate the diagnostic potential of the *Stiffness Damage Test (SDT)* and *Damage Rating Index* (DRI) for quantifying damage in DEF and DEF+ASR-affected concrete under various moisture gradients and reinforcement-induced restraint conditions;
- Validation/discussion of the global charts as "reference" values for estimating the current damage condition of DEF and DEF+ASR-affected concrete under moisture gradients and reinforcement-induced restraint;
- Advancing a semi-empirical modelling of moisture transfer to estimate the moisture gradients and adding the contribution of late water supply sourced from the top of DEF and DEF+ASR-affected beams;

- Proposal of a diagnosis-to-prognosis approach, combining estimated current-induced expansion and Bayesian modelling of residual expansion.

Chapter 11: Conclusion and recommendations

11.1 Conclusions

The main goals of this PhD work, for which detailed results were presented and analyzed in the four scientific papers, are presented hereafter, as a function of the main objectives of the research described in Chapter 3:

- Moisture gradients governed the development of DEF- and DEF+ASR-induced microscopic deterioration, and the microscopy analysis using the Damage Rating Index (DRI) provided a consistent basis to interpret damage distributions, crack-network characteristics, and the contribution of DEF- and ASR-induced features of deterioration to the "overall damage" as a function of water availability, with DEF-related features concentrating in the most water-accessible locations and ASR-related features remaining significant under less favourable moisture conditions.
- Distinct moisture histories produced distinct diagnosis-to-prognosis trajectories in non-reinforced members, in which locations exposed late water supply (i.e., rewetting) exhibited deterioration extent at coring but comparable to, or greater than, that observed under early and persistently to moisture exhibited advanced deterioration at coring and slightly lower residual expansion potential; the combined interpretation of microscopic (i.e., DRI), mechanical (i.e., SDT) diagnostic tools, and residual expansion therefore required a clear estimation of moisture-transfer history to avoid interpreting damage extent and future damage potential without reference to the prior exposure.
- Reinforcement-induced restraint modified both the magnitude and the directional DEF-induced deterioration under moisture gradients, limiting crack opening and stiffness loss in the most restrained directions while preserving higher susceptibility to additional induced deterioration in the less restrained directions, and producing direction-dependent anisotropy in DRI indicators, SDT indices, and residual expansion that reflects redistribution of induced expansion and associated damage.
- The stiffness damage test (SDT) and the Damage Rating Index (DRI) are diagnostic tools sensitive to evaluating and understanding the impact of moisture gradients and reinforcement-induced restraint on the current damage extent condition of DEF- and

DEF+ASR-affected members at the materials scale. The structural effects of under-dead-weight members are reflected in damage assessments combining mechanical (i.e., SDT) and microscopic (i.e., DRI) diagnostic tools. This is a very important finding to be considered in the condition assessment of DEF- and DEF+ASR-affected members in the field.

- A thorough analysis of the specimens retrieved from the different directions of DEF- and DEF+ASR-affected beams through the mechanical (i.e., SDT-NLI) tool indicates preferential orientation for DEF- and DEF+ASR-induced crack propagation. The majority of the cracks were developed parallel to longitudinal reinforcement-induced restrained directions. However, in some cases, the orientation of the cracks was identified towards another direction (e.g., transverse), which was attributed to the structural behaviour of the affected member. These findings are essential to be considered for assessing and understanding the structural performance of DEF- and DEF+ASR-affected reinforcement-induced restrained members.
- The additional development of the semi-empirical moisture-transfer modeling to estimate the drying front and late water supply provided an exposure-history understanding that clarified apparent contrasts between damage extent, stiffness degradation, and residual expansion across the height of the beams when the concrete experienced non-uniform humidity.
- The Bayesian formulation of residual expansion, combined with the induced expansion estimate at coring, replaced a single deterministic residual increment by bounded projection intervals that represent measurement scatter and limited replication, and it provides a practical screening framework in which conservative assessment can be supported by the upper envelope of projected induced expansion while preserving transparent uncertainty attribution.
- Evaluations of the reconstruction-based “potential chemical advancement” and the multi-level induced-expansion estimates clearly showed that the “potential chemical advancement” under continuously favourable moisture can substantially exceed the induced-expansion estimates in members subjected to non-uniform humidity and

reinforcement-induced restraint. This is attributed to internal self-restraint between wetter and drier zones and to the direction-dependent restraint imposed by reinforcement, which limits and redistributes induced expansion and the associated mechanical and microscopic induced damage at the member scale.

11.2 Recommendations for future works

After conducting extensive experimental research on the effect of moisture gradients and reinforcement-induced restraint on DEF- and DEF+ASR-affected concrete members, and considering the conclusions stated in Section 11.1, some recommendations and suggestions for future research can be proposed, as follows:

- Extend the experimental database by testing additional DEF- and DEF+ASR-affected members with broader reinforcement ratios and detailing (including distinct transverse-to-longitudinal reinforcement ratios) and additional moisture-gradient boundary conditions, with sampling throughout the aging process, in order to improve the diagnosis-to-prognosis trajectories and the robustness of direction-dependent interpretations at the material scale.
- Validate the proposed diagnosis-to-prognosis framework against member-scale monitoring under known boundary conditions and, when possible, field observations, by linking measured deformation, cracking evolution, and stiffness changes to the multi-level indicators (DRI, SDT, residual expansion) derived from extracted cores, with explicit accounting for the effects of dead weight, restraint, and time-dependent exposure history.
- Refine the interpretation of residual expansion for concretes with prior heterogeneous swelling by systematically quantifying the influence of coring-induced stress release, moisture re-equilibration, ionic leaching, and specimen geometry on residual expansion kinetics and magnitude, and by defining conditioning protocols and acceptance criteria that remain consistent across moisture histories and restraint conditions.
- Increase replication at the location and direction levels and expand the uncertainty quantification strategy by using the Bayesian formulation to establish statistically stable projection intervals, define conservative screening thresholds based on upper-envelope trajectories, and evaluate the sensitivity of projected future expansion to prior exposure history, cracking condition, and temperature and moisture conditioning.

- Integrate additional microstructural and chemical characterization to support the interpretation of mechanism contributions and reaction development, including systematic quantification of harmful ettringite features, ASR gel composition and distribution, and aggregate–paste interface degradation, and relate these observations to DRI approach to estimate the contribution of each mechanism to “overall damage”.
- Evaluate the contribution of implementing the finding in the materials scale as inputs for structural reassessment to better inform the characteristics of the material comprising the affected structure.